NTNU – Trondheim
Norwegian University of
Science and Technology

Dynamic Analysis of Offshore Concrete Structures subjected to Earthquake

Morten Amundsen

Civil and Environmental Engineering
Submission date: June 2012
Supervisor: Anders Rönnquist, KT
Co-supervisor: Ragnar Sigbjörnsson, KT

Norwegian University of Science and Technology
Department of Structural Engineering

Norges teknisk-
naturvitenskapelige universitet
NTNU
Institutt for konstruksjonsteknikk

Masteroppgave for Stud techn. Morten Amundsen, våren 2012

Dynamisk analyse av offshore betongkonstruksjoner belastet av jordskjelv

Dynamic analysis of offshore concrete structures subjected to earthquake

Jordskjelvsdimensjonering ble for fullt introdusert for norske konstruksjoner med den nye standarden NS 3491-12. Den nye standarden ble innført som en overgangsordning til den nå gjeldende standarden Eurocode 8. Med unntak av noen konstruksjonstyper skal alle bygninger, så vel nybygg som tilbygg, kontrolleres for jordskjelvbelastning.

I dag er vanlig praksis å benytte elastisk design med en kontroll om bygningen muligens tilfredsstiller kriterier for å utelate videre kontroll av seismisk påkjenning. Dersom seismisk design ikke kan utelates beregnes konstruksjonselementer og forbindelser etter de elastiske kreftene. I offshorekonstruksjoner er det nødvendig å implementere flere ikke-lineariteter i analysemodellen. Det er behov for å undersøke effekten som oppnås ved inkludering av disse, i forhold til vanlige dimensjoneringstilnærmelser.

Oppgaven skal kartlegge hvordan massive offshore konstruksjoner oppfører seg under jordskjelv. Det skal identifiseres og konkritiseres problemstillinger knyttet opp mot en representativ betongkonstruksjon, inklusive de analysemetoder som skal benyttes avhengig av type konstruksjon. Framtredende elementer i oppgaven er:

- Numerisk modell av representativ konstruksjon i Abaqus
- Vurdering av interne og eksterne dempingsforhold
- Hva skjer når konstruksjonen blir utsatt for store deformasjoner og flytning oppstår?
- Sammenligning av global analyse og kvasi-statisk lokal analyse
- Evaluering av vanlige dimensjoneringstilnærmelser

Det vil være opp til kandidaten å vektlegge de enkelte delene i oppgaven, der oppgaven utføres i henhold til retningslinjer for utførelse av hovedoppgaven ved Institutt for konstruksjonsteknikk, gitt på instituttets hjemmesider.

Faglærer: Anders Rönnquist og Ragnar Sigbjörnsson, NTNU

Besvarelsen skal leveres til Institutt for konstruksjonsteknikk innen 11. juni 2012

Preface

This thesis was written at the Norwegian University of Science and Technology (NTNU) in the time period between the 16. of January and the 11. of June. The thesis was aided by Multiconsult, with their involvement mainly consisting of the use of and support on their in-house design software.

I would like to thank my supervisors Anders Rønnquist and Ragnar Sigbjörnsson at NTNU and Erik Åldstedt at Multiconsult for their help throughout the semester.

Gratitude is also extended to Jan Arve Øverli and Kjell Magne Mathisen at NTNU, Erlend Eithun Aasheim, Dan Evert Brekke and Andrew Bekkelund at Multiconsult and Nils Arne Rakstad at Aker Solutions who greatly facilitated the work on this thesis.

A special thank you to Helene Alexandra Kornbrekke for her invaluable help with the layout of the thesis.

Summary

This thesis attempts to study the dynamic response of offshore concrete structures by sequentially introducing physical phenomena which are related to those types of analyses. This is done by modelling a simplified part of a typical offshore concrete structure, with the purpose of establishing a reference case, on which more advanced analyses can be based, as well as evaluate simplified approaches that serve to shorten the analysis time.

To establish characteristic earthquakes for the selected return periods of 475, 1000, 3000 and 10 000 years, a seismic hazard analysis is performed for an area slightly off the southwest coast of Norway. Here, information from 964 earthquakes was collected, such that the Gutenberg-Richter relationship could be established. Based on this, 50 000 earthquakes were generated based on Monte Carlo simulations, which served as an extrapolation from which order statistics could be performed. The determined characteristic earthquake parameters for the different return periods were found to have a remarkable similarity with the seismic zonation maps used in most design codes. Finally, the applied accelerogram for a given return period was simulated from a response spectrum which was chosen to be similar to the mean response spectrum for that return period.

A comparison was made between the time history and response spectrum analysis, where three modal combination methods were evaluated. It was found that the results were either impractically conservative, or dangerously unconservative for all return periods, suggesting that the response spectrum analysis is not applicable for the investigated structure.

A material model which included plasticity was evaluated, which resulted in marginally lower stresses, slightly reduced eigenfrequencies and small changes displacements of the top of the shaft. With the inclusion of elastic stiffness degradation, the results were similar, leading to the conclusion that plasticity is an unnecessary complication, as the large dimensions of the structure combined with the low seismicity of the North Sea results in a structural behaviour which is approximately elastic for all return periods.

Two methods for the modelling of surrounding water was tested. The first was the added mass method, where the stresses mostly increased, except for the 10 000-year earthquake. The second method was an acoustic-structural interaction, where the fluid around the structure was modelled. This resulted in similar stresses for all return periods, and gives credibility to the simplified method. For either methods, the eigenfrequencies were reduced significantly.

The soil upon which the structure rests was included into the analysis by two methods. The first method involved the use of springs and dashpots which were made to represent the stiffness and damping of the soil. The other method was a finite element analysis of the soil layer. Both soft and hard soil was tested, and for the soft soil, the stresses were radically reduced, as the structure became almost fully

isolated from the earthquake. The stiffer soil resulted in higher stresses. The two methods agreed for the soft soil, but not for the hard soil. This was found to be caused by the spring method being overly simplistic.

Sammendrag

Denne oppgaven forsøker å studere dynamisk respons av offshore betongkonstruksjoner ved å enkeltvis introdusere fysiske fenomener som er typiske for slike analyser. Dette gjøres ved å modellere en forenklet del av en typisk offshore betongkonstruksjon, med den hensikt å etablere et referansepunkt som mer avanserte analyser kan basere seg på, så vel som å evaluere forenklede framgangsmåter som har som hensikt å forkorte analysetiden.

For å etablere karakteristiske jordskjelv for de valgte returperiodene på 475, 1000, 3000 og 10 000 år, utføres en seismisk risikoanalyse for et område rett utenfor Norges sørvestre kyst. Her ble det samlet informasjon om 964 jordskjelv, slik at Gutenberg-Richter-relasjonen kunne etableres. Basert på dette, ble 50 000 jordskjelv generert ved hjelp av Monte Carlo-simuleringer, som fungerte som en ekstrapolering ordrestatistikk kunne benyttes på. De bestemte karakteristiske jordskjelvparametrene for de forskjellige returperiodene var funnet å ha bemerkelsesverdig likhet med de seismiske sonekartene som de fleste design-koder baserer seg på. Til slutt, ble det endelige akselerogrammet for en gitt returperiode simulert ut ifra et responsspektrum som var valgt slik at det lignet det midlere responsspektrum for denne returperioden.

En sammenligning mellom tidshistorie- og responsspekteranalyse ble utført, hvor tre modale kombinasjonsmetoder ble vurdert. Det ble funnet at resultatene var enten upraktisk konservative eller farlig ukonservative, som gir inntrykk av at en responsspekteranalyse ikke er anvendbar på den undersøkte konstruksjon.

En materialmodell som inkluderte plastisitet ble vurdert, som resulterte i marginalt lavere spenninger, så vidt reduserte egenfrekvenser og små forandringer i forskyvninger av toppen av skaftet. Med elastisk stivhetsdegradering inkludert ble resultatene lignende, som fører fram til konklusjonen at plastisitet er en unødvendig komplikasjon, siden de store dimensjonene til konstruksjonen kombinert med den lave jordskjelvsaktiviteten i Nordsjøen resulterer i at konstruksjonen oppfører seg omtrent elastisk for alle returperioder.

To metoder for modellering av omkringliggende vann ble testet. Den første var tilleggsmassemetoden, hvor spenningene hovedsaklig økte, bortsatt fra for 10 000-årsjordskjelvet. Den andre metoden var en interaksjon mellom et akustisk medium og konstruksjonen, hvor væsken rundt konstruksjonen ble modellert. Dette resulterte i lignende spenninger for all returperioder, og gir tillit til den forenklede metoden. For begge metodene ble egenfrekvensene markant redusert.

Jorden som konstruksjonen står på ble inkludert i analysen via to metoder. Den første metoden involverte bruken av fjærer og dempningselementer som representerte stivheten og dempingen til jorda. Den andre metoden var en elementmetodeanalyse av jordlaget. Både myk og hard jord ble undersøkt, og for den myke jorda ble spenningene kraftig redusert, siden konstruksjonen ble nesten fullstending isolert fra jordskjelvet. Den stivere jorda resulterte i høyere spenninger. De to metodene ga lignende resultater for den myke jorda, men ikke for den harde. Dette ble funnet

å ha sin forklaring i at fjærmetoden er for enkel.

Contents

List of Figures

List of Tables

1 Introduction

In the offshore industry today, much uncertainty exists in the treatment of seismic loads. The dynamic analysis of offshore structures can indeed be a challenge, with complex environmental interactions and inherent nonlinearities. This issue is exacerbated by a lack of reference cases for which the influence of these difficulties are known. In this thesis, such a reference case is established, with a number of complicating factors investigated.

The purpose of this study is to explore the effects of many difficulties one might encounter in the dynamic analysis of offshore structures, as well as evaluate simplifications that lead to lower analysis times. This is an interpretation of the thesis definition which more loosely answers the issues posed. The notion of investigating the structural response when a complication is applied is expanded to involve several complexities, rather than just plasticity. It is intended to start with as few assumptions as possible, and axiomatically establish a thorough analysis of the structural response due to the seismicity of the North Sea. To accomplish this, an earthquake hazard analysis is performed, contributing significantly to the contents of this thesis.

The basis for comparison is an elastic structure with surrounding water omitted. This omittance implies that the goal adopted herein is not to provide a practical case study, but rather a theoretical investigation of complicating factors in a dynamic analysis, wherein surrounding water is one of them. Two methods of modelling water will be attempted; the use of added mass and an acoustic-structural analysis. As previously mentioned, the effects of plasticity will be investigated, with a proper material model which can realistically describe oscillatory motion. The effects of cracking will also be included. Two methods of soil-structure interaction is evaluated for both soft and stiff soil, namely soil springs and a full on finite element modelling of the underlying soil. Based on the results from the different analyses, the applicability of the simplified approaches used will be tested. Additionally, a comparison of the time history and response spectrum analysis will be given a great deal of attention, motivated by the desirability of the response spectrum as an analysis tool for design purposes.

2 Theory

In the following, general theoretical relations used in the thesis will be derived. However, specialized subjects will be deferred to their respective sections.

2.1 The equation of motion

For a dynamic problem, the solution strategy is to transform it into a statically equivalent by applying damping and inertia as external loads, as stated by d'Alembert. Thus, for a system with stiffness, damping and mass matrices of $\boldsymbol{K}$, $\boldsymbol{C}$ and $\boldsymbol{M}$ respectively, this can be written as

$$\boldsymbol{M}(\ddot{\boldsymbol{r}} + \ddot{\boldsymbol{r}}_g) + \boldsymbol{C}\dot{\boldsymbol{r}} + \boldsymbol{K}\boldsymbol{r} = \boldsymbol{0} \tag{2.1}$$

with $\boldsymbol{r}$ being the degrees of freedom of the system and $\ddot{\boldsymbol{r}}_g$ the imposed ground acceleration. This system of equations is coupled, as generally neither $\boldsymbol{K}$, $\boldsymbol{C}$ or $\boldsymbol{M}$ are diagonal. In the process of decoupling these equations, it is necessary to find the eigenfrequencies. This is done by solving the undamped free vibration problem:

$$\boldsymbol{M}\ddot{\boldsymbol{r}} + \boldsymbol{K}\boldsymbol{r} = \boldsymbol{0} \tag{2.2}$$

A solution can be found by introducing a vector $\hat{\boldsymbol{r}}_n$ satisfying $\hat{\ddot{\boldsymbol{r}}}_n = -\omega_n^2 \hat{\boldsymbol{r}}_n$. Inserting this into equation 2.2 gives the eigenvalue problem

$$|\boldsymbol{K} - \omega_n^2 \boldsymbol{M}| = \boldsymbol{0} \tag{2.3}$$

The eigenvalues, ω_n are the eigenfrequencies of the system and the eigenvectors $\hat{\boldsymbol{r}}_n$ define the vibration shape of that mode. The normalized equivalents to $\hat{\boldsymbol{r}}_n$ are ϕ_n and satisfies

$$\boldsymbol{\phi}^T \boldsymbol{M} \boldsymbol{\phi} = \boldsymbol{M}^* \tag{2.4}$$

where $\boldsymbol{\phi}$ is a matrix with ϕ_n as columns and $\boldsymbol{M}^*$ is a diagonal mass matrix. Equivalently, for a diagonal stiffness matrix:

$$\boldsymbol{\phi}^T \boldsymbol{K} \boldsymbol{\phi} = \boldsymbol{K}^* \tag{2.5}$$

As both the mass and stiffness matrices now are diagonal, what remains is the damping matrix. In order to ensure that $\boldsymbol{C}$ becomes diagonal by the same transformation as in equation 2.4 and 2.5, Rayleigh damping is assumed:

$$\boldsymbol{C} = \alpha \boldsymbol{M} + \beta \boldsymbol{K} \tag{2.6}$$

where α and β are mass and stiffness proportional damping coefficients, respectively, and can be determined as[4]

$$\frac{\alpha}{\omega} + \beta\omega = 2\xi \tag{2.7}$$

Using the orthogonality of the mode shapes, a new variable, y_n, for mode n can be introduced, defined by

$$\boldsymbol{r} = \boldsymbol{\phi y} = \sum_{n=1}^{N} \phi_n y_n \tag{2.8}$$

where N is the number of degrees of freedom. Introducing equation 2.8 into equation 2.1 and premultiplying by $\boldsymbol{\phi}^T$ results in N uncoupled equations which can be separately solved, as shown in equation 2.9

$$\ddot{y}_n + 2\xi_n w_n \dot{y} + w_n^2 y = -\frac{\phi_n^T \boldsymbol{M}}{m_n} \ddot{\boldsymbol{r}}_g \tag{2.9}$$

where m_n is the generalized mass of mode n; an element of the diagonal mass matrix $\boldsymbol{M}^*$. It has been used that $c_n = 2\xi_n w_n m_n$, where c_n is equivalently an element of $\boldsymbol{C}^*$. Finally ξ_n is the modal damping. By defining the ground acceleration as a time varying amplitude $\ddot{r}_g$ times a distribution vector, $\boldsymbol{T}$ - which relates the ground acceleration to the degrees of freedom of the system, one can find the modal participation factor as

$$\Gamma_n = \frac{\phi_n \boldsymbol{M} \boldsymbol{T}}{m_n} \tag{2.10}$$

The effective modal mass, $\bar{M}_n$, which states the fraction of the total structural mass that is associated with a given mode is given by

$$\bar{M}_n = \Gamma_n^2 m_n \tag{2.11}$$

The sum of the effective mass of all modes should equal the total structural mass.

As the equation of motion has been reduced to a series of single degree of freedom systems, they can be solved as such. While there are several ways of solving equation 2.9, an efficient approach is introducing the Laplace transform throughout the equation, yielding

$$s^2 Y_n + 2\xi_n \omega_n s Y_n + \omega_n^2 Y_n = -L_n \ddot{R}_g \tag{2.12}$$

where $Y_n = \mathcal{L}(y_n)$ and $\ddot{R}_g = \mathcal{L}(\ddot{r}_g)$ are the Laplace transformed of y_n and $\ddot{r}_g$ respectively. The transfer function can then be given as

$$H(s) = -\frac{1}{s^2 + 2\xi_n\omega_n s + \omega_n^2} \tag{2.13}$$

As it is not possible to solve equation 2.9 analytically, discretization is done by a first order approximation to the z-transformed, given by the Tustin transformation

$$s = 2f_s\frac{z-1}{z+1} \tag{2.14}$$

where f_s is the sampling frequency of $\ddot{r}_g$. Introducing equation 2.14 into 2.13 gives

$$H(z) = -\frac{1}{\gamma_n}\left[\frac{1 + 2z^{-1} + z^{-2}}{1 + \frac{2\omega_n^2 - 8f_s^2}{\gamma_n}z^{-1} + \frac{\omega_n^2 - 4\xi_n f_s + 4f_s^2}{\gamma_n}z^{-2}}\right] \tag{2.15}$$

where for clarity, $\gamma_n = \omega_n^2 + 4\xi_n f_s + 4f_s$ has been introduced. Equation 2.15 is a filter, which when applied to the earthquake accelerogram, gives the response of the system. This becomes apparent when the filter is written in the form of a difference equation

$$y_n[i] = -\frac{1}{\gamma_n}\left(\ddot{r}_g[i] + 2\ddot{r}_g[i-1] + \ddot{r}_g[i-2]\right) + \frac{2\omega_n^2 - 8f_s^2}{\gamma_n}y_n[i-1] + \frac{\omega_n^2 - 4\xi_n f_s + 4f_s^2}{\gamma_n}y_n[i-2] \tag{2.16}$$

Equation 2.16 can be efficiently solved by a number of software, for instance MATLAB[22]. Having solved for all uncoupled equations and obtained y_n for all modes, n, the solution for the structural degrees of freedom are found by insertion into equation 2.8. In other words, such a solution is only valid for a linear system such that the principle of superposition can be invoked.

2.2 Finite element analysis

Solving dynamic problems for real structures is a difficult task and cannot be done analytically. Instead, the finite element method may be used, where either time history or response spectrum analyses are commonly used methods.

2.2.1 Time history analysis

A time history analysis implies solving the equation of motion for a structure subjected to an earthquake. The earthquake motion may be represented by either acceleration, velocity or displacement time histories, which are either measured from

a previous earthquake, or synthetically produced. This is the most accurate way of simulating earthquake response, and the only way to take non-linearities into account as it does not make use of the principle of superposition. It is however a time consuming process when applied to large, non-linear models with many degrees of freedom - as is the case here.

In a finite element format and for time increment i, the equation of motion as given in equation 2.1 takes the form[4]

$$\boldsymbol{M}\ddot{\boldsymbol{D}}_i^{tot} + \boldsymbol{C}\dot{\boldsymbol{D}}_i + \boldsymbol{R}_i^{int} = \boldsymbol{P}_i \tag{2.17}$$

where $\ddot{\boldsymbol{D}}_i^{tot}$ is a vector of the total accelerations experienced by the degrees of freedom defined by the finite element model and given as

$$\ddot{\boldsymbol{D}}_i^{tot} = \ddot{\boldsymbol{D}}_i + \ddot{\boldsymbol{D}}_{\boldsymbol{g},i} \tag{2.18}$$

with $\ddot{\boldsymbol{D}}_{\boldsymbol{g},i}$ being the time dependent imposed earthquake accelerations. Furthermore, $\boldsymbol{M}$ is the mass matrix, $\boldsymbol{C}$ is the damping matrix, $\boldsymbol{P}$ is a vector of the applied loads and $\ddot{\boldsymbol{D}}_i$ and $\dot{\boldsymbol{D}}_i$ are the global acceleration and velocity vectors respectively.

The internal force vector, $\boldsymbol{R}_i^{int}$, is for a linear analysis merely given as stiffness times displacement. For a non-linear analysis, however, the stiffness matrix $\boldsymbol{K}$ needs to be updated for each time increment, i. Moreover, the correct equilibrium path needs to be found by way of Newton-Raphson iterations, k, for each increment. An illustration of the method is shown in figure 2.1. This results in the internal force vector being given as

$$\boldsymbol{R}_i^{int,k} = \boldsymbol{K}_i^k \boldsymbol{D}_i^k \tag{2.19}$$

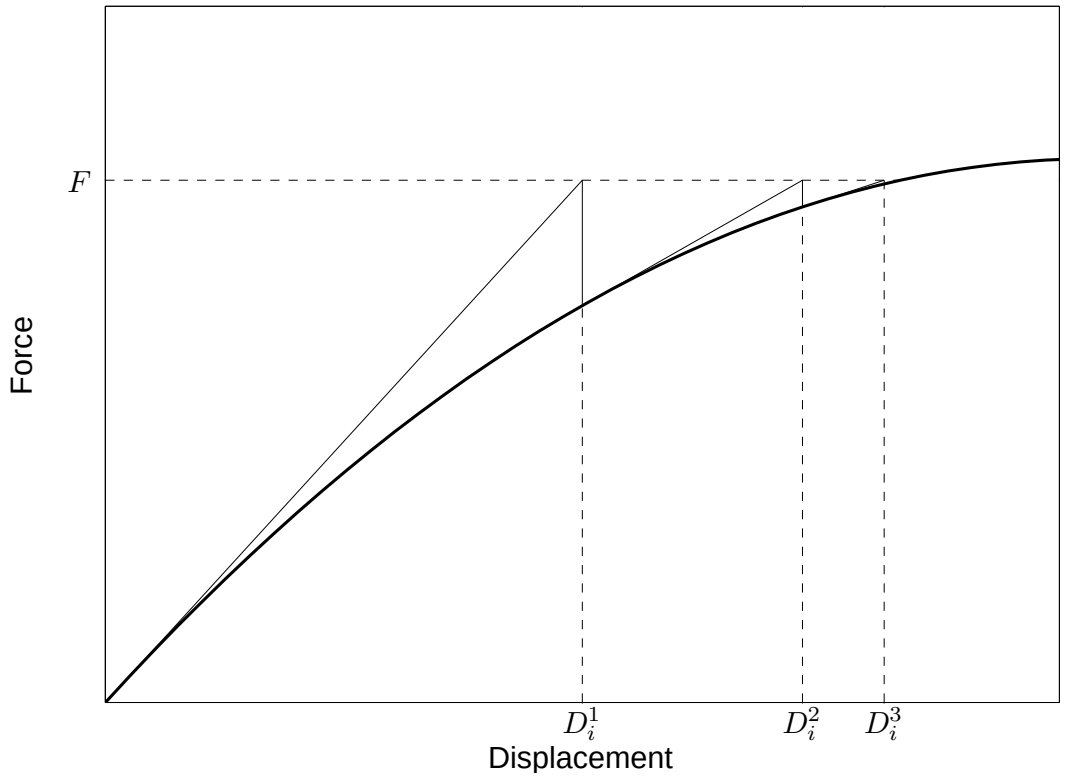

Figure 2.1: A graphical illustration of Newton-Raphson iterations used in non-linear finite element analysis, shown here for $k = 1 - 3$ iterations.

Combining equations 2.17-2.19 and rearranging gives

$$\boldsymbol{M}\ddot{\boldsymbol{D}}_i + \boldsymbol{C}\dot{\boldsymbol{D}}_i + \boldsymbol{K}_i^k \boldsymbol{D}_i^k = \boldsymbol{P}_i - \boldsymbol{M}\ddot{\boldsymbol{D}}_{\boldsymbol{g},i} = \boldsymbol{R}_i^{ext} \tag{2.20}$$

In order to obtain the displacement field, from which all stresses and strains are calculated, it is necessary to integrate equation 2.20. This can either be done explicitly or implicitly. An explicit method solves equation 2.20 for a given time increment $i+1$ by using only information from the previous step, i. This implies that no system of equations needs to be solved, and each step is calculated quickly. On the other hand, in order to achieve a stable solution, small time steps are necessary. Thus for an earthquake of duration 10 to 35 seconds, literally millions of time steps are necessary. This makes an explicit integration scheme inappropriate for the problem at hand. The implicit method solves the differential equation by establishing a system of equations at time step $i+1$. This means that each increment takes longer to calculate, but the solution is much more stable than the explicit method, resulting in fewer time steps. In fact, for a linear analysis the implicit method is unconditionally stable. This is, however not the case for a non-linear analysis. Nevertheless, an implicit method known as *Hilber-Hughes-Taylor's α (HHT) method* will be assumed, and is elaborated upon in the following.

The essence of numerical solution of differential equations lies in the approximation of their differentials. This is done by use of the Newmark relations[4]

$$\begin{aligned}\ddot{\boldsymbol{D}}_{i+1} &= \frac{1}{\beta\Delta t^2}\left(\boldsymbol{D}_{i+1} - \boldsymbol{D}_i - \Delta t\dot{\boldsymbol{D}}_i - 1\right) - \left(\frac{1}{2\beta}\right)\ddot{\boldsymbol{D}}_i \\ \dot{\boldsymbol{D}}_{i+1} &= \frac{\gamma}{\beta\Delta t}\left(\boldsymbol{D}_{i+1} - \boldsymbol{D}_i\right) - \left(\frac{\gamma}{\beta} - 1\right)\dot{\boldsymbol{D}}_i - \Delta t\left(\frac{\gamma}{2\beta} - 1\right)\ddot{\boldsymbol{D}}_i\end{aligned} \tag{2.21}$$

The HHT-method is obtained by editing equation 2.20 in the following manner[16]

$$\boldsymbol{M}\ddot{\boldsymbol{D}}_{i+1} + (1+\alpha)\boldsymbol{M}\ddot{\boldsymbol{D}}_i - \alpha\boldsymbol{M}\ddot{\boldsymbol{D}}_i + (1+\alpha)\boldsymbol{K}_i^k\boldsymbol{D}_{i+1} - \alpha\boldsymbol{K}_i^k\boldsymbol{D}_i = (1+\alpha)\boldsymbol{R}_{i+1}^{ext} - \alpha\boldsymbol{R}_i^{ext} \tag{2.22}$$

where $-\frac{1}{3} \leq \alpha \leq 0$ is a parameter which controls the amount of numerical damping applied to the solution. The default in Abaqus[29] is $\alpha = -0.05$, which is sufficient to damp out much of the high frequency noise, and have a negligible influence on the solution[32]. From this, the parameters γ and β can be determined as

$$\begin{aligned}\gamma &= \frac{1}{2}(1-2\alpha) \\ \beta &= \frac{1}{4}(1-\alpha)^2\end{aligned} \tag{2.23}$$

2.2.2 Response spectrum analysis

For large finite element analyses, where no nonlinearities are exptected, it is often too cumbersome to employ time integration of the equation of motion. Instead an approximative approach in the frequency domain can be used, namely the response spectrum analysis.

From equation 2.15, it is seen that the transfer function is dependent upon the frequency of a given mode, ω_n. Obviously, the solution of the modal equation, y_n, must also be a function of frequency. Solving equation 2.16 for a set of frequencies, each representing the eigenfrequency of a single degree of freedom system, and extracting the maximum absolute value of $|y_n|$ from each of them, the displacement response spectrum, $S_D(\omega)$, can be obtained. The pseudo-velocity response spectrum, which is approximately equal to the velocity response spectrum $S_V(\omega)$, is then given by

$$S_V(\omega) = \omega S_D(\omega) \tag{2.24}$$

where ω now represents a set of frequencies, corresponding to eigenfrequencies of single degree of freedom systems. Similarly, the pseudo-acceleration response spectrum, approximately equal to $S_A(\omega)$, is given by

$$S_A(\omega) = \omega^2 S_D(\omega) \tag{2.25}$$

It is the acceleration response spectrum that is normally given in design codes.

For a multi degree of freedom system with N separated modal equations, the maximum displacement for a given mode n, in a given direction i, is given by

$$|y_n|_i^{max} = \frac{\Gamma_n}{\omega_n^2} S_A(\omega_n) \tag{2.26}$$

It is now possible to return to time domain by multiplying with the appropriate eigenvector, ϕ_n

$$|\boldsymbol{D}_n|_i^{max} = \phi_n |y_n|_i^{max} \tag{2.27}$$

This results in a set of N peak displacement vectors, from which the force, moment and stress can be derived. Their application to the finite element model is however not completely unproblematic. The biggest approximation in the response spectrum analysis is the combination of modes. Several combination methods exist, each with different implications as to their correlation. Here, three such methods will be explored, the first of which is the absolute sum of modal peak values. It is given by

$$\boldsymbol{D}_i^{max} = \sum_{n=1}^{N} |\boldsymbol{D}_n|_i^{max} \tag{2.28}$$

Equation 2.28 is the most conservative approximation of the response of the structure, as it assumes that the contributions from the different modes are all in effect at the same time. It is obvious that such an estimate can yield a structural response that is much higher than those from an equivalent time history analysis. On the other end of the spectrum, one finds the method of the square root of the sum of squares (SRSS):

$$\boldsymbol{D}_i^{max} = \sqrt{\sum_{n=1}^{N} \left(\boldsymbol{D}_{n,i}^{max}\right)^2} \tag{2.29}$$

The approach of equation 2.29 assumes no correlation between modes. While this generally produces better results than equation 2.28 if the modes are well separated, it may also lead to unconservative results if modes closely packed - which is the case for three-dimensional structures.

A compromise between equation 2.28 and 2.29 is the complete quadratic combination[35]. It is given by

$$\boldsymbol{D}i^{max} = \sqrt{\sum_{n=1}^{N} \sum_{m=1}^{N} \boldsymbol{D}_{n,i}^{max} \rho_{mn} \boldsymbol{D}_{m,i}^{max}} \tag{2.30}$$

The correlation coefficient, ρ_{mn} is derived from random vibration theory, and is given by

$$\rho_{mn} = \frac{8\xi^2(1+r_{mn})r_{mn}^{3/2}}{(1-r_{mn}^2)^2 + 4\xi^2 r_{mn}(1+r_{mn}^2) + 8\xi^2 r_{mn}^2} \tag{2.31}$$

where $r_{mn} = \frac{\omega_m}{\omega_n}$ is the ratio between eigenfrequencies ω_m and ω_n, and ξ is the modal damping ratio, here assumed constant for all modes. A closer examination of equation 2.31 reveals that $\rho_{mn} = 1$ if $\omega_m = \omega_n$, and much smaller than one if the two eigenfrequencies are well separated. In these two limiting cases, equation 2.30 converges to equation 2.28 and 2.29 respectively. For this reason it is expected that the complete quadratic combination should produce results which lie somewhere in-between the absolute sum and the SRSS methods.

To account for seismic action from all three directions, a response spectrum needs to be defined for each of them, thus introducing the problem of directional combination. A conservative approach is algebraic summation, which gives the total displacement as

$$\boldsymbol{D}^{max} = \sum_{i=1}^{3} \boldsymbol{D}_i^{max} \tag{2.32}$$

To reiterate, an inherent problem in a response spectrum analysis is that all measure of simultaneity is lost - it is not possible to determine when a given mode provides its contribution. Equation 2.32 assumes that all modes are applied simultaneously Another option is the square root of the sum of the squares, which one might intuitively opt to use for a directional combination, however this also implies that all the modes are completely uncorrelated - which can yield unconservative results. Another issue is that in the establishment of the response spectrum, absolute values have been used, such that all information about signs are lost. This implies that both positive and negative values returned by response spectrum calculations need be considered.

3 Material properties

3.1 Concrete

In order to describe the plastic behaviour, a yield condition needs to be specified. For concrete, such a condition needs to be dependent upon the hydrostatic pressure, and thus the von Mises yield condition cannot be used. Instead, a modified version of the Drucker-Prager yield surface will be used.

3.1.1 Yield condition

The Drucker-Prager yield condition is defined by[9]

$$\sqrt{J_2} + \alpha I_1 = k \tag{3.1}$$

where $I_1 = \sigma_1 + \sigma_2 + \sigma_3$ is the first principle stress invariant, with σ_i being the principle stress in direction i. The second stress deviator, J_2, is given as

$$J_2 = \frac{1}{6}\left[(\sigma_1 - \sigma_2)^2 + (\sigma_2 - \sigma_3)^2 + (\sigma_3 - \sigma_1)^2\right] \tag{3.2}$$

For a uniaxial stress state, where yielding is given by f_c, equation 3.1 takes the form

$$\frac{1}{\sqrt{3}} f_c + \alpha f_c = k \tag{3.3}$$

Equivalently, for an equibiaxial stress state with yield stress of f_b:

$$\frac{1}{\sqrt{3}} f_b + 2\alpha f_b = k \tag{3.4}$$

Combining equations 3.3 and 3.4 gives the constants as $\alpha = \frac{1}{\sqrt{3}} \frac{f_b/f_c - 1}{2(f_b/f_c) - 1}$ and $k = \frac{1}{\sqrt{3}}(1 - \alpha) f_c$. Inserting this into equation 3.1, and allowing for a hardening model one gets after a little algebra

$$f(\boldsymbol{\sigma}) = \frac{1}{1 - \alpha}\left[\sigma_e + 3\alpha\sigma_m\right] - \sigma_c \leq 0 \tag{3.5}$$

where $\sigma_e = \sqrt{3J_2}$ is the von Mises equivalent stress and $\sigma_m = \frac{1}{3} I_1$ is the hydrostatic stress. Furthermore σ_c is the yield stress, defined to be equal f_c before hardening takes place.

Equation 3.5 gives good results for compressive stress, however as it is derived for the purpose of describing soil plasticity, it fails to represent the behaviour of concrete in tension. To mend this, *Lubliner et al* proposed the following modified yield condition[21]

$$f(\boldsymbol{\sigma}) = \frac{1}{1-\alpha}\left[\sigma_e + 3\alpha\sigma_m + \beta\langle\hat{\sigma}_{max}\rangle - \gamma\langle\hat{\sigma}_{max}\rangle\right] - \sigma_c \leq 0 \tag{3.6}$$

where $\langle x\rangle = \frac{1}{2}(|x|+x)$ and $\hat{\sigma}_{max}$ is the maximum eigenvalue of the stress tensor $\boldsymbol{\sigma}$. This implies that the Drucker-Prager yield condition is obtained for biaxial compression, where $\hat{\sigma}_{max} = 0$.

The constant γ is a function of the material parameter K_c and is given as

$$\gamma = \frac{3(1-K_c)}{2K_c - 1} \tag{3.7}$$

Finally, the parameter β is given by *Lee & Fenves* as[19]

$$\beta = \frac{\sigma_c}{\sigma_t}(1-\alpha) - (1+\alpha) \tag{3.8}$$

where σ_c and σ_t are the yield stresses in compression and tension respectively, dependent upon the selected hardening rule.

The plastic flow is assumed to be non-associated, giving the equivalent plastic strain rate, $\dot{p}$, as

$$\dot{p} = \dot{\lambda}\frac{\partial g(\boldsymbol{\sigma})}{\partial \boldsymbol{\sigma}} \tag{3.9}$$

where $\dot{\lambda} \geq 0$ is the rate of the non-negative plasticity parameter and $g(\boldsymbol{\sigma})$ is the plastic flow potential, given here as[31]

$$g(\boldsymbol{\sigma}) = \sqrt{(\epsilon f_t \tan\psi)^2 + \sigma_e^2} - \sigma_m \tan\psi \tag{3.10}$$

where ϵ is the eccentricity, f_t the uniaxial cracking stress and ψ is the dilation angle.

3.1.2 Hardening rule

Eurocode 2[10] has been used to define most of the material properties. The concrete type B45 has been selected, and various material constants are given in

Table 3.1: Material constants for concrete type B45, taken from Eurocode 2[10].

Parameter	Value
f_{cm}	53 MPa
f_{ctm}	3.8 MPa
E_{cm}	36 000 MPa
ε_{c1}	0.24%
ε_{cu1}	0.35%

In compression, the non-linear stress-strain relation suggested by Eurocode 2 is adopted. It is given as

$$\sigma = f_{cm}\frac{k\eta - \eta^2}{1 + (k-2)\eta} \tag{3.11}$$

where $k = 1.05E_{cm}\frac{|\varepsilon_{c1}|}{f_{cm}}$ and $\eta = \frac{\varepsilon}{\varepsilon_{c1}}$.

Equation 3.11 is valid for all strains in the interval $0 \leq \varepsilon \leq \varepsilon_{cu1}$, which implies a non-linear elastic relationship. Such a relation is not supported by Abaqus[29], with which all analyses are performed. This problem is solved by introducing an approximate linear-elastic regime, with a yield stress $f_c = 0.4f_{cm} = 21.2$MPa. This results in equation 3.11 being reduced to a hardening rule in compression. For strains larger than ε_{cu1}, the stress-strain relationship is extrapolated linearly towards zero resistance, representing total compressive failure.

In table 3.1 the parameter f_{ctm} is adapted herein as the uniaxial cracking stress in tension f_t. At strains higher than that which leads to cracking, the tensile resistance of the concrete is linearly reduced to one percent of the cracking stress, after which it is kept constant due to convergence difficulties. The slope is determined such that the maximum reduction occurs at a plastic strain of $p = 0.2\%$.

The stress-strain relationship is shown in figure 3.1.

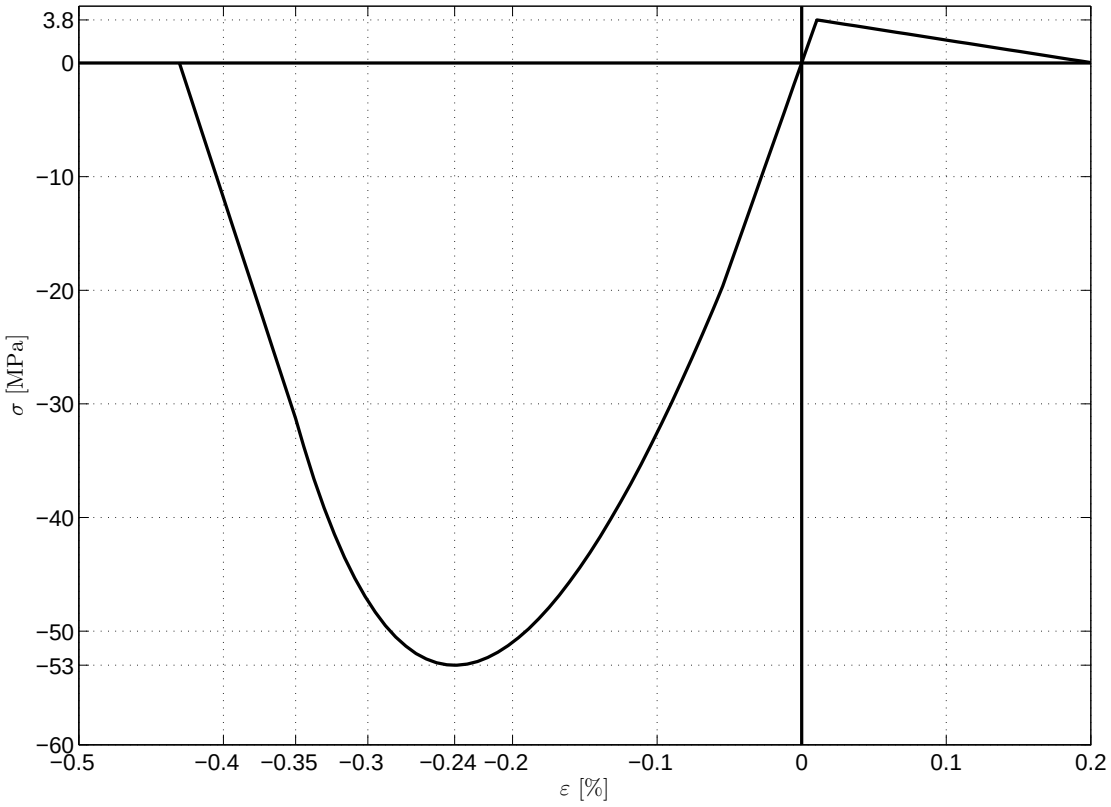

Figure 3.1: Stress-Strain relationship, slightly modified from Eurocode 2.

3.1.3 Cracking

Any material model which hopes to describe the behaviour of concrete with any realism, will have to take cracking into account. This creates a challenge when trying to simulate earthquake loads, as the stresses fluctuate between tension and compression. This causes areas which at one point were subjected to tension, so that cracking occurred, to be compressed. This, in turn, closes some of the cracks causing some of the elasticity of the material to be regained. To properly take such effects into account, the concept if elastic stiffness degradation[31] has been assumed. It will be derived in the following.

It is henceforth assumed that the additive strain rate decomposition is valid, which is given as

$$\dot{\boldsymbol{\varepsilon}} = \dot{\boldsymbol{\varepsilon}}^{el} + \dot{\boldsymbol{\varepsilon}}^{pl} \tag{3.12}$$

The effective stress represents the stresses that would be observed had the material been undamaged. It is given as

$$\boldsymbol{\sigma}_{eff} = \boldsymbol{C}_0 \left(\boldsymbol{\varepsilon} - \boldsymbol{\varepsilon}^{pl} \right) \tag{3.13}$$

where $\boldsymbol{C}_0$ is the undamaged elasticity matrix.

As cracking takes place, the value of the elasticity matrix is reduced by the scalar damage parameter, d, in the following manner:

$$\boldsymbol{C} = (1-d)\,\boldsymbol{C}_0, \qquad 0 < d < 1 \tag{3.14}$$

It is noted that d can vary between 0 and 1, where a value of zero implies that the material is undamaged. Equivalently, a value of one means that the structure has lost all its stiffness. For a given strain state, the stresses are given as

$$\boldsymbol{\sigma} = (1-d)\,\boldsymbol{\sigma}_{eff} = (1-d)\,\boldsymbol{C}_0\left(\boldsymbol{\varepsilon} - \boldsymbol{\varepsilon}^{pl}\right) \tag{3.15}$$

From equation 3.15 the main principle of the elastic stiffness degradation becomes obvious. The observed stresses are assumed to be a fraction of the stresses which would have occurred if the material had been undamaged. This fraction gets smaller as damage is accumulated and d increases. In a finite element formulation of concrete, as is attempted here, the above implies that the elasticity matrix needs to be continuously updated. However, the complete loss of strength as d reaches a value of 1 is easily implemented, as one merely needs to remove the element in question.

As mentioned earlier, the effects of regained elasticity as tension shifts to compression is to be included in the model. To this end, the scalar damage parameter d is assumed to consist of a contribution from tension, d_t, and a contribution from compression, d_c, with their relationship being

$$(1-d) = (1-s_t d_c)(1-s_c d_t), \qquad 0 < s_t, s_c < 1 \tag{3.16}$$

where s_t and s_c are stiffness recovery parameters in tension and compression, respectively. A reasonable assumption when modelling concrete is that the compressive stiffness is recovered upon the closing of cracks, and that no tension stiffness is regained - as this is a situation in which cracks are opening. This assumption assigns the following values to the stiffness recovery paramters:

$$\begin{aligned} s_t &= 0 \\ s_c &= 1 \end{aligned} \tag{3.17}$$

In other words, equation 3.17 does not give any damage reduction when recovering from compression into tension. On the other hand, the damage parameter d_c is completely reset for each cross-over from tension to compression.

3.2 Reinforcement Properties

The definition of constitutive relations for steel is much simpler than for concrete for several reasons. First of all, steel is isotropic and pressure independent, such that the von Mises yield condition can be used, including only a single yield stress σ_Y, valid both in tension and compression. It is given as

$$f(\boldsymbol{\sigma}) = \sqrt{\frac{1}{2}\left(\sigma_1 - \sigma_2\right)^2 + \frac{1}{2}\left(\sigma_2 - \sigma_3\right)^2 + \frac{1}{2}\left(\sigma_3 - \sigma_1\right)^2} - \sigma_Y \leq 0 \tag{3.18}$$

Another simplifying factor is that plastic flow is associative, which means that the equivalent plastic strain rate now is given as

$$\dot{p} = \dot{\lambda}\frac{\partial f(\boldsymbol{\sigma})}{\partial \boldsymbol{\sigma}} \tag{3.19}$$

Finally, the hardening rules are the same both in tension and compression, and no brittle cracking needs to be taken into account. Based on this, and the realisation that great accuracy is not needed for the yielding of reinforcement, a perfectly plastic hardening rule is assumed, as is shown in figure 3.2. In this study, a yield stress of $\sigma_Y = 500\text{MPa}$ and an elasticity modulus of $E_s = 200\,000\text{MPa}$ has been used, in accordance with Eurocode 2.

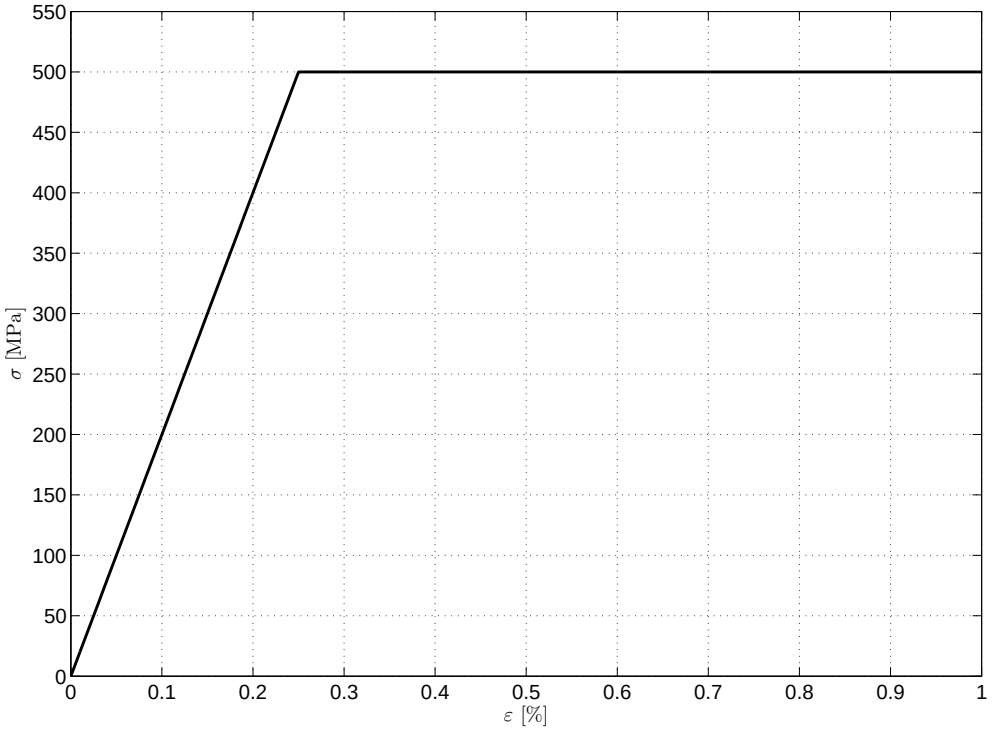

Figure 3.2: Stress-strain relationship for the reinforcement.

3.3 Water

The effect of a surrounding fluid on a moving object is a difficult subject, and even more so for large structures. The surrounding water is here assumed to be still. This is a simplification, as in a real design situation currents and waves are necessary elements in the analysis. For the sake of this study however, it is believed that those effects serve only to obscure the results. Presented here are two ways of describing the properties of water under this assumption.

3.3.1 Morison's equation

As a simple estimate for the loads per unit length, $F(t)$, incurred by oscillations through water, the Morison equation[8] can be used. It is given in equation 3.20

$$F(t) = \rho C_A A\ddot{r} + \frac{1}{2} C_D D\dot{r}|\dot{r}| \tag{3.20}$$

where $\rho = 1025\text{kg/m}^3$ is the density of water, A is the projected area of the object, C_A is the added mass coefficient, C_D is the drag coefficient, D is a characteristic width and $\ddot{r}$ and $\dot{r}$ are the acceleration and velocity of the moving object, respectively. In a finite element format, equation 3.20 refers to the nodal accelerations, velocities and mass.

The use of equation 3.20 on large volume concrete structures is in fact erroneous as the equation is strictly speaking only valid for widths $D < \lambda/5$, where λ is the wavelength of, in this case, generated waves[8]. This implies that equation 3.20 only can be used for slender structures, which is not the case at all here. This limitation is ignored however, in the belief that the results do not stray too far from reality. It is also assumed that the drag term can be neglected as the velocities in the structure are assumed to be small due to the rapid oscillations of the ground acceleration. The earthquake motion generates waves around the structure, rather than a flow of water around it, for this reason it is radiation damping that poses the velocity dependent water resistance, rather than drag force. Radiation damping cannot be described by the Morison formula.

Having neglected the drag force of Morison's equation, the problem of fluid-structure interaction has been reduced to a matter of finding the appropriate added mass coefficient, C_A. This is unfortunately quite problematic, as the motion through water creates separated flow behind the structure, which alters water resistance. The added mass coefficient is in other words frequency dependent. Very few experimental results which determine empirical relationships for C_A exist, thus forcing the use of coefficients valid for steady current - without considering frequency variation. By comparing with figure 4.1, which describes the geometry of the structure, possible choices for added mass coefficients have been selected. Geometries for which DNV recommends added mass coefficients are given in figure 3.3[8].

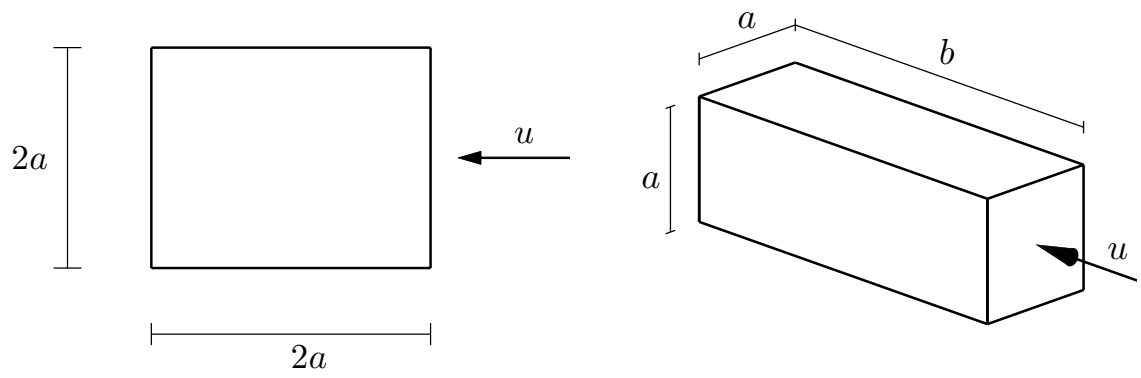

(a) $C_A = 1.51$, $A = a^2$ **(b)** $C_A = 0.68$, $V = a^2 b$

Figure 3.3: Geometries for which added mass coefficients are known, where u is the water particle velocity. Adapted from *DNV-RP: Environmental conditions and environmental loads*[8].

Figure 3.3a has a two-dimensional geometry, which is applicable when the structure penetrates the surface, thus preventing water from flowing over it. For fully submerged structures, where the fluid has the option of flowing around all four sides, figure 3.3b is a better fit, although it applies the restriction of quadratic cross section.

From equation 3.20, it is seen that the remaining load term is proportional to the acceleration of the structure, such that it is possible to apply it as an addition to the structural mass. The following expression for the added mass, M_A, can then be established:

$$M_A = \rho C_A V = \rho C_A A H \tag{3.21}$$

where V is the effective volume of the structure and H is the height affected by added mass effects - applicable when two-dimensional geometry is assumed. The effective volume V and area A are given in figure 3.3b and 3.3a respectively.

A source of error when using equation 3.21 is the distribution of added mass. Certainly, it is necessary to apply it as evenly distributed along all surfaces of the structure which interacts with water. This causes additional gravity forces throughout the structure, and thus artificial compressive stresses - an effect which could yield unconservative results in concrete structures as otherwise occurring tensile stresses may be reduced or cancelled out completely. For oscillatory motion of the structure, an applied acceleration activates the loading posed by water resistance. However, the same acceleration is equally felt in the structures wake, thus errantly generating loads there as well. Indeed, the fluid-structure interaction proposed in this section is highly simplified, and should be viewed only as an order of magnitude approximation - which is adequate for the purpose of this study.

3.3.2 Navier-Stokes' equations

Raising the level of ambition slightly, it is possible to establish a better approximation for the fluid-structure interaction by introducing the famous Navier-Stokes' equations for the fluid, although a few simplifications are necessary. Firstly, fluid convection is neglected, meaning that

$$\boldsymbol{v} \cdot (\nabla \boldsymbol{v}) = \mathbf{0} \tag{3.22}$$

where $\boldsymbol{v}$ is the velocity field of the fluid. Furthermore, the fluid is assumed inviscid such that its viscosity is equal to zero, meaning that no shear stresses at fluid boundaries can be described. Finally, compressibility is assumed. The resulting, simplified expression for momentum conservation is then given by[5]

$$\rho \frac{\partial \boldsymbol{v}}{\partial t} - B \nabla (\nabla \cdot \boldsymbol{v}) = \mathbf{0} \tag{3.23}$$

which is the equation that Abaqus introduces, with volumetric drag neglected, to solve the fluid-structure interaction problem under the given assumptions[30]. In equation 3.23, ρ is the density and B is the bulk modulus. Conservation of momentum generates pressure waves as the submerged structure oscillates, thus producing both an acceleration dependent force and radiation damping. Equation 3.23 is considered an improvement over the Morison equation, given in 3.20, however a few limitations exists. No transversal waves can be generated, only longitudinal, meaning that the transfer of momentum is not entirely accurate. Also, the pressure gradient has been defined as equal to zero, implying that equation 3.23 is valid only for small pressure changes, which is the case for massive concrete structures as small displacements are expected. Another limitation is that no turbulence can be included. Because of this, the acceleration proportional loading, like the Morison equation, can only describe a steady current, and as such does not provide a better estimate for the added mass effect. On the other hand, the added mas coefficients are no longer submitted to as large a degree of speculation as was the case in section 3.3.1. The biggest improvement lies in that the loading is only applied to surfaces which pushes water ahead, rather than being evenly distributed. Furthermore, no artificial compression is induced and radiation damping by means of pressure wave generation is included.

4 Investigated structure

As the purpose of this report is to investigate the dynamic response of massive concrete structures located in the North Sea, a natural choice of geometry is one which resembles a typical gravity based structure - such as an offshore oil platform. Obviously, non-linear analysis of an entire oil platform is an enormous undertaking, yielding impractical time consumption. For this reason, the following simplifications to geometry are assumed:

- Where one might expect an oil platform to have four legs, symmetry is imposed such that only one leg is included in the analysis.
- No topside is included, instead one quarter of its assumed mass is represented as a point mass placed on the symmetry axis of the structure, at the top of the shaft.
- The leg of a platform is usually a cylindrical, hollow shaft. In a finite element analysis this causes numerical difficulties as an irregular mesh occurs in the transition zones between circular and rectangular parts of the structure. For this reason, the shaft is assumed to have a quadratic cross section.

The point mass of a topside structure varies largely with the size of a platform, its purpose and even time. For the sake of this study, it is assumed equal to 20 000 tonnes. This means that the chosen structure, which represents one quarter of an oil platform, is subjected to 5000 tonnes atop its shaft. The structure is also assumed to stand on the seabed, at a depth of 35 m, meaning that 15 meters of the shaft are above water.

4.1 Geometry

The discussion above results in a model as shown in figure 4.1 which is elaborate enough to represent an offshore structure, but not so much that its intricacies overshadow the results of the numerical study.

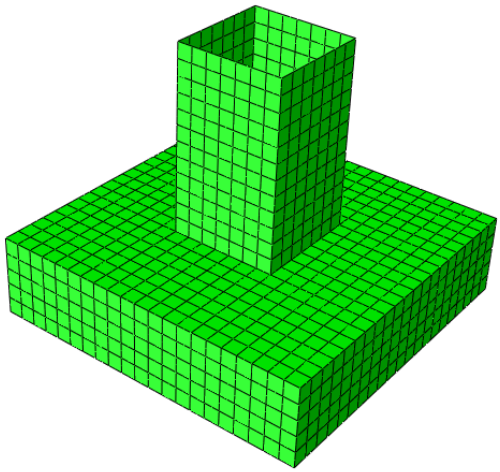

Figure 4.1: General view of the finite element model used in the numerical study, assumed to be representative of a typical offshore strucutre.

As is also seen in figure 4.1, the shaft rests upon a lower wall structure, henceforth referred to as a caisson, which consists of several internal walls whose purpose are to transfer moment and shear forces from the shaft to the ground. This is shown in figure 4.2.

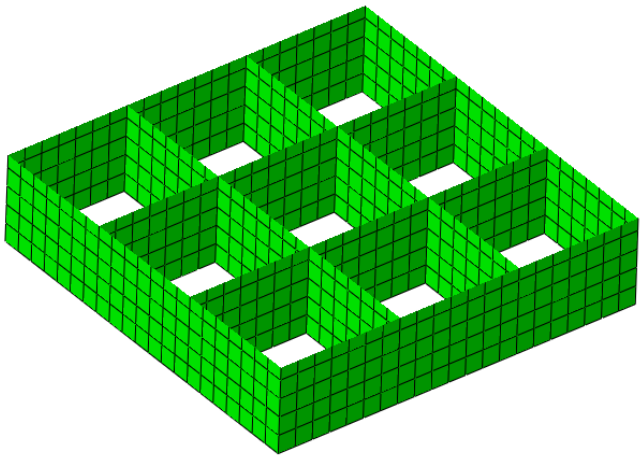

Figure 4.2: General view of the internal wall system of the caisson.

The total height of the structure is chosen to be 50 meters, with the shaft contributing 35 meters and the caisson the remaining 15 meters. The shaft and caisson have widths of 20 and 60 meters respectively, and the internal walls are placed 20 meters apart. This is shown diagrammatically in figure 4.3.

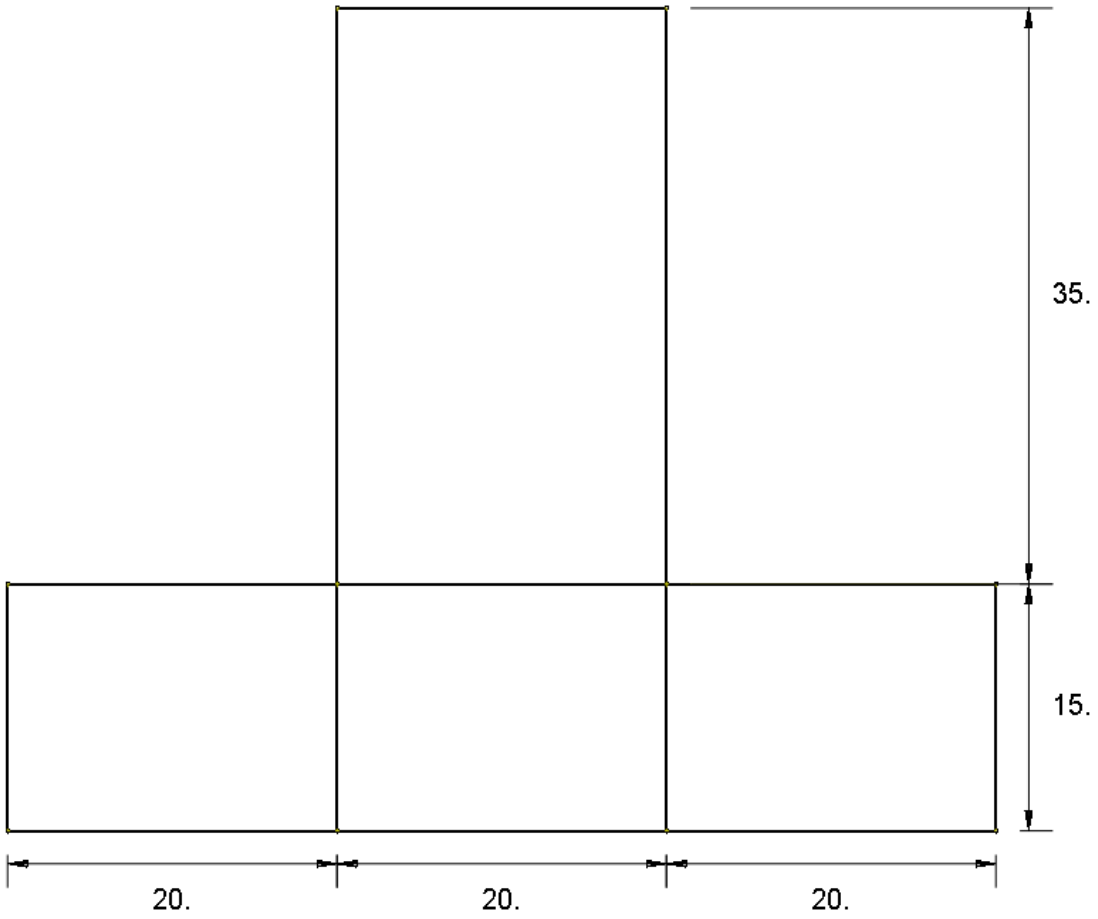

Figure 4.3: External dimensions of the structure. All units are in meters.

Not shown in figure 4.3 is the water level, which is assumed to be 35 meters above the seabed. In order to cancel out the hydrostatic pressures acting on the external walls, it is assumed that the structure is filled with water up until the same level as the water surface. This is represented in the dynamic analysis by an additional mass density added to the walls which are supposed to lie below the water surface.

4.2 Design

A great deal of focus has not been dedicated to finding the most efficient or economic design. On the other hand, the structure needs to comply with design specifications in order to produce results of any interest. In this study, design has been performed in accordance with the Eurocodes.

A time history analysis has been used for the determination of seismic loading. For this purpose, artificial accelerograms, generated as described in chapter 5, have been used. Eurocode 8 states several requirements to the implementation of the accelerograms in the finite element analysis. These are elaborated upon in the following.

- **3.2.3.1.1(2)P**
  When a spatial model of the structure is required, the seismic motion shall consist of three simultaneously acting accelerograms. The same accelerogram may not be used simultaneously along both directions.

  The two horizontal, orthogonal accelerograms are simulated from the same response spectrum - representing 475 year return period earthquakes. However, as they are created by Monte Carlo simulations, they are made to be statistically independent. In other words, this condition is satisfied. The vertical accelerogram also uses the same response spectrum as basis for simulation, but it has been scaled down by a factor of 0.7. This representation of seismic loading is similar, but slightly more conservative, to the recommendations of the NORSOK standard. It suggests having one of the horizontal accelerograms as dominant, with the other two directions having their contributions scaled down by a factor $\frac{2}{3}$[26].

- **3.2.3.1.2(1)P**
  Artifical accelerograms shall be generated so as to match the elastic response spectra given in **3.2.2.2** *and* **3.2.2.3** *for* 5% *viscous damping* ($\xi = 5\%$).

  This requirement is found to be too lenient for the design of offshore concrete structures. Instead, a viscous damping of 1% has been used. The basis for simulation has been response spectra of recorded earthquakes, which are picked such that they are as similar as possible to a mean response spectrum for a given return period. This is further investigated in chapter 5.

- **3.2.3.1.2(2)P**
  The duration of the accelerogram shall be consistent with the magnitude and the other relevant features of the seismic event underlying the establishment of a_g.

  All simulated accelerograms are designed to have a duration of 15 seconds,

regardless of return period. For the 475 year return period, which Eurocode 8 concerns itself with, this is realistic - as such a duration is found to be quite average. The parameter a_g is the peak ground acceleration, PGA.

- **3.2.3.1.2(3)**
  When site-specific data are not available, the minimum duration T_s of the stationary part of the accelerograms should be equal to 10s.

  This is satisfied, almost to a fault. It can be debated whether such a long duration of significant ground motion is physical for earthquakes of such low return period. This problem is exemplified by figure 5.7. Here, a closer examination reveals that the overall shape of the accelerogram is perhaps not typical of an earthquake. It is noted that all generated accelerograms are quite similar, though statistically independent, such that the problem persists. This issue is ignored however, as it is less prominent for earthquakes of larger return periods.

In addition to the requirements above, three accelerograms have been used in the design process, with all of them generated such that their peak ground acceleration is equal to the characteristic value for the given return period. This is in compliance with section 3.2.3.1.2(4) of Eurocode 8.

With the seismic loading in place, design of the concrete structure is performed according to Eurocode 2. Additional load is subjected by the mass of the topside structure, equal to 5000 tonnes. Furthermore, the concrete is assumed to have a density of $\rho = 2500\text{kg/m}^3$, thus causing distributed gravity loads. Finally, loads are also caused from the internal water of the structure, which is modelled as distributed mass.

The thickness of the walls are chosen such that they have sufficient capacity in compression and shear. This leads to wall thicknesses of 0.7 meters throughout the structure. An exception is the roof of the caisson, with reference to figure 4.1. Here, problems with shear compression demands a cross section of 1.5 meters. It is observed in appendix D that even with the thickness increase, the slab is at maximum utilization. This is however still in compliance with Eurocode 2, and since the task at hand is not to design a structure which is to be part of an existing project, no further changes are made.

For simplicity, a reinforcement mesh of doubly placed rebars with diameters of 20 millimeters and spacing of $s = 150$ millimeters have been used throughout the structure - both in the vertical and horizontal direction, and on both faces of the walls. This is shown in figure 4.4. The reinforcement coverage, c, is chosen to be 55 millimeters, thus ignoring environmental effects. In places where shear reinforcement is needed, shown in figure D.29, this is taken care of by the inclusion of hoop reinforcement with a diameter of 14 millimeters and spacings of 250 millimeters in each

direction. No long term effects, such as creep or relaxation are included, as it is not appropriate for accidental load cases such as earthquakes.

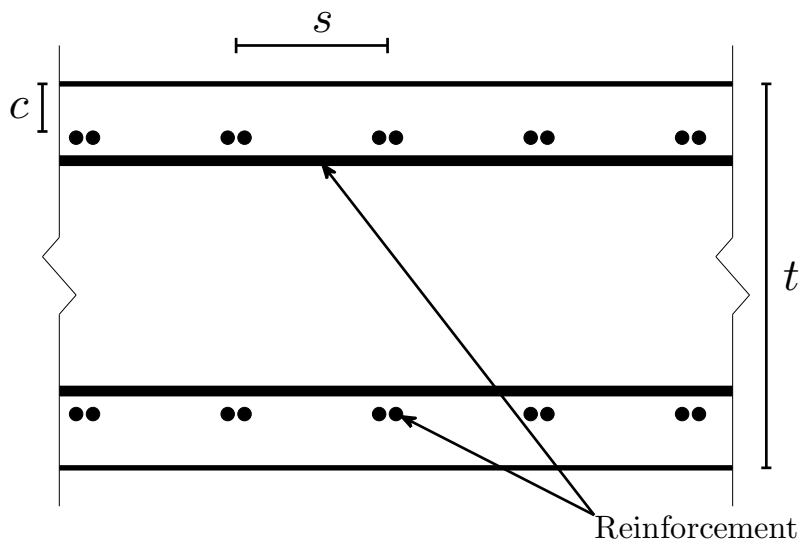

Figure 4.4: Cross section of a typical wall with thickness t, reinforcement spacing s and reinforcement cover c.

The capacity checks are performed based on analysis with Abaqus[29], with the post-processing software MultiCon[23]. It determines the loading by assuming each time increment is a load case, such that envelope curves of section forces can be created. The utilization of both the concrete capacity in compression and shear, as well as the reinforcement capacity can then be evaluated. This is shown in appendix D. This procedure implies that an elastic finite element analysis has to be performed, otherwise the load cases cannot be superposed. Its application rests upon the assumption that an elastic structure is stiffer than an equivalent yielding structure, such that higher loads are generated, giving a conservative design.

4.3 Modelling

All analyses are performed with the finite element software Abaqus[29]. In this section, a summary of general modelling considerations within the Abaqus environment is presented. However, details pertaining to the modelling of specific analyses - such as the interaction with water - are deferred to sections in which they become necessary.

The structure itself is modelled entirely with shell elements. The reason for this is that the wall thicknesses are much smaller than the other dimensions, making the choice of shell elements appropriate. Another motivating factor is simplicity - the thickness of a shell element is an imposed property, rather than a dimension which needs to be modelled. This makes it easier to adjust the model if necessary. The deciding factor, however, was the simple implementation of reinforcement. While vol-

ume elements require the reinforcement to be modelled as embedded one-dimensional beam elements, shell elements distribute the reinforcement area into rebar layers at specified locations in the cross section. The thickness of such a section is defined by[33]

$$t_s = \frac{A_s}{s} \tag{4.1}$$

where t_s is the rebar layer thickness, A_s reinforcement area and s the spacing between rebars. For the present model, a few simplifications were made.

- Both the vertical and horizontal reinforcement are placed in the same reinforcement layers, thus rendering an otherwise highly orthotropic layer almost isotropic. Obviously, in reality the orthogonal rebars cannot intersect each other, but it is believed that the neglect of this offset - a few centimeters at most - will constitute an error smaller than that introduced by the smearing of reinforcement area.
- Shear reinforcement is ignored. This is perhaps a more controversial choice than the above, however, looking at appendix D it is seen that the areas of the structure which require shear reinforcement are localized to the connection zones between vertical walls and the roof of the caisson. Figure 6.13 shows that the presence of reinforcement does not constitute a radical change to the material behaviour. Finally, the material model is not accurate enough to predict shear failure. These reasons lead to the conclusion that shear reinforcement, to the extent which is needed here, will have a negligible effect on the global response of the structure.

The choice of an appropriate shell element is not entirely straightforward for the problem at hand. Such a selection cannot be arbitrary, as the use of thick-shell elements for a thin-plate problem may lead to shear locking. Equivalently, the use of thin-shell elements to thick-plate problems may lead to severe inaccuracies as the transverse shear is ignored. For thin shell theory to apply, the ratio of thickness to a characteristic length should be smaller than 1/15. The characteristic length can be determined by the wavelength of a significant natural mode[34], or the distance between two areas of the structure which are constrained - such as the intersection of walls. This criterion is satisfied in some areas - suggesting the use of thin shell elements, but not in others.

A complicating factor in non-linear analyses is thickness change of the shell element, which may change the applicability of a thick shell element. Furthermore, the inclusion of rebar layers transforms the homogeneous shell element into a sandwich element, in which case transverse shear may be important[34], and thin shell elements inappropriate. In order to overcome this, Abaqus supplies a family of so called *general-purpose shell elements*. These elements apply Mindlin plate theory for thick-plate problems and Discrete Kirchhoff plate theory for thin-plate problems, interpolating in-between[34].

The element selected is a 4-node, linear, quadrilateral element known as S4 - since

there are no quadratic general-purpose elements. As these elements model a three-dimensional structure, subjected to three-dimensional loading, in-plane bending is expected. In this case, the Abaqus manual[34] recommends the use of full integration - an advice which is taken.

An important issue in all finite element analyses is the one of convergence. The element size needs to be chosen such that sufficient accuracy is achieved, however there are limits to how many elements can be included before the problem size becomes prohibitively large. In order to choose an adequately accurate element size, a comparison of eigenfrequencies were performed. The results are shown in figure 4.5. Here it is seen that difference between the 3 and 1 meter mesh are smaller than between the 5 and 3 meter mesh, suggesting that decreasing element size leads towards a converged solution.

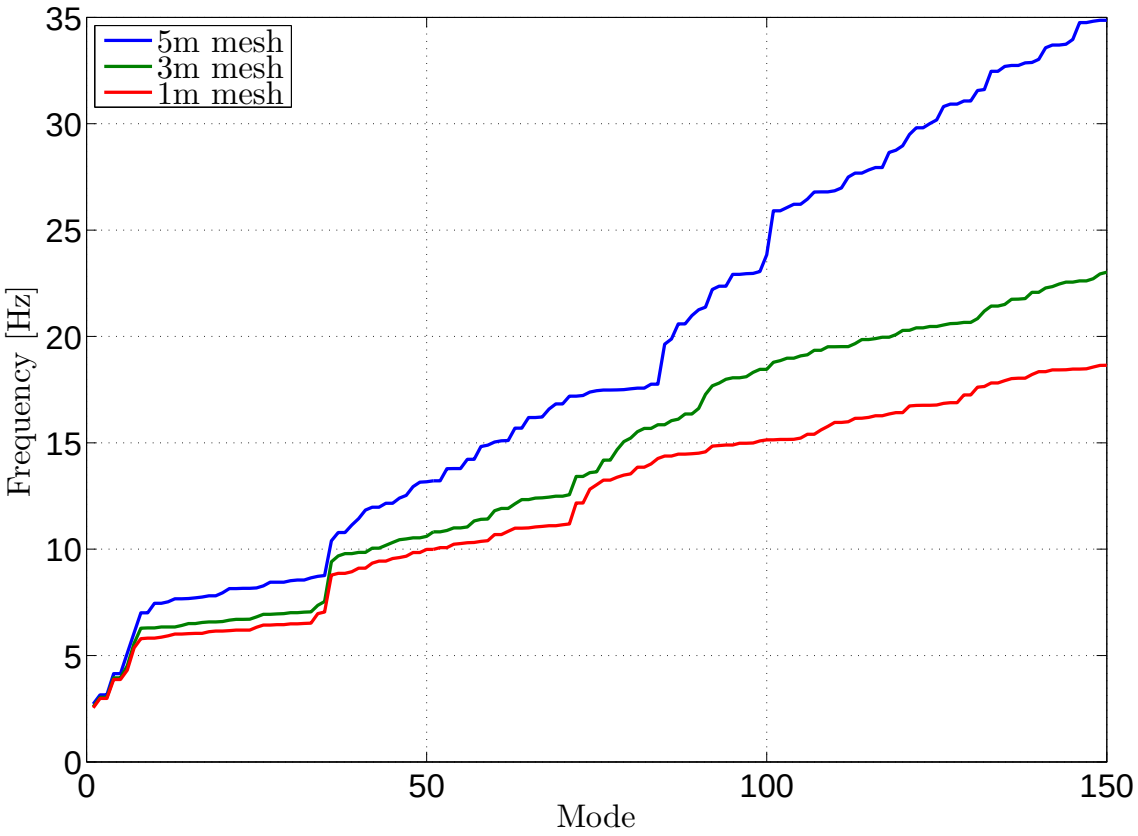

Figure 4.5: Eigenfrequencies for different mesh sizes.

To further investigate the influence of mesh size, the structure is subjected to a horizontal jolt with the intention of simulating seismic loads. This is represented by an imposed burst of acceleration to the foundation of the model over a time period of one second and analysed with an implicit dynamic procedure. The duration of the analysis was 5 seconds, the last four of which consisted of free vibration. The parameter for which mesh size comparison is made is the von Mises stress of the shaft. Its spatial distribution is linearised and measured along one of its corners, down to the caisson roof. The results are shown in figure 4.6, where it is shown

that decreasing mesh size leads to a smoother stress distribution and a higher peak value. It is noted however that the curves are similar.

To reiterate, the choice of element size is a weigh-off between longer analysis time and higher accuracy. This leads to the choice of a 3 meter mesh size, as figure 4.5 and 4.6 show that this yields reasonable accuracy. Further, the analysis time for the stress analysis, using 1000 increments, was 29.2 minutes, as opposed to 4.2 hours for the 1 meter mesh model.

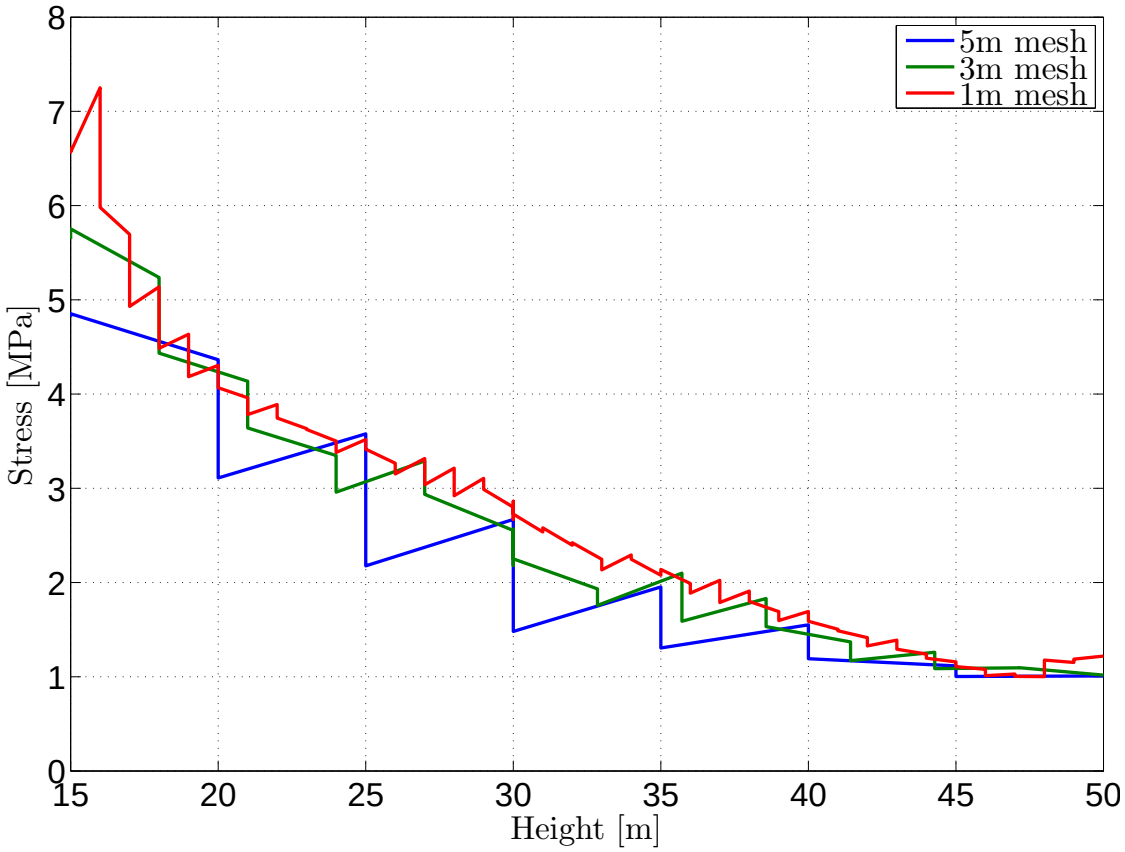

Figure 4.6: Eigenfrequencies for different mesh sizes.

What remains in order to have a trustworthy implicit dynamic analysis is a time step small enough such that accuracy is achieved. A measure used in the selection of an appropriate time step is the sum of all energy in the system - which is supposed to be approximately constant. The results are shown in figure 4.7.

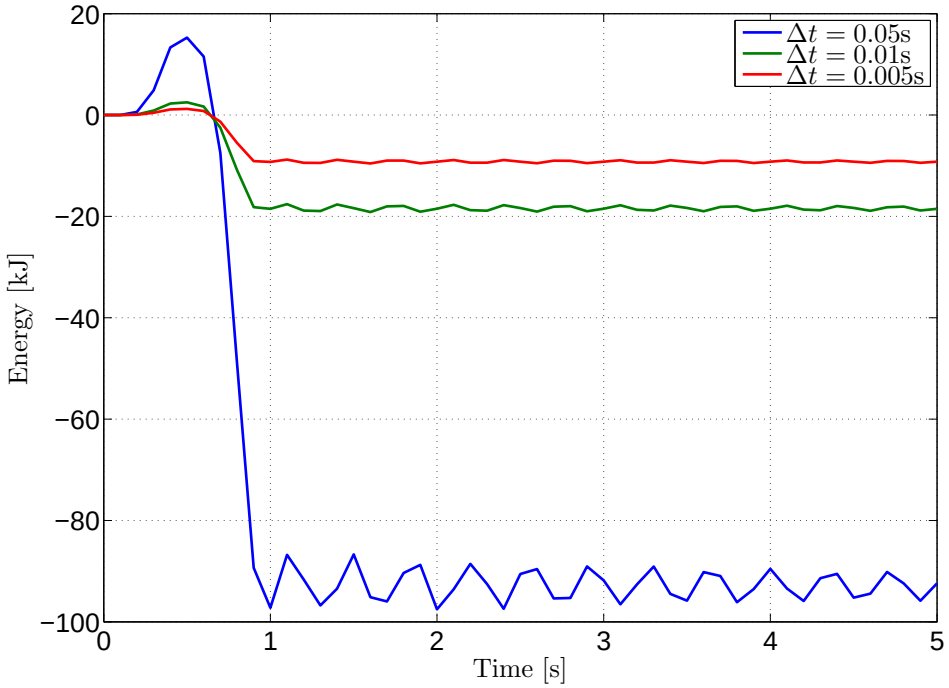

Figure 4.7: The total energy of the model for different time steps.

From figure 4.7 it is observed a jump in the supposedly constant total energy - for all time steps. This occurs when the structure is accelerated, as kinetic energy is introduced to the model. When the external loading is removed, such that only free vibration remains, the total energy becomes approximately constant. This effect is reduced when the time steps are decreased, which is only natural as the implicit procedure becomes accurate enough to resolve the motion of the structure such that energy balance can be achieved. It should be noted that the scale of figure 4.7 makes it misleading. A more proper representation is a comparison with the kinetic energy, where the jump of energy is less dramatic. In this case however, a selection of time step is the purpose, such that relative differences between time steps suffices.

It is essential to choose a time step small enough to produce accurate results. To achieve this, a time step of $\Delta t = 0.005$s is used.

5 Seismic hazard analysis

The purpose of this study is to investigate the response of a structure to increasingly large earthquakes, such that displacements become larger and the influence of the complicating factors become greater. In order to do that, it is necessary to determine characteristic earthquakes of certain return periods. Here, ground motion accelerograms that represents return periods of 475, 1000, 3000 and 10 000 years respectively will be generated.

5.1 Establishment of statistical data

To determine seismic parameters which represent a return period, a rectangular area of the North Sea is chosen, with the coordinates of the opposing corners being $(58°, 0°)$ and $(63°, 5°)$ respectively. Within this area, which is called the estimation area and shown in figure 5.1, information of earlier earthquakes is gathered. The structure is located in the middle of the estimation area, at coordinates $(60.5°, 2.5°)$. It should be noted that no effort has been made to ascertain the conditions of this location with respect to water depth and ocean floor topography - it is merely a point chosen for the purpose of seismic hazard analysis.

Due to the size of the estimation area, earthquakes located towards the boarders will have attenuated greatly by the time they reach the location of the structure and thus yield a negligible contribution to observed acceleration. This causes inaccuracies when one attempts to establish probabilistic relationships for the ground acceleration as measured earthquakes are not uniformly distributed throughout the estimation window, which creates a bias towards earthquakes that occur close to the structure over those that occur further away. For this reason, an area of radius 100 kilometers around the structure is chosen to be the simulation area, where earthquakes are simulated based on magnitude relations determined from the estimation window. The simulation window is shown in figure 5.1.

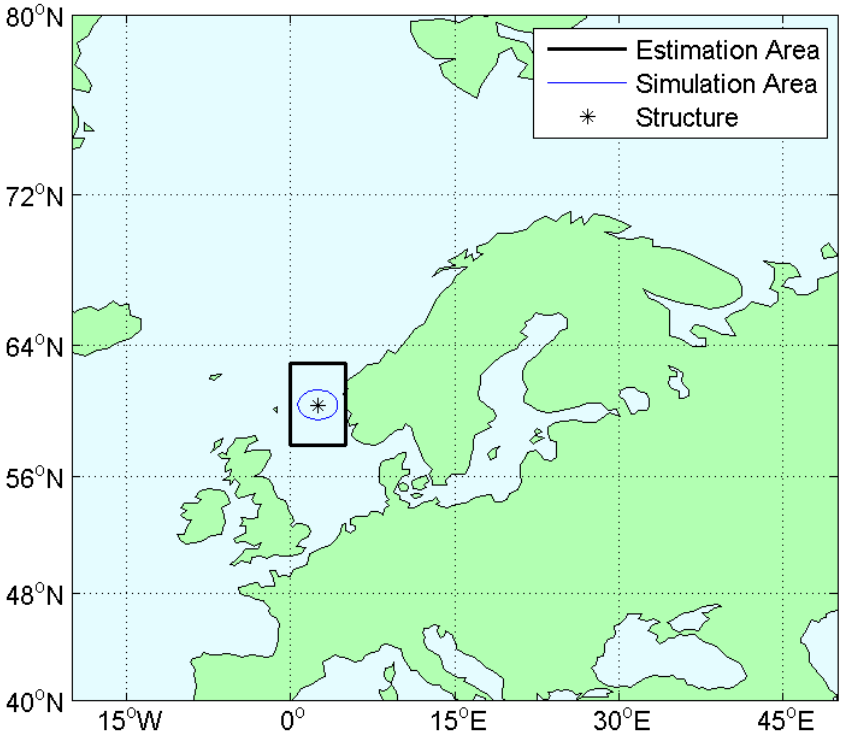

Figure 5.1: Location of the structure, estimation window and simulation window.

As a basis for the statistical analysis, the magnitude and location of 964 earthquakes which have occurred within the estimation area between 1979 and 2010 have been collected from the NORSAR earthquake catalogue[24]. Their locations are shown in figure 5.2.

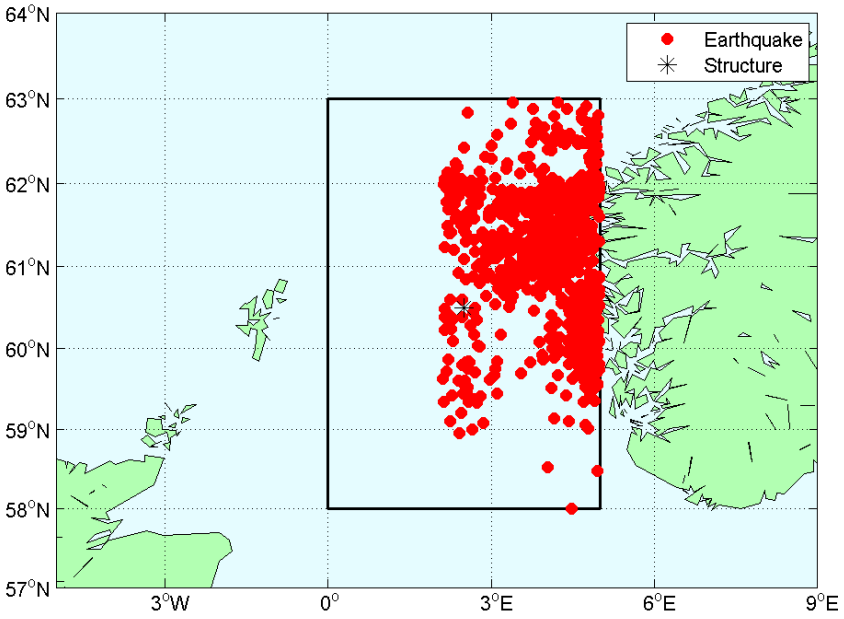

Figure 5.2: Locations of the 964 earthquakes collected.

From figure 5.2 it is observed a large concentration of earthquakes along the south-western coast of Norway. This may be caused by deglaciation, as the right half was approximately covered by ice during the last ice age[27]. As the ice melted, post-glacial uplifting started occurring, causing stresses in the crust, and thus creating the seismic activity observed. This claim is supported by *Dahle & Bungum et al*[6]. Other sources[3] argue that tectonic forces and loads from deposits are the main catalysts of the seismic activity. Nevertheless, the statistical relations derived from the observed earthquakes are assumed valid for the entire estimation area.

The earthquakes considered here are assumed to follow *Gutenberg-Richter's law*[15], given as

$$\log(N) = a - bM \tag{5.1}$$

where N is the number of earthquakes having a magnitude larger or equal to M. The coefficients a and b are determined by curve fitting, the results of which are shown in figure 5.3. The linear regression gives the coefficients as $a = 4.58$ and $b = 0.87$. It is observed from figure 5.3 that around magnitude $M = 2$, the earthquake records no longer adhere to equation 5.1. The reason for this is that far too many earthquakes occur at low magnitudes than can be recorded, thus creating an incomplete dataset for those magnitudes. For this study, only magnitudes larger than 2 are included.

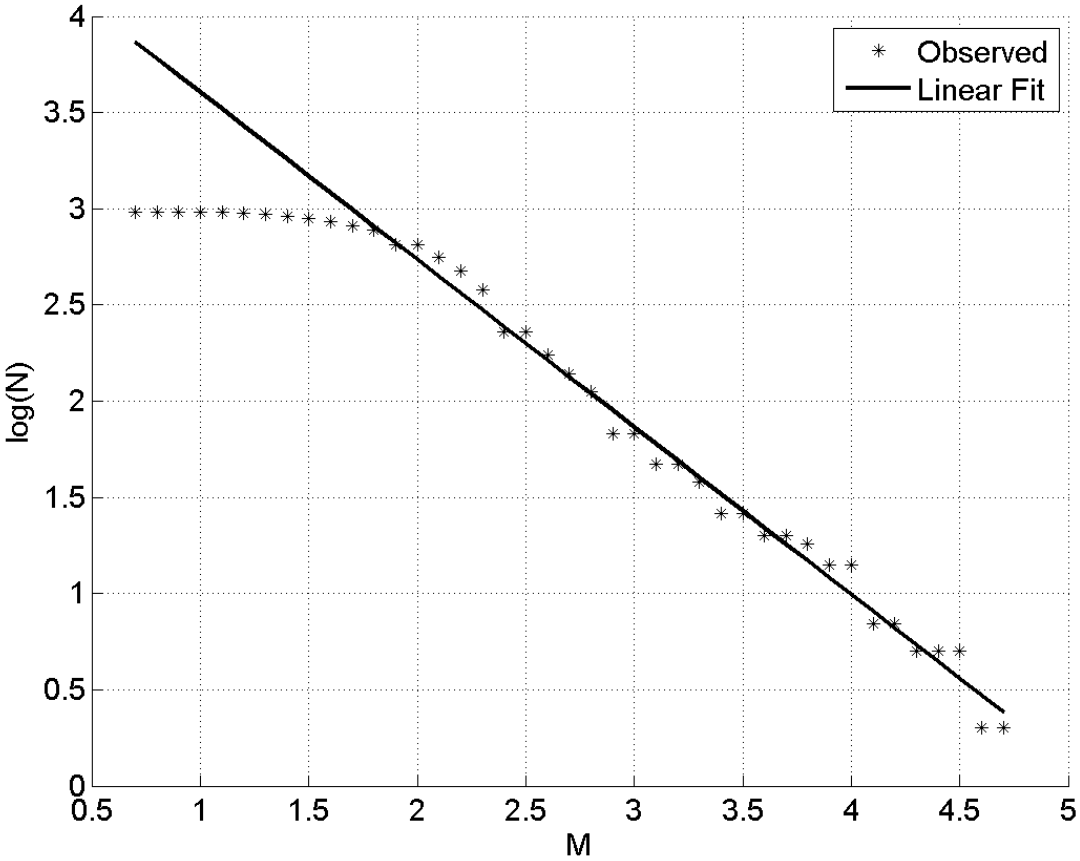

Figure 5.3: Curve fitting of 964 earthquake records to Gutenberg-Richter's law, yielding the coefficients $a = 4.58$ and $b = 0.87$.

While the constant a is of little physical meaning, b describes the relative number of small to large earthquakes in the region. These constants seem to agree well with earlier investigations performed by *Marrow*[14], yielding $a = 4.42$ and $b = 0.84$. Another result which agrees with the present calculations are those obtained by *Kanamori & Anderson*[17]. They argue that the constant b should be close to unity based on the assumption that the number of earthquakes at a given magnitude times the equivalent area is constant.

5.2 Monte Carlo simulation of earthquakes

Due to lack of data, it is difficult to determine what constitutes earthquakes of large return periods. Another complicating factor is that while equation 5.1 gives a relationship between magnitude and frequency of occurrence, it is not necessarily true that an earthquake of larger magnitude creates ground motions at the location of the structure that are consistent with a given return period. The reason for this is the attenuation of energy, and as a result, the location of the epicenter is of utmost importance when one wants to quantify seismic risk. For these reasons, the information gained from the estimation area is extrapolated by use of Monte Carlo simulations within the simulation area.

The simulation is performed by generating 50 000 earthquakes which are uniformly distributed within the simulation area - a circle of radius 100 kilometers around the structure, thus implying that no generated earthquake has an epicentral distance from the structure greater than that. If one manipulates equation 5.1, and apply it as an annual probability distribution, one can find the magnitude M by

$$M = \frac{log(\phi N_{eq}) - a}{b} \tag{5.2}$$

where N_{eq} is the total number of earthquakes one wishes to simulate - in this case 50 000, ϕ is a pseudo-random number generated for each of the earthquakes and a and b are the coefficients determined from the linear regression of equation 5.1. Obviously, such an abstraction is a step away from reality as there are no limits to the magnitude one can create with a lucky roll of the dice. To amend this, a lower bound of $M = 2$ has been used, as information of earthquakes with magnitudes lower than that are of doubtful quality. Equivalently, and more importantly, it is highly unlikely that an earthquake of very large magnitude can occur in the North Sea. For this reason, an upper bound of $M = 6.4$ is imposed, complying with *Seismic Zonation for Norway*[25].

So far, 50 000 earthquakes with a defined location and magnitude have been generated, but as previously discussed this is in no way sufficient to quantify seismic risk, as one needs the acceleration experienced by the structure. With such an acceleration being dependent upon the epicentral distance, it is necessary to find an appropriate way of expressing that relationship. To this end, the following intraplate attenuation relationship is used[7]:

$$\ln(PGA) = c_1 + c_2 M + c_4 \sqrt{R^2 + 15^2} - \ln\left(\sqrt{R^2 + 15^2}\right) + \epsilon, \quad R \leq 100\,\text{km} \tag{5.3}$$

where R is the epicentral distance in kilometers, M is the magnitude and PGA is the peak ground acceleration at a given location in m/s^2. Furthermore a focal depth of 15 kilometers is assumed. The additional parameters used in equation 5.3 are defined as $c_1 = -1.471$, $c_2 = 0.849$ and $c_4 = -0.00418$. The term ϵ expresses a normal distributed error with zero mean and a standard deviation of $\sigma = 0.83$.

For each of the 50 000 earthquakes, equation 5.3 is used to determine peak ground acceleration at the location of the structure, thus yielding a distribution of PGA values. The error term is accounted for by generating pseudo-random numbers following the normal distribution specified. The hazard analysis is performed by order statistics with the cumulative standard Gumbel distribution, given as

$$P(T \leq t) = e^{-e^{-t}} \tag{5.4}$$

An assumption necessary is that the relation $P(T_R) = \frac{1}{T_R}$ holds, where T_R is the return period of a given earthquake. Using equation 5.4 one can introduce the following transformed probability, y:

$$y(T_R) = -\ln\left[-\ln\left(\frac{1}{T_R}\right)\right] \tag{5.5}$$

Plotting y as a function of PGA, sorted in ascending order, uncovers a linear relation for large enough PGA, as is shown in figure 5.4, where a plotting position of $P_i = \frac{i}{N+1}$ has been used. In other words, the following can be written

$$y = \alpha + \beta PGA \tag{5.6}$$

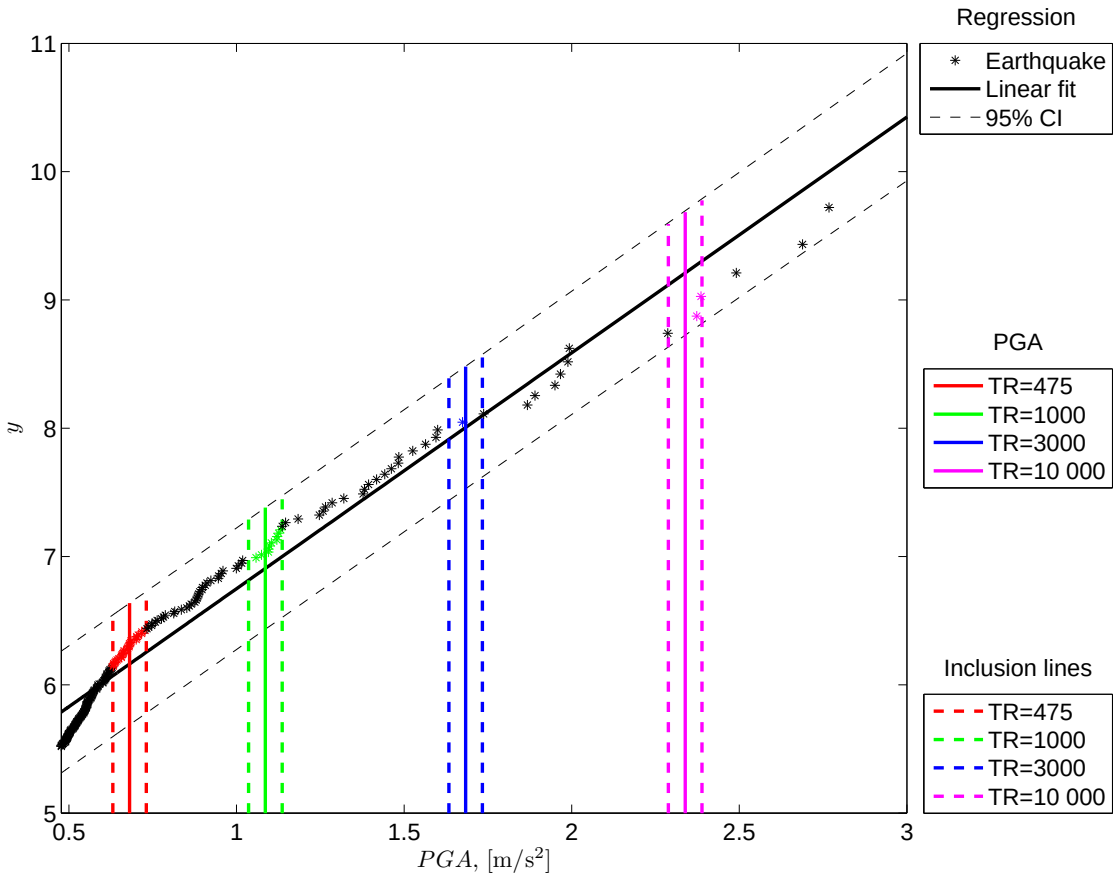

Figure 5.4: Order statistics for one simulation, where PGA values are read for each transformed probability y equivalent to a given return period T_R. The inclusion lines mark boarders within which earthquakes for the return period are selected.

What is not shown in figure 5.4 is that equation 5.6 does not hold for low PGA-values, as it abruptly breaks off towards the origin. This does not matter however, as the relation is valid for the considered interval.

Because of the error term, ϵ, in equation 5.3, the regression line of equation 5.6 is not a deterministic quantity, rather an ensemble of such lines needs to be created. Here, 100 lines have been created, and for each of them a PGA-value assumed to represent a given return period has been calculated by

$$PGA_R = \frac{-\ln\left[-\ln\left(1-\frac{1}{T_R}\right)\right]-\alpha}{\beta} \tag{5.7}$$

where it has been used that $P(X > x) = 1 - P(X \leq x)$, thus providing a probability of exceedance. At the same time as the representative peak ground acceleration, PGA_R is found, earthquakes with PGA-values that lie within $\pm 0.05\,\mathrm{m/s^2}$ of PGA_R are selected, as exemplified in figure 5.4. These earthquakes are assumed characteristic of that return period, yielding three parameters which can be used for time

history selection, namely the magnitude, M, the epicentral distance, R and the peak ground acceleration, PGA.

Obviously, the procedure described above is only applicable as a rough estimate. First of all, its entire basis is an extrapolation, which can yield inaccurate results. The upper and lower magnitude limits are artificially imposed, and even they are estimates. The attenuation relationship, while derived for intraplate earthquakes, does not take local geology into account. The order statistics is ripe with inaccuracies for several reasons. Firstly the database of recorded earthquakes does not only include the largest earthquakes each year, but all earthquakes registered within a 30 year period. This implies that the probabilities are estimates. Secondly, the choice of fraction for which to perform the linear regression of equation 5.6 affects the results. Lastly, the choice of earthquakes by the method shown in figure 5.4 is dubious at best. However, due to the lack of available data it is believed that for the task at hand, where great accuracy is not required, such an estimate is the most appropriate way of doing it, with respect to available time.

As the characteristic peak ground accelerations are largely created by simulations rather than measurements, it is necessary to compare them with earlier work. For this purpose, the acceleration zonation maps of *Seismic Zonation for Norway*[25] has been used, as it has been adopted by both Eurocode 8[11] and the NORSOK standard[26]. The comparison is shown in table 5.1.

Table 5.1: Comparison of simulated results with those given by *Seismic Zonation for Norway*[25].

Return period [years]	Simulated [m/s^2]	Standards [m/s^2]
475	0.61 ± 0.09	0.6
1000	1.1 ± 0.2	1.0
3000	1.8 ± 0.5	-
10000	2.7 ± 0.9	2.7

The simulated results show remarkable similarity with the zonation maps, giving credibility to the procedure used in this study.

5.3 Accelerogram generation

Based on generated triplets of earthquake parameters - namely magnitude, epicentral distance and peak ground acceleration, 10 recorded earthquake accelerograms are selected for each return period, as can be seen in table 5.2. For an extended version of this table, the reader is referred to appendix B.

Table 5.2: Parameters of the chosen earthquakes, where each of them comply with the selection criteria for a given return period.

$T_R = 475$ years			$T_R = 1000$ years			$T_R = 3000$ years			$T_R = 10\,000$ years		
M	R [km]	PGA [m/s^2]	M	R [km]	PGA [m/s^2]	M	R [km]	PGA [m/s^2]	M	R [km]	PGA [m/s^2]
3.3	11	0.6	4.3	16	1.1	5.6	40	1.8	6.9	65	2.5
4.2	8	0.6	4.9	5	1.1	5.7	23	1.8	6.3	30	2.6
4.2	15	0.6	4.8	24	1.2	5.4	9	1.9	4.2	6	2.5
3.4	15	0.6	4.8	4	1.2	5.4	6	1.7	5.9	11	2.7
3.3	3	0.6	4.8	18	1.1	5.6	27	1.8	5.2	16	2.6
4.4	10	0.6	5.2	27	1.2	5.3	13	2.0	6.2	33	2.7
4.5	24	0.6	4.7	2	1.1	5.7	9	1.7	5.4	10	2.5
4.3	7	0.7	4.8	8	1.0	5.2	12	2.0	5.8	11	2.8
4.9	32	0.7	4.9	10	1.2	5.2	9	2.0	5.7	14	2.4
4.9	20	0.8	5.0	12	1.1	5.0	9	1.9	6.0	13	2.5

The databases from which selections are made is the European Strong Motion Database (ESD)[2] as well as the Pacific Earthquake Engineering Research Center (PEER)[1]. Due to the difficulty of finding records with parameters of reasonable similarity to those sought after, a few simplifications have been made. First of all, no difference has been made between the several types of magnitude definitions. This introduces inaccuracies as these definitions are generally different, and only valid for certain, perhaps non-overlapping, intervals. In this study, a generalized magnitude scale, M, has been used which is assumed valid for all magnitudes. This rationale is based on the fact that all the magnitude scales are defined to be similar, thus by concatenating the different scales, valid for different intervals, it is possible to reduce them to one approximate magnitude scale. Further errors are introduced as the selection of earthquake records include all types of seismicity. There has been made no difference between fault type, plate tectonics, or whether an earthquake is land based or subsea - which is also provoked by lack of appropriate data. It is however believed that magnitude and epicentral distance combinations help sort out earthquakes that are similar to those of the North Sea. Another problem is that it is generally more difficult to find earthquake recordings satisfying earthquakes of higher amplitude, thus yielding larger separation between simulated and recorded parameters. The reason for this difficulty is that the simulation process will, by design, select fewer and fewer earthquakes as the return period increases - as they are less probable. Furthermore, due to the low seismicity of the North Sea, these

earthquakes more commonly consist of low magnitude earthquakes with low epicentral distance. Records of such earthquakes are next to impossible to find and have to be excluded, leaving quite few parameters with which to compare. This problem is exemplified by the first entry of the 10 000 year return period column of table 5.2 where the magnitude is listed as $M = 6.9$. This is larger than the maximum probable earthquake in the North Sea. Efforts have been made however to reduce the effect of such inconsistencies, as is seen in the following.

For each return period, a response spectrum has been made based on the mean of the response spectra of the individual earthquakes within a return period. This is done in lieu of any better form of ensemble statistics, in order to avoid selecting an accelerogram which only coincidentally satisfies the return period parameters, but actually is an outlier with respect to the mean. The mean response spectra for each return period are shown in figure 5.5.

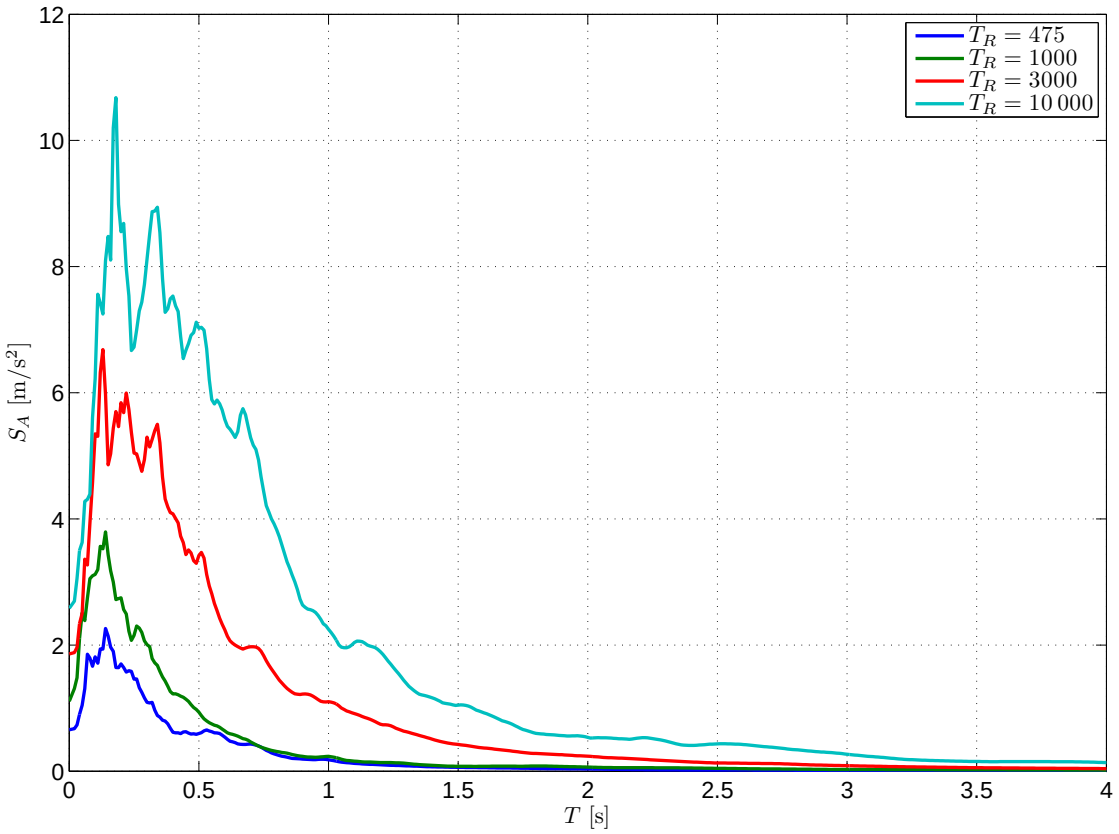

Figure 5.5: Mean acceleration response spectra for the four return periods considered.

Figure 5.5 shows that the mean acceleration response spectra have a typical shape, with low period response dominating. Further, it is observed that increasing return period brings with it higher response and includes longer periods, which seems reasonable. In order to establish a reference point, the mean response spectrum of the 475-year return period is compared with the equivalent design spectrum of Eurocode 8[11]. Assuming that the structure rests upon solid rock, which implies

ground type A, the calculated mean response spectrum corresponds well with the design spectrum, with Eurocode 8 being on the conservative side - as it should be.

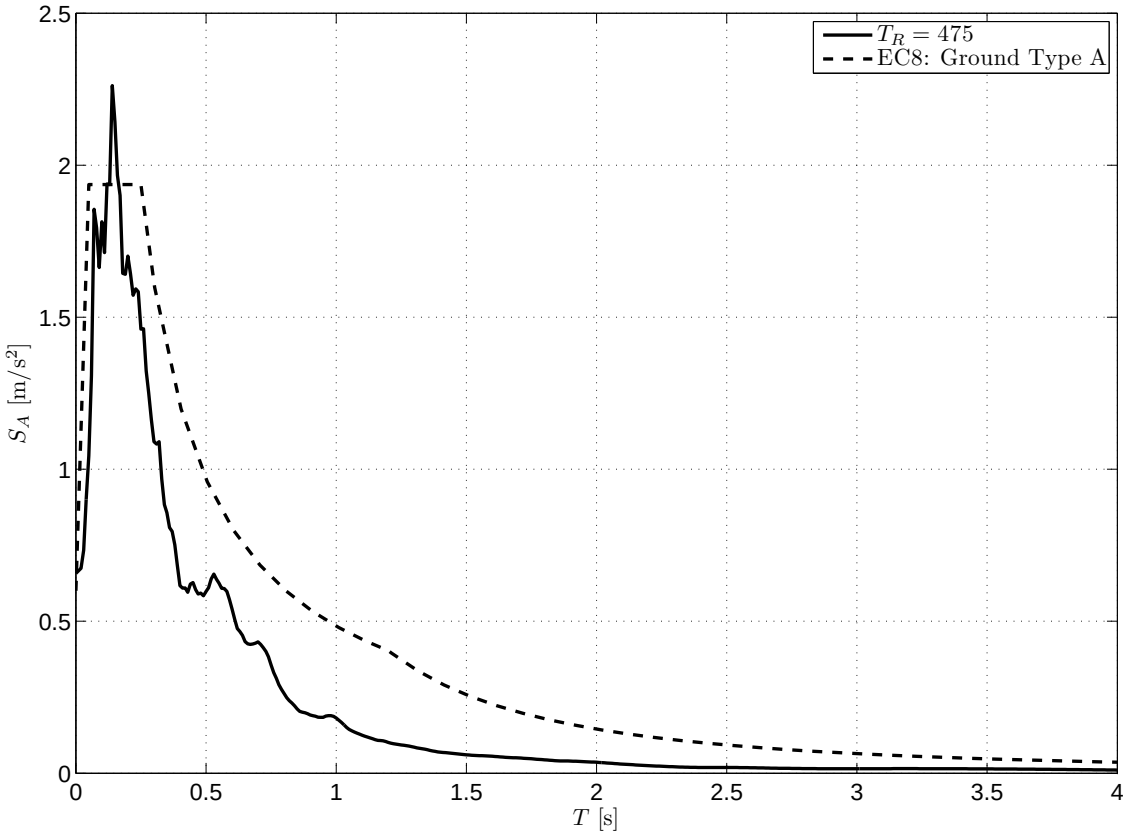

Figure 5.6: Comparison of generated response spectrum with Eurocode 8 - showing reasonable similarity with ground type A.

The fact that the generated response spectrum corresponds with a stiff rock design spectrum from Eurocode 8 is not surprising, as the selection and averaging of many earthquakes filters away individual soil amplifications, leaving only a trend. Looking at table B.1 in appendix B shows that of the earthquake accelerograms collected, the majority of them represents recordings taken on solid rock - thus determining said trend. The reason for this is that most earthquakes are recorded by seismic listening devices mounted on buildings. There is obviously an abundance of buildings founded on solid rock, as several, perhaps non-surpassable, difficulties arise when one attempts to use soft soil as a foundation.

Continuing with the response spectra of figure 5.5, and thus accepting that they are only valid for structures standing directly on solid rock, it is tempting to use them as a basis for accelerogram simulation. This would however result in unrealistic earthquakes, as the frequency content resulting from simulations based on the mean response spectrum in no way resembles that of a real earthquake. For this reason, a single response spectrum of a recorded earthquake is chosen for each return period, which resembles the mean response spectrum as closely as possible.

By using the software SIMQKE[12], response spectrum compatible accelereograms are generated. In order to make them comparable between return periods, a duration of 15 seconds has been imposed on all accelerograms. Furthermore, the simulation method applied by the software is basically an alteration of the frequency content of random white noise. Such signals are stationary in nature. In order to mold them into the shape of a typical earthquake, the modulation function given in equation 5.8 has been chosen, thus rendering the signals quasi-stationary.

$$I(t) = A\left(e^{-\alpha t} - e^{-\beta t}\right) \tag{5.8}$$

In equation 5.8 the constants $\alpha = 0.3$ and $\beta = 0.45$ ensure that by the time 15 seconds has passed, approximately 90% of the amplitude has abated. The coefficient A is a normalization constant. The final result is a set of characteristic earthquake accelerograms, one for each return period, which will be used for structural analysis. They are shown in figure 5.7.

While the generation of realistic earthquake accelerograms has been important, a few irregularities remain. The 475-year earthquake shown in figure 5.7 has a duration of significant ground motion which is longer than a natural earthquake - a tell-tale sign of simulation. The 1000-year earthquake also stands out from the rest with a higher frequency content, which is a result of the frequency iteration procedure and is elaborated on further in section 6.1.2. The created accelerograms may not be geophysically immaculate, but they will suffice in generating structural loads which are accurate enough to represent reality.

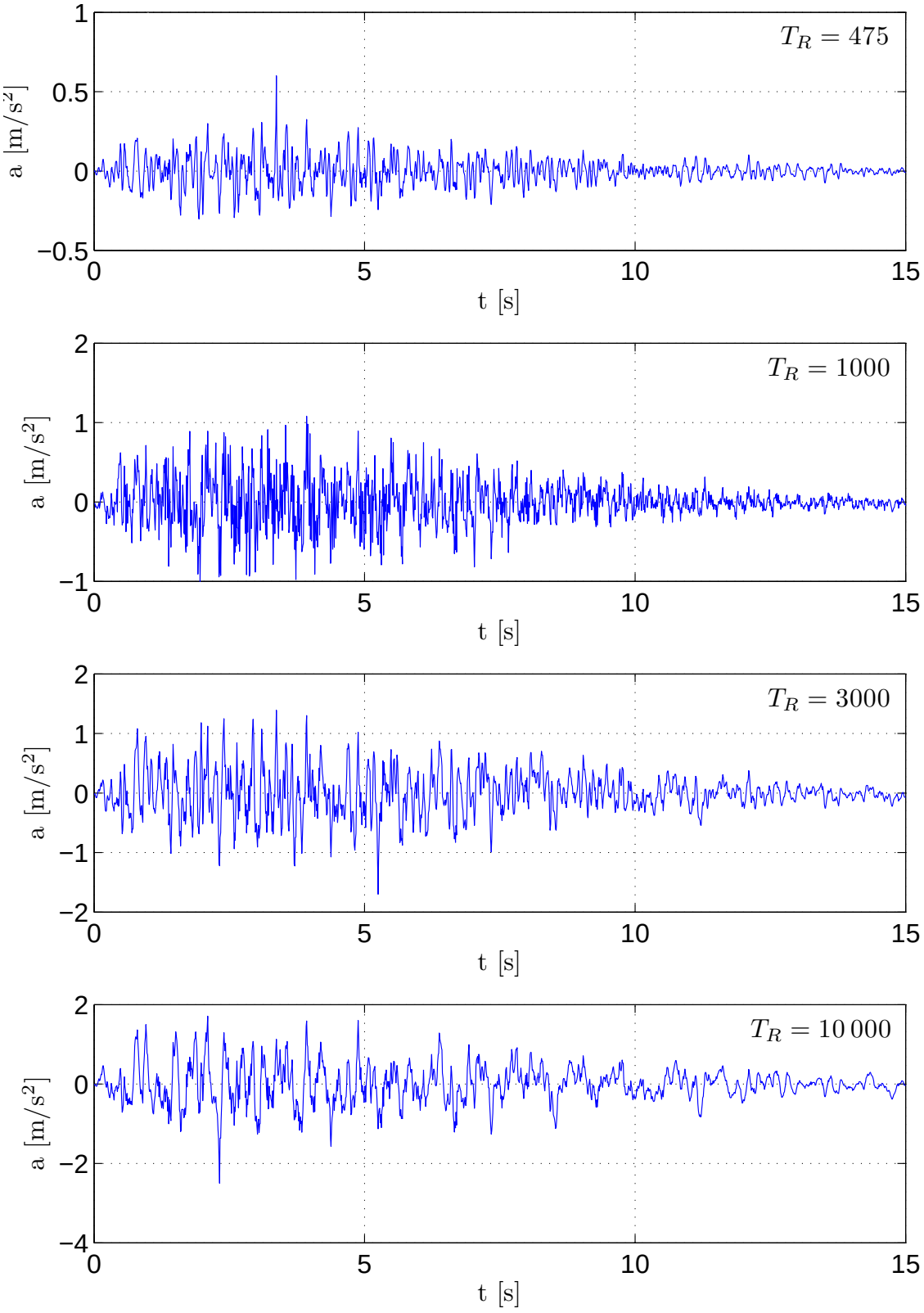

Figure 5.7: Earthquake accelerogram simulated for each of the four return periods.

6 Results and discussion

In this chapter, the main results of the various analyses will be presented. First the elastic time history analysis without surrounding water is presented, providing a basis for comparison for all following analyses.

6.1 Elastic analysis

For massive concrete structures, such as the one studied here, it is normal design practice to assume elastic behaviour. For this reason, it is a natural choice to don the very same assumption as a first approach.

A basis for comparison are the eigenfrequencies of the structure, the first ten of which are given in table 6.1.

Table 6.1: Unique eigenfrequencies

Mode	Frequency [Hz]
1	2.5965
2*	3.0380
3*	3.9487
4	4.5218
5	5.5669
6	6.2844
7*	6.3006
8	6.3399
9*	6.3419
10	6.4126

* Double Eigenfrequencies

It is observed that the eigenfrequencies are quite high, implying a stiff structure - which is realistic. Also worth noting are the occurrence of double eigenfrequencies. They are created by the symmetry of the structure, as there is no difference between the energy demand of a perturbation along either of the two horizontal principle axes for these modes.

6.1.1 Time history analysis

A time history analysis is performed by applying accelerograms similar to, but statistically independent from, those of figure 5.7 in both of the horizontal directions, and a scaled down version in the vertical direction. From this, maximum envelope plots of the von Mises stress can be generated, as shown in figure 6.1.

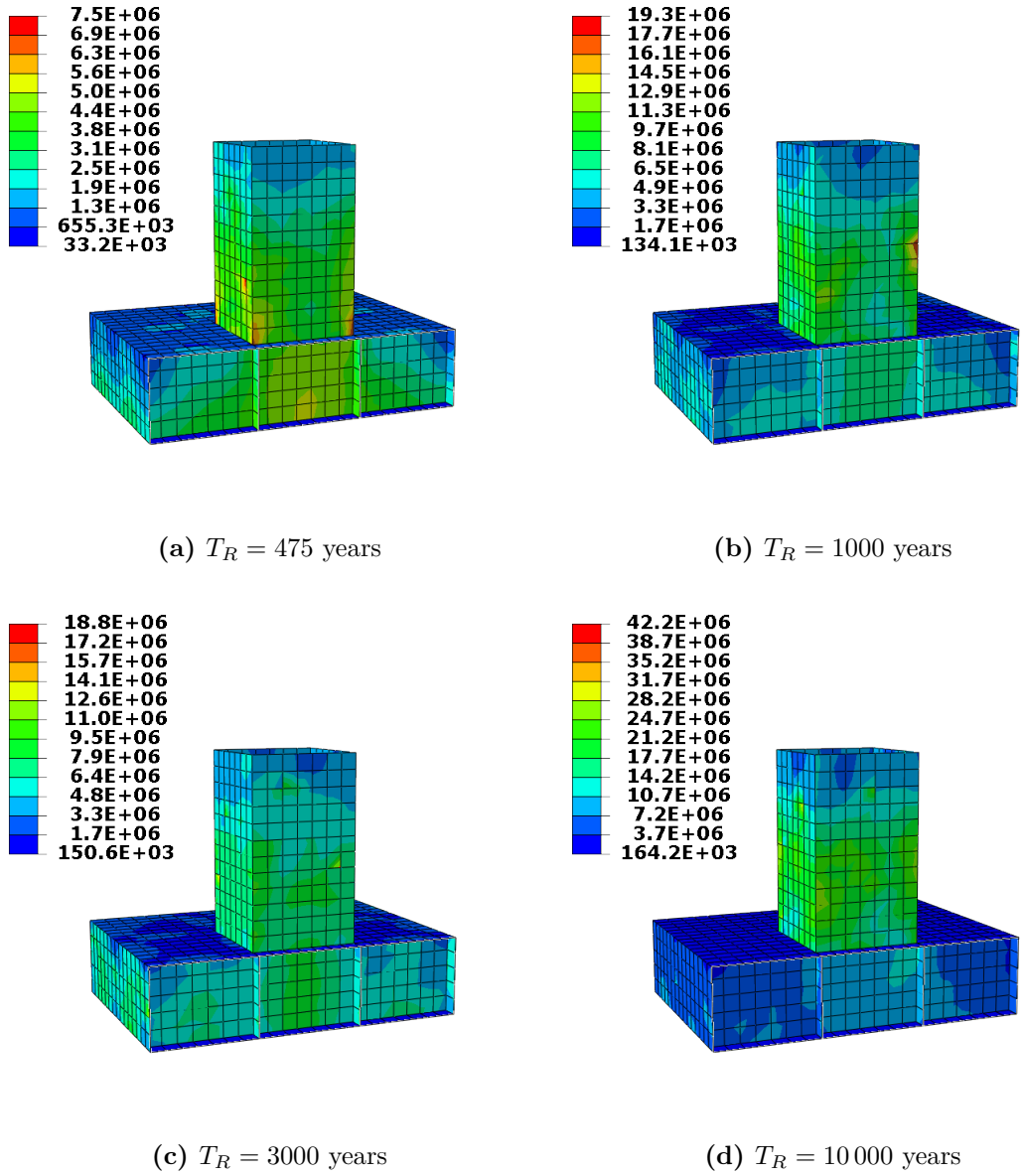

(a) $T_R = 475$ years

(b) $T_R = 1000$ years

(c) $T_R = 3000$ years

(d) $T_R = 10\,000$ years

Figure 6.1: Contour plots of the maximum envelope von Mises stress of the four return periods considered. Units are in Pascal.

What is especially noticeable about figure 6.1 is the similarity between the 1000- and 3000-year earthquake response, shown in figures 6.1b and 6.1c respectively. It is apparent that the 1000-year earthquake produces stresses in the structure which

are almost identical to those resulting from the 3000-year earthquake, with peak values that are slightly higher. This occurs in spite of simulating the 3000-year accelerogram from an acceleration response spectrum which suggests stronger ground motion than the equivalent 1000-year response spectrum, as can be seen in figure 5.5. While this might at first glance seem like a paradox, a closer investigation of the simulated earthquake Fourier spectra in appendix B.3 reveal the cause of the discrepancy. From figure B.6 it is seen that the culprit is an unfortunate side effect of the generation of quasi-stationary earthquakes. As previously mentioned, the simulation procedure is based on white noise, which is iteratively altered in the frequency domain such that its response spectrum matches a target response spectrum. The remnants of this procedure is observed as stationary oscillations of the Fourier spectrum for large frequencies. A real earthquake normally does not present with such oscillations, but instead decays towards zero as the frequencies become sufficiently large. The artificial oscillations are particularly high for the 1000-year earthquake, which excites a larger number of structural modes, and thus provokes a higher response. For the other three return periods, the spurious oscillations are not as prevalent, resulting in a better approximation to real earthquakes.

6.1.2 Response spectrum analysis

It is interesting to see how well a response spectrum analysis can estimate the results from the time history analysis, as it completes in a fraction of the time. To investigate this, 500 modes have been used, accounting for approximately 90% of the structural mass in terms of effective mass, in each direction. The three modal combination methods described in section 2.2.2 have been compared. The same comparison has been performed for all four return periods, but for brevity, only the results for the 475-year earthquake are presented here, with the rest being available in appendix E.

The absolute sum combination method, which is the most conservative, is explored first. Due to the inability of Abaqus to perform modal combination for the von Mises stress, the nodal moments have been used instead. A contour plot of the ratio between time history and response spectrum analysis is shown in figure 6.2.

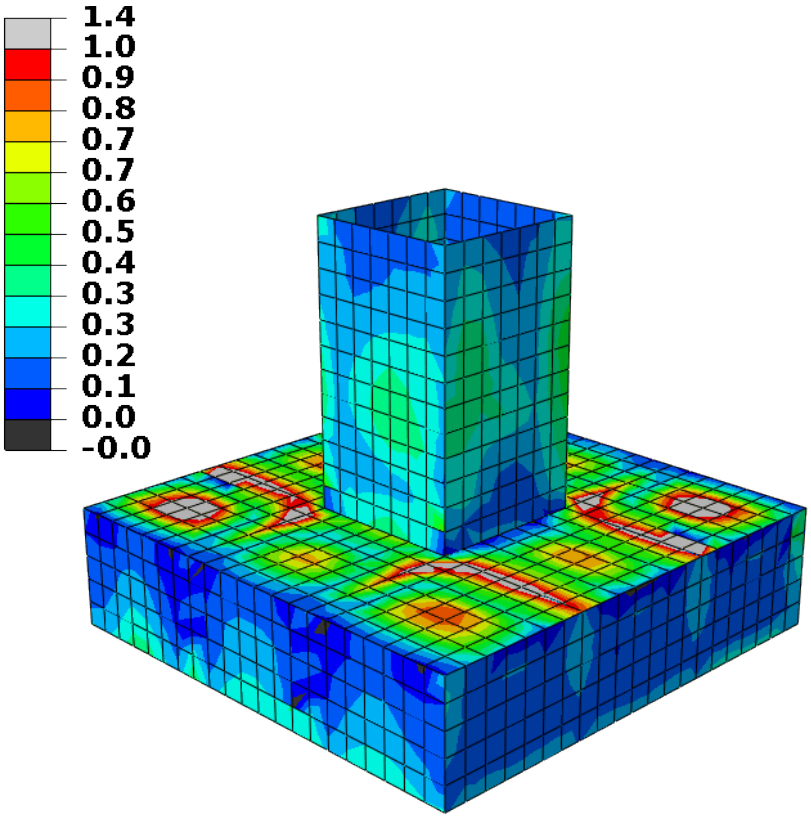

Figure 6.2: Contour plot of the ratio between the moment along one of the axes of symmetry as calculated using time history and response spectrum analysis respectively.

From figure 6.2 it can be seen that the response spectrum analysis with modal combination by use of absolute summation is mostly conservative, however there are areas in which the time history analysis results in a larger moment. These areas are marked in gray on figure 6.2. It is worth noting that while there are points which receive a negative ratio, absolute values have been used in establishing the contour plot. These values are in other words erroneously produced by Abaqus. Fortunately, there are only a few nodes that are affected, which can be ignored.

Also seen from figure 6.2 is that the unconservative areas are fairly concentrated. Furthermore, the results are only unconservative by a maximum of 40%. In evaluating whether a response spectrum analysis is applicable, it is necessary to investigate whether the unconservatism occur for large or small moments. Obviously, a 40% increase of an otherwise negligible quantity might also be negligible - meaning that the response spectrum analysis could be appropriate still. For each of the nodes in the structure, the moments determined by the response spectrum analysis has been gathered and plotted relative to the time history analysis, henceforth referred to as an RS-TH plot, resulting in figure 6.3.

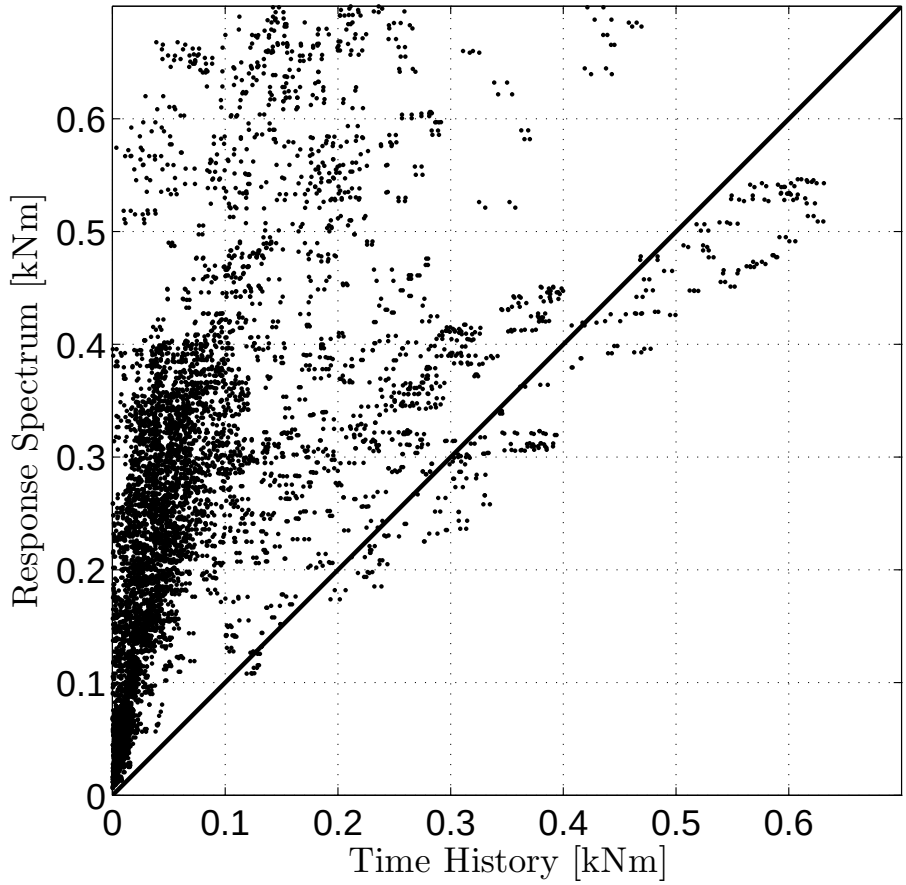

Figure 6.3: Nodal moments determined by response spectrum and time history, plotted relative to each other. The slanted line represents the boarder of conservatism, below which results are unconservative.

Figure 6.3 shows that it is the larger moments which are unconservative, however they do not stray far into unconservative territory. Furthermore, the moments present in the structure during the 475-year earthquake are minuscule. By looking at figure 6.1a it is seen that the maximum von Mises stress that occurs in the structure is barely twice the stress at which initial cracking takes place. Because of this, the method of summation of absolute values is considered applicable. This does not, however, mean that the results are very accurate. Obviously, the best results would be an almost linear cloud of points slightly above the line of conservatism. This is not the case in figure 6.3 however, where it is observed largely scattered values, with a concentration along a line with a much higher slope than the conservatism line. Such a result implies that large parts of the structure is given an overly conservative response. This is typical for the absolute sum of peak values - as it assumes that all modes contribute simultaneously, which is quite unrealistic.

Looking at appendix E, it is seen that summation of absolute values is indeed an approach which is possible to use, yielding no unconservative results for return perids higher than 475 years. On the other hand, the results are very conservative. For

instance, the 10 000 year earthquake, shown in figure E.9, has a moment ratio of 0.1-0.3 for large parts of the structure. Seeing as an earthquake of such a long return period imposes large moments, this is an unacceptable simplification for use in practice. Also shown in appendix E is a comparison of shear forces - along one of the axes of symmetry - determined by the two methods. The same results are observed here as with the moments: Slightly unconservative results for the 475-year earthquake, but otherwise the response spectrum analysis produces a much larger response, making it impractical for design purposes.

Modal combination by use of square root of the sum of squares (SRSS) is investigated next. In contrast to an absolute sum of peak values, SRSS assumes no correlation between modes. It is generally accepted that such a method provides better results if the modes are well spaced. The resulting ratio plot is shown in figure 6.4.

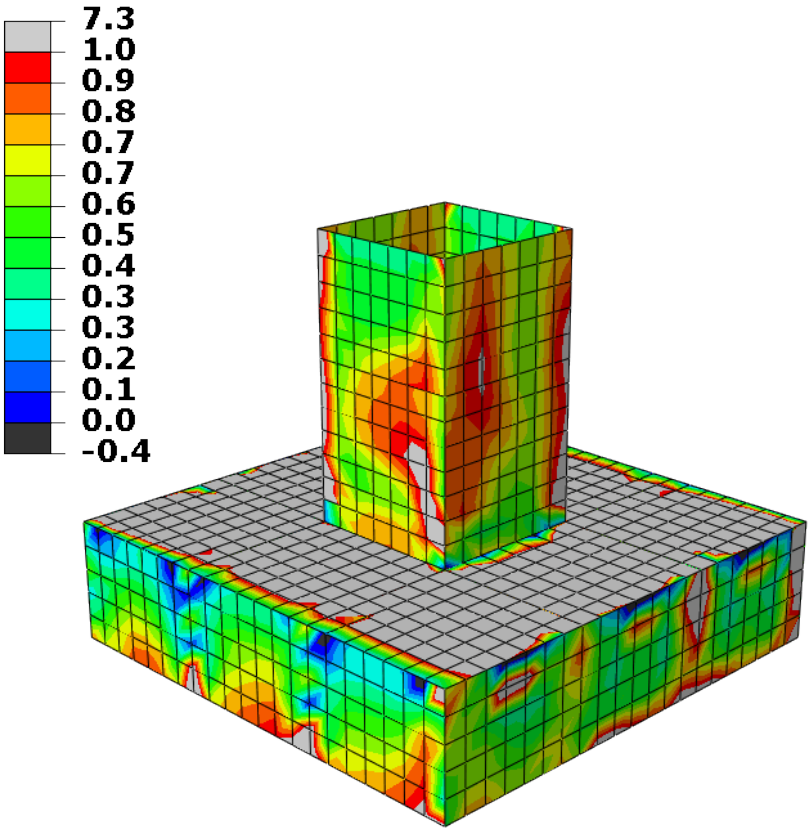

Figure 6.4: Ratio plot between moments determined by time history and response spectrum analysis using the SRSS method.

The results show large areas which are unconservative, mostly in the roof and side walls of the caisson, but also in the shaft. This suggests that the interaction between modes is significant, which is to be expected if one looks at table 6.1. The eigenfrequencies are closely packed, meaning that it is unlikely they occur completely independent of each other. This also implies that double eigenfrequencies, produced by symmetry, do not correlate, which is obviously erroneous. The RS-TH plot for the SRSS method is shown in figure 6.5.

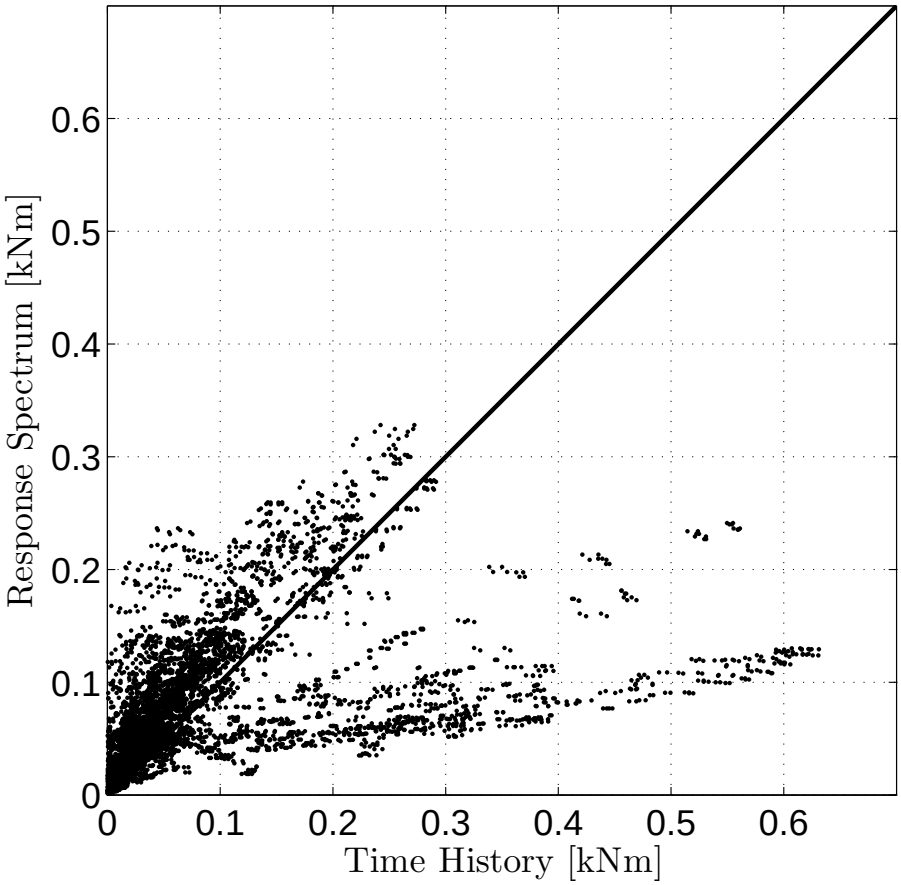

Figure 6.5: Nodal moments of the time history analysis plotted against those of the response spectrum analysis, using the SRSS method.

As expected from the ratio plot of figure 6.4, a larger part of the nodes have moments which are unconservative when determined by response spectrum analysis. It is also seen from figure 6.5 that the largest unconservatism occurs for the largest moments such that a great deal of scepticism should be directed towards the use of the SRSS method. On the other hand, looking at the nodes which have moments that are on the conservative side, it is seen that these results correspond more closely to those determined by the time history analysis. This demonstrates what is expected of the SRSS modal combination method: it is supposed be a better approximation than the absolute sum, however it may yield unconservative results when the density of frequencies is high. A mixture between good and unconservative results is then to

be expected depending on which areas are affected by the different modes.

Although the eigenfrequencies of table 6.1 are closely packed, that does not mean the modes with significant contribution to the particular motion come close together. To get a sense of this, the modal participation factors of the structure are shown in figure 6.6. Here it is seen that the non-negligible participation factors are grouped around certain frequencies. For instance, in the interval of ∼0-50Hz a large number of modes have large participation factors. The same can be said for the interval ∼75-150Hz - although with significantly smaller participation factors. Inside such a packet, the response is underestimated, as correlation is likely to occur, however intergroup correlation is less probable, suggesting better approximation here.

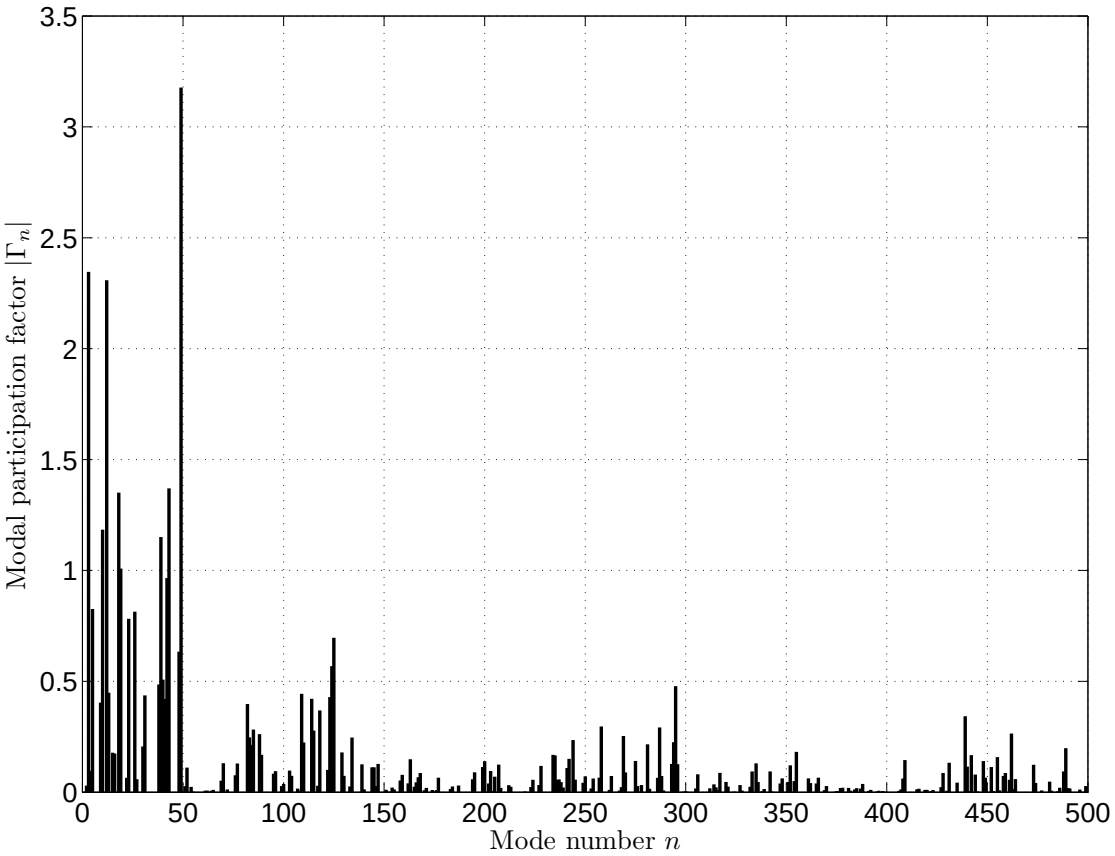

Figure 6.6: Absolute value of the modal participation factors for the 475-year earthquake.

The final repetition is performed for the complete quadratic combination method (CQC), which is supposed to provide a compromise between the sum of absolute values and SRSS. The ratio plot is shown in figure 6.7, where it is seen that this is not the case. In fact, the unconservative areas have a larger extent than for the SRSS method. Furthermore, the maximum underestimation of the response is larger.

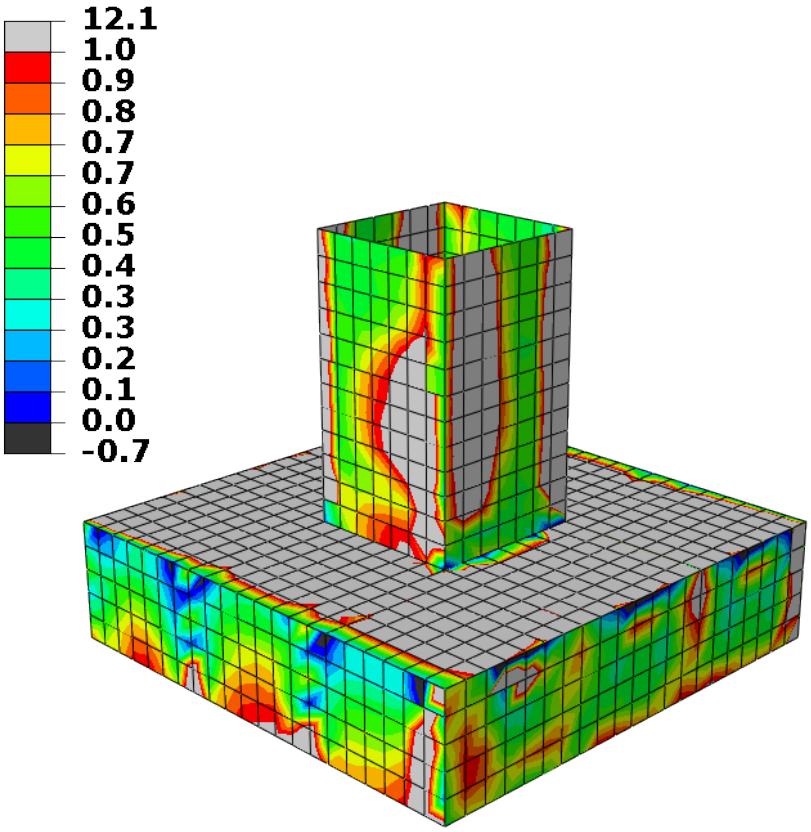

Figure 6.7: Ratio plot between moments determined by time history and response spectrum analysis using the CQC method.

Further clarification is presented by the RS-TH plot:

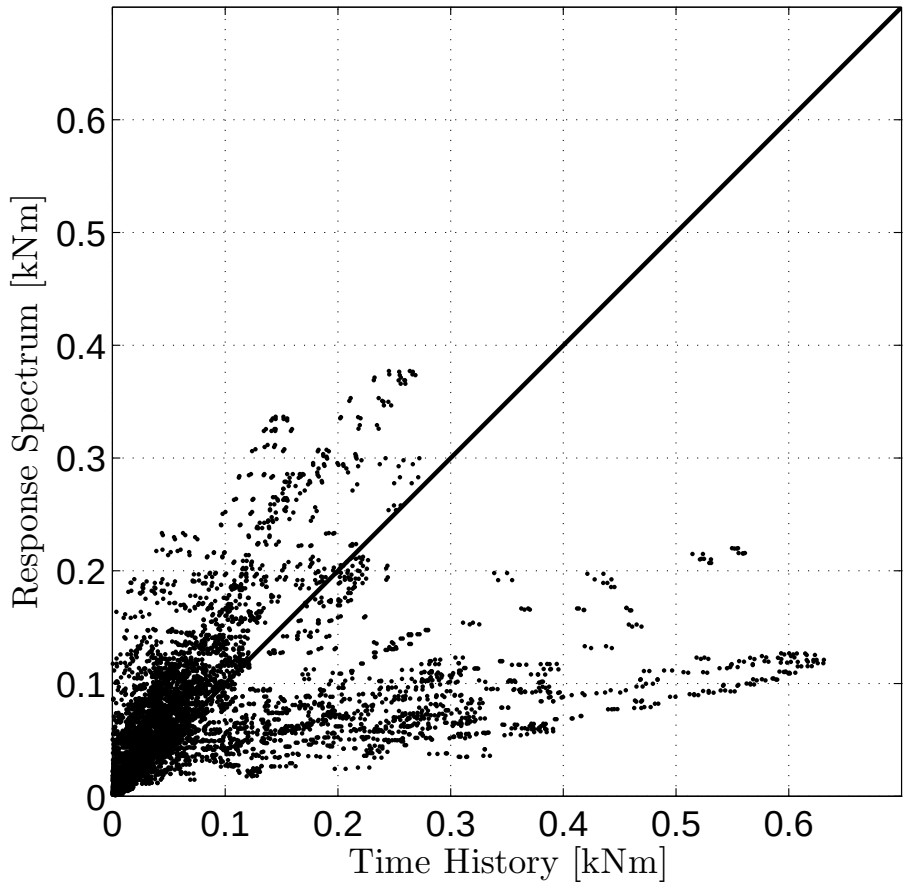

Figure 6.8: Nodal moments of the time history analysis plotted against those of the response spectrum analysis, using the SRSS method.

An important discovery is that figure 6.8 bares a striking resemblance to the RS-TH plot of the SRSS method, as can be seen in figure 6.5. Apparently, the CQC method does not adequately account for modal interaction. The reason for this lies in the correlation coefficient, ρ_{mn}, given in equation 2.31, which is unable to accurately describe the modal interaction for this geometry and motion. This is demonstrated further by figure 6.9, where the correlation coefficient is plotted for the 500 eigenfrequencies used. It has a value equal to one for identical eigenfrequencies. For well spaced eigenfrequencies, there is assumed no correlation, thus yielding a correlation coefficient of zero here. These are two limiting cases which seem reasonable. It is however also noticed that the correlation coefficient decays to zero very quickly, resulting in a perhaps too restrictive relationship between eigenmodes. As can be seen from figure 6.9, this is especially true for low frequencies, which also have the highest participation factors. The claim of too restrictive correlation relationship is justified by the similarity between the RS-TH plot of the SRSS and CQC methods, as using a correlation coefficient which is equal to one only for interaction with itself, and zero elsewhere is indeed the SRSS method.

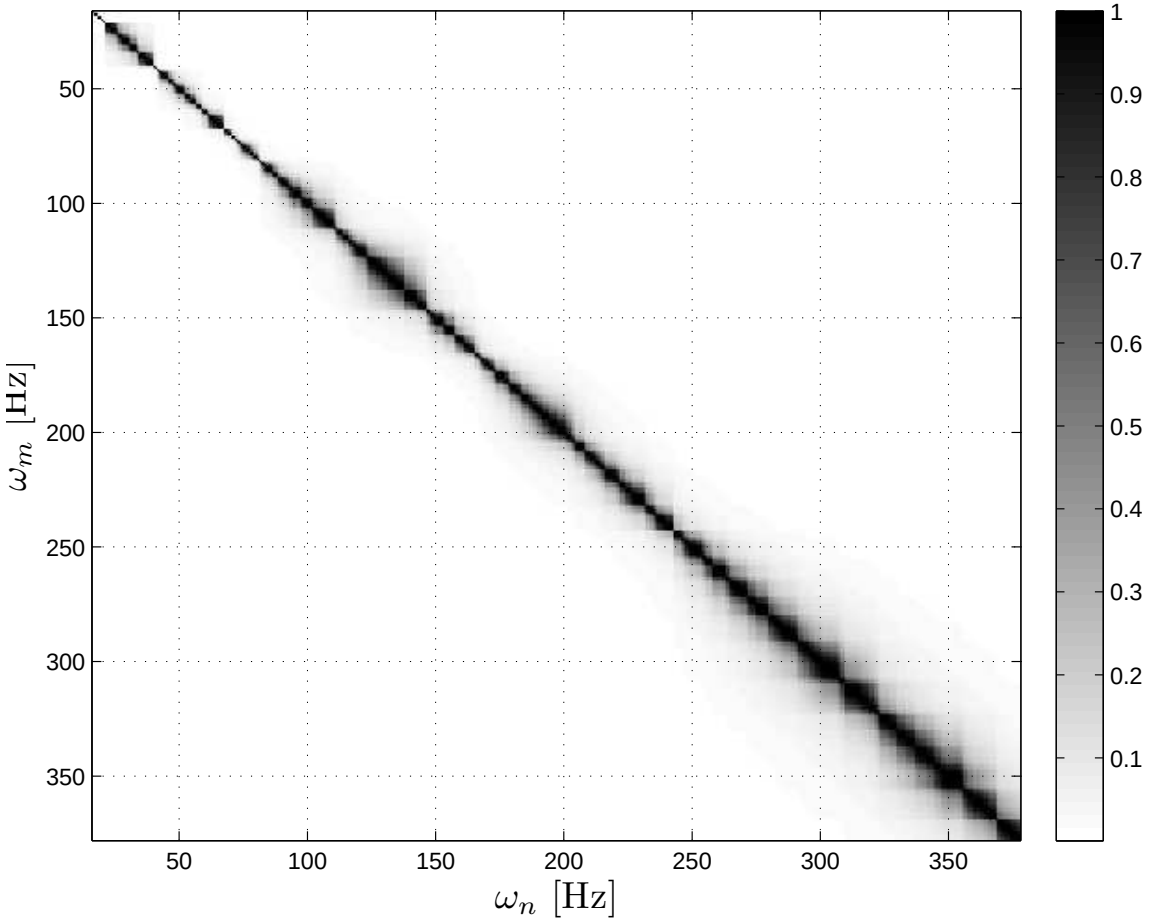

Figure 6.9: Nodal moments of the time history analysis plotted against those of the response spectrum analysis, using the SRSS method.

Generally speaking, with reference to appendix E, it is apparent that the SRSS and CQC method predict a structural response whose mean coincides reasonably well with the time history analysis. On the other hand, the response has a larger spread, resulting in an underestimation of response in large parts of the structure. This spread is increasing for nodes with larger loads. Contrarily, the absolute sum of peak values provides a smaller spread, but its mean is a poorer approximation of the time history analysis, though erring on the conservative side. This behaviour is exemplified by figure E.2.

It is obvious that the use of the SRSS and CQC method for the considered structure is not viable, as the response is generally underestimated. The absolute summation is impractical to use due to the large overestimation. The inevitable conclusion is that a response spectrum analysis fails to predict the response of the considered structure accurately, and because of this, time history analyses should be used instead.

6.2 Effect of plasticity

The material model derived in chapter 3 will be applied to the time history analyses, but the effects of elastic stiffness degradation will be included as a separate study. This is prefaced by a simple investigation of the behaviour of the material model.

6.2.1 Numerical Study: Material model

In order to comprehend the workings of the relations derived in chapter 3, a numerical study in Abaqus[29] of the behaviour of a single, linear shell element is undertaken. The model is shown in figure 6.10, where it is seen that the left and bottom edges are restrained from horizontal and vertical motion respectively, while load is applied by the prescribing of displacement at the right and upper edges.

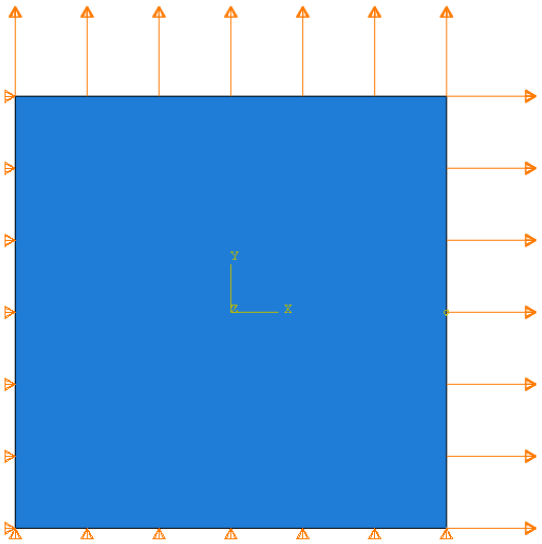

Figure 6.10: Simple model used for numerical study of the constitutive models.

Necessary parameters of the material model, in addition to those specified for B45 concrete in Eurocode 2, are given in table 6.2 and are selected based on recommended values in the Abaqus manual[31]. This is done because a detailed study on the optimal values is deemed unnecessary for the task at hand.

Table 6.2: Concrete material parameters.

Symbol	Value	Description
K_c	$\frac{2}{3}$	-
ϵ	0.1	Eccentricity
ψ	31°	Dilation angle

First off, the element is modelled without reinforcement and subjected to cyclically applied loads, in such a way that the yield surface is charted at various degrees of plasticity. This is shown in figure 6.11, where it is seen that for the initial yielding, represented by the blue curve, the Drucker-Prager yield surface is recreated for biaxial compression stress states. It has the form of an ellipse, as it is basically a modification of the von Mises yield surface, as shown in equation 3.5. In the other three quadrants, the effects of the alterations in equation 3.6 come into play, creating a lower resistance here, and thus creating a discontinuous slope at the transition points. The uniaxial yield stress in compression is found where the curve crosses the negative x- and y-axis. Equivalently, the uniaxial yield stress in tension is found where the curve crosses the positive axes - as it should be. It is also observed that the yield surface is symmetric about the equibiaxial stress line, which is intuitively reasonable, as it would be non-physical if pulling on one edge of the element gives a different response than pulling on the other.

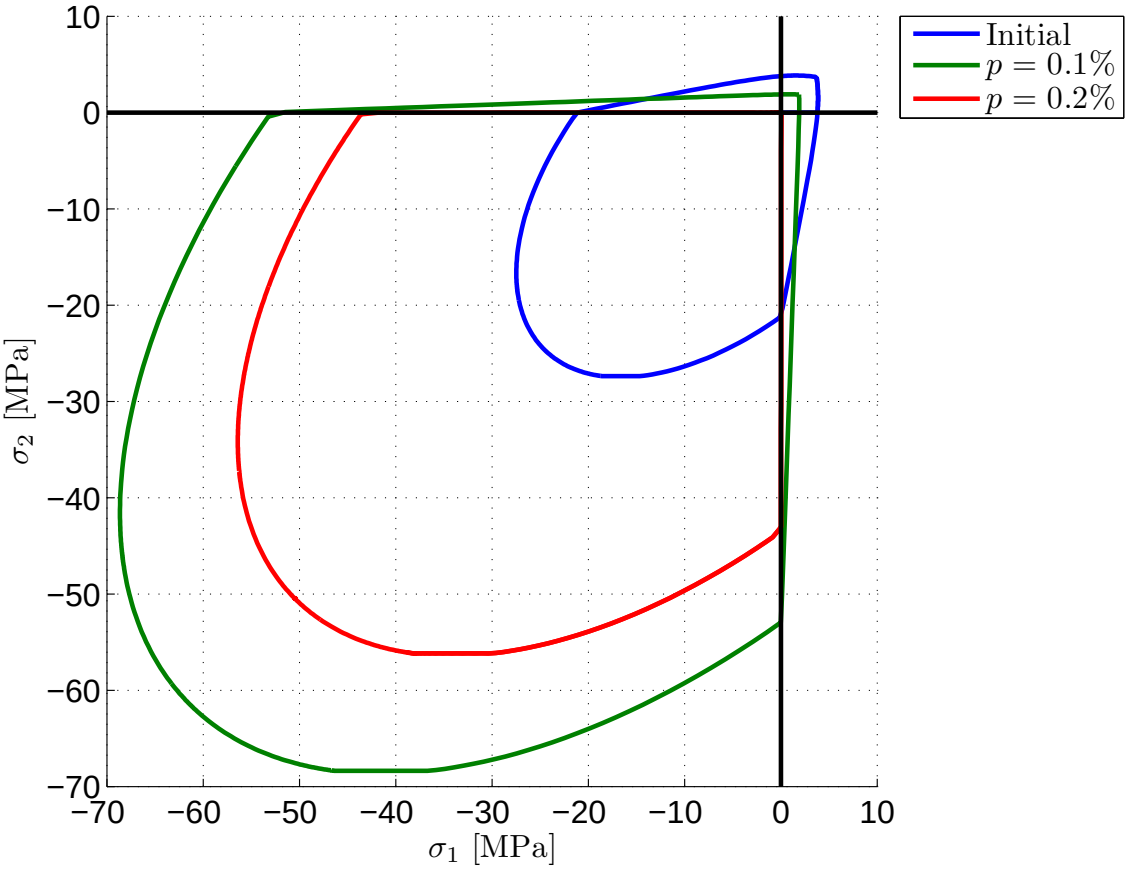

Figure 6.11: Yield surface created by a single shell element for different plastic strains.

For a plastic strain of $p = 0.1\%$ it is seen that the yield surface has expanded in the third quadrant, where biaxial compression takes place. This indicates hardening, in accordance with equation 3.11. Contrarily, in the first quadrant, the yield surface shows a decline. This results from plastic stress evolution, as no hardening takes

place, but instead a severe softening.

At $p = 0.2\%$, represented by the red curve, one can see how softening starts taking place in the third quadrant, as the yield surface has declined relative to the surface representing $p = 0.1\%$. It is also noticed that the tensile resistance is negligible, which is by design.

The conclusion is that the expansion or contraction of the yield surface does indeed follow the hardening rules. This implies that the tensile resistance is monotonically decreasing after the stress at which initial cracking occurs, while in compression initial hardening takes place, followed by softening towards failure. In a dynamic analysis, where stresses fluctuate between compression and tension, such a model brings a certain degree of realism to the analysis as both regimes are described in a consistent manner.

To investigate the effect of the reinforcement, the element of figure 6.10 is subjected to uniaxial, time dependent loading. This is done by assigning the modulated sinusoidal displacement shown in figure 6.12 to the right edge of the element. The same amount of reinforcement is placed in both the vertical and horizontal direction. Further, the reinforcement is placed symmetrically in the cross section, with cover, diameter and spacing as chosen in section 4.2. An illustration of the reinforcement placement is shown in figure 4.4. From this, hysteresis curves are made such that the response of the material is visualized.

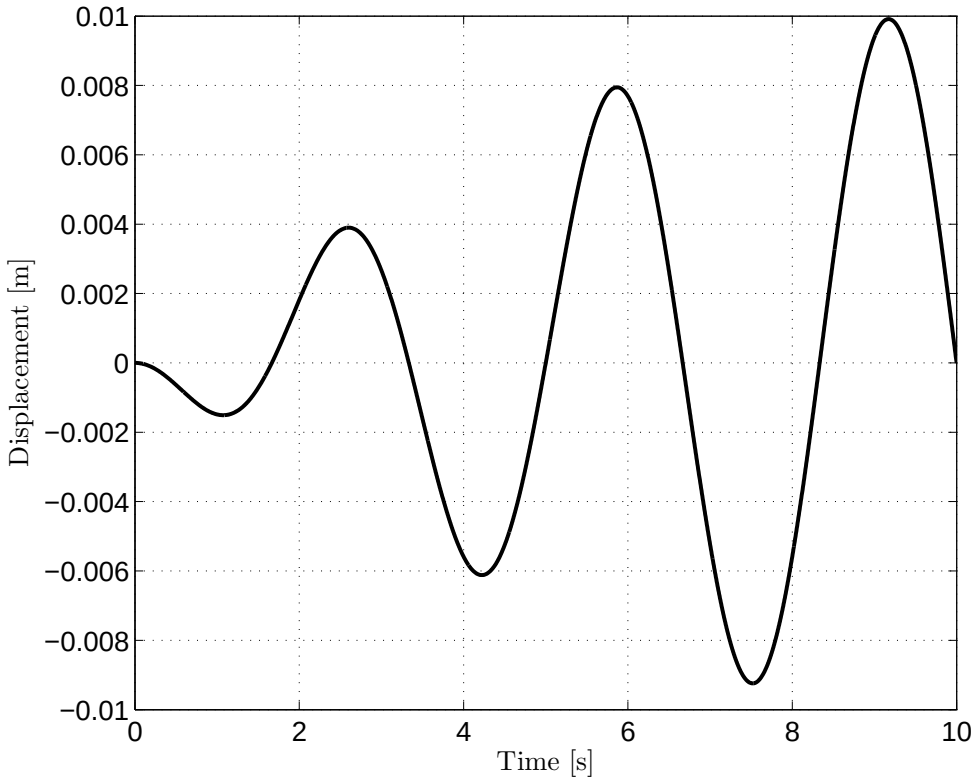

Figure 6.12: Displacement of the left edge of the element shown in figure 6.10.

The results are shown in figure 6.13, where it is seen how the resistance of the material without reinforcement corresponds to the yield surfaces in figure 6.11. For the first period of displacement, the material behaves linearly in compression. First yielding occurs during the second period, followed by further yielding in the third period. In tension, the concrete quickly loses its capacity until only the artificial residual remains - represented by a levelling off of the tensile response in the third period.

The inclusion of reinforcement gives similar results in compression as with only concrete. In tension however, a noticeable difference is observed. The softening caused by the tensile resistance declination, as shown in the hysteresis curve of the element without reinforcement, is negated by an elastic response of the reinforcement.

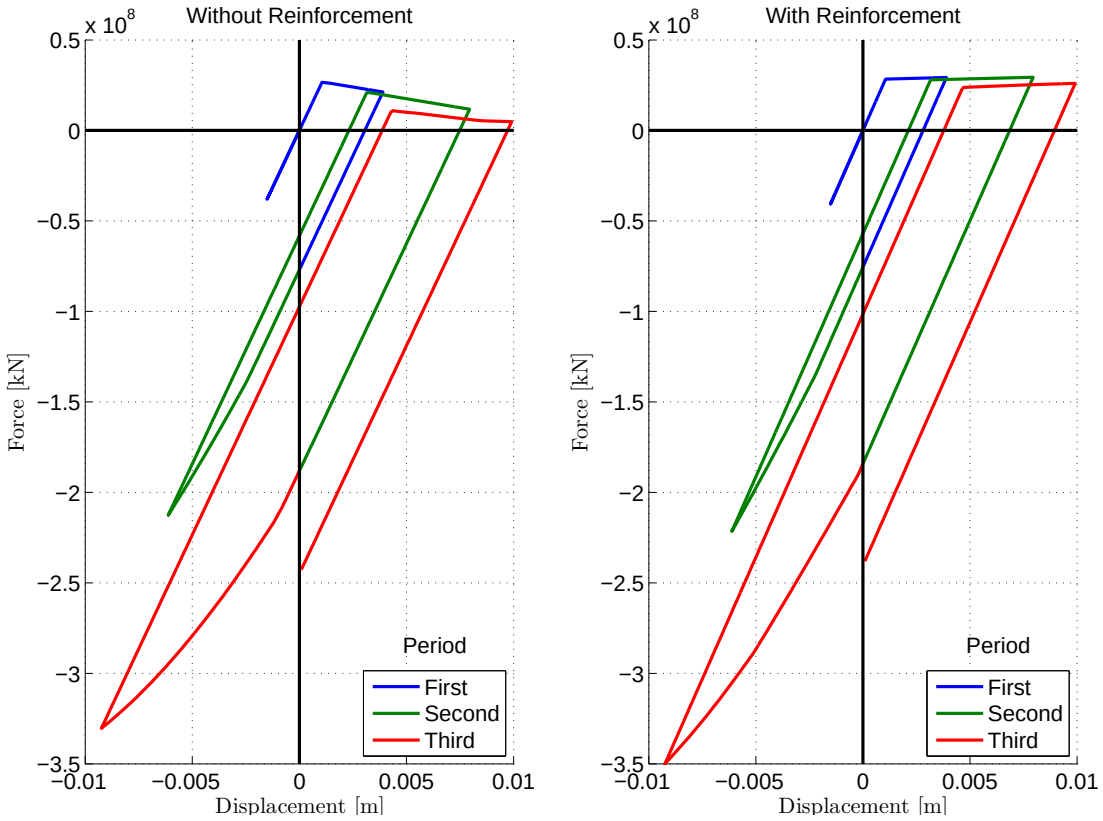

Figure 6.13: Hysteresis curves for a single shell element, both with and without reinforcement. Plotted for three periods of a modulated sinusoidal loading.

6.2.2 Seismic analysis

Applying the concrete material model of chapter 3, with parameters from table 6.2 and reinforcement from section 4.2, it is now possible to more accurately describe the structural behaviour, relative to a purely elastic analysis. Contour plots of maximum envelope von Mises stress when plasticity is considered are shown in figure 6.14.

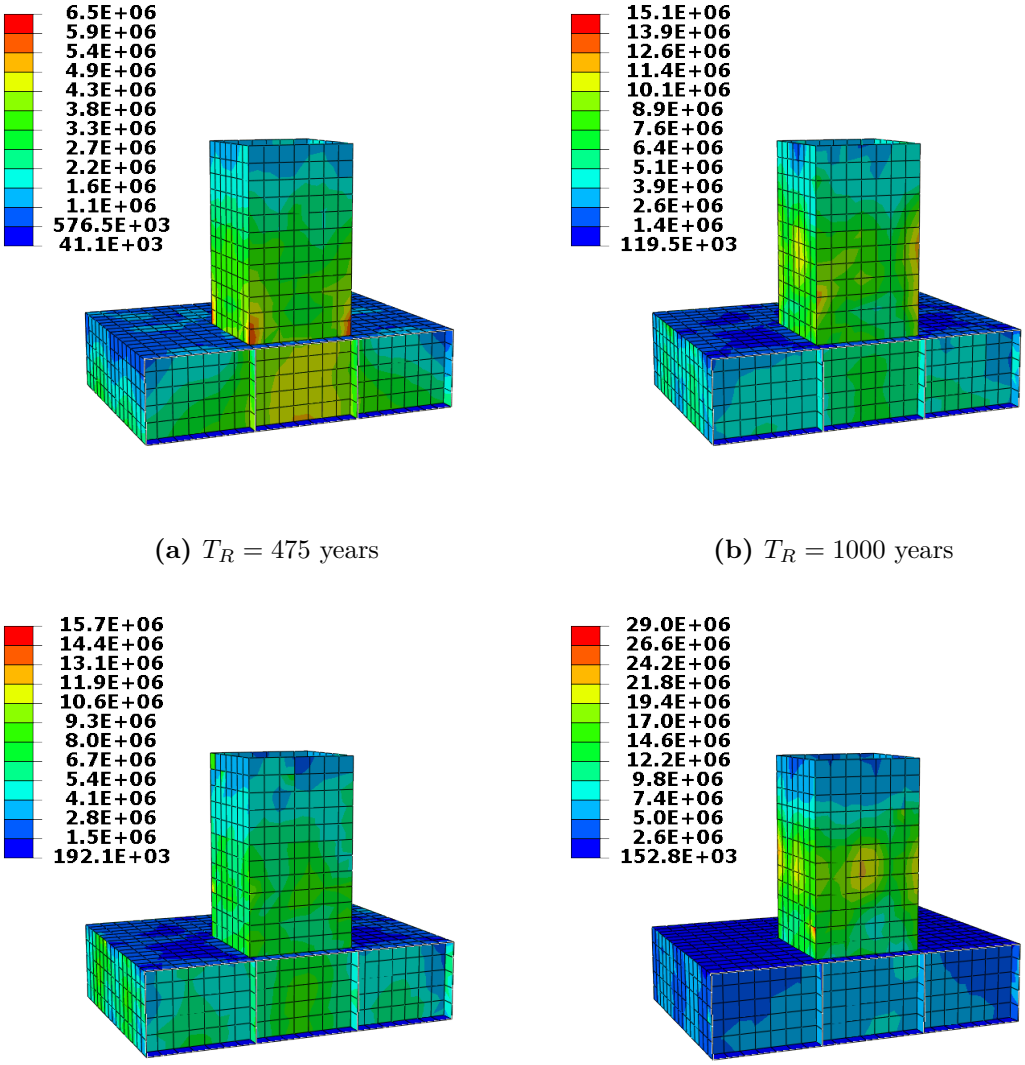

(a) $T_R = 475$ years

(b) $T_R = 1000$ years

(c) $T_R = 3000$ years

(d) $T_R = 10\,000$ years

Figure 6.14: Contour plots of the maximum envelope von Mises stress of the four return periods considered. Units are in Pascal.

By comparing figure 6.14 with figure 6.1 it is seen that the results for the plastic analysis are generally lower than for the elastic analysis. This seems reasonable as the structure becomes more ductile as yielding takes place.

The plastic dissipation taking place in the structure for a given return period is shown in figure 6.15.

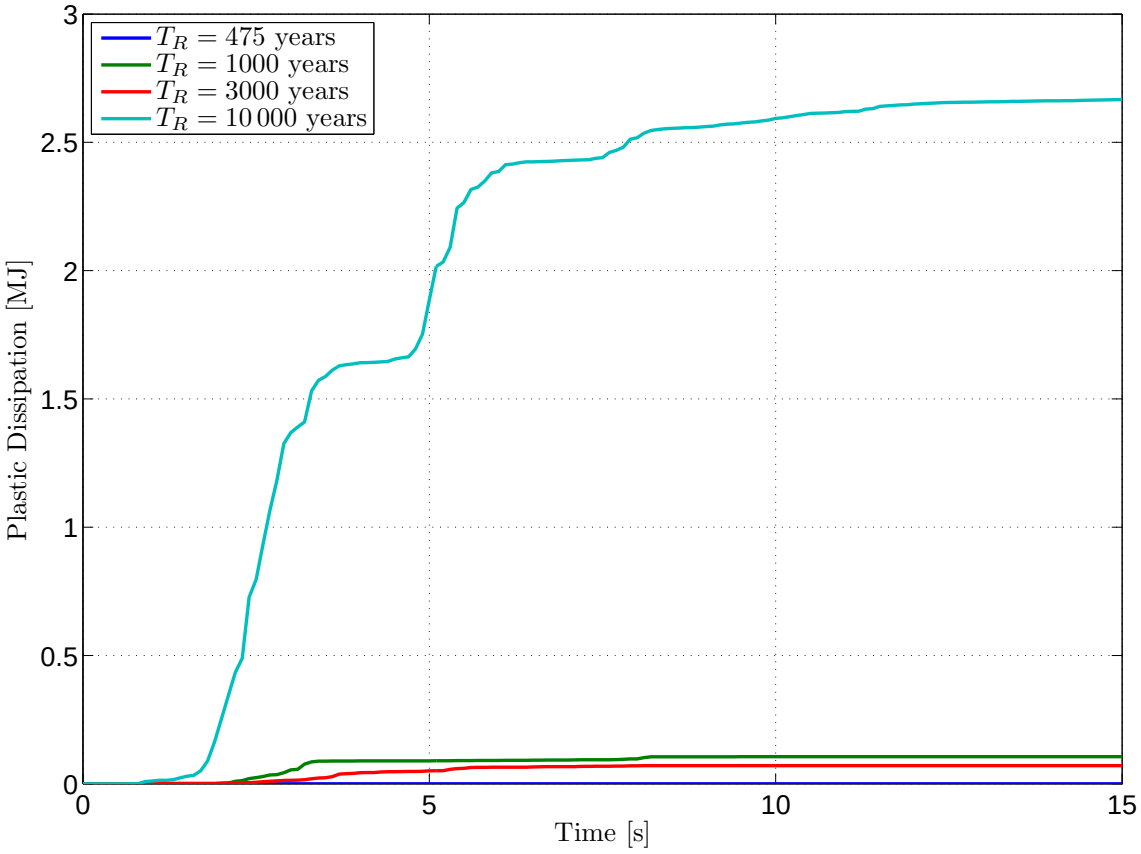

Figure 6.15: Plastic dissipation for yielding in compression.

An interesting obeservation is that figure 6.14a shows lower peak stress than figure 6.1a in spite of figure 6.15 showing no signs of plastic dissipation. This effect is explained by the reinforcement layers, which alters the material properties of the element, and serves to more evenly distribute the stresses, rather than localising them. It is noted though that the difference between figure 6.1a and 6.14a is small, which is reasonable.

Comparing the other three return periods of figure 6.14 to their elastic counterparts, it is seen that stresses are on average lower by a few Megapascals. Furthermore, the peak values shown in the contour plots of figure 6.1, which are concentrated to a spatial distribution of a few nodes, are filtered off by the yielding of the structure. Comparing the reduction of peak stresses with the plastic dissipation plots of figure 6.15, it is seen that the amount of reduction agrees with the amount of dissipation. Noting also, that areas in which the largest degree of stress reduction takes place - marked in red on the contour plots of figures 6.1 and 6.14 - are so highly concentrated that they are hardly visible. From this it can be concluded that while there are limited areas that experience large excursions into the plastic

domain, most of the structure does not, even for the 10 000-year earthquake. This implies that the elastic approximation adequately and conservatively describes the structural response without producing an impractical overestimation. Further evidence of this is provided in table 6.3, where the equivalent eigenfrequencies to those of the elastic structure are calculated as a linear perturbation after the earthquake has taken place, thus providing a measure of the change in geometry and stiffness. The term equivalent eigenfrequncies is used here as they are not the real eigenfrequencies of the structure, which are determined from the elastic model, but rather a distortion of them due to plastic deformations. They are however evaluated as such because they give insight into the extent of influence a given earthquake has on the structure.

Table 6.3: Equivalent eigenfrequencies after the earthquake of a given return period has taken place.

Mode	$T_R = 475$ [years]	$T_R = 1000$ [years]	$T_R = 3000$ [years]	$T_R = 10\,000$ [years]
1	2.6782	2.6766	2.6769	2.6709
2	3.1046	3.1038	3.1038	3.0988
3	3.1046	3.1040	3.1042	3.0999
4	4.0577	4.0566	4.0565	4.0504
5	4.0577	4.0573	4.0573	4.0532
6	4.7203	4.7189	4.7189	4.7036
7	5.6773	5.6763	5.6765	5.6745
8	6.4945	6.4934	6.4932	6.4870
9	6.5419	6.4936	6.4942	6.4915
10	6.5626	6.5418	6.5412	6.5389
11	6.5626	6.5624	6.5617	6.5585
12	6.5906	6.5625	6.5621	6.5604
13	6.6690	6.5905	6.5899	6.5877
14	6.7618	6.6688	6.6681	6.6656
15	6.7618	6.7616	6.7609	6.7584

Table 6.3 shows that no change to the number of decimals used occur for the 475-year earthquake, meaning that this column is identical to table 6.1, except that the double eigenfrequencies are explicitly given. Looking at the higher return periods, it is seen that the symmetric eigenfrequencies are lost, but even so the difference from the real eigenfrequencies - as given by the elastic structure - are negligible.

6.2.3 Effect of cracking

An additional effect is included to the plasticity model, namely cracking. This is done by introducing a rudimentary damage evolution parameter, d_t which takes into account cracking in tension. There is assumed that no cracking takes place for concrete in compression. The chosen relationship for d_t can be looked upon as

a normalized inverse of the post-cracking stress-strain relationship in tension, with $d_t = 0$ at initial cracking, and increasing linearly until $d_t = 0.99$ at a plastic strain of $p = 0.2\%$.

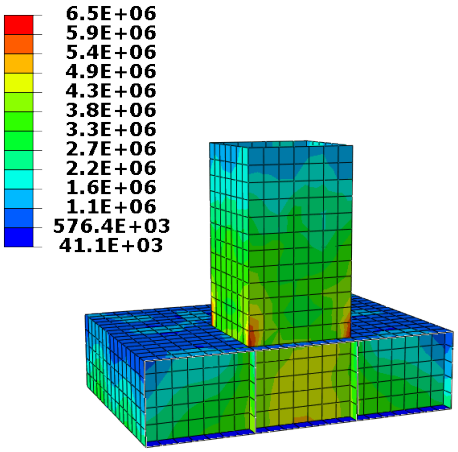

(a) $T_R = 475$ years

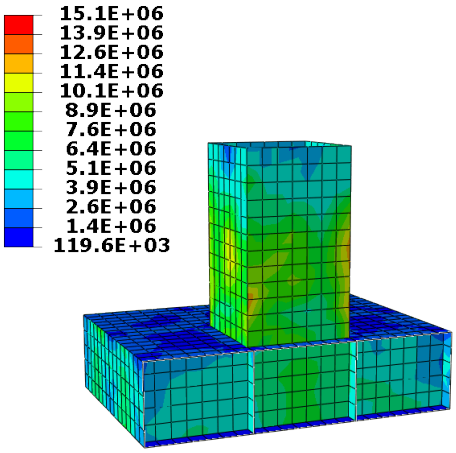

(b) $T_R = 1000$ years

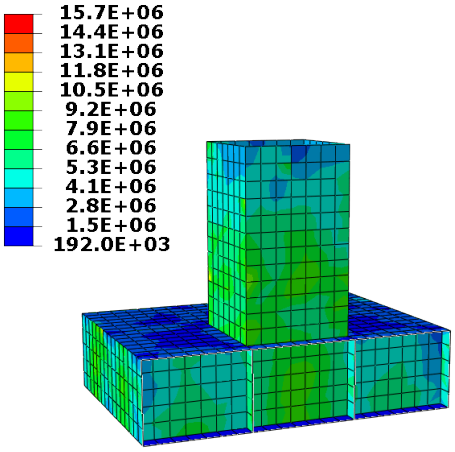

(c) $T_R = 3000$ years

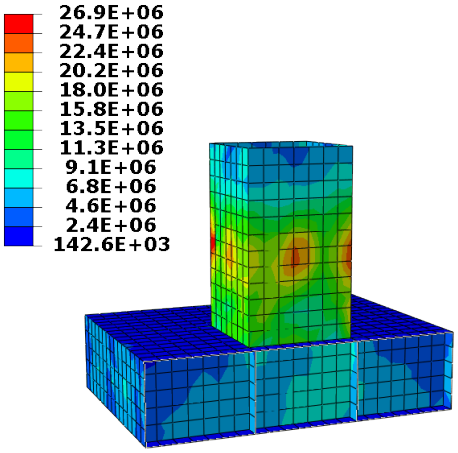

(d) $T_R = 10\,000$ years

Figure 6.16: Contour plots of the maximum envelope von Mises stress, considering cracking. The units are in Pascal.

Comparing figure 6.16 with figure 6.14 shows no change in the maximum envelope stresses of the structure for neither of the return periods, except for the 10 000-year earthquake in figure 6.16d. Here it is seen that the stresses are generally equal for large parts of the structure, however signs of cracking induced stress concentrations show in the middle of the shaft. In order to investigate the extent to which cracking has taken place in the structure, contour plots of the damage evolution parameter are shown in figure 6.17.

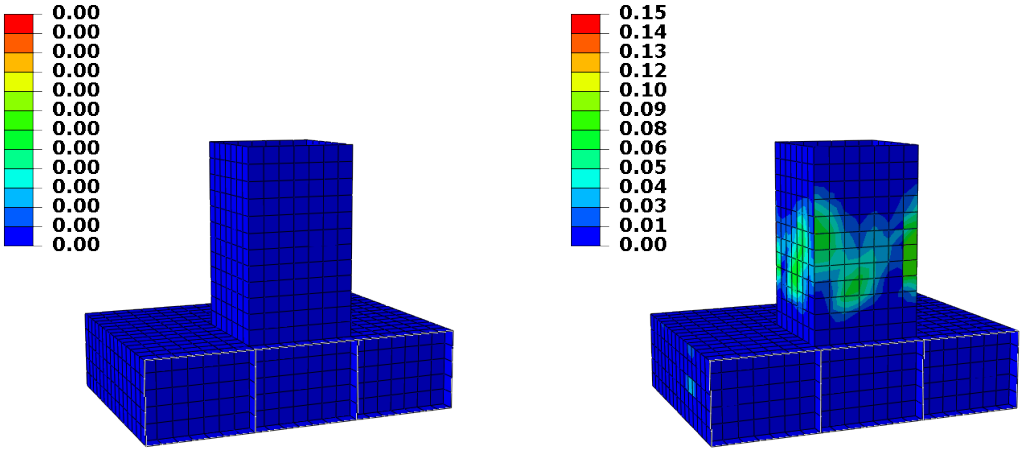

(a) $T_R = 475$ years **(b)** $T_R = 1000$ years

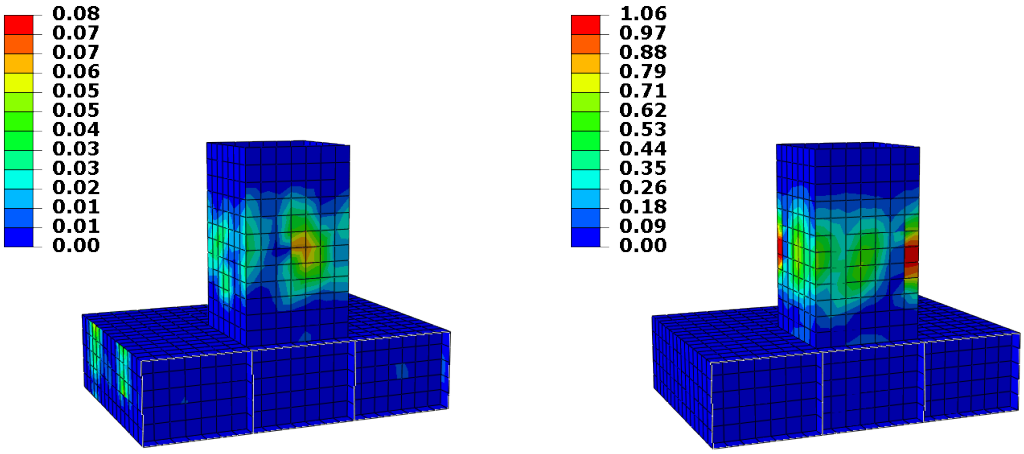

(c) $T_R = 3000$ years **(d)** $T_R = 10\,000$ years

Figure 6.17: Contour plots of the damage evolution parameter, d_t.

Figure 6.17 shows that the 475-year earthquake causes no cracking, owing to the low seismicity of the North Sea. This verifies figure 6.15 which demonstrates that the structure remains elastic for this particular earthquake. Comparing the 1000- and 3000-year earthquakes of figure 6.17b and 6.17c respectively shows that the 1000-year earthquake produces very similar, if not larger degrees of tensile damage than the 3000-year earthquake. This is however not a mystery, and as previously discussed, it is caused by simulation error in the 1000-year earthquake, as well as the jump in return period not being large enough to produce uniquely larger 3000-year earthquakes. The 10 000-year earthquake is influenced the most by tensile damage, as is also predicted by the plastic dissipation in figure 6.15. Furthermore, this explains the stress concentrations of figure 6.16d, as their location correspond with

the areas of the most severe cracking. It is seen that the damage evolution parameter of figure 6.17d exceeds one - as marked in red. This is caused by numerical error in the averaging of integration point values, and should instead be viewed as $d_t = 0.99$, implying that the structure has lost all its stiffness in these areas. Physically, this represents large cracks, which only the reinforcement keeps together. Finally, the equivalent eigenfrequencies after the earthquake has passed are given in table 6.4.

Table 6.4: Equivalent eigenfrequencies after the earthquake of a given return period has taken place.

Mode	$T_R = 475$ [years]	$T_R = 1000$ [years]	$T_R = 3000$ [years]	$T_R = 10\,000$ [years]
1	2.6782	2.6766	2.6730	2.6654
2	3.1046	3.1036	3.1001	3.0808
3	3.1046	3.1038	3.1009	3.0843
4	4.0577	4.0563	4.0493	4.0248
5	4.0577	4.0569	4.0527	4.0289
6	4.7203	4.7182	4.7113	4.6865
7	5.6773	5.6758	5.6715	5.6592
8	6.4945	6.4930	6.4866	6.4727
9	6.5419	6.4932	6.4899	6.4754
10	6.5626	6.5416	6.5349	6.5371
11	6.5626	6.5622	6.5546	6.5555
12	6.5906	6.5623	6.5569	6.5582
13	6.6690	6.5903	6.5838	6.5857
14	6.7618	6.6687	6.6617	6.6641
15	6.7618	6.7614	6.7543	6.7563

No big surprises reveal themselves from table 6.4. An additional reduction of the equivalent eigenfrequencies are observed, which is reasonable as the structural stiffness is reduced by the elastic stiffness degradation. Comparing with table 6.1 it is seen that the differences are still small even with cracking taking place. Moreover, the stress envelopes show negligible changes from the purely plastic model of figure 6.14, so it can be concluded that the elastic stiffness degradation such as it has been included here, is an unnecessary complication of the analysis of the massive concrete structure evaluated.

6.3 Effect of surrounding water

It is apparent that large errors are made when the surrounding water is neglected in the structural analysis, but even so the basis for comparison is a model where this is the case. The fluid is therefore treated as a complicating factor, in the same manner as plasticity is in section 6.2. Efforts have been made to investigate how much difference the inclusion of surrounding water makes on the response of the structure. This is done by applying both methods described in section 3.3.

6.3.1 Evenly distributed added mass

The outer surfaces of the structure has had its mass increased in accordance with equation 3.21. Unfortunately, there is further need for simplification, in addition to those discussed in section 3.3.1. In figure 3.3 are shown the available geometries for which the added mass coefficient is known. For the shaft, figure 3.3a seems to be appropriate, although only valid for slender structures. It does however imply that the influence of the caisson below on the flow of water around the shaft is neglected. The selected added mass coefficient is thus $C_A = 1.51$.

The caisson provides a larger challenge than the shaft in terms of finding an appropriate added mass coefficient. Figure 3.3b is of a similar geometry and predicts an added mass coefficient of $C_A = 0.68$, but is restricted to quadratic cross sections in the direction of flow. Furthermore, water is not allowed to flow beneath the structure, as it is placed firmly on the seabed. The shaft serves as an additional obstruction which cannot be taken into account. In the following, the choice has been made to use the added mass coefficient of an equivalent quadratic cross section, with sides equal to the width of the caisson. This is conservative, as the actual projected area perpendicular to the flow of water has one fourth of the height. To account for the fluid only being able to flow around three sides of the structure, a larger added mass coefficient has been selected, resulting in a value of $C_A = 1.00$.

Fluid displacement due to vertical motion has been ignored, as its influence is assumed to be small. Furthermore, the addition to gravity forces on the roof of the caisson would severely distort the results there.

The eigenfrequencies calculated with the effects of water show a significant change, which is expected by looking at equation 3.21 as the large surface of the structure creates a monumental added mass effect. They are shown in table 6.5, where it is seen that the first eigenenfrequency differs from that given in table 6.1 by approximately 0.6Hz, with the difference increasing for increasing modes. As the structure was initially very stiff, larger seismic loads are expected by the inclusion of water in the analysis. This is seen by comparing the change in eigenfrequencies to the mean response spectra of figure 5.5, noting that the increase in periods is in the direction of the spectrum peaks - thus predicting an increase in response.

Table 6.5: Unique eigenfrequencies with added mass.

Mode	Frequency [Hz]
1	2.0054
2*	2.4640
3	3.4862
4*	3.5908
5	4.0747
6	4.0793
7*	4.0853
8	4.1651
9*	4.2108
10	4.2859

* Double eigenfrequencies

Figure 6.18 shows contour plots of the maximum von Mises stress of the structure. It is observed that the stress fields are similar to those of figure 6.1, which is reasonable as the structure is assumed filled with water of equal height as the surrounding water level. This means that the surfaces onto which the added mass is applied are already influenced by an artificial mass caused by the internal water, such that the mode shapes do not change radically.

By comparing with figure 6.1 it is seen that the seismic response with the addition of mass is not quite as black and white as previously expected. For instance, the 10 000-year earthquake produces on average a response which is lower when water is included than when it is not. The peak values are of little significance for the global response because of their limited spatial distribution. Furthermore, they are a result of the elastic approximation, and cannot be assumed realistic, as is verified by figure 6.14, where the more accurate material model provides a response which does not include such localised peak values.

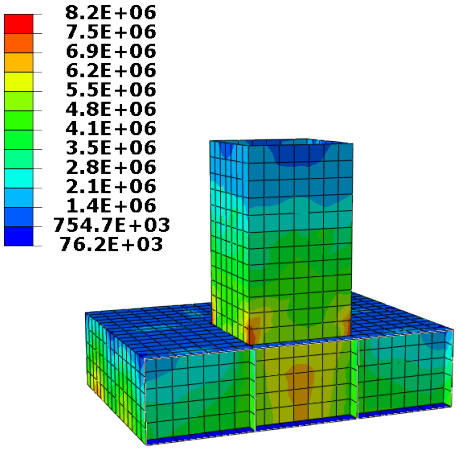

(a) $T_R = 475$ years

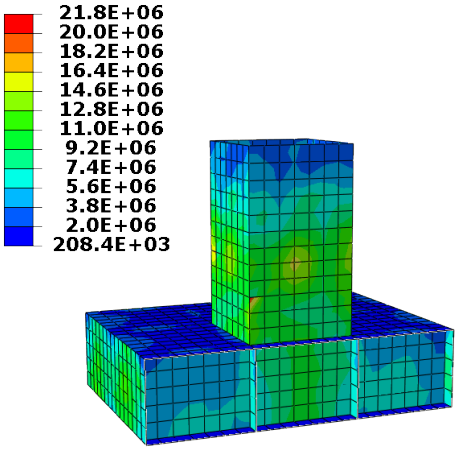

(b) $T_R = 1000$ years

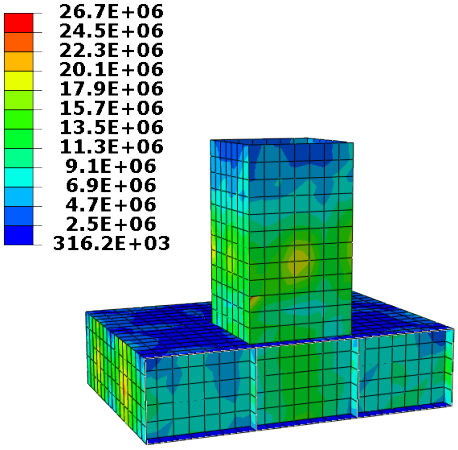

(c) $T_R = 3000$ years

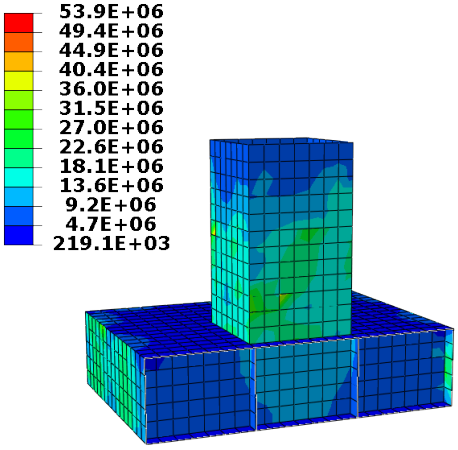

(d) $T_R = 10\,000$ years

Figure 6.18: Contour plots of the maximum envelope von Mises stress with surrounding water modelled as additional mass. Units are in Pascal.

The reason for the lower structural response when water is included is illustrated in appendix F, where a comparison of response spectra and participation factors are shown. It is seen that by the inclusion of water, the participation factors with significant contributions are shifted to frequencies for which the structural response is lower. Because of this, the ground accelerations of the 10 000-year earthquake are mitigated to a greater extent than without water. The 3000-year earthquake shows the opposite trend. By looking at figure F.3, it is seen that several of the participation factors are shifted towards local peaks in the response spectrum, such that the structural response is greater. Furthermore, the added mass increases the inertia of the structure. This results in an increase in stresses. It also implies that

for the stresses to decrease, the reduction in acceleration will have to cancel out the increase in inertia. The 475- and 1000-year earthquake analyses are also worse off by the presence of water, but to a lesser degree.

6.3.2 Numerical study: Infinite elements

The pressure wave formulation derived in section 3.3.2 is applied by Abaqus as an acoustic interaction with the structure. The radiation damping is then caused by the transfer of momentum from the structure, which generates pressure waves that propagate through the acoustic medium. The use of such an approach in a finite element analysis introduces the problem of reflection at the boundaries. If the domain of the acoustic medium is not large enough, reflected waves could affect the structure, and thus introduce spurious loads. To reduce the volume of water necessary to achieve an accurate solution, infinite elements have been used, which are elements that simulate the conditions of a half-space by extending the fluid domain numerically with polynomials[30]. This implies that infinite elements constitute absorbing boundaries, such that incoming waves are not reflected. The behaviour of these elements, as well as the acoustic medium, consisting of solid elements, is investigated by letting a pressure wave propagate through a channel, which is supposed to extend to infinity.

(a) $t = 1$ ms

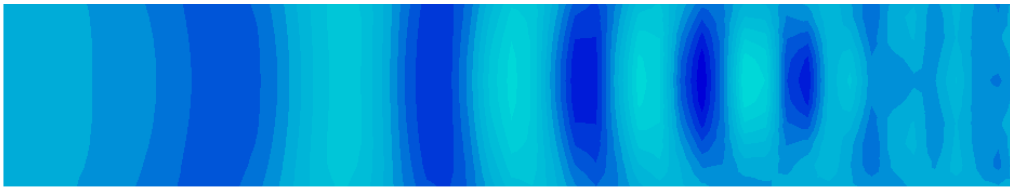

(b) $t = 30$ ms

(c) $t = 0.1$ s

Figure 6.19: Wave propagation through an acoustic medium, with infinite elements on the left end.

Figure 6.19 shows the results of the numerical study, where waves are shown propagating through the acoustic medium, towards the infinite elements on the left end. The density of the water was set to $\rho = 1025$ kg/m^3 and a bulk modulus of $B = 2.2$ GPa was used. The duration of the simulation was 0.1 s. It is seen that as the waves reach the left end, most of the energy is dissipated, giving the illusion that the waves continue through. Standing waves are observed, suggesting reflection, however the pressure amplitudes are much lower than for the incoming waves so the accuracy is deemed adequate.

6.3.3 Acoustic-structure interaction

A better approximation for the fluid-structure interaction is the modelling of the fluid within which the structure is oscillating. This is done by using an acoustic medium that surrounds the structure. The properties of the fluid were set to $\rho = 1025\,\mathrm{kg/m^3}$ and $B = 2.2$ GPa. Figure 6.20 shows the structural model submerged in a cylinder of the acoustic medium, consisting of solid elements. The diameter of the cylinder is 120 meters, meaning that the smallest distance from the structure to the fluid boundary is approximately 18 meters. Needless to say, such an analysis is quite computer intensive, and in order to reduce the analysis time, the element size is radially increased towards the infinite element fluid boundary, with the finest element mesh immediately surrounding the structure.

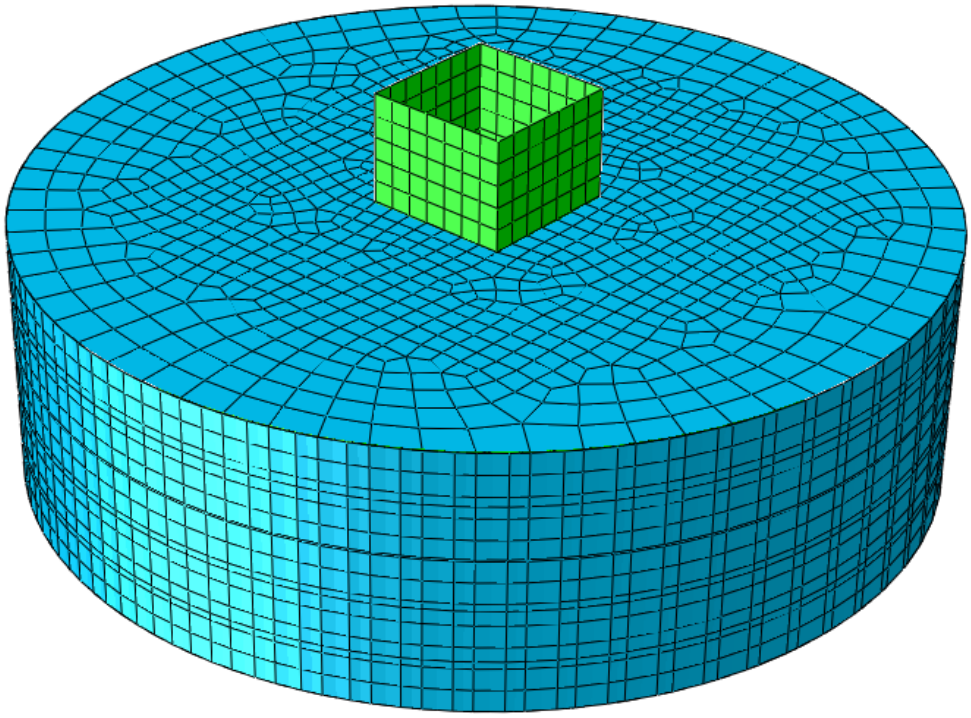

Figure 6.20: Finite element model for the fluid-structure interaction.

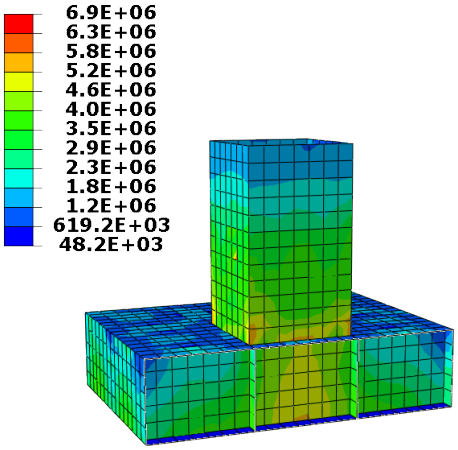

(a) $T_R = 475$ years

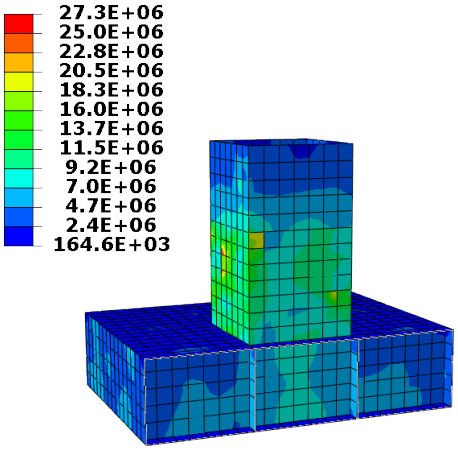

(b) $T_R = 1000$ years

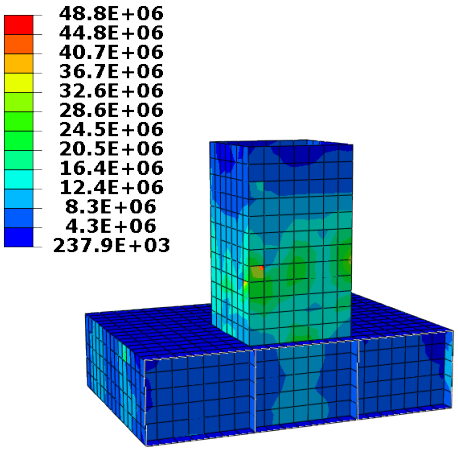

(c) $T_R = 3000$ years

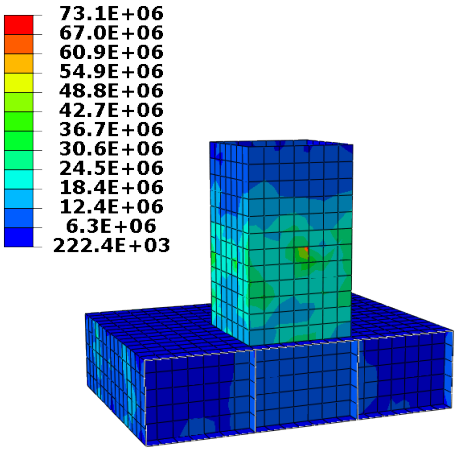

(d) $T_R = 10\,000$ years

Figure 6.21: Contour plots of the maximum envelope von Mises stress with surrounding water modelled as acoustic elements. Units are in Pascal.

Figure 6.21 shows the von Mises maximum envelope curves for the structural-acoustic analysis. Once again, the results are plagued with a few points that show improbably high stresses. These points are once again ignored, based on previous arguments. Otherwise, it is seen that the stresses are generally quite similar to the added mass method, suggesting that the simplified approach is reasonably accurate. This is especially true for the 3000- and 10 000-year earthquake. Looking at appendix F it is seen that the interaction with the acoustic medium causes the significant participation factors to occur for small periods, and thus escape the peaks of the response spectrum. This results in lower accelerations experienced by the structure than with water omitted, however as previously mentioned, the added inertia

due to the surrounding water cancels out this beneficial effect, and even increases stresses slightly for the 10 000-year earthquake.

The eigenfrequencies are given in table 6.6.

Table 6.6: Unique eigenfrequencies with added mass.

Mode	Frequency [Hz]
1	1.8533
2a	2.1466
2b	2.1473
3	2.2033
4a	3.6422
4b	3.6424
5	4.0168
6a	4.3950
6b	4.3957
7	4.6032
8	4.7546
9a	4.9165
9b	4.9388
10	4.9411

The most notable about table 6.6 is perhaps that additional modes are included. The reason for this is that the eigenfrequencies are no longer double, and in order to keep the table consistent with table 6.1, these previous pairs are given the same mode number, and separated alphabetically instead. It is believed that this effect is caused by numerical error, as the structure is still symmetric. Furthermore, the differences are so small that the most likely explanation is that they represent the same mode. Comparing table 6.6 to table 6.5 gives credibility to the analysis, as it is seen that the eigenfrequencies are similar, with the acoustic-structural analysis predicting slightly lower frequencies for the lower modes, but eventually surpassing the dry analysis as the modenumber increases. An exception is the third mode, which is significantly lower for the acoustic-structural analysis - for unknown reasons.

6.4 Effect of soil

The influence of the foundation upon which the structure rests is a highly complex subject due to the fact that soil properties rarely lend themselves to analytical relationships. Furthermore, the material behaviour leads to great variation in properties, even for the same soil types, and because of this, laboratory testing of samples from the area in question is necessary if one is to even have a chance at establishing realistic results. A geotechnical survey is beyond the scope of this thesis, and soil pa-

rameters will be assumed based on typical values. Because of this, no sophisticated material model will be attempted, instead, an elastic soil layer is used.

6.4.1 Soil springs

A simplified approach is used, in which the structure is assumed to stand on an elastic halfspace. This is represented by springs and dashpots which connects each node in the caisson floor to a reference node, where the earthquake accelerations are applied. This is shown in figure 6.22.

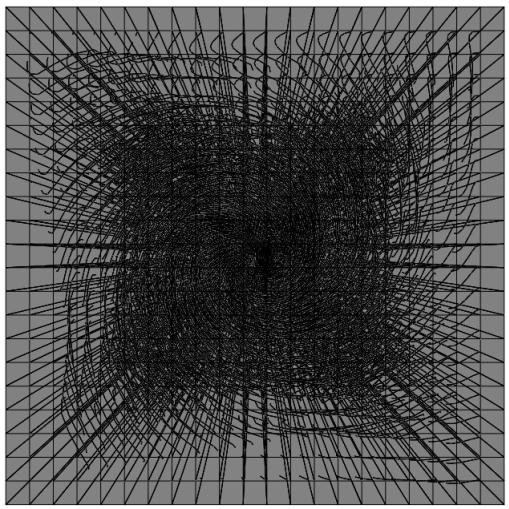

Figure 6.22: Foundation of the structure, where 484 springs and dashpots individually connects each node to a reference point, where the earthquake is applied.

Analytical expressions for the static stiffness and damping constants for a rigid circular footing is used, thus ignoring the frequency dependency of these coefficients. These are given in equation 6.2[36],[18]. Such a model is usually applied for single degree of freedom systems, but is averaged here over all nodes in the bottom slab.

$$\begin{aligned} K_x &= \frac{8GR}{2-\nu} \\ K_y &= \frac{4GR}{1-\nu} \\ C &= \frac{4.6}{2-\nu}\rho V_s R^2 \end{aligned} \tag{6.1}$$

In equation 6.2, R is the radius of the footing, $\nu = 0.3$, $\rho = 2000\,\mathrm{kg/m^3}$ and V_s are the Poisson ratio, mass density and shear wave velocity of the soil, respectively. G is the shear modulus of the soil, and is given as

$$G = \rho V_s^2 \tag{6.2}$$

To ease the modelling, no distinction has been made between the damping constant in vertical and horizontal directions, although this is obviously the case. Furthermore, the circular footing is assumed inscribed into the square footing of the structure, which implies a radius of $R = 30\,\mathrm{m}$.

Soft soil

Previous investigations have revealed that the topmost soil layer at the site of the structure consists of sand[13]. It is assumed that the underlying sand is quite dense based on the weight of the structure, which leads to a selection of shear wave velocity as $V_s = 180\,\mathrm{m/s}$. A huge spread in applicable shear wave velocities have been found, owing to the empirical nature of geotechnics, however the chosen value is in accordance with Eurocode 8. Maximum envelope von Mises stress contour plots are shown in figure 6.23.

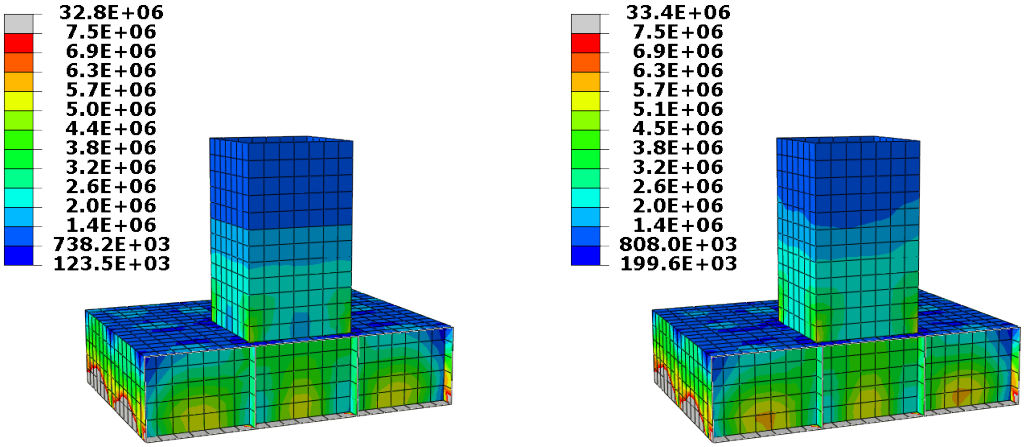

(a) $T_R = 475$ years

(b) $T_R = 1000$ years

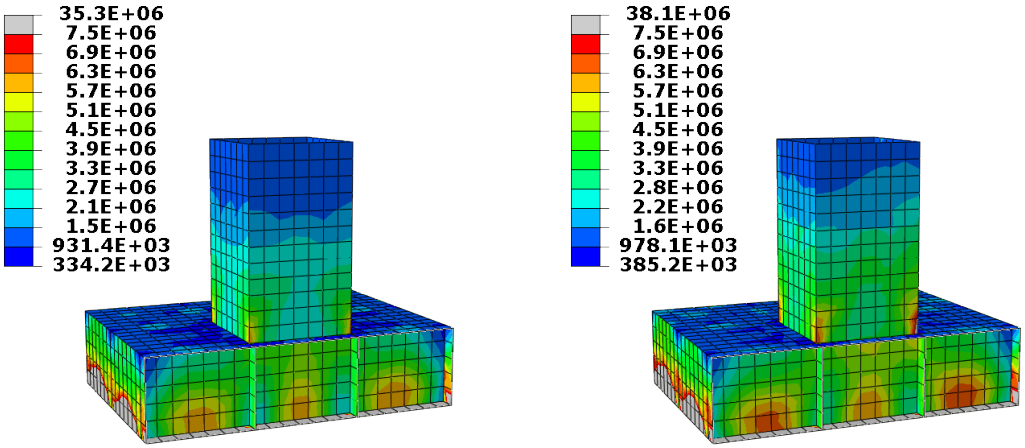

(c) $T_R = 3000$ years

(d) $T_R = 10\,000$ years

Figure 6.23: Contour plots of the maximum envelope von Mises stress when underlying, soft, soil is represented by springs and dashpots. Units are in Pascal.

Marked in gray on the contour plots of figure 6.23 are shown irrepresentatively large stresses at around $30 - 40$ MPa for all return periods. These occur because of the mathematically constrained bottom slab and are artificial. A real structure would not be attached to the ground in such a way as is done here, and because of this, these stresses should be ignored. In the rest of the structure however, it is observed that the soft soil has the same effect as base isolation, as the structure hardly feels the earthquake at all. From a modelling point of view, this is a natural result, as springs have been used. The realism of such a result is debatable, however the results do align with the general statement that structures resting on soft soil

often experience a beneficial effect, with an increase in its influence with increasing stiffness[36].

Table 6.7: Unique eigenfrequencies with soft soil springs.

Mode	Frequency [Hz]
1	2.5962
2*	3.4024
3*	3.9681
4	4.5212
5	5.5637
6	5.7023
7*	5.7280
8	5.9308
9*	6.3733
10	5.7757

* Double Eigenfrequencies

The eigenfrequencies of the system, as shown in table 6.7, show little difference for eigenmodes that mainly involve the perturbation of the shaft, with respect to the constrained base case. For the caisson however, the difference in eigenfrequencies is significant - which is obvious as the bottom slab is resting on springs rather than firm ground, thus reducing the overall stiffness and increasing the period of vibration. Not included here are intermittent eigenmodes which are generated by the interaction with the springs.

Hard soil

The structure is so stiff that even if it was placed directly on solid rock, soil-structure interaction could have a great deal of influence. Because of this, an instance in which the structure is placed on hard soil, with a shear wave velocity of $V_s = 800\,\mathrm{m/s}$ is tested. The stress contours are shown in figure 6.24.

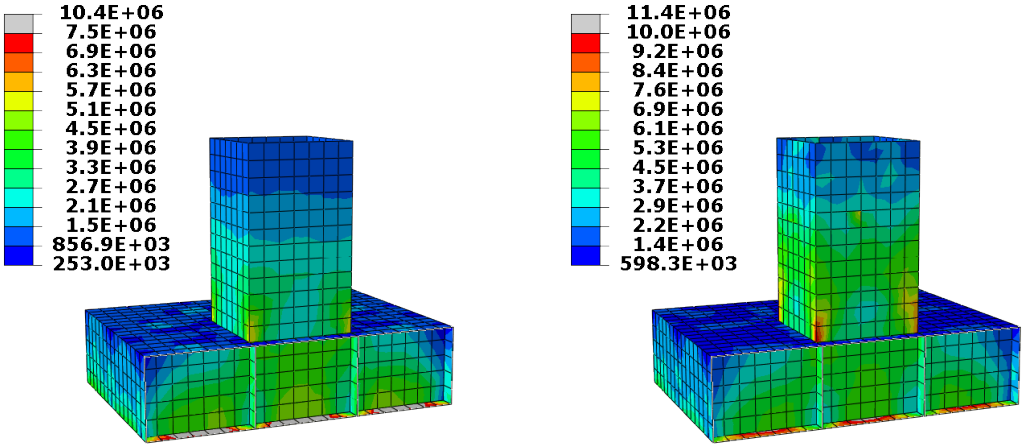

(a) $T_R = 475$ years **(b)** $T_R = 1000$ years

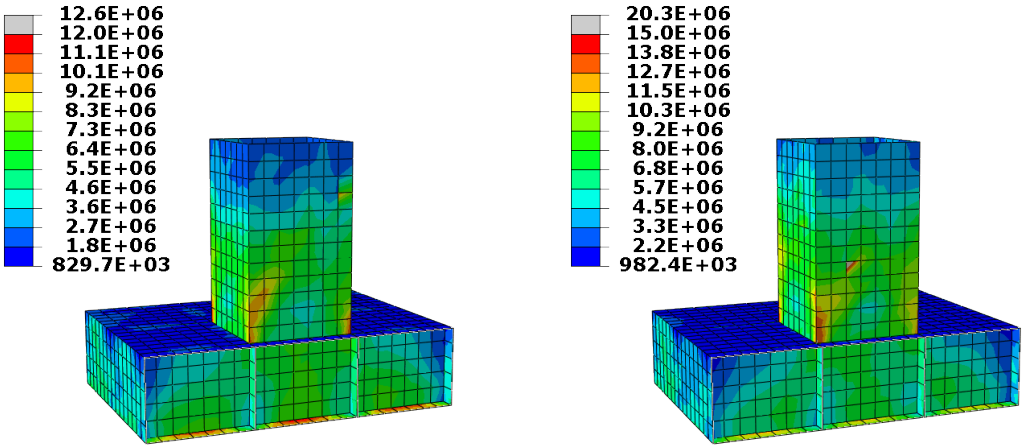

(c) $T_R = 3000$ years **(d)** $T_R = 10\,000$ years

Figure 6.24: Contour plots of the maximum envelope von Mises stress when underlying, hard, soil is represented by springs and dashpots. Units are in Pascal.

With respect to the soft soil, the stresses observed by the structure is increased by the increased stiffness of the underlying soil, however the results are still very beneficial compared to the base case. It is expected that the seismic loads increase as the springs stiffen, however the spring stiffness should be stiff enough to result in a response similar to those of the structure on an infinitely stiff foundation. This is not the case. Equivalently, the eigenfrequencies should also increase, which they do, as can be seen in table 6.8. It should be noted that both in table 6.7 and 6.8, the mode numbering does not represent the actual order of modes, but instead the given eigenmode is chosen such that its mode shape corresponds with that of the

base case, making them comparable.

Table 6.8: Unique eigenfrequencies with hard soil springs.

Mode	Frequency [Hz]
1	2.5420
2*	2.5963
3*	3.7046
4	4.5214
5	5.5656
6	5.58613
7*	6.0599
8	6.1195
9*	6.3561
10	5.9921

* Double Eigenfrequencies

The simplicity of the model used to describe the underlying soil results in a mathematical, and perhaps trivial result that the structural loads are reduced when the previously fully constrained boundary conditions are relaxed.

6.4.2 Direct method

A more accurate approach for the treatment of soil-structure interaction is attempted next. This is known as the direct method, where the underlying soil and the structure is modelled using the finite element method. To this end, a 50 meter thick soil layer was modelled, below which the earthquake was applied. To avoid the influence of edge effects, the width of the soil layer was extended 50 meters beyond the sides of the structure on each side, thus giving it a volume of $50 \cdot 160 \cdot 160$ meters. Surrounding the soil layer are infinite elements, which serve to hinder reflection at the outer boundaries, along the same lines as described in section 6.3. The resulting model is shown in figure 6.25.

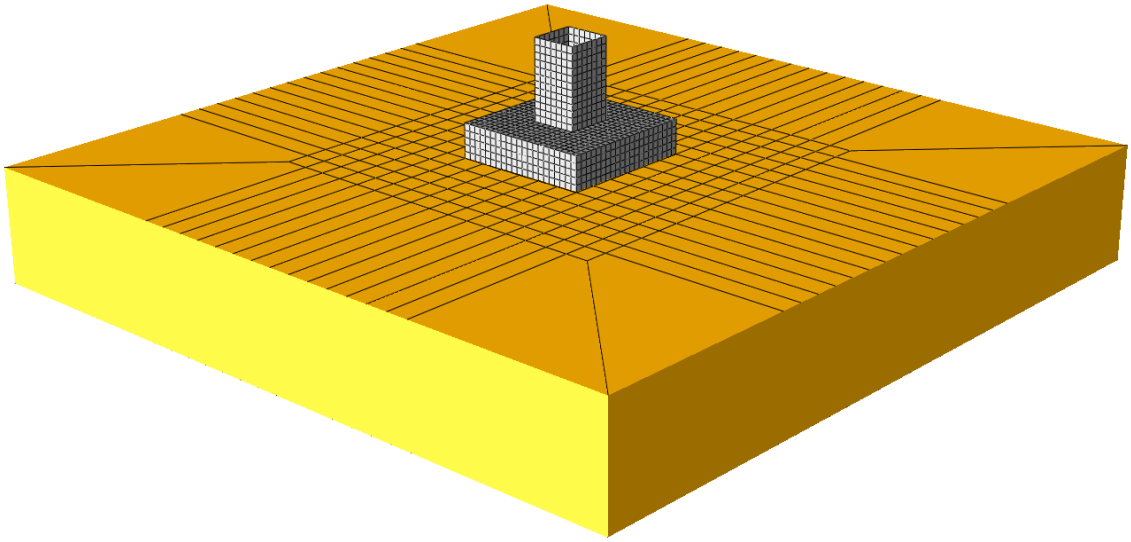

Figure 6.25: Finite element model of the structure resting upon a soil layer.

The massiveness of the model used requires the use of a rather coarse mesh. In this regard, the horizontal expansion of the generated waves have been deemed less important than the vertical, and because of this, twice as large elements have been used horizontally as vertically, giving the soil layer a thickness of 10 solid elements.

The material is assumed fully elastic, with an elasticity modulus determined by

$$E_s = 2(1+\nu)G = 2(1+\nu)\rho V_s^2 \tag{6.3}$$

Material damping of the soil layer has been applied, and a damping ratio of $\xi = 1\%$ appears to be appropriate[28]. Furthermore, stiffness proportional Rayleigh damping is applicable[20], wherein the first significant eigenfrequency has been used.

With a proper soil layer now defined, it is possible to express the eigenfrequencies of the soil for transverse motion as

$$f_h = \frac{V_s}{4H}(2n-1) \tag{6.4}$$

where H is the thickness of the layer and n is the mode number. Equivalently, the first eigenfrequency for longitudinal motion is given as

$$f_v = \frac{V_p}{4H} = \sqrt{\frac{2(1-\nu)}{1-2\nu}} f_h \tag{6.5}$$

Appendix F.2 shows the soil amplification, which results from the elastic layer, plotted as a ratio between acceleration response spectra on soil and rock respectively. Here, the values f_s and f_h represents the first analytical eigenfrequency of the relevant motion for soft and hard soil respectively. It is seen that for the transverse

motion, this eigenfrequency, given in equation 6.4, fits quite well with the amplification peaks for all return periods, and for both soft and hard soil. The peaks corresponding to the higher modes are more difficult to resolve, and are not shown. For the longitudinal motion, i.e. as caused by pressure waves, the analytical expression shows less correlation with the peaks of the amplification plot, but even so, the results are somewhat reasonable, as can for instance be seen in figure F.6. In general, the results are better for the soft soil than for the hard soil with respect to longitudinal motion. Such a result serves to verify the finite element model, and makes sure that it behaves as expected.

Table 6.9 shows the ten first eigenfrequencies of the soil layer without the structure present.

Table 6.9: Soil layer eigenfrequencies.

Mode	Soft soil [Hz]	Hard soil [Hz]
1	0.81126	3.6056
2	0.84178	3.7412
3	1.0204	4.5350
4	1.0922	4.8541
5	1.1920	5.2979
6	1.2539	5.5730
7	1.4446	6.4204
8	1.4763	6.5614
9	1.5315	6.8066
10	1.5671	6.9650

The first transverse eigenfrequency for the two soil types are $f_h^{soft} = 0.9\,\text{Hz}$ and $f_h^{hard} = 4.0\,\text{Hz}$ respectively, and show good agreement with the first mode. It is observed that the eigenfrequencies of the finite element model is not quite as discrete as the analytical formulas dictate. However, by looking at the mode shapes of appendix A, it is seen that for the lower modes, with eigenfrequencies close to f_h, the transverse vibration dominates. The first longitudinal eigenfrequency of the two soil types are given as $f_v^{soft} = 1.7\,\text{Hz}$ and $f_v^{hard} = 7.5\,\text{Hz}$, and as the eigenfrequencies of the finite element model approaches these values, it is observed from appendix A that longitudinal modes of vibrations starts being influential. These results imply that the coarse mesh used is indeed adequately refined for the purpose of this study.

Soft soil

The use of the direct method in modelling the underlying soil layer results in similar stresses as with the use of springs. This is shown in figure 6.26.

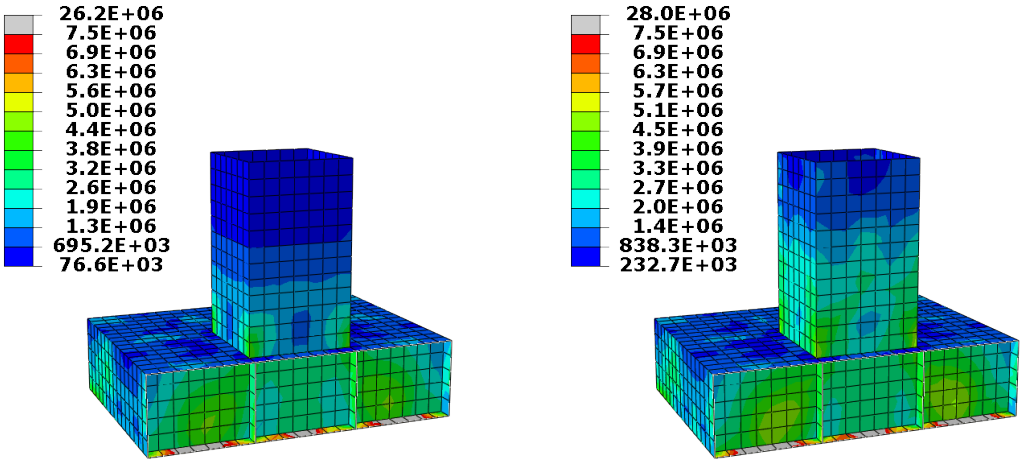

(a) $T_R = 475$ years

(b) $T_R = 1000$ years

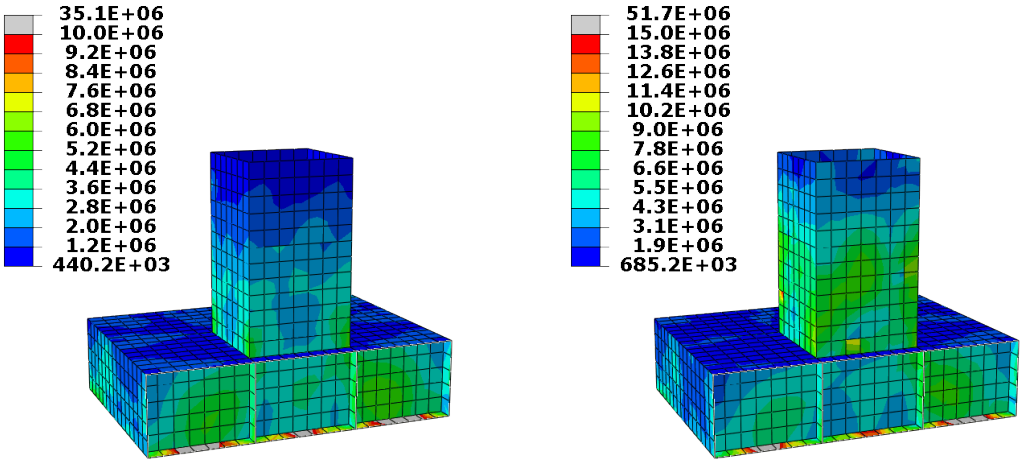

(c) $T_R = 3000$ years

(d) $T_R = 10\,000$ years

Figure 6.26: Contour plots of the maximum envelope von Mises stress when underlying soil is soft, and represented by finite elements. Units are in Pascal.

It is seen that for the 475-year earthquake, stresses are generally lower than for the springs, but the differences are small. The same can be said for the other earthquakes as well. The floor of the caisson is subjected to unrealistically high stresses also for this analysis. The reason is that the structure is modelled as fully constrained onto

the soil with only the bottom slab as the contact surface, which is not the case for real structures, and because of this, these stresses are ignored. It is noticed that the artificial stresses are lower than for the spring foundation, which seems reasonable as the direct method improves upon the realism of the model.

Hard soil

Increasing the soil stiffness also increases the seismic loads, as is obvious, and can be seen in figure 6.27. A comparison with figure 6.1 shows that the stresses approach the base case from below as the soil stiffness increase. Using the stiffness of solid rock, by assuming a shear wave velocity of $V_s = 800\,\mathrm{m/s}$, shows that the stresses are only slightly reduced. The soil springs however, do not appear to converge towards the results for an infinitely stiff foundation. Instead they suggest significantly lower stresses, as can be seen in figure 6.24. This results in a poor, unconservative approximation to the full on finite element modelling of the direct method, and is therefore deemed inapplicable - at least in the manner in which it is implemented here. Seeing as the results agree better for the soft soil, it is believed that the discrepancies between the two methods are caused by reduced accuracy in the kinematic coupling of the simplified spring method. Here, both torsion and rocking are ignored, as the motion of the structure is fully controlled by displacement of a single reference point. The direct method does not suffer from such a simplification, and as the soil is stiffened, and motion at the top of the soil layer due to the ground accelerations becomes more violent, the results start to differ.

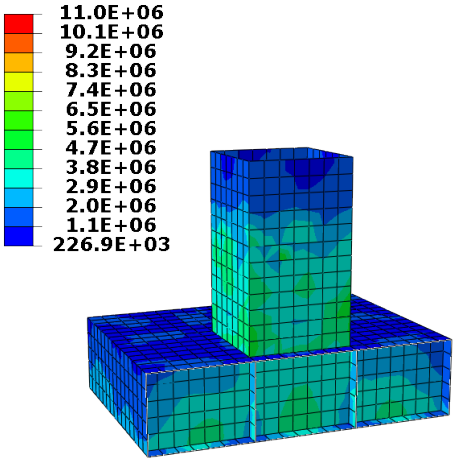

(a) $T_R = 475$ years

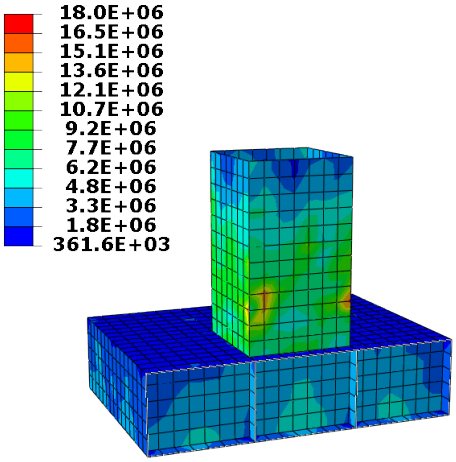

(b) $T_R = 1000$ years

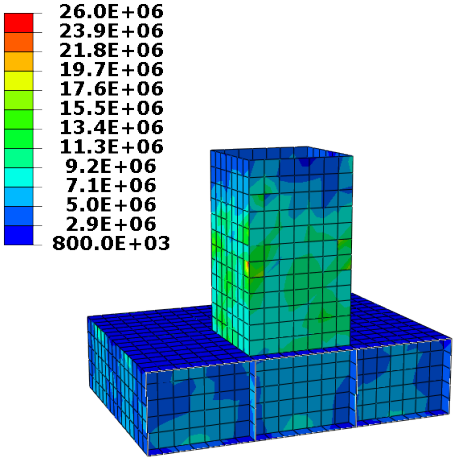

(c) $T_R = 3000$ years

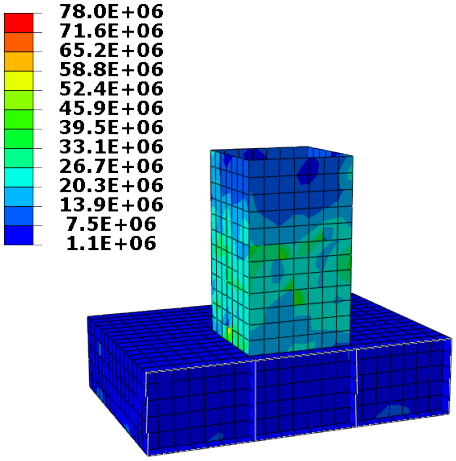

(d) $T_R = 10\,000$ years

Figure 6.27: Contour plots of the maximum envelope von Mises stress when underlying soil is stiff, and represented by finite elements.

Due to interaction with the soil layer, the eigenmodes are mostly concerned with the deformation of the soil, creating rocking, torsion and translation of the structure. Because of this, the eigenfrequencies for this model is not comparable to the base case. However, the eigenfrequencies for the soil-structure system - for both soft and hard soil - are given in table 6.10, with the ten first eigenmodes given in appendix A.

Table 6.10: Eigenfrequencies of the soil-structure system.

Mode	Soft soil [Hz]	Hard soil [Hz]
1	0.56143	2.4952
2	0.56294	2.5018
3	0.56305	2.5021
4	0.56332	2.5033
5	0.56935	2.5300
6	0.57486	2.5543
7	0.57776	2.5678
8	0.58160	2.5845
9	0.58863	2.6073
10	0.58953	2.6159

It is noticed that the soft soil results in lower eigenfrequencies than the hard soil, which is reasonable as the as the stiffness is equivalently lower. Looking at the eigenmodes in appendix A, it is seen that the soft soil results in perturbation of the caisson, with the rest of the structure subjected to rigid body motion. This corresponds with the generally low stresses of figure 6.26, as well as the high stresses in the bottom slab. With the structure resting upon the hard soil, more of the structure is involved, with mode shapes that begin to resemble those of the structure on infinitely stiff foundation. This is especially apparent for the ninth mode shape, which relates to the first mode of the base case.

6.5 Vibration characteristics

For the 10 000-year earthquake, an attempt has been made to identify damping caused by the inclusion of plasticity, as well as the radiation damping of the surrounding water. This is done by comparing the energy dissipation to that of an equivalent elastic model with a spectrum of known damping ratios. The artificial damping is applied by use of mass proportional Rayleigh-damping, using the first eigenfrequency to find α from equation 2.7. Mass proportional damping has been chosen over a stiffness proportional equivalent because in the case of plasticity, the stiffness is changed, which results in a global damping that is not velocity proportional. It is realised that the dissipated energy by the investigated phenomena not necessarily are velocity proportional either, and as such, these results are highly speculative. On the other hand, the equivalence of energy does provide at least a notion of the physics involved. The results are shown in figure 6.28.

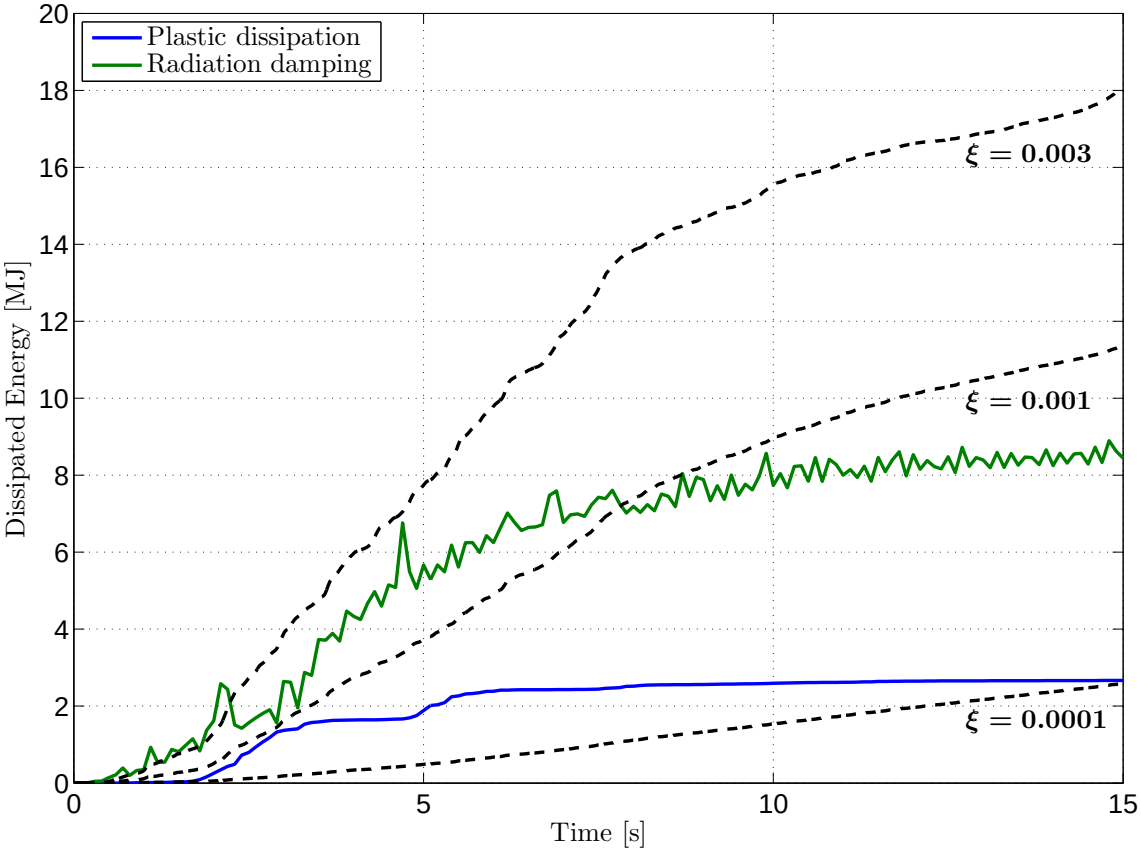

Figure 6.28: A comparison of energy dissipated from plasticity and to the surrounding water, with energy dissipated by viscous damping.

Abaqus presents energy as a cumulative quantity, which means that energy is dissipated only when the slope is non-zero in figure 6.28. This also implies that no damping due to plastic dissipation occurs after approximately 6 seconds. The highest contribution to energy dissipation caused by the surrounding water takes place in this time period as well, however a slight increase is also observed after 6 seconds.

Looking at the plastic dissipation, it is seen that the energy is dissipated in two steps, at around 2.5 and 5 seconds. In-between, no energy is dissipated. It is seen that the amount of plastic dissipation taking place in each step is approximately equal to that of a viscous damping of $\xi = 1\%$, however as it is not continuously dissipated, an average viscous damping ratio over the first 6 seconds could be estimated as $\xi = 0.5\%$. For the radiation damping it is seen that the dissipated energy lies between the energy dissipated by a viscous damping ratio of $\xi = 1\%$ and $\xi = 3\%$, and as such one can estimate the radiation damping as approximately $\xi = 2\%$ for the time period up until 6 seconds.

It should be noted that while the comparison of dissipated energy from the modelled phenomena to that of an equivalently viscous damped structure may not be entirely realistic, the results are brought further away from reality by the simplicity of the models used. This is especially true for the plastic dissipation, as the real energy

dissipation of damaged concrete is much more complex than is assumed here, and may result in an entirely different damping effect. The same can be said for the fluid-structure interaction.

The displacement of the top of the shaft has been examined for all analyses performed. Due to the large amounts of data generated, only results for the 10 000-year earthquake is presented here, and given in figures 6.29-6.32, with the rest of the results available in appendix C. Comparison is made with the base case, which is the elastic analysis without surrounding water. Figure 6.29a shows the shaft displacement for the plastic material model. It is observed a substantially lower amplitude than for the elastic model. Especially noticeable amplitude reductions are found where plastic dissipation takes place, as can be seen in figure 6.15. It shows how yielding of the structure absorbs the largest displacements. At the beginning and towards the end of the analysis, the displacements are similar to those of the base case, which is reasonable as the loads are in the elastic regime here. The analysis with cracking included shows similar displacements as with the plastic model, however the amplitudes are slightly higher. This is reasonable as the same material model has been used, but the stiffness degradation causes larger displacements.

With the presence of water, the added mass method produces interesting results, shown in figure 6.30. A period elongation can be observed, although faint. At the beginning of the motion, the vibration of the shaft relates to the base case, however, at approximately the same time as the peak ground accelerations occur, the added mass method leads to an almost complete cancellation of displacements. This can be explained by the larger mass of the shaft, which increases its inertia, and thus requires longer time to accelerate. At this point, the ground accelerations fluctuate too quickly for the structure to be able to gain any momentum in a given direction. As the period of strongest ground accelerations have passed, the displacements become more in line with the base case again, which is reasonable as the change in acceleration slows down, and the structure has time to react. The same trend is seen for the acoustic-structural interaction, in figure 6.30b. The displacements are similar to the base case at the beginning of the motion, and reduced as the highest ground accelerations are imposed. As the earthquake begins to die out, however, the shaft presents with a different envelope of displacement, with a noticeably longer period. This is caused by the resistance of the acoustic medium, and is intuitively reasonable, as period elongation is expected by the inclusion of surrounding water.

For the analysis where the structure is resting upon soft soil, it is seen from figure 6.31 that large displacements of the top of the shaft occur. This motion is characterised by long periods. This is as one would intuitively expect, as the soil layer acts as springs, regardless of modelling method - be it explicitly as springs or as an elastic soil layer. The structure is then given some leeway, rather than being forced to follow the oscillations of the earthquake. This causes larger displacements, as the structure can continue in a given direction for an extended amount of time, before eventually being dragged along by the elastic foundation. It is noticed that the direct method results in slightly larger displacements, as rocking of the structure is taken into account. For the hard soil, given in figure 6.32, discrepancies between the two methods are seen in the shaft displacement. The spring foundation method

provides larger displacements and a slightly larger vibration period, consistent with the lower stresses in figure 6.24. The direct method predicts lower displacements for the majority of the earthquake, but with higher seismic loads. The reason for this is that significant eigenmodes of the soil-structure system consists of modes of vibration where the top of the shaft remains immobile, and plate bending in the middle of the shaft takes place instead, generated by rigid body motion of the rest of the structure. This is shown in appendix A.

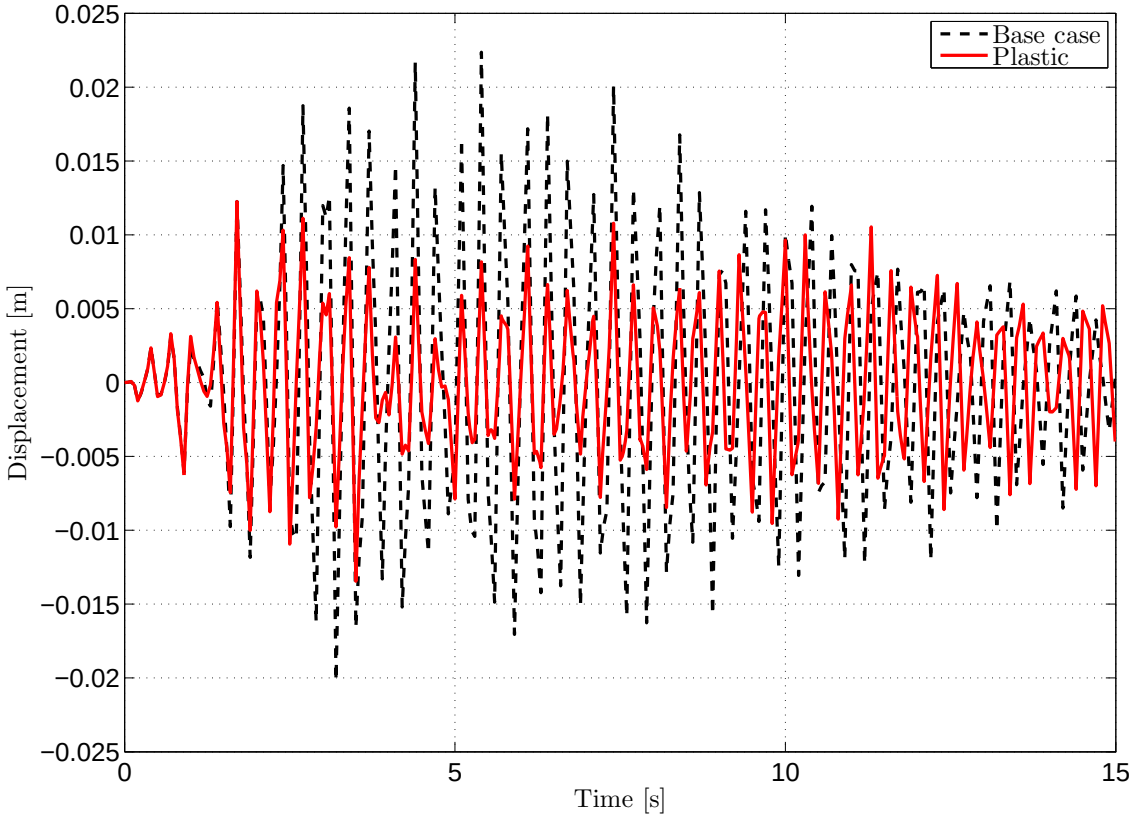

(a)

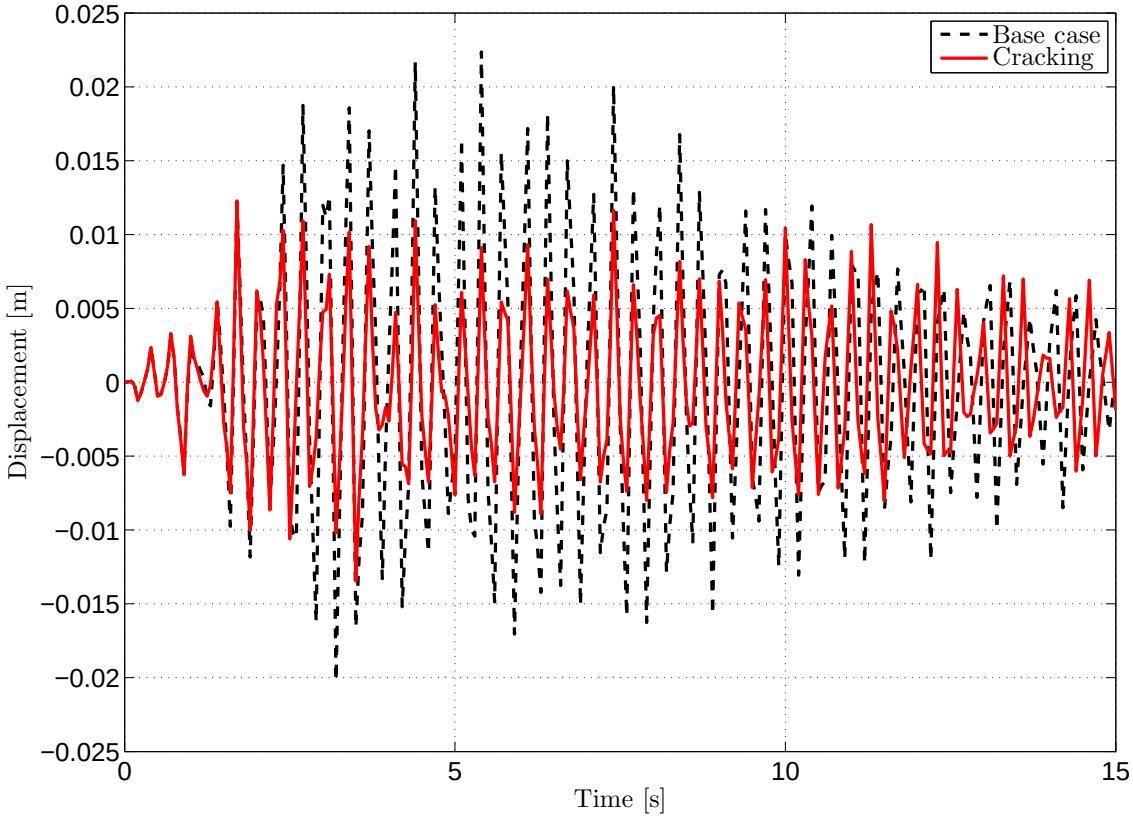

(b)

Figure 6.29: Relative displacement of the top of the shaft: Plasticity.

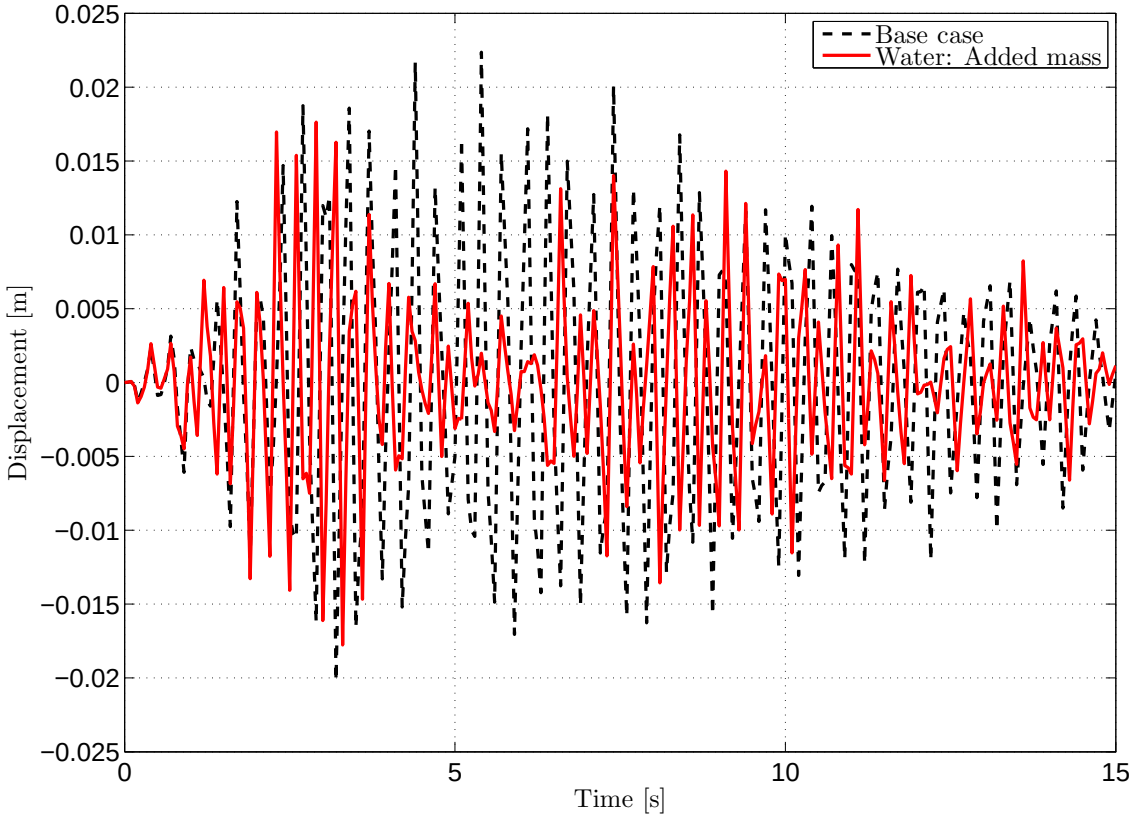

(a)

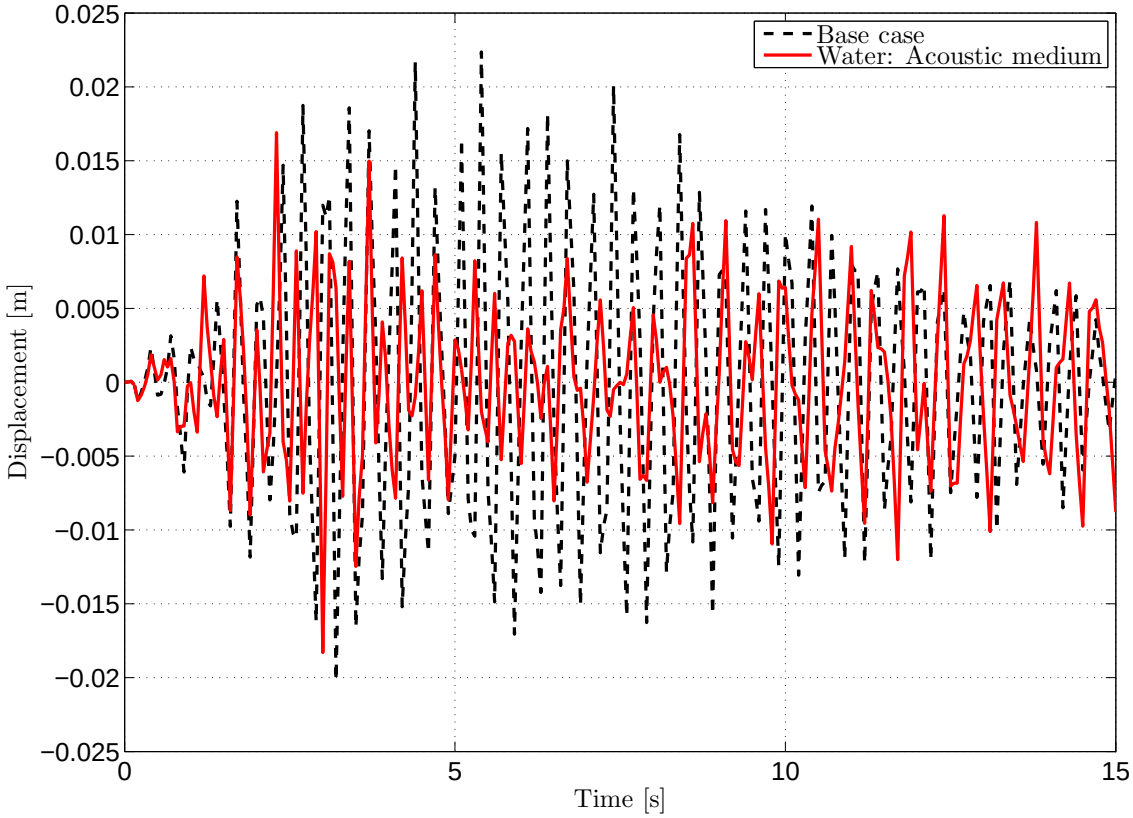

(b)

Figure 6.30: Relative displacement of the top of the shaft: Surrounding water.

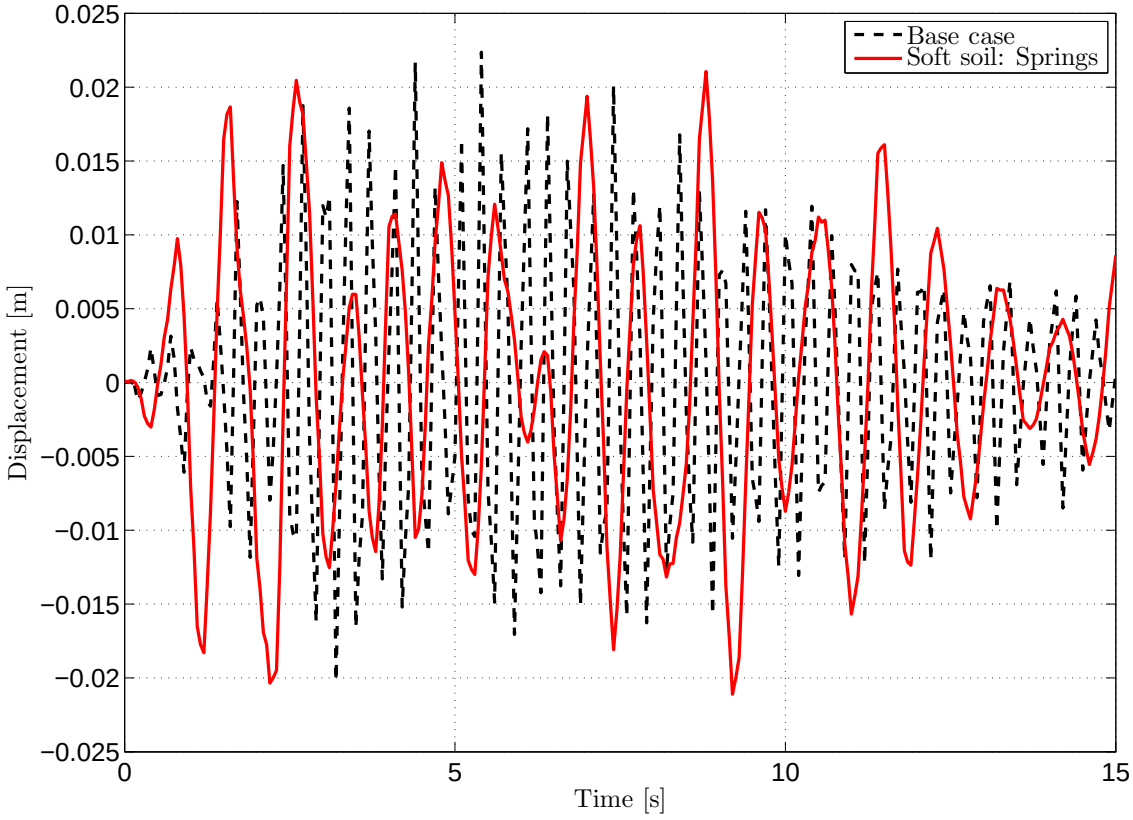

(a)

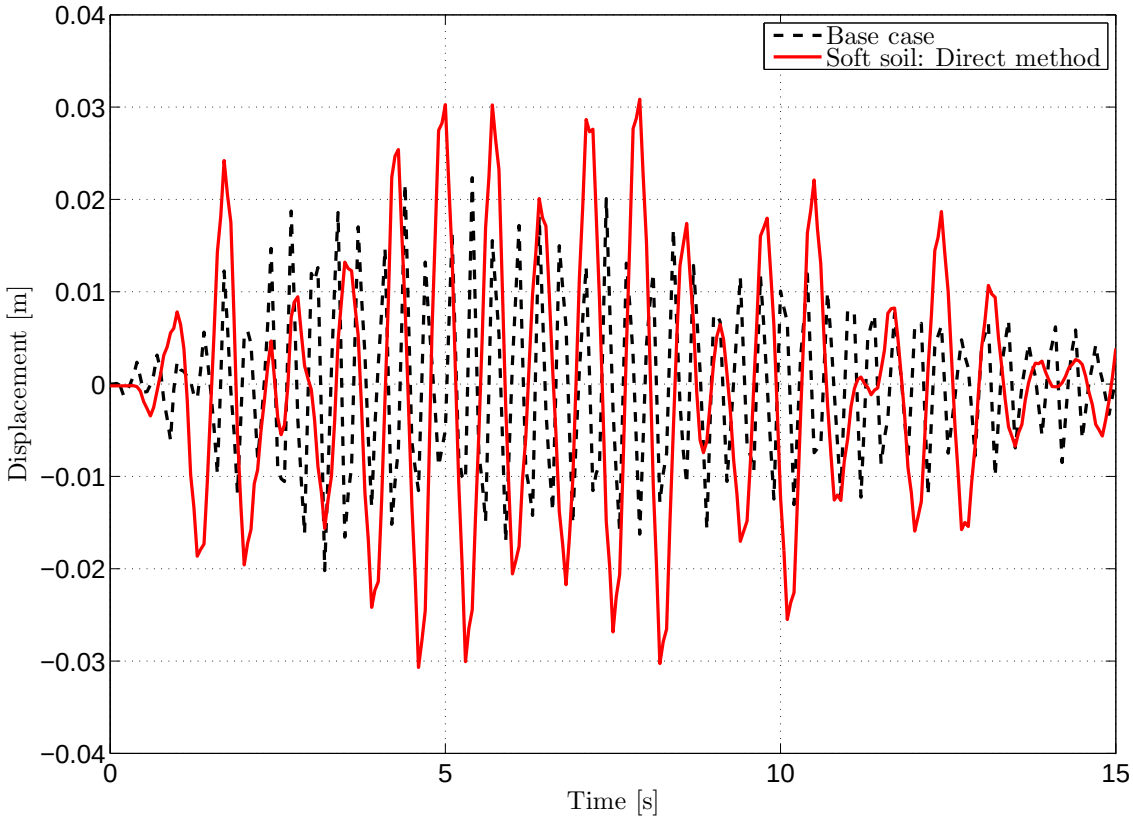

(b)

Figure 6.31: Relative displacement of the top of the shaft: Soft soil.

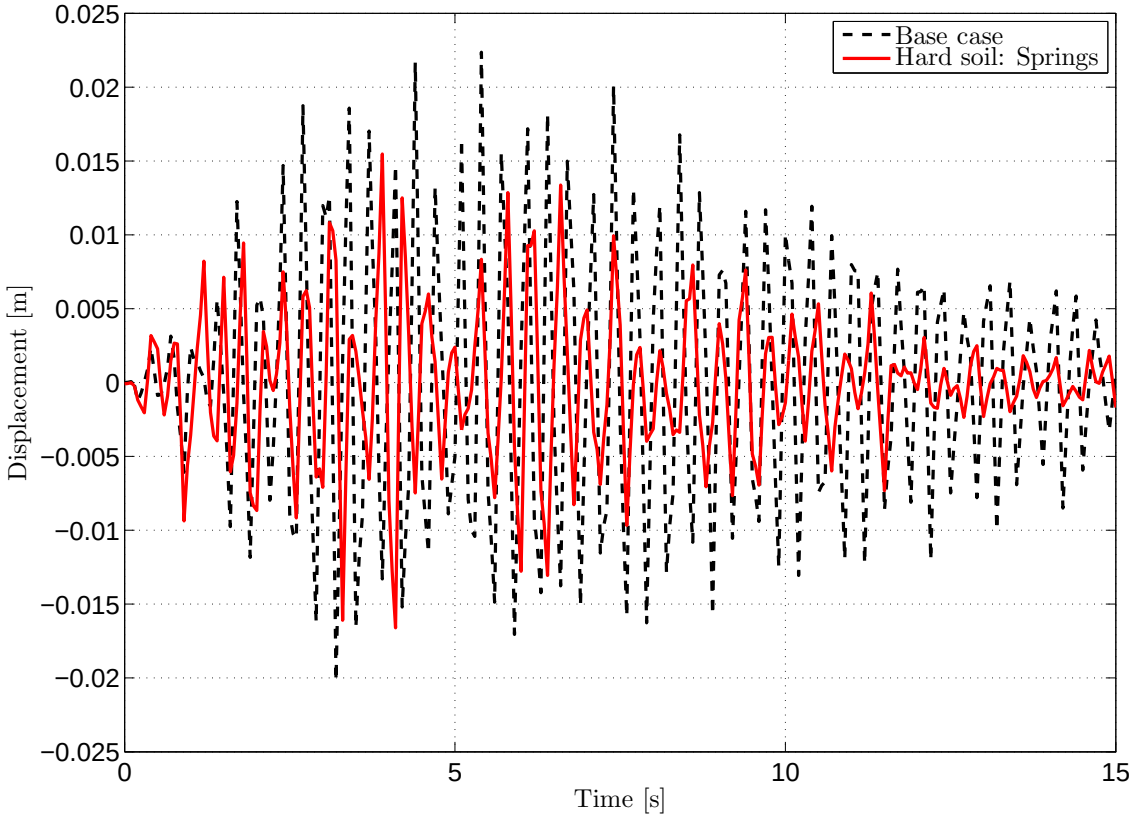

(a)

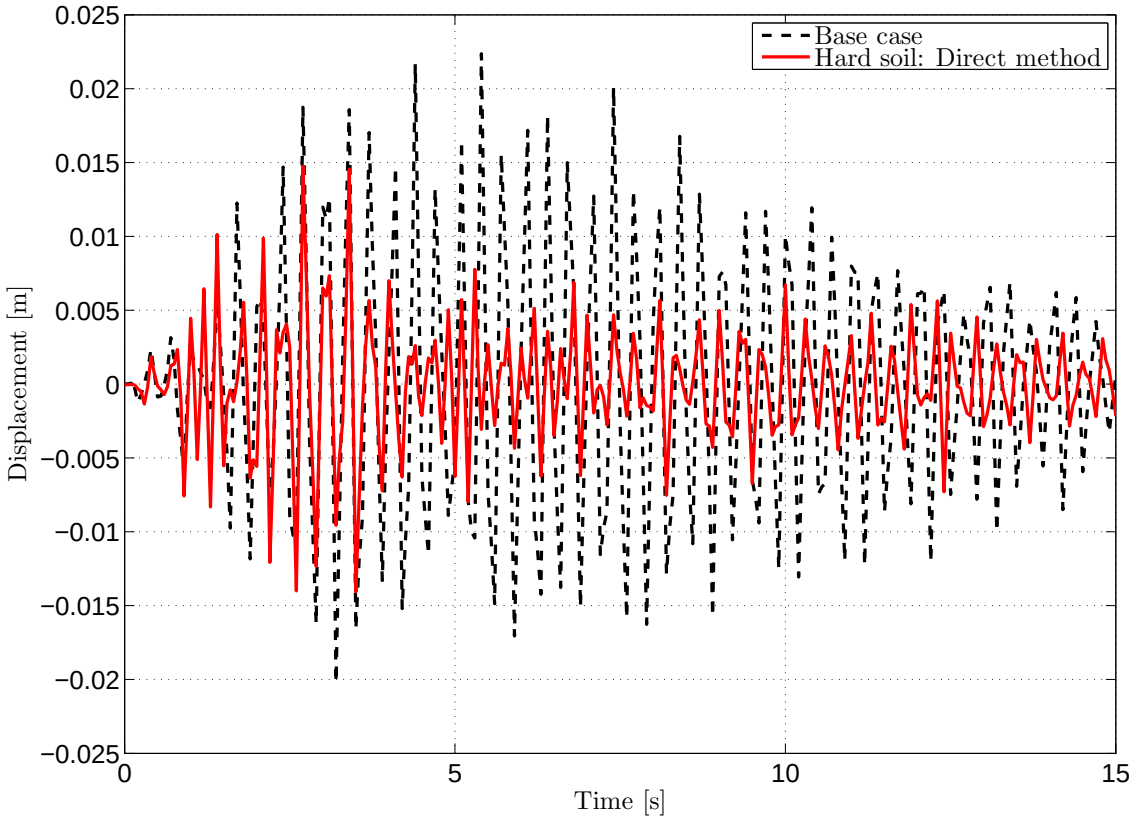

(b)

Figure 6.32: Relative displacement of the top of the shaft: Hard soil.

Looking at the remaining results in appendix C, it is first of all noticed that the vertical vibrations oscillate about an equilibrium line which is displaced from the initial configuration. This is caused by the weight of the structure for which equilibrium is established before onset of vibratory motion, such that the structure settles slightly. This effect is greater for the soil springs and elastic layer analyses, as the tower is additionally displaced with respect to the outer walls of the caisson, to which the displacement is relative. This is caused by the increased weight in the middle of the structure due to the shaft. It is indeed this motion which causes the large increase in displacements shown in, for instance, figure C.15b. The motion consists of rigid body motion of the shaft, combined with flexural bending of the caisson, thus producing the large stresses in the bottom slab - an effect which is especially prominent in the soft soil analysis. The results from the other return periods are quite similar to those discussed in this section, however it is interesting to observe the soft soil analysis for the 475-year earthquake, shown in figure C.3, where it is seen that the earthquake at the base of the structure is almost completely damped out by the soil layer, thus exemplifying the isolating effect the low shear stiffness has on the structure.

7 Conclusion

Seismic analysis of offshore concrete structures is a difficult subject, and several important challenges one is likely to encounter have been discussed. These difficulties span from theoretical complexity to numerical implementation and include lack of experimental verification as a complicating factor. The latter is especially problematic as nonlinear analyses bring with them the burden of proof with respect to their realism.

In this thesis, the starting point has been a simplified geometry of a part of a typical offshore concrete structure. The purpose has then been to axiomatically establish a thorough analysis of the phenomena pertaining to offshore seismic analysis. This was done by first establishing characteristic earthquakes for increasing return periods such that the effects of their increase in size could be compared. These return periods were chosen to be 475, 1000, 3000 and 10 000 years. In the process of determining appropriate earthquakes for these return periods, a statistical basis of 964 earthquakes were gathered within an estimation area slightly off the southwestern coast of Norway. The magnitude as a function of frequency of occurrence was found to follow Gutenberg-Richter's law for magnitudes larger than $M_{min} = 2$. This is important because it proves the completeness of the earthquake catalogue used, as well as providing a probability function for use with earthquake simulation.

Unfortunately, the earthquake catalogue was not nearly large enough to provide sufficient data to find appropriate return period parameters, thus forcing the use of extrapolation. This was done by simulating 50 000 uniformly distributed earthquakes within a radius of 100 km from the structure. There are two sources of error which significantly influence the results. Firstly, the recordings of the catalogue were not evenly distributed throughout the estimation window, which creates a bias towards the closer earthquakes and introduces error. Secondly, the attenuation of seismic energy means that an earthquake occurring far away dissipates before it reaches the structure. The simulation of earthquakes within the limited radius solves these issues, while resting upon the assumption that the derived relations are valid also there.

Triplets of peak ground acceleration, distance and magnitude were simulated for each of the 50 000 earthquakes using the attenuation relationship of *Dahle & Bungum* with a normally distributed error term, thus yielding a distribution of peak ground accelerations at the site of the structure, for which order statistics was performed. Such an approach falls victim to the lack of recordings available in the North Sea. The attenuation relationship is general, and ideally one would establish an attenuation relationship for the investigated site, thus taking local geology into account. However, even if that was a possibility there is hardly any easily available information of the geology of the site in question. Other sources of error is the order statistics approach, which assumes that the input consists of the largest earthquake for a given year. This is not the case. Instead, all 964 earthquakes were used, thus making the probabilities less accurate. This is amended by only using the largest simulated

values in the regression analysis, but in doing so, the solution becomes dependent upon that fraction. While order statistics only give the characteristic PGA-value, the other two parameters were selected by picking simulated earthquakes according to figure 5.4. This provides only a rough estimate. Even with these errors, a remarkable correspondence with the seismic zonation maps used by the design codes are found. It can then be concluded that the probabilistic extrapolation approach used herein provides a decent estimate of the seismic hazard in the considered area.

Having determined three parameters which are assumed to define a return period, these were used to select appropriate earthquake accelerograms. No such accelerograms are available for the North Sea, and instead the European Strong-Motion and PEER databases were used. For each return period, ten accelerograms were selected and a mean response spectrum generated. A comparison with Eurocode 8 showed that the 475-year mean response spectrum shows similarity between the equivalent design spectrum, which is natural as most of the recordings were from buildings on solid rock. This does however mean that the local geology of the investigated area is not considered, nor was it expected to. The comparison does show that the determined mean response spectra are not unrealistic, and produce sufficiently good results if only a rough estimate is sought, which was the case for this study.

Recorded earthquake accelerograms vary greatly in both their duration and shape, which made it difficult to compare the results between return periods. Because of this, earthquake accelerograms were simulated, by using a recorded response spectrum for a given return period as a target for iteration. The mean response spectrum was not used for this purpose, as it would generate time histories with unrealistic frequency content. Even so, complete realism was not attained, as the simulation process introduced spurious peaks in the Fourier spectrum. This was particularly the case for the 1000-year earthquake, which resulted in the 1000- and 3000-year earthquake response to be similar. Another contributing factor to this was that the jump in return period between them was not large enough to create uniquely larger 3000-year earthquakes.

The basis for comparison was an elastic incarnation of the investigated structure, with no surrounding water present, but with internal water included as an increase in mass. The time series analysis revealed for the 10 000-year earthquake that peak stresses occur which are significantly larger than the mean response of the structure. These are a result of the elastic approximation and are unrealistic, as proven by the more accurate material model used, which filters them off.

An evaluation of the response spectrum method was performed. This was done by using the absolute sum of peak values, SRSS and CQC methods, with the parameters used for comparison being the nodal moments and shear forces. The 475-year earthquake was worst off with respect to conservatism, with all three methods yielding unconservative results. The absolute sum of peak values provided the smallest extent of areas with unconservative results, but these areas had the largest nodal loads. On the other hand, the degree of unconservatism was small, and the loads caused by the 475-year earthquake were of such low magnitude that the absolute sum of peak values was deemed applicable.

The absolute sum of peak values produce conservative results for the three other return periods, but the other two methods yield very unconservative results - also for the 475-year earthquake. The SRSS method was expected to do so, as it assumes no correlation between modes. This is inappropriate for 3D models, as the eigenfrequencies are usually closely packed. The CQC method uses random vibration theory to establish a correlation between modes and was expected to yield better results. This was not the case however, and instead the structural response was almost identical to the SRSS method. The reason for this was found to be the correlation factor, which in this case did not describe the relationship between nodes. Rather, it was discovered that the correlation factor was reduced to zero too fast - especially for the lowest eigenfrequencies where the participation factors were largest. This caused only the autocorrelation to remain, converging the CQC method towards the SRSS method as the results show.

On average the absolute sum of peak values is less accurate than the other two as it converges around an overly conservative result, although with little spread. CQC and SRSS have means which agree nicely with the time history analysis, but as the loads increase, the spread in results do also, which makes them unattractive. These observations were found for all earthquakes and return periods considered, which makes it apparent that the response spectrum method is an inappropriate analysis tool for the investigated structure.

A material model which includes reinforcement and plasticity was applied to the structure, and its influence on the results were investigated. It was seen that the stresses were generally lower than for the elastic analysis by a few Megapascals, in other words no great difference. As previously mentioned, the plastic material model does not produce large, concentrated peak values, as the yielding of the structure does not allow it, thus giving a peak stress value which more closely corresponds with stresses observed in large parts of the structure. The plastic dissipation for the four return periods show that only the 10 000-year earthquake produce a non-negligible excursion into the plastic domain, although yielding takes place also for the 1000- and 3000-year earthquakes. The 475-year earthquake remains elastic. Such a result is reasonable due to the low seismicity of the North Sea, the large dimensions of the structure and the neglect of simultaneously acting external loads. These results correspond with the stress difference between the elastic and plastic material models, with a larger difference occurring for the larger return period. Most of the structure remains elastic, or nearly so, for all analyses. This result is reflected in the equivalent eigenfrequencies, calculated after the structure had been subjected to an earthquake, showing negligible differences - thus proving that little geometry or stiffness change has taken place.

The effect of cracking was included as a sub-study of the plastic material model, where the elastic stiffness of the structure was allowed to degrade in tension. Its implementation had little effect on the lowest three return periods, but led to noticeable stress concentrations at the areas of most severe cracking for the 10 000-year earthquake. The occurring stresses were also slightly reduced with respect to the pure plasticity model, suggesting further increase in ductility. No cracking took place for the 475-year earthquake, which is as expected as the imposed ground ac-

celerations were quite small. The calculated eigenfrequencies after the cracking took place show further reduction, but the difference from the pristine, elastic structure is still negligible. The conclusion is that the use of a plastic material model, both with and without cracking, is unnecessary, as the structural response remains very close to that of an elastic model, which provides a great advantage with respect to analysis time.

The effects of surrounding water were investigated by comparing with analyses where water was omitted. Two methods of modelling water were tested. The first made use of the simplification that Morison's equation was applicable, although the structure is nowhere close to being slender. Furthermore, the added mass coefficients of steady current were used, ignoring the frequency dependence caused by the oscillatory motion. These coefficients themselves were subject to speculation, as values for appropriate geometries were hard to come by. The added mass was evenly distributed over surfaces submerged in water, thus introducing additional error as the added mass also occurs in the wake of the structure for a given motion. Finally, the drag force is ignored, as motivated by the large volume of the structure, making wave generation a more likely source for energy dissipation.

The inclusion of water by means of added mass serves to reduce the eigenfrequencies, and this reduction is significant. The modal participation factors are also shifted, which causes a lower response in the 10 000-year earthquake, and a larger response in the 3000-year earthquake. A higher response is also observed in the 475- and 1000-year earthquakes, but to a lesser degree.

The second method used in the application of water interaction was an explicit model of the medium within which the structure oscillates. This was done by an acoustic-structural interaction, under the assumption that the pressure changes are small. Such an approach is more accurate than Morison's equation, as no slender approximation is necessary, no added mass coefficients need be found and radiation damping is included. On the other hand the analysis time is larger. Significant alteration of the eigenfrequencies is found, however a resemblance with the eigenfrequencies determined with the added mass method is observed - suggesting that the approach is reasonable. The significant modal participation factors are mostly found for low periods, thus reducing the accelerations experienced by the structure - as can be seen from the comparisons of participation factors and response spectra in appendix F. However, due to the increase in inertia, the introduction of water generally ended up being detrimental, with a few exceptions.

A soil-structure analysis was performed, where two methods were tested - a simplified spring foundation, and a full on finite element analysis where a 50 meter thick, elastic soil layer was modelled beneath the structure. The two methods agreed for the soft soil analysis, and predicted a significant reduction in seismic loads. It is however suspected that such a method does not represent reality, as a real structure cannot merely be placed atop a sand layer and be expected to behave as if standing on springs. At the very least, a much more sophisticated model, taking into account the upheaval of the sand and perhaps liquefaction needs to be considered if one is to trust the results for such an analysis. With the structure modelled as resting upon

hard soil it is seen that the two models do not agree, with the spring foundation giving much lower stresses than the infinitely stiff case. The elastic soil layer on the other hand, predicts almost the same results as the base case, which seems reasonable. It is believed that the spring foundation is a poor approximation when the influence of the ground accelerations on the structure become larger, as this model does not take into account rocking or torsional motion. The soft soil model served to almost entirely isolate the structure from the ground accelerations, and because of this the problem approaches a quasi-static analysis, in which case the two models gave similar results - which is only reasonable as the spring foundation does indeed describe the static stiffness of the soil.

It has been the purpose of this thesis to provide a reference case, where several physical phenomena one encounters in the analysis of offshore concrete structures is investigated. This has been done by introducing a level of complexity which is high enough to evaluate their influence on the solution, but not so much that the results are obscured. At the same time, and where applicable, an evaluation of simplified approaches has been undertaken, thus providing results which the author hopes is of interest both for the practising engineer, and the academic.

Bibliography

[1] Pacific earthquake engineering research centre (PEER), strong ground motion database. `http://peer.berkely.edu`, 2010.

[2] N. Ambraseys, P. Smit, R. Sigbjörnsson, P. Suhadolc, and B. Margaris. Internet-Site for European Strong-Motion Data. `http://www.isesd.hi.is`, European Commission, Research-Directorate General, Environment and Climate Programme, 2002.

[3] H. Bungum, O. Olesen, S. Gibbons, C. Lindhold, and O. Vestøl. To what extent is the present seismicity of norway driven by post-glacial rebound? *Journal of the Geological Society*, 167:373–384, 2010.

[4] R. D. Cook, D. S. Malkus, M. E. Plesha, and R. J. Witt. *Concepts and Applications of Finite Element Analysis*. John Wiley & Sons inc, fourth edition, 2002.

[5] C. T. Crowe, D. F. Elger, and J. A. Roberson. *Engineering Fluid Mechanics*. John Wiley & Sons inc, eighth edition, 2005.

[6] A. Dahle, H. Bungum, J. Havskov, and B. Aspen, editors. *Seismic surveillance of the Blåsjø reservoir*, volume 1. Proceedings of the Tenth World Conference on Earthquake Engineering, July 1992.

[7] A. Dahle, H. Bungum, and L. B. Kvamme, editors. *Attenuation modelling based on intraplate earthquake recordings*, volume 4-A. Proceedings of the Ninth European Conferece on Earthquake Engineering, 1990.

[8] Det Norske Veritas. *DNV-RP-C205: Environmental conditions and environmental loads*, 2010.

[9] D. C. Drucker and W. Prager. Soil mechanics and plastic analysis or limit design. *Quarterly of Applied Mathematics*, 10(2):157–165, 1952.

[10] European Committee for Standardization. *NS-EN 1992-1-1:2004+NA:2008, Eurocode 2: Design of concrete structures. General rules and rules for buildings*, 2004.

[11] European Committee for Standardization. *NS-EN 1998-1:2004+NA:2008, Eurocode 8: Design of structures for earthquake resistance, Part 1: General rules, seismic actions and rules for buildings*, 2004.

[12] D. Gasparini and E. Vanmarke. SIMQKE 1. `http://nisee.berkeley.edu`.

[13] R. E. Gibson and B. E. W. Dowse. The influence of geotechnical engineering on the evolution of offshore structures in the north sea. *Canadian Geotechnical Journal*, 18:171–178, 1981.

[14] P. C. Marrow, Global Seismolgy Research Group. Seismic monitoring of the north sea. British Geological Survey, 1992.

[15] B. Gutenberg and C. F. Richter. *Seismicity of the earth and associated phenomena*. Princeton University Press, 1954.

[16] H. M. Hilber, T. J. R. Hughes, and R. L. Taylor. Improved numerical dissipation for time integration algorithms in structural dynamics. *Earthquake Engineering and Structural Dynamics*, 5:283–292, 1977.

[17] H. Kanamori and D. L. Anderson. Theoretical basis of some empirical relations in seismology. *Bulletin of the Seismological Society of America*, 65(5):1073–1095, 1975.

[18] S. L. Kramer. *Geotechnical Earthquake Engineering*. Prentice-Hall, 1996.

[19] J. Lee and G. L. Fenves. A plastic-damage concrete model for analysis of dams. *Earthquake Engineering and Structural Dynamics*, 27(9):937–956, 1998.

[20] Xilin Lu, Peizhen Li, Bo Chen, and Yueqing Chen. Computer simulation of the dynamic layered soil? pile?structure interaction system. *Canadian Geotechnical Journal*, 42:742–751, 2005.

[21] J. Lubliner, J. Oliver, S. Oller, and E. O nate. A plastic-damage model for concrete. *International Journal of Solids and Structures*, 25(3):299–326, 1989.

[22] Mathworks. Matlab r2011a. `http://www.mathworks.se/`.

[23] Dan Evert Brekke, Multiconsult. MultiCon.

[24] NORSAR. NORSAR: jordskjelv.no. `http://www.jordskjelv.no/`, 2010.

[25] NORSAR and NGI. Seismic zonation for norway. Technical report, Norwegian Council for Building Standardization, 2007.

[26] The Norwegian Oil Industry Association and The Federation of Norwegian Industry. *NORSOK N-003, Norsk Sokkels Konkurranseposisjon*, third edition, September.

[27] Arne J. Reite. Sør-trøndelag fylke, kvartœrgeologisk kart m 1:250000, veiledning til kartet. Skrifter 96, NGU, 1996.

[28] W. P. Stewart and R. G. Campanella. Practical aspects of in situ measurements of material damping with the seismic cone penetration test. *Canadian Geotechnical Journal*, 30:211–219, 1993.

[29] "Dassault Systèmes. Abaqus 6.10-2. `http://www.3ds.com/products/simulia/portfolio/abaqus/overview/`.

[30] Dassault Systèmes. Abaqus Theory Manual: Coupled acoustic-structural medium analysis. `http://ivt-abaqusdoc.ivt.ntnu.no:2080/v6.10/books/stm/default.htm`, April 2010.

[31] Dassault Systèmes. Abaqus Theory Manual: Damaged plasticity model for concrete and other quasi-brittle materials. `http://ivt-abaqusdoc.ivt.ntnu.no:2080/v6.10/books/stm/default.htm`, April 2010.

[32] Dassault Systèmes. Abaqus Theory Manual: Implicit Dynamic Analysis. http://ivt-abaqusdoc.ivt.ntnu.no:2080/v6.10/books/stm/default.htm, April 2010.

[33] Dassault Systèmes. Abaqus Theory Manual: Rebar modeling in shell, membrane, and surface elements. http://ivt-abaqusdoc.ivt.ntnu.no:2080/v6.10/books/stm/default.htm, April 2010.

[34] Dassault Systèmes. Abaqus Theory Manual: Shell elements. http://ivt-abaqusdoc.ivt.ntnu.no:2080/v6.10/books/stm/default.htm, April 2010.

[35] E. L. Wilson, A. Der Kiureghian, and E. P. Bayo. Short communication: A replacement for the srss method in seismic analysis. *Journal of Earthquake Engineering and Structural Dynamics*, 9:187–194, 1981.

[36] J. P. Wolf. *Dynamic Soil-Structure Interaction*. Prentice-Hall, 1985.

A Eigenmodes

A.1 Eigenmodes of the structure

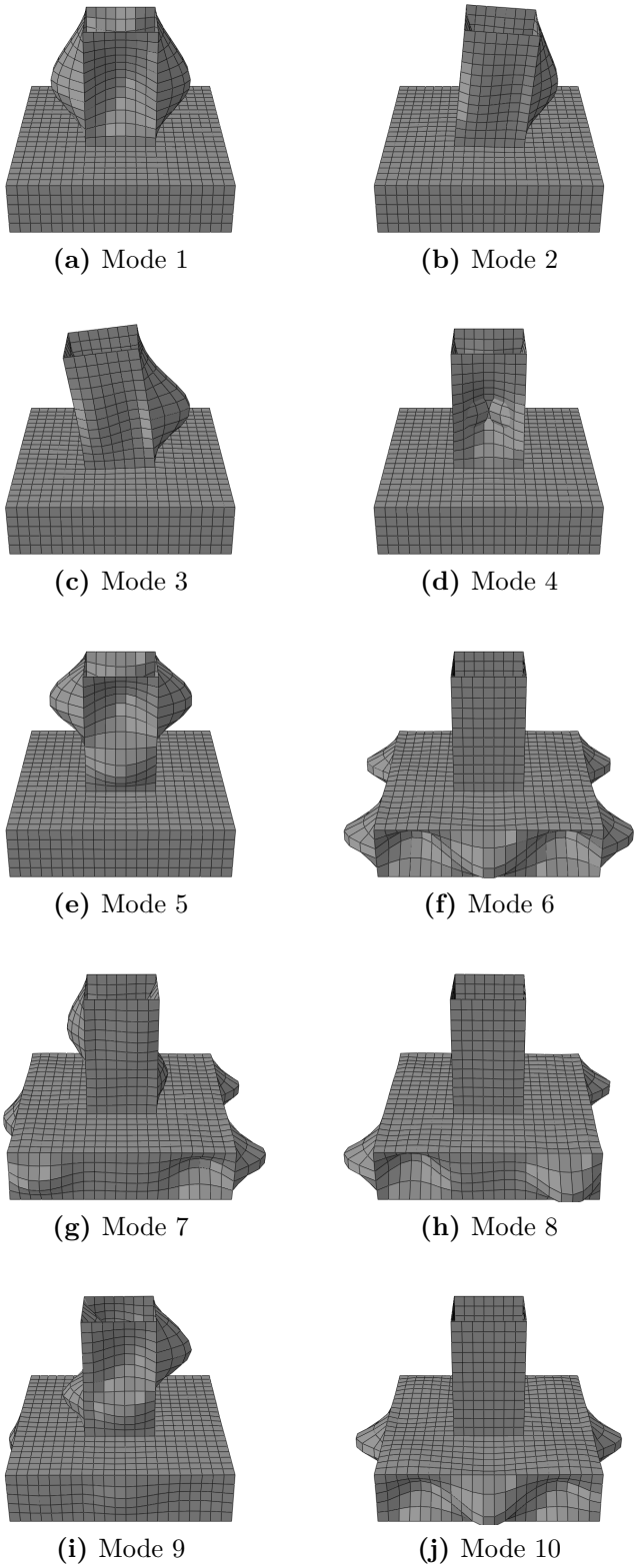

(a) Mode 1 **(b)** Mode 2

(c) Mode 3 **(d)** Mode 4

(e) Mode 5 **(f)** Mode 6

(g) Mode 7 **(h)** Mode 8

(i) Mode 9 **(j)** Mode 10

Figure A.1: Eigenmodes of the base case.

A.2 Eigenmodes of the soil

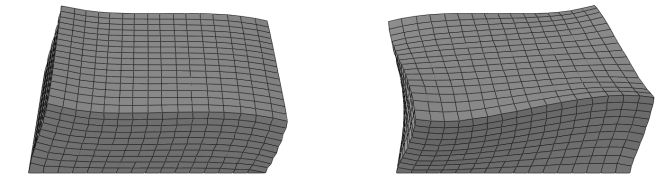

(a) Mode 1 **(b)** Mode 2

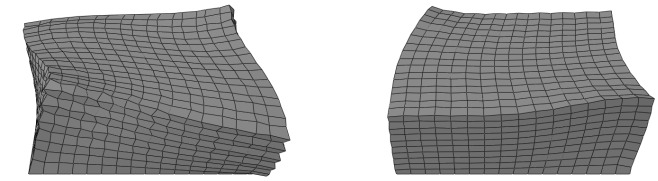

(c) Mode 3 **(d)** Mode 4

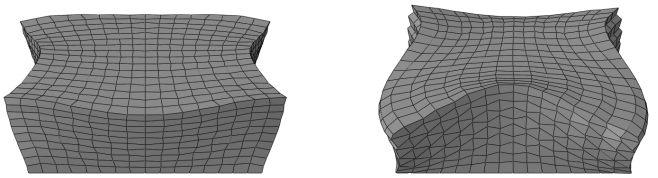

(e) Mode 5 **(f)** Mode 6

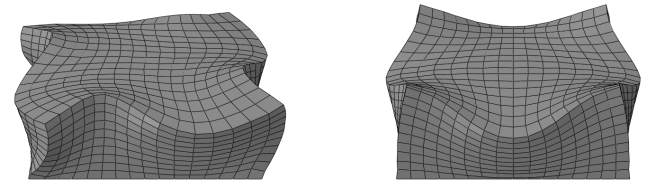

(g) Mode 7 **(h)** Mode 8

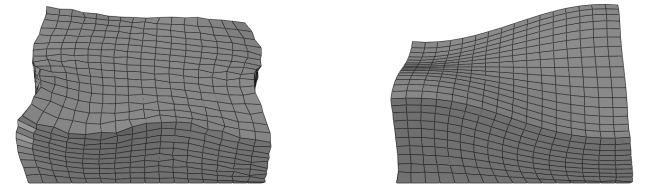

(i) Mode 9 **(j)** Mode 10

Figure A.2: Eigenmodes of the elastic soil layer.

A.3 Eigenmodes of the soft soil-structure system

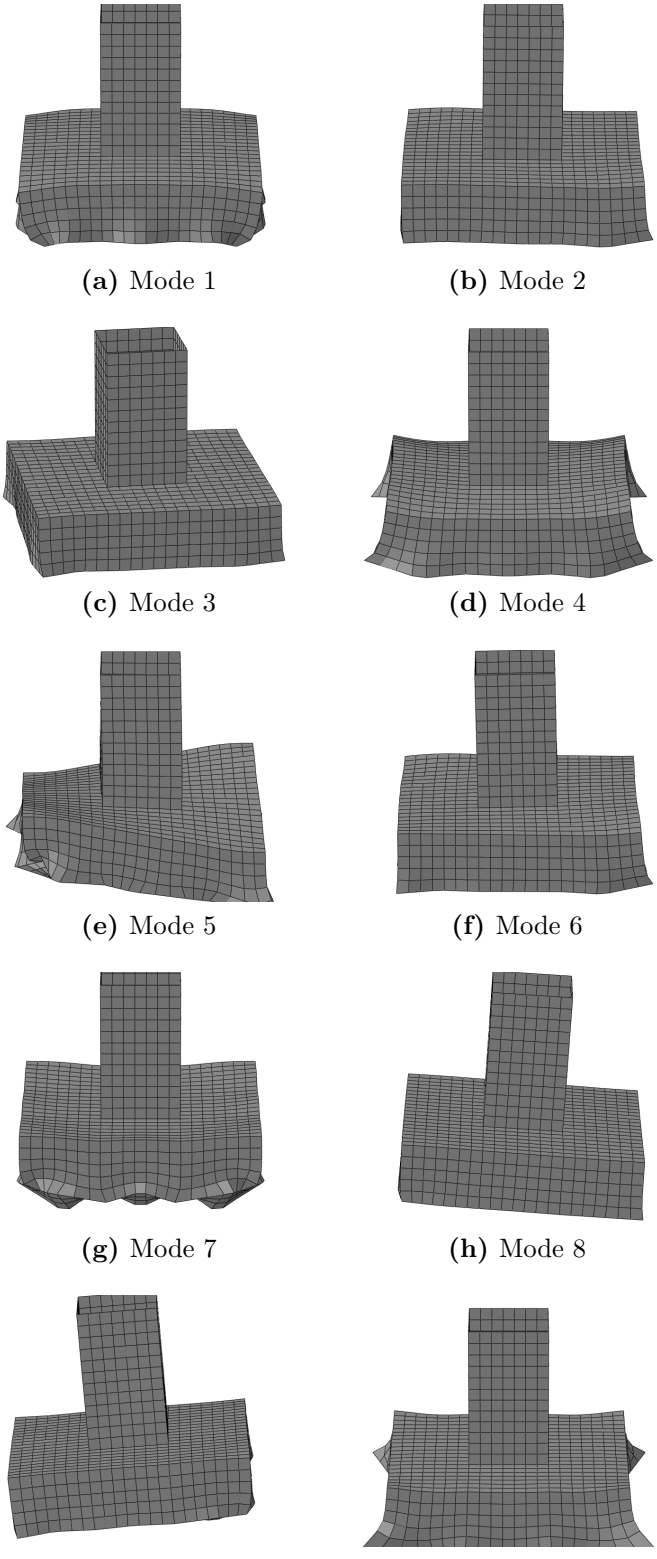

(a) Mode 1 **(b)** Mode 2

(c) Mode 3 **(d)** Mode 4

(e) Mode 5 **(f)** Mode 6

(g) Mode 7 **(h)** Mode 8

(i) Mode 9 **(j)** Mode 10

Figure A.3: Eigenmodes of the soft soil-structure system.

A.4 Eigenmodes of the hard soil-structure system

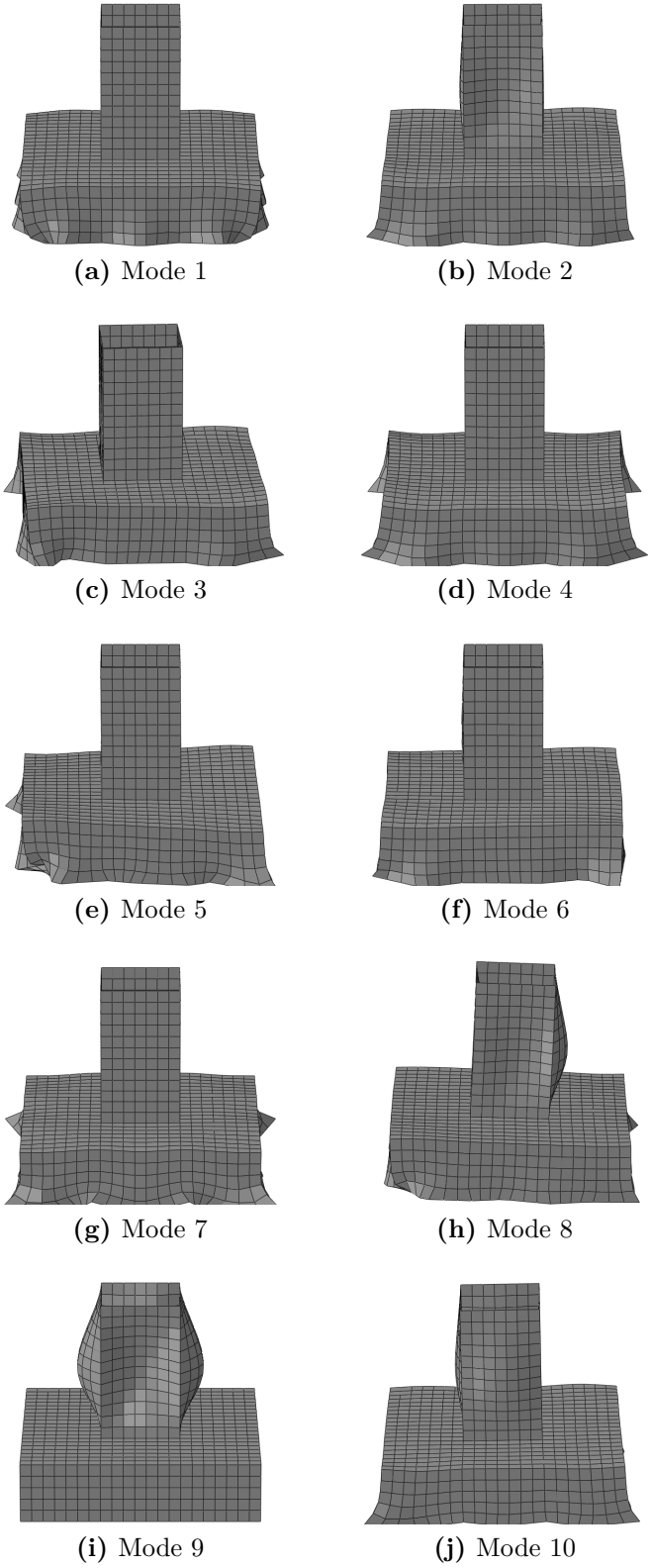

(a) Mode 1 **(b)** Mode 2

(c) Mode 3 **(d)** Mode 4

(e) Mode 5 **(f)** Mode 6

(g) Mode 7 **(h)** Mode 8

(i) Mode 9 **(j)** Mode 10

Figure A.4: Eigenmodes of the hard soil-structure system.

B Earthquakes

B.1 Recorded earthquakes

This section contains all information gathered from the two databases. A prefix on the earthquake ID of NGA means that the recorded accelerogram has been collected from PEER, and no prefix describes an earthquake collected from ESD.

Table B.1: $T_R = 475$ years

475				
ID	M	d [km]	PGA [m/s^2]	Soil type
25	3.31	11	0.610	Alluvium
552	4.23	8	0.645	Soft soil
576	4.20	15	0.599	Stiff soil
702	3.40	15	0.627	Unknown
2001	3.30	3	0.603	Stiff soil
NGA109	4.37	10	0.594	Rock
NGA1903	4.53	24	0.595	Rock
NGA2048	4.27	7	0.708	Rock
NGA1967	4.92	32	0.658	Rock
NGA2030	4.90	20	0.753	Rock

Table B.2: $T_R = 1000$ years

1000				
ID	M	d [km]	PGA [m/s^2]	Soil type
7	4.32	16	1.080	Alluvium
446	4.90	5	1.090	Stiff soil
5669	4.80	24	1.160	Soft soil
6893	4.80	4	1.160	Stiff soil
7934	4.80	18	1.060	Rock
59	5.20	27	1.247	Rock
NGa116	4.70	2	1.114	Rock
NGA262	4.80	8	0.972	Rock
NGa1958	4.92	10	1.248	Rock
NGA195	5.01	12	1.140	Rock

Table B.3: $T_R = 3000$ years

3000				
ID	M	d [km]	PGA [m/s^2]	Soil type
347	5.60	40	1.782	Stiff soil
665	5.70	23	1.796	Rock
982	5.40	9	1.869	Rock
5079	5.40	6	1.702	Rock
363	5.60	27	1.846	Rock
NGA50	5.30	13	1.965	Rock
NGA233	5.69	9	1.749	Rock
NGA397	5.18	12	1.200	Rock
NGA1670	5.20	9	2.016	Rock
NGA205	5.01	9	1.881	Rock

Table B.4: $T_R = 10\,000$ years

10000				
ID	M	d [km]	PGA [m/s^2]	Soil type
200	6.90	65	2.509	Rock
1726	6.30	30	2.644	Soft soil
5485	4.24	6	2.540	Unknown
414	5.90	11	2.670	Stiff soil
6093	5.20	16	2.601	Stiff soil
228	6.20	33	2.652	Stif soil
NGA222	5.40	10	2.476	Rock
NGA547	5.77	11	2.796	Rock
NGA243	5.70	14	2.403	Rock
NGA683	6.00	13	2.527	Rock

B.2 Spectrum comparison

Below is shown a comparison of the chosen recorded earthquake response spectrum, with the mean response spectrum, for each return period.

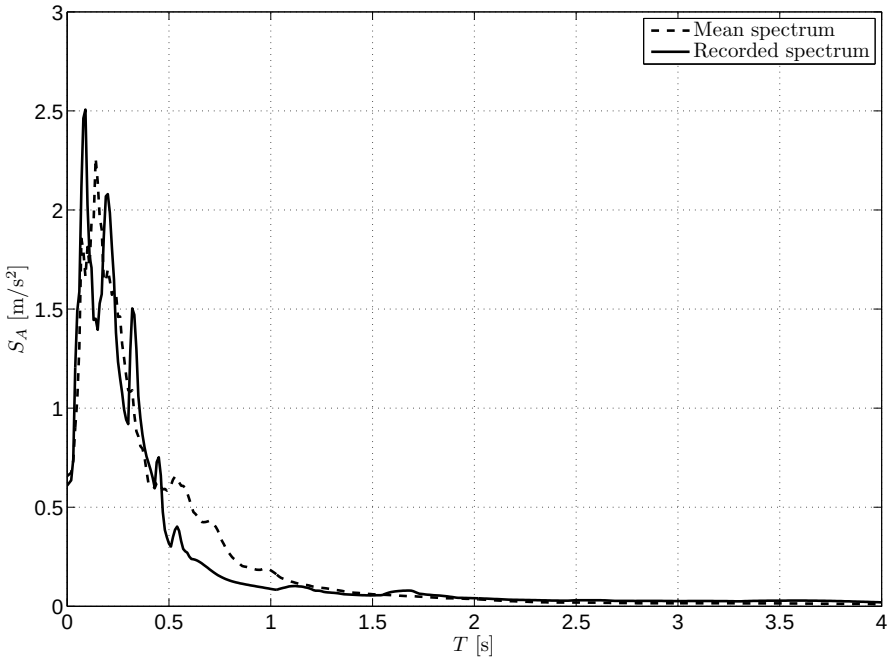

Figure B.1: $T_R = 475\,\text{years}$

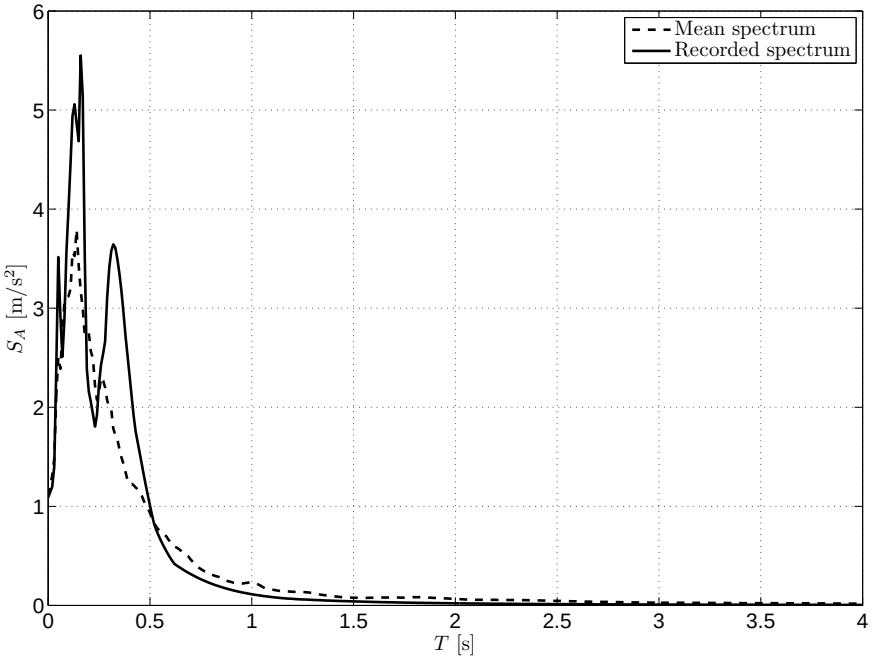

Figure B.2: $T_R = 1000\,\text{years}$

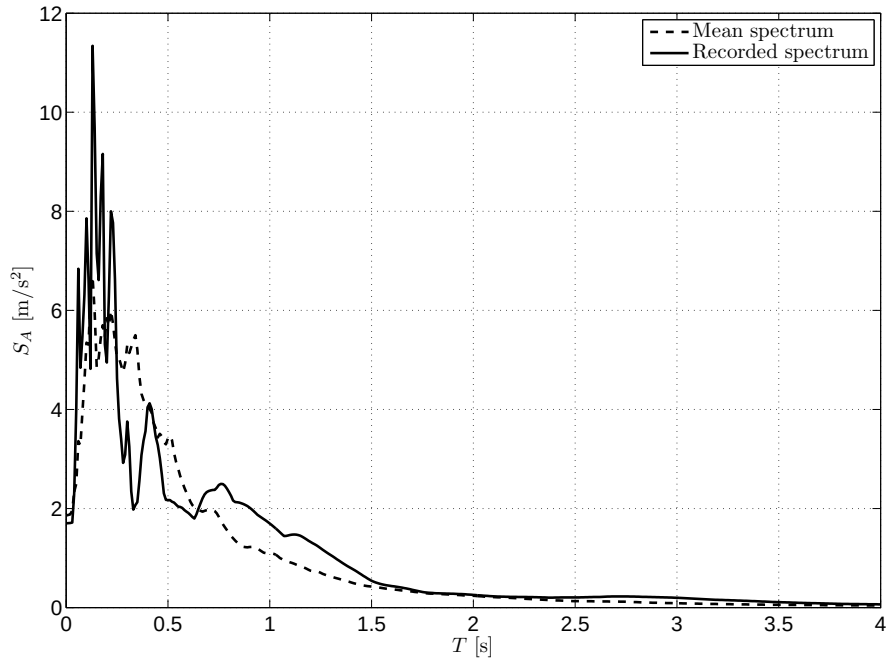

Figure B.3: $T_R = 3000\,\text{years}$

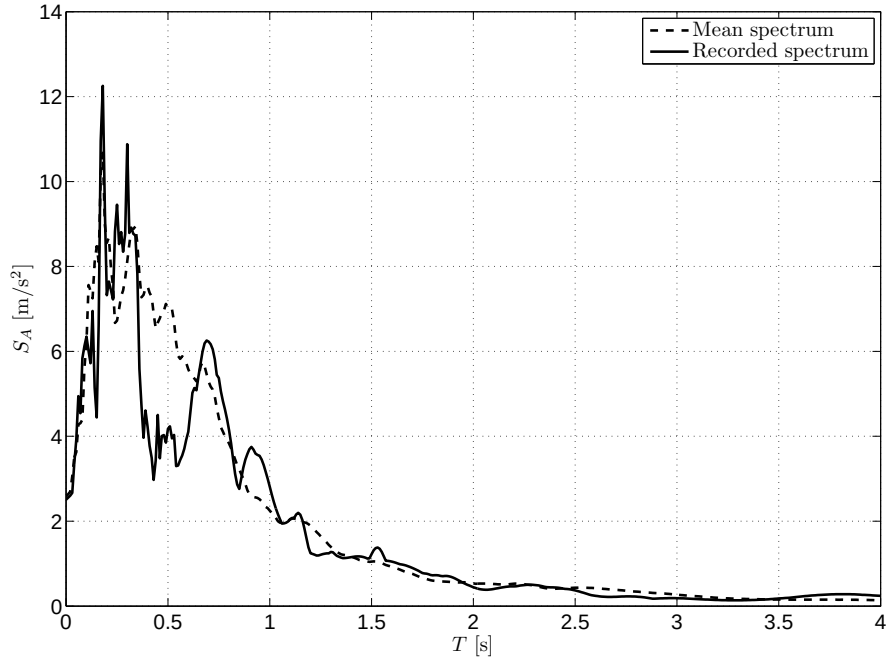

Figure B.4: $T_R = 10\,000\,\text{years}$

B.3 Fourier spectra of simulated accelerograms

The Fourier spectrum for the simulated accelerograms are shown below.

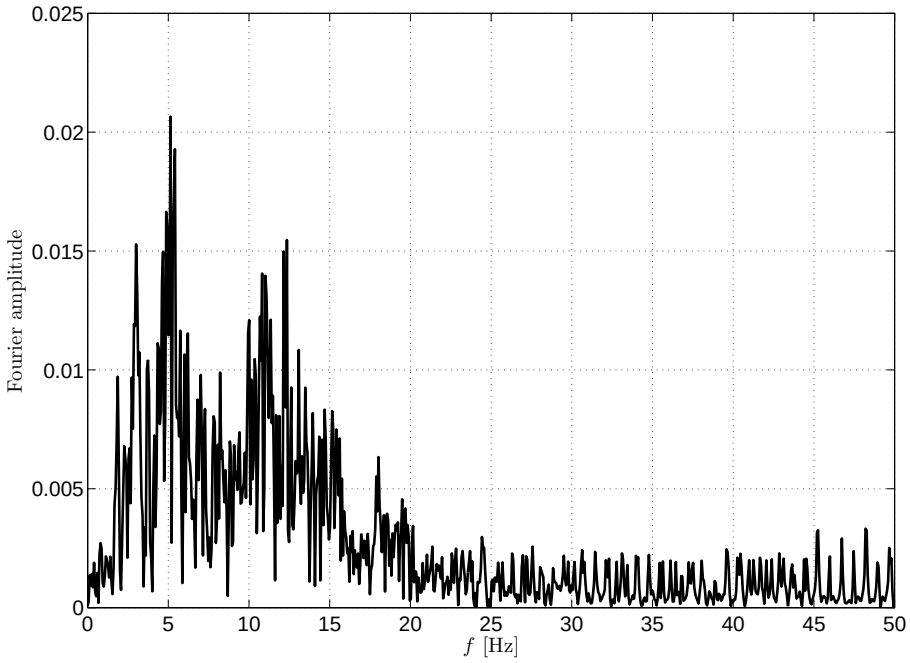

Figure B.5: $T_R = 475\,\text{years}$

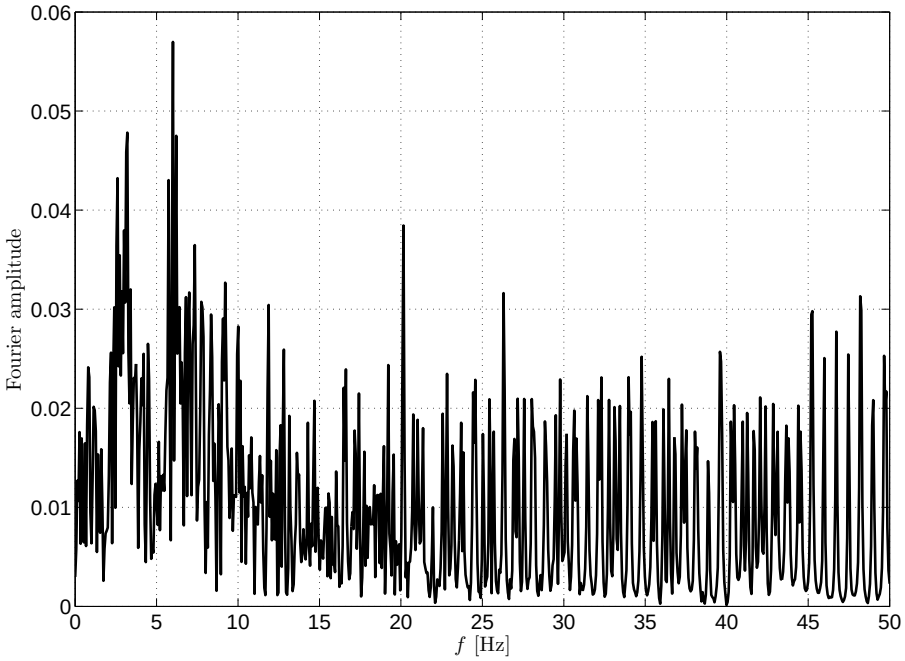

Figure B.6: $T_R = 1000\,\text{years}$

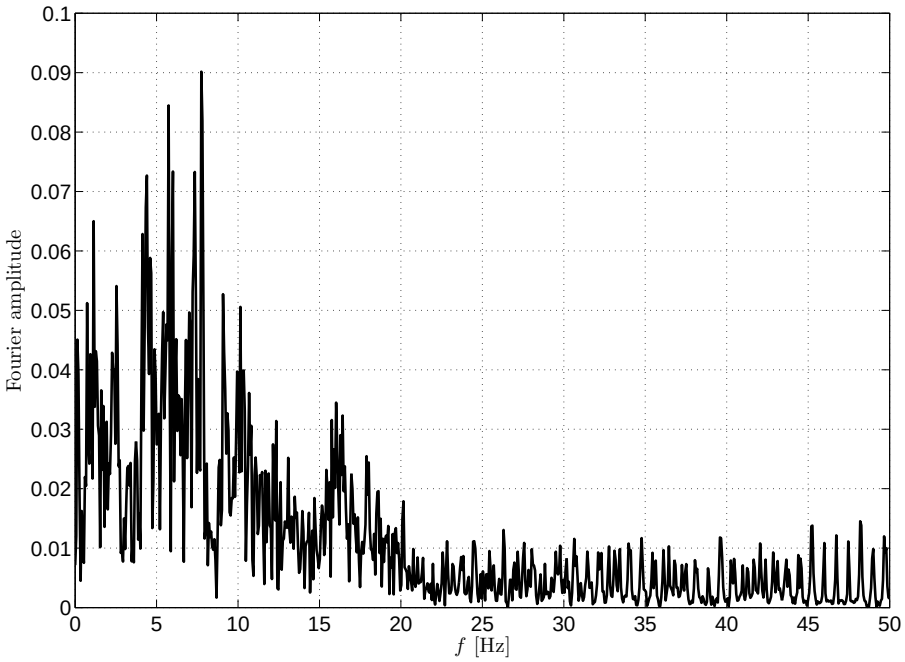

Figure B.7: $T_R = 3000\,\text{years}$

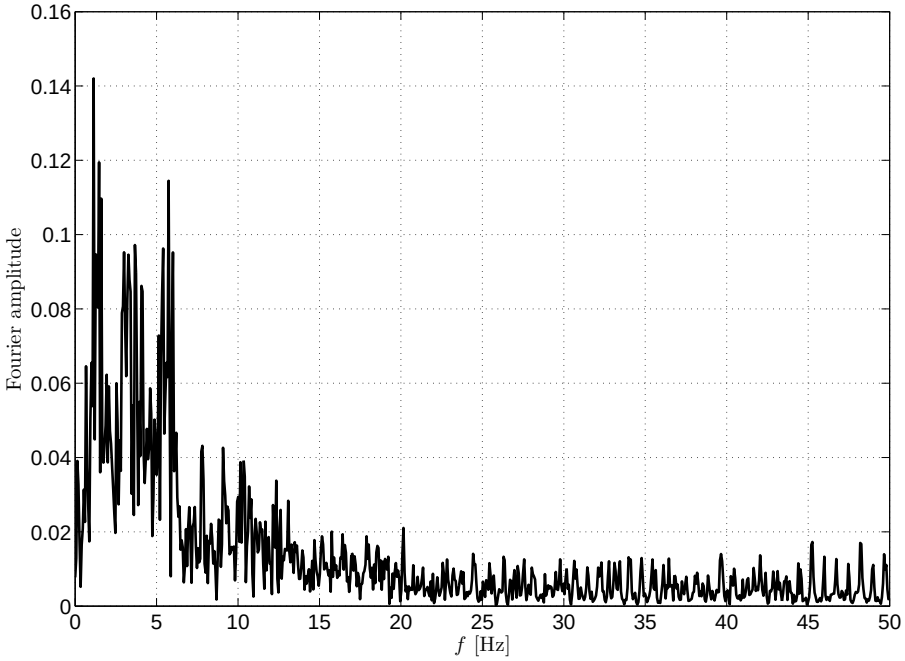

Figure B.8: $T_R = 10\,000\,\text{years}$

C Shaft displacement

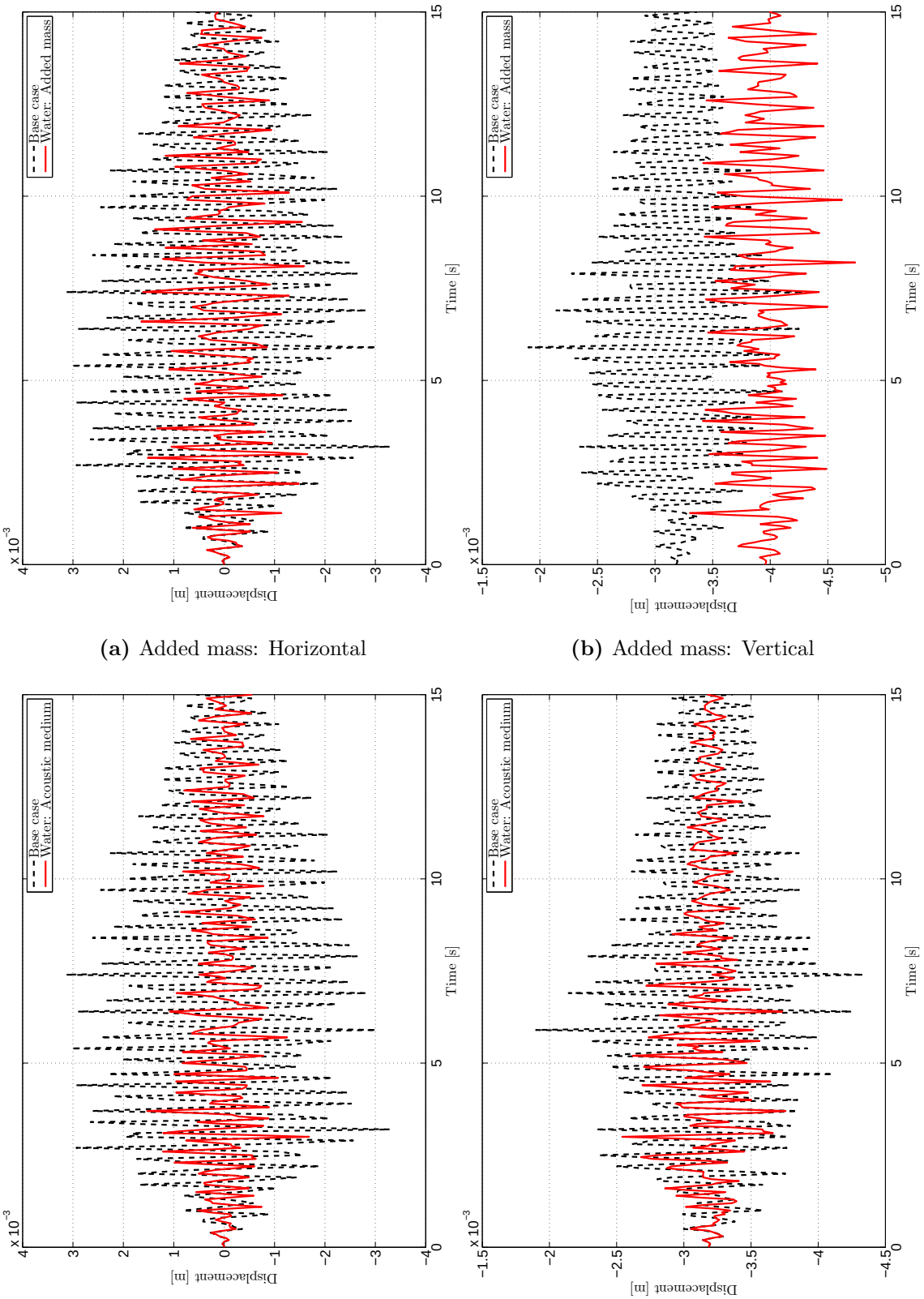

(a) Added mass: Horizontal

(b) Added mass: Vertical

(c) Acoustic: Horizontal

(d) Acoustic: Vertical

Figure C.1: $T_R = 475$ years

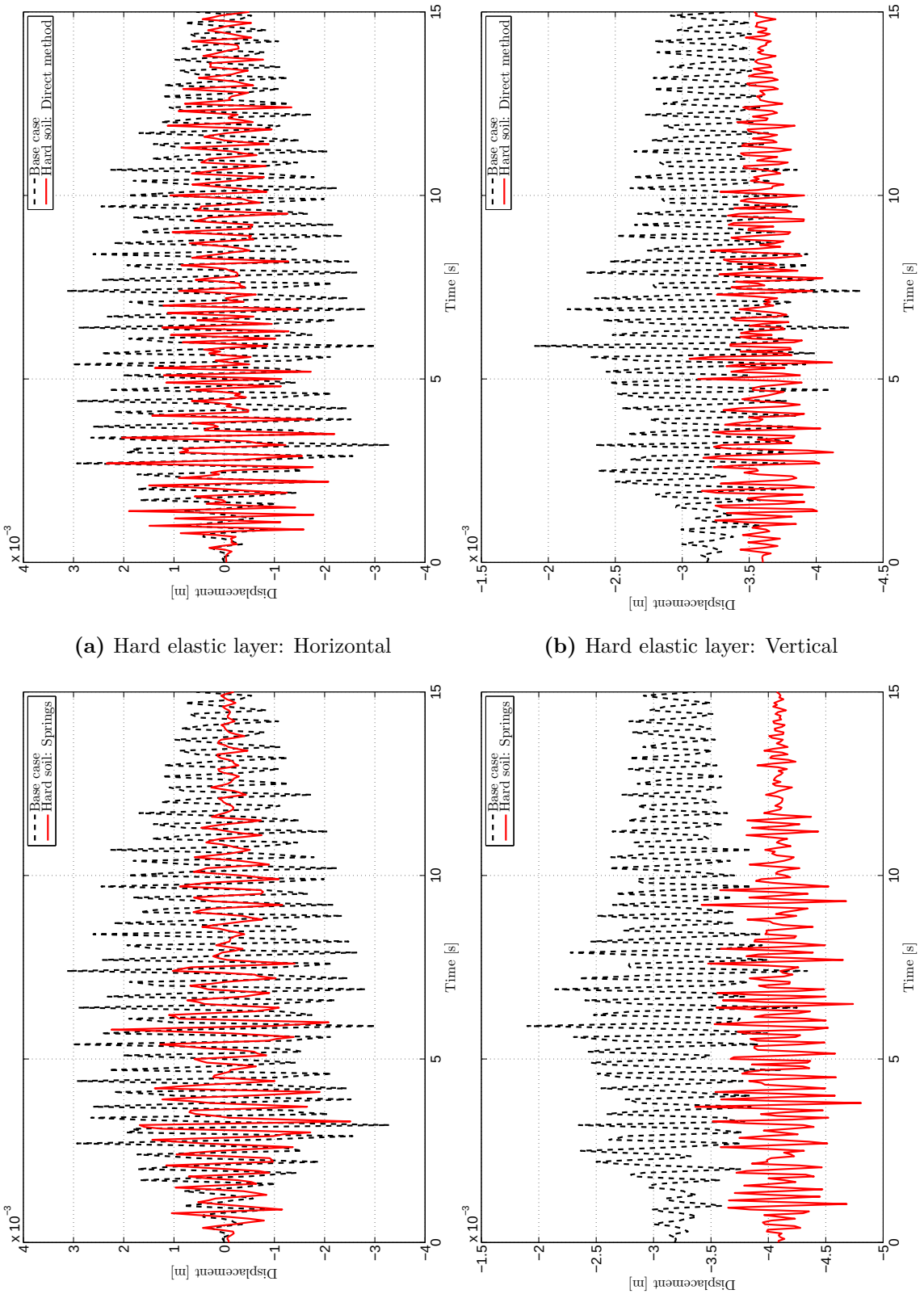

(a) Hard elastic layer: Horizontal

(b) Hard elastic layer: Vertical

(c) Hard soil springs: Horizontal

(d) Hard soil springs: Vertical

Figure C.2: $T_R = 475$ years

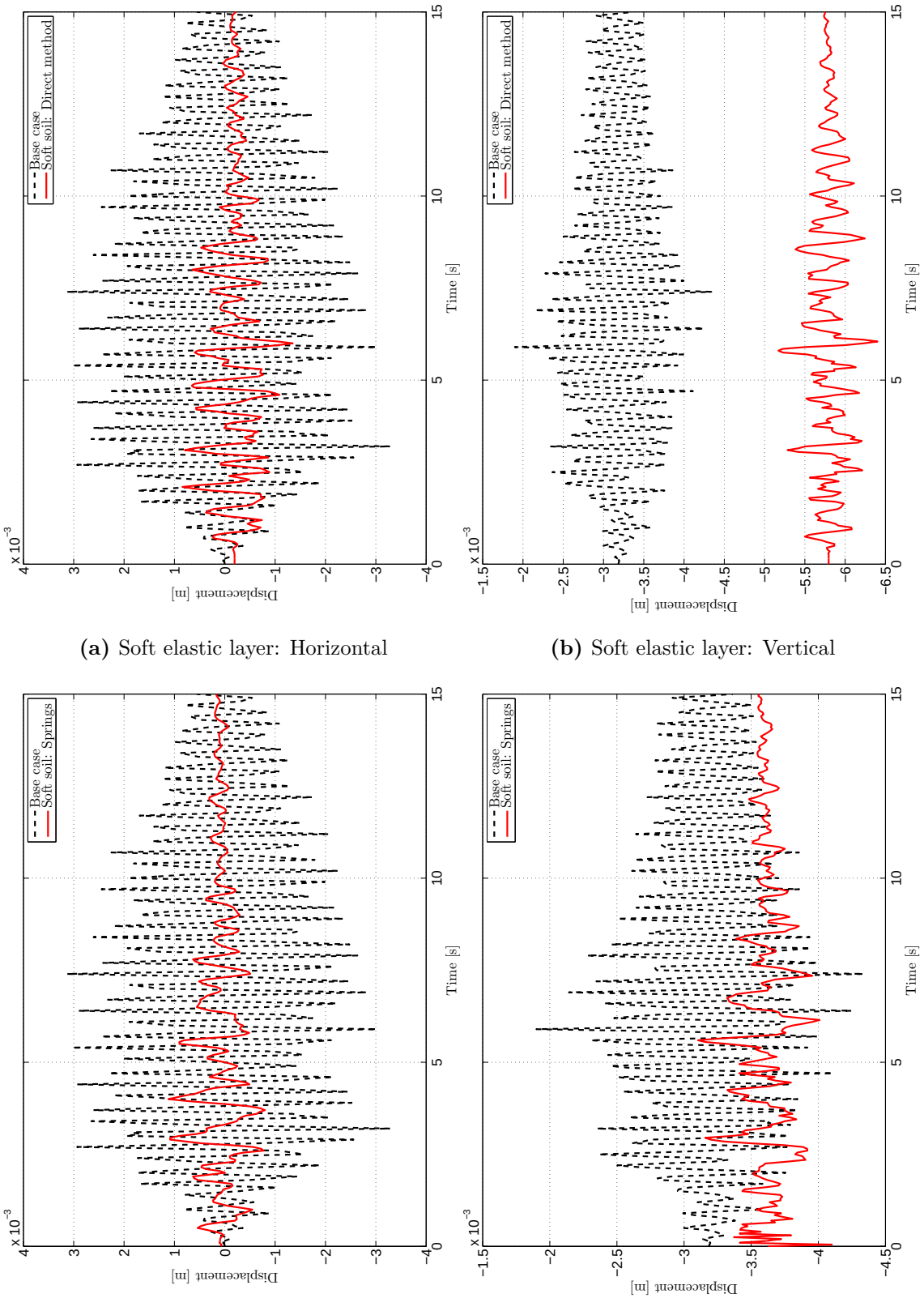

(a) Soft elastic layer: Horizontal

(b) Soft elastic layer: Vertical

(c) Soft soil springs: Horizontal

(d) Soft soil springs: Vertical

Figure C.3: $T_R = 475$ years

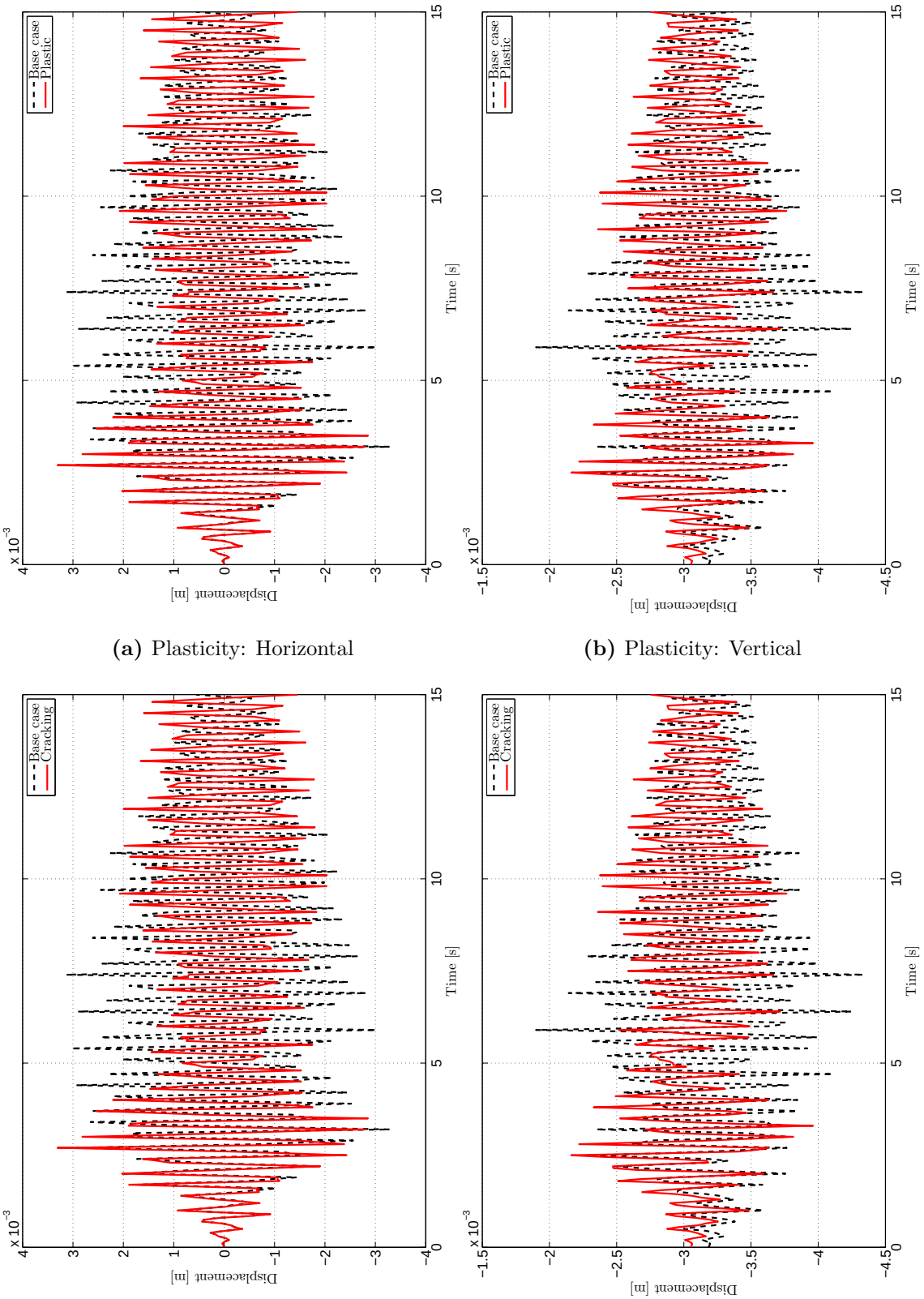

(a) Plasticity: Horizontal

(b) Plasticity: Vertical

(c) Cracking: Horizontal

(d) Cracking: Vertical

Figure C.4: $T_R = 475$ years

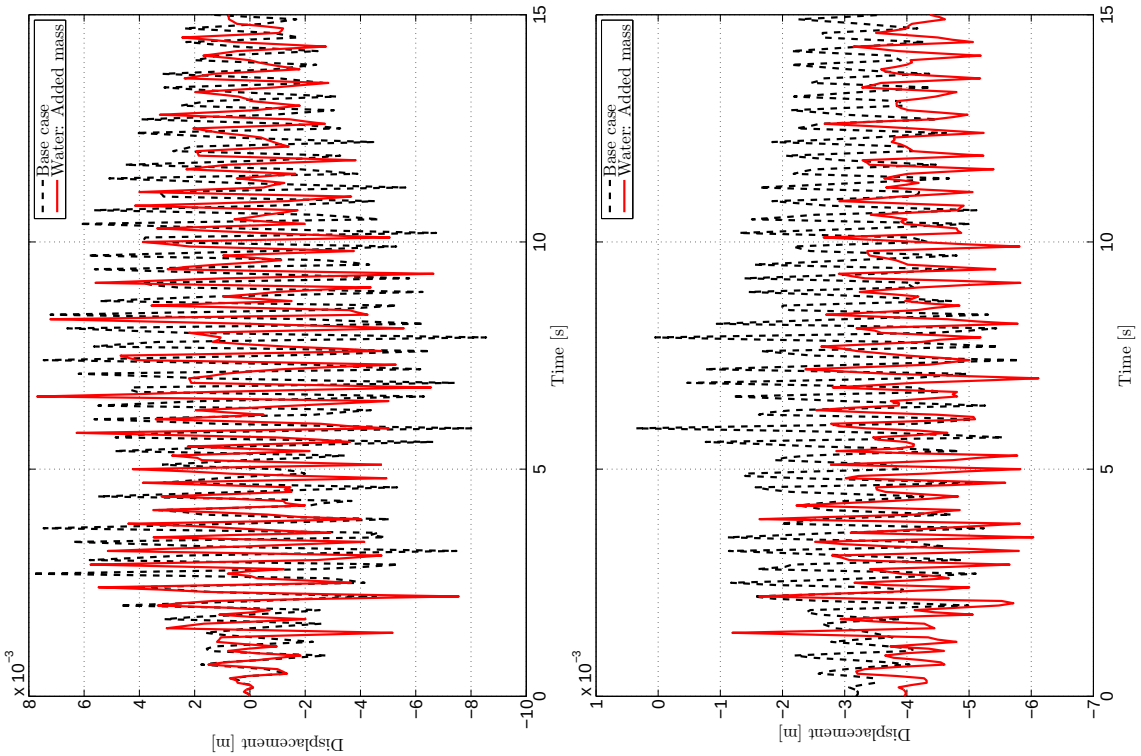

(a) Added mass: Horizontal

(b) Added mass: Vertical

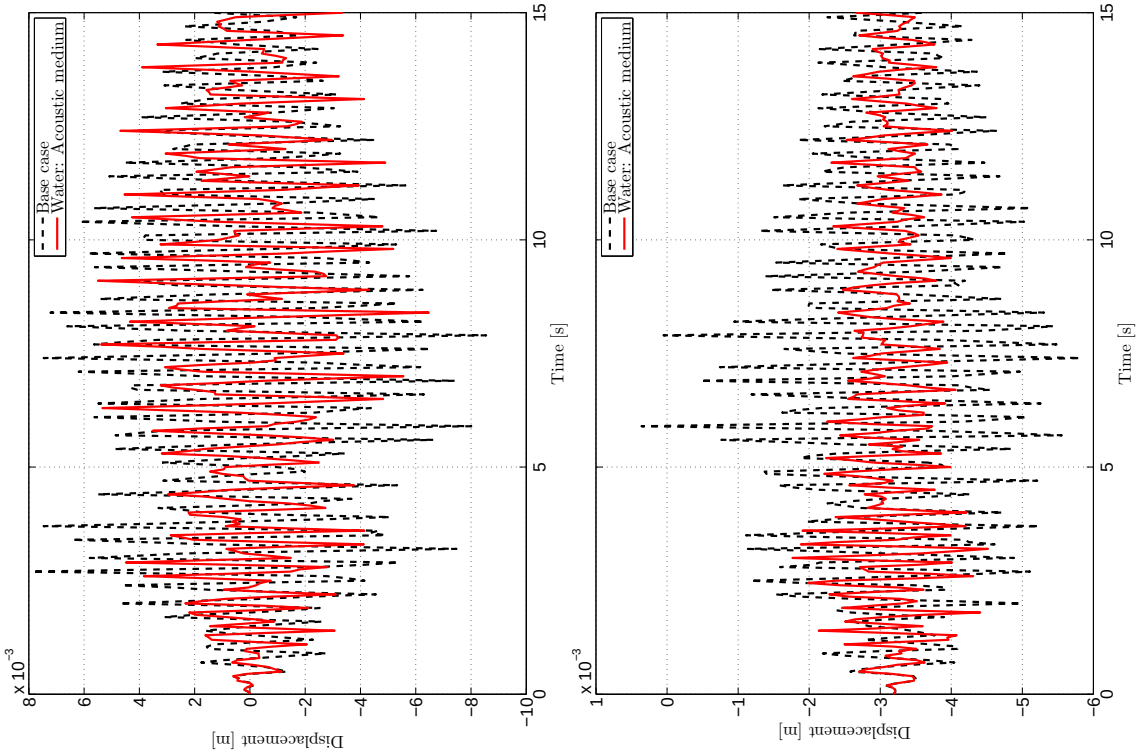

(c) Acoustic: Horizontal

(d) Acoustic: Vertical

Figure C.5: $T_R = 1000\,\text{years}$

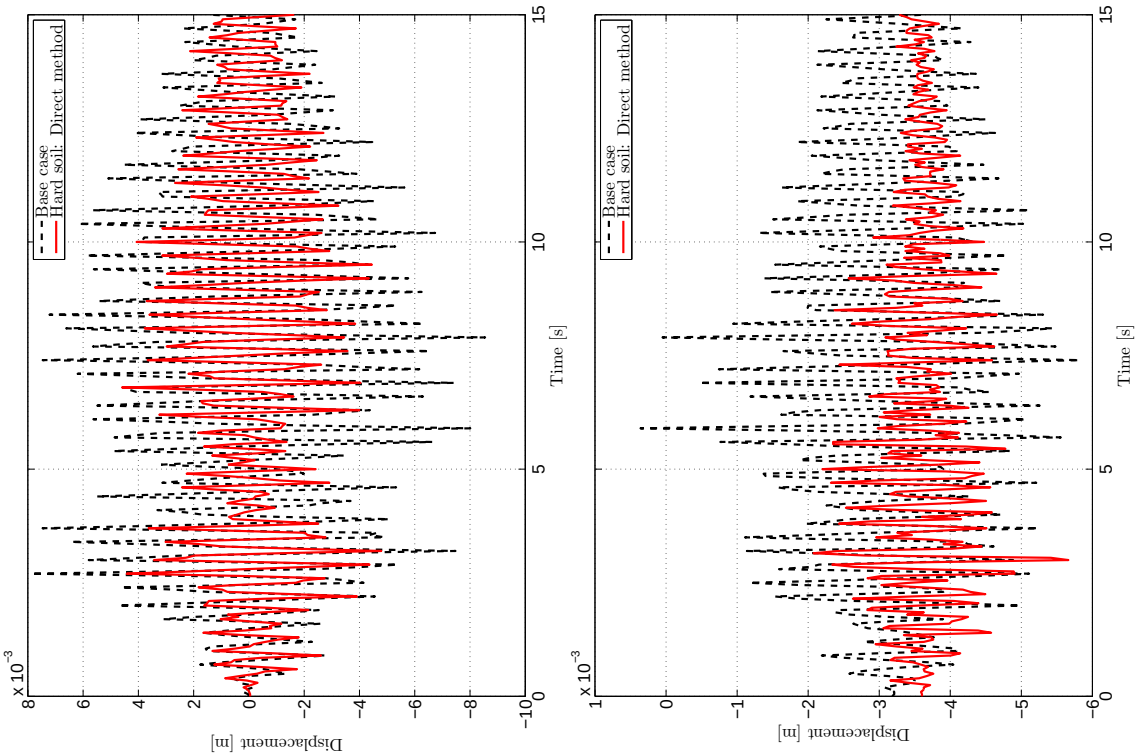

(a) Hard elastic layer: Horizontal

(b) Hard elastic layer: Vertical

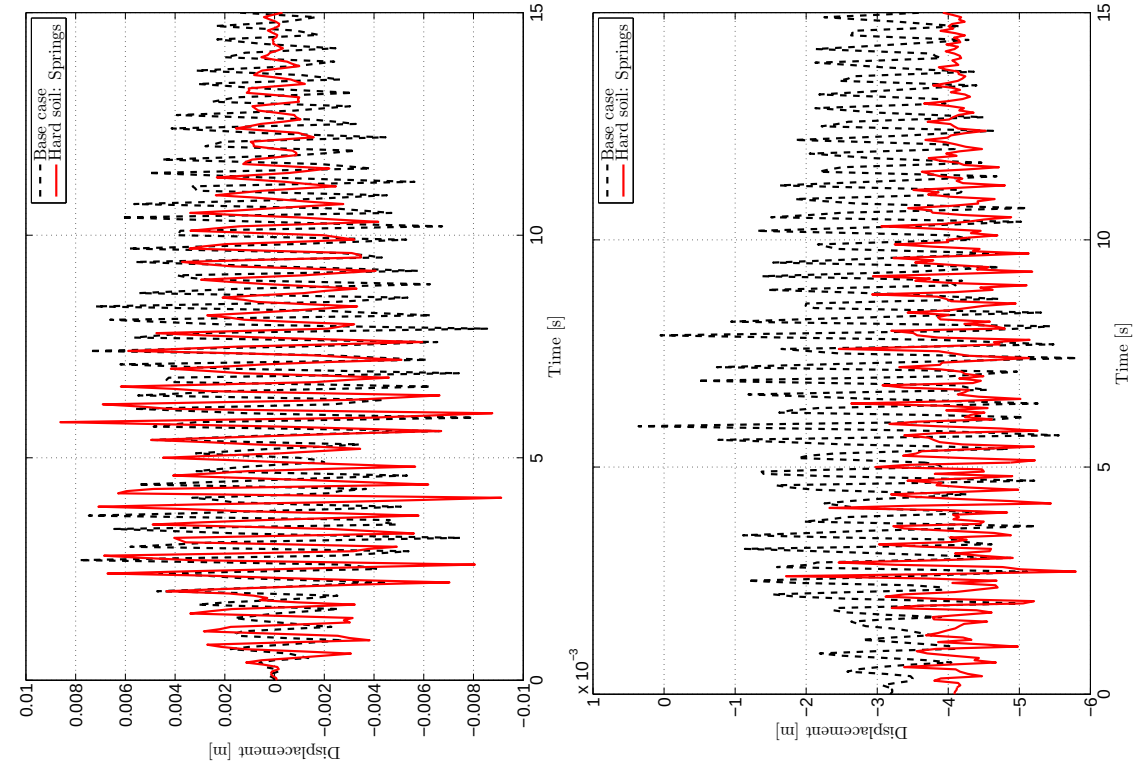

(c) Hard soil springs: Horizontal

(d) Hard soil springs: Vertical

Figure C.6: $T_R = 1000\,\text{years}$

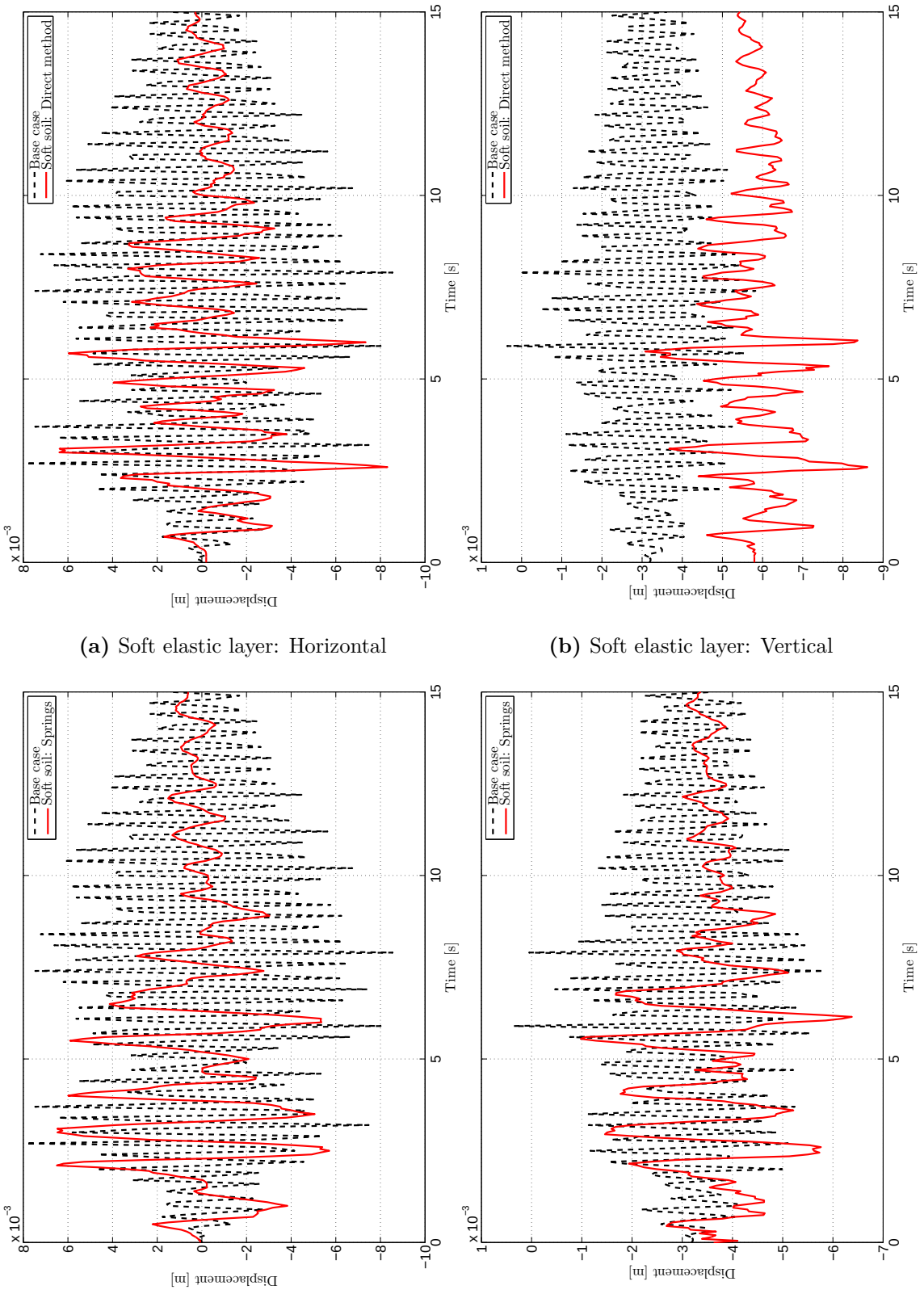

(a) Soft elastic layer: Horizontal

(b) Soft elastic layer: Vertical

(c) Soft soil springs: Horizontal

(d) Soft soil springs: Vertical

Figure C.7: $T_R = 1000\,\text{years}$

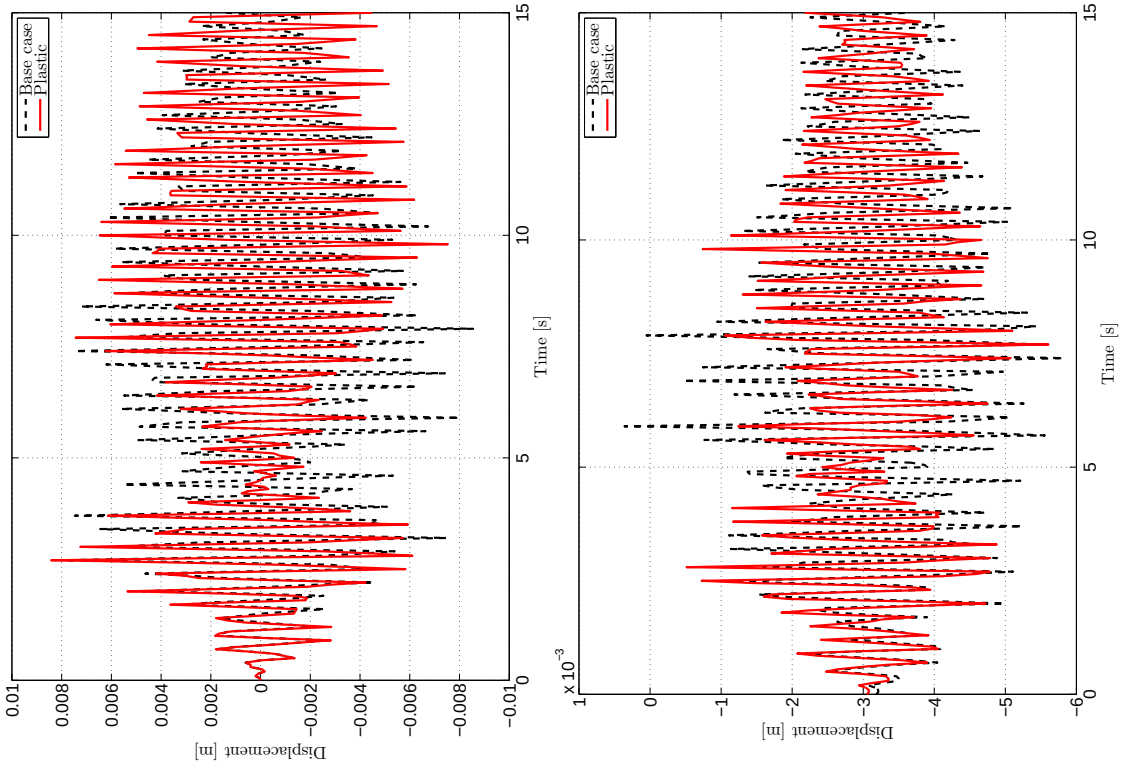

(a) Plasticity: Horizontal

(b) Plasticity: Vertical

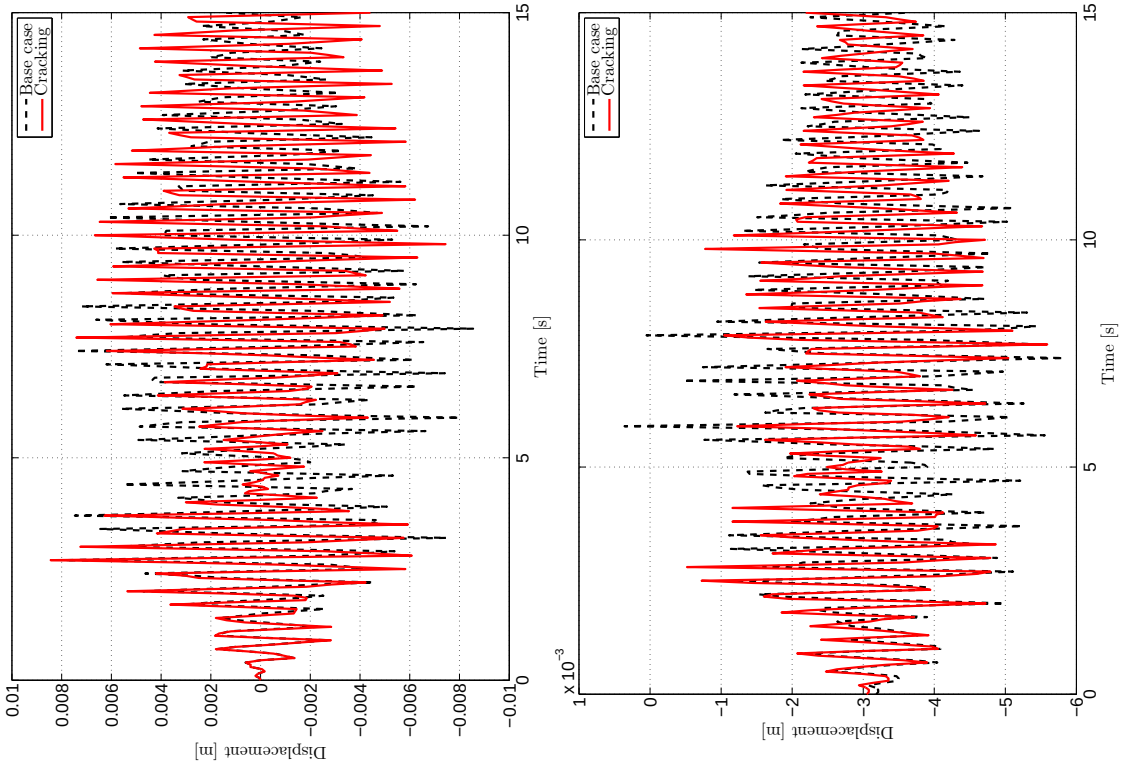

(c) Cracking: Horizontal

(d) Cracking: Vertical

Figure C.8: $T_R = 1000\,\text{years}$

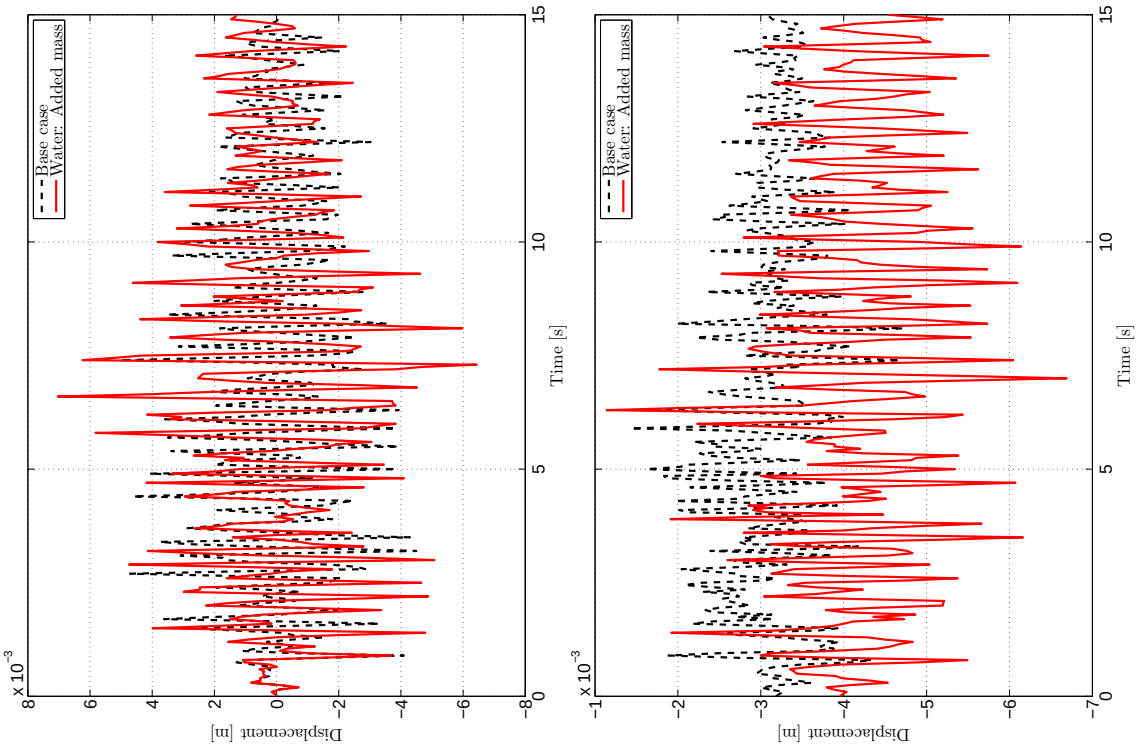

(a) Added mass: Horizontal

(b) Added mass: Vertical

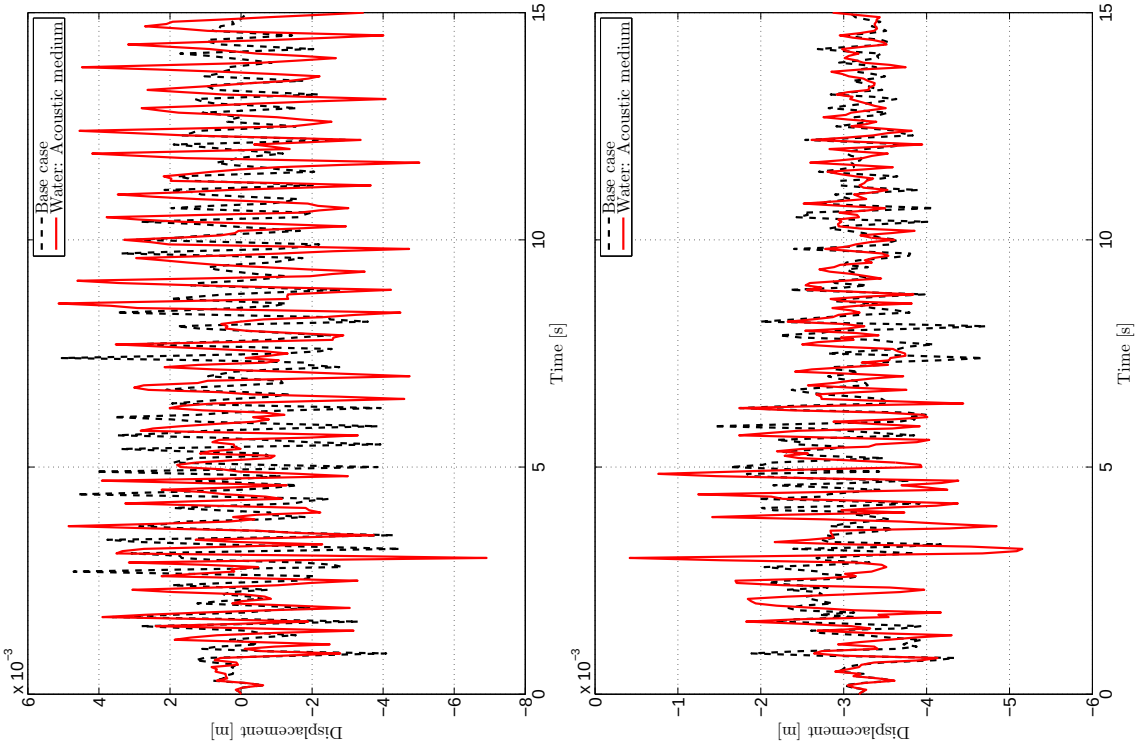

(c) Acoustic: Horizontal

(d) Acoustic: Vertical

Figure C.9: $T_R = 3000\,\text{years}$

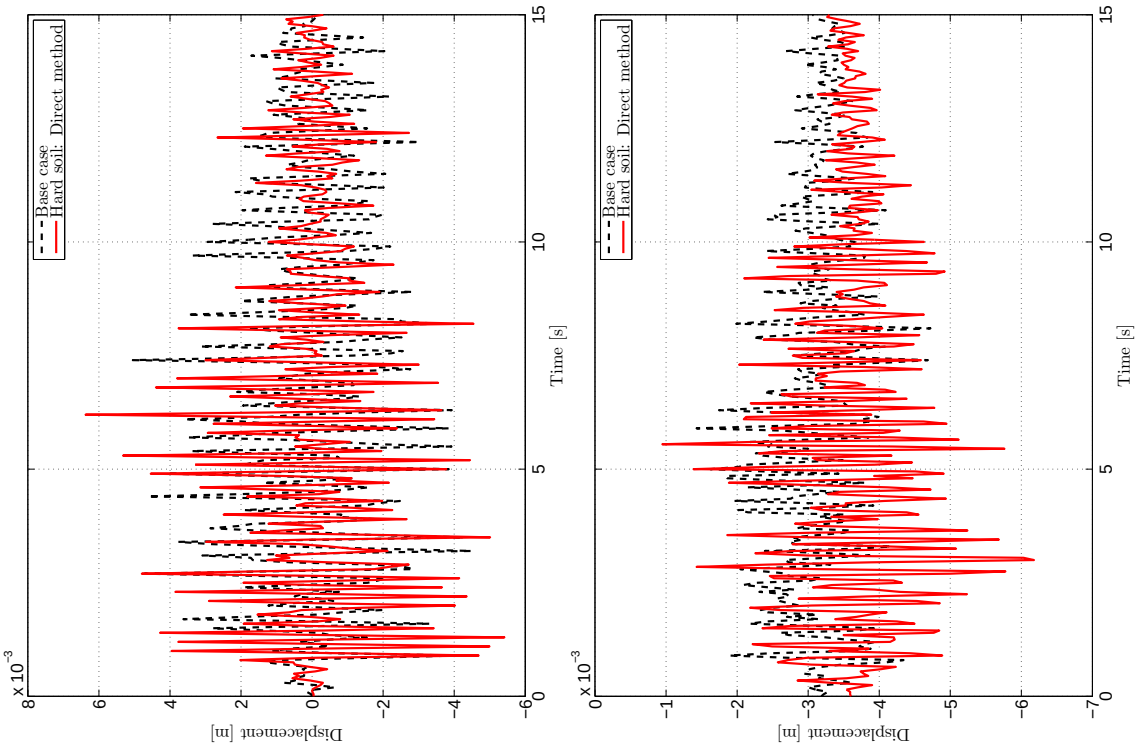

(a) Hard elastic layer: Horizontal

(b) Hard elastic layer: Vertical

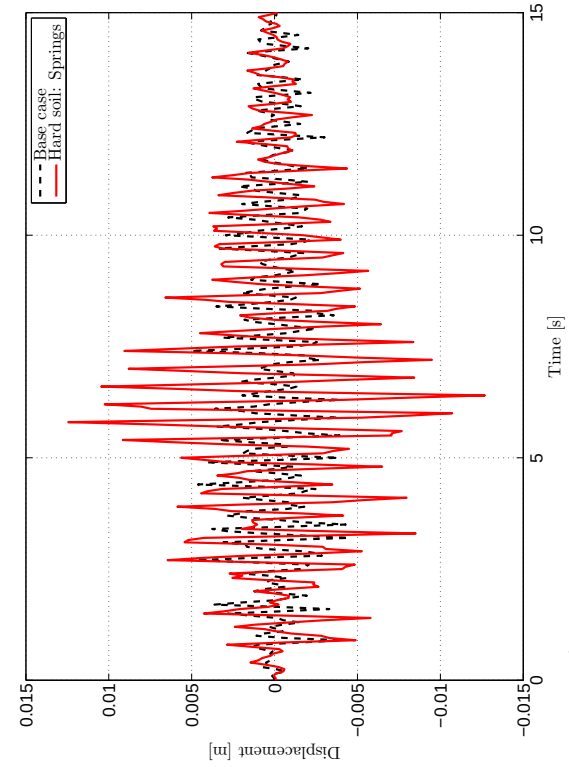

(c) Hard soil springs: Horizontal

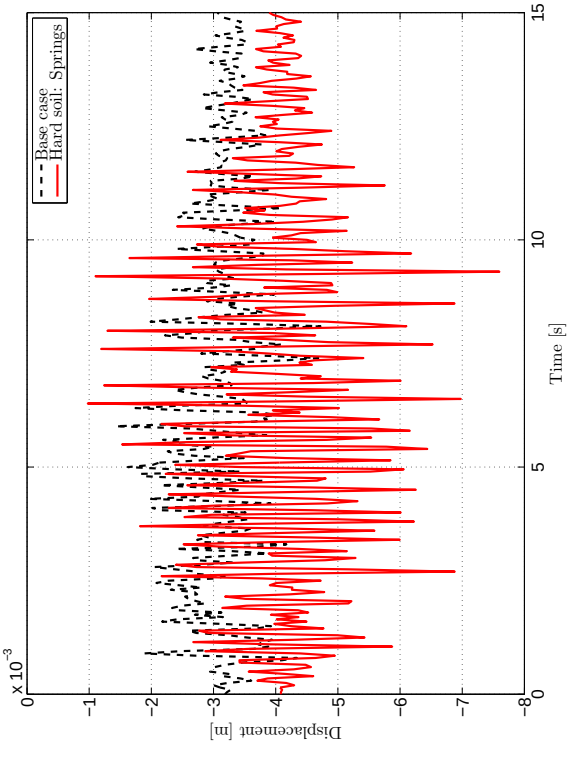

(d) Hard soil springs: Vertical

Figure C.10: $T_R = 3000$ years

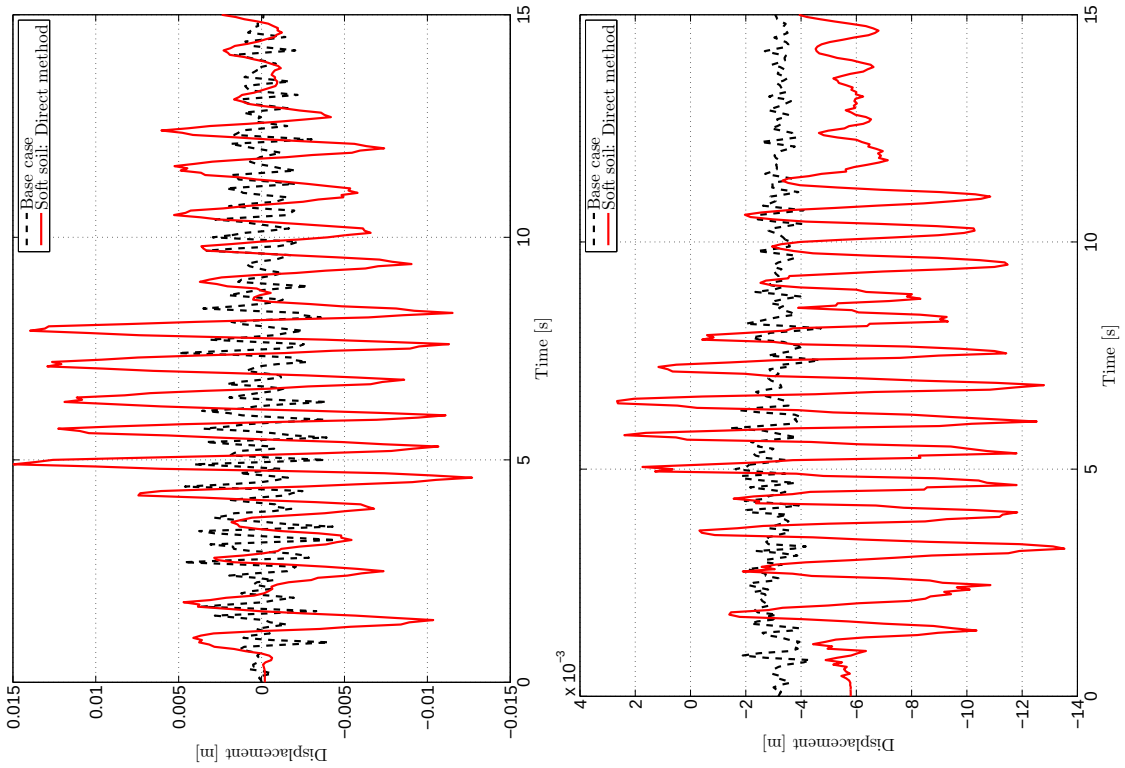

(a) Soft elastic layer: Horizontal

(b) Soft elastic layer: Vertical

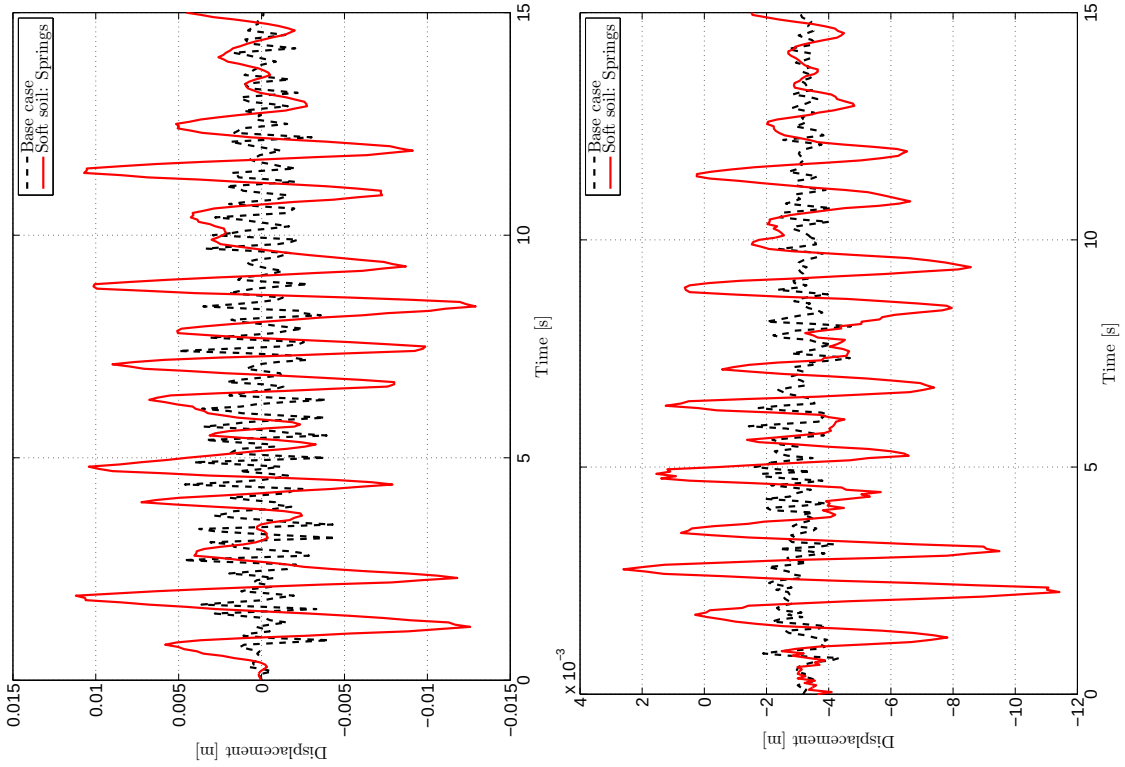

(c) Soft soil springs: Horizontal

(d) Soft soil springs: Vertical

Figure C.11: $T_R = 3000$ years

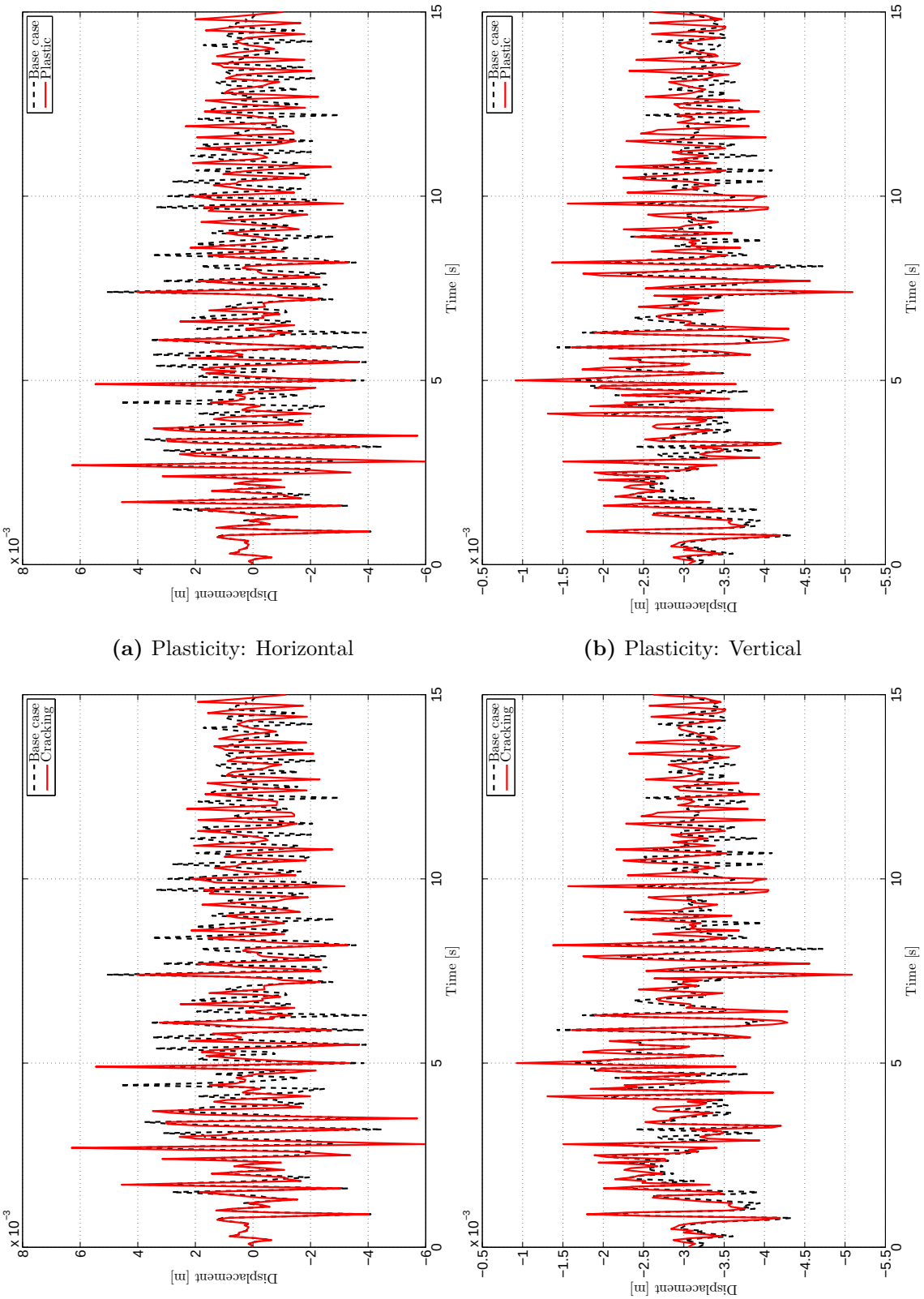

(a) Plasticity: Horizontal

(b) Plasticity: Vertical

(c) Cracking: Horizontal

(d) Cracking: Vertical

Figure C.12: $T_R = 3000$ years

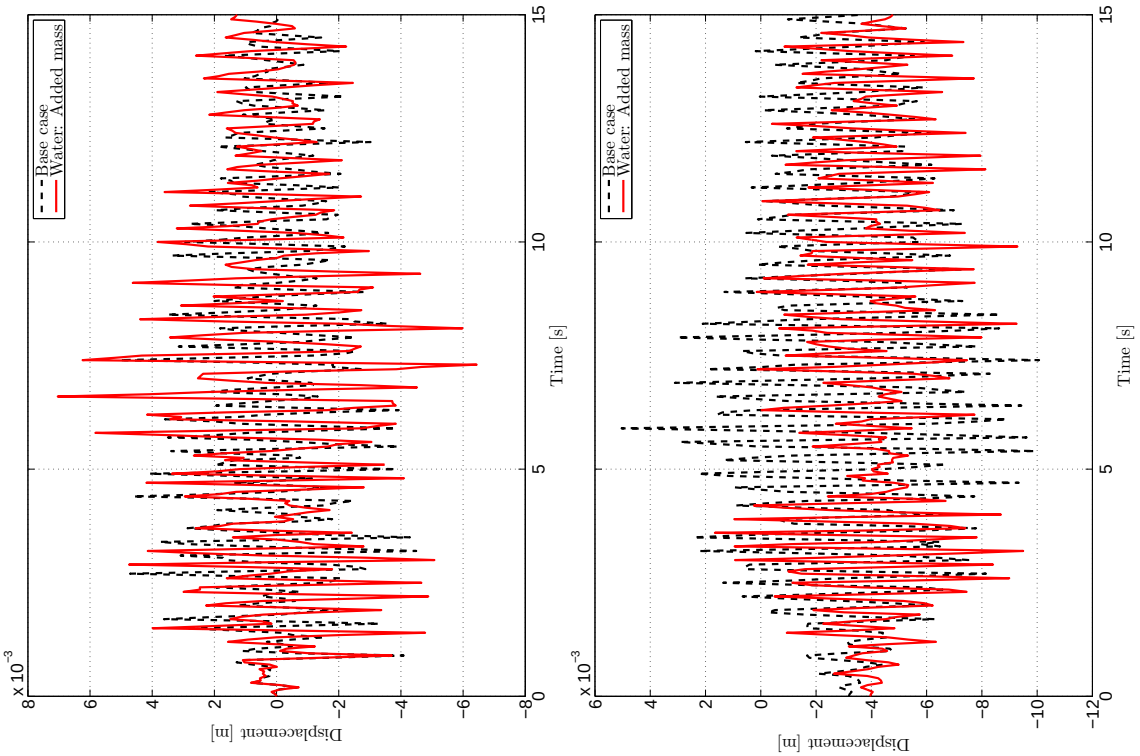

(a) Added mass: Horizontal

(b) Added mass: Vertical

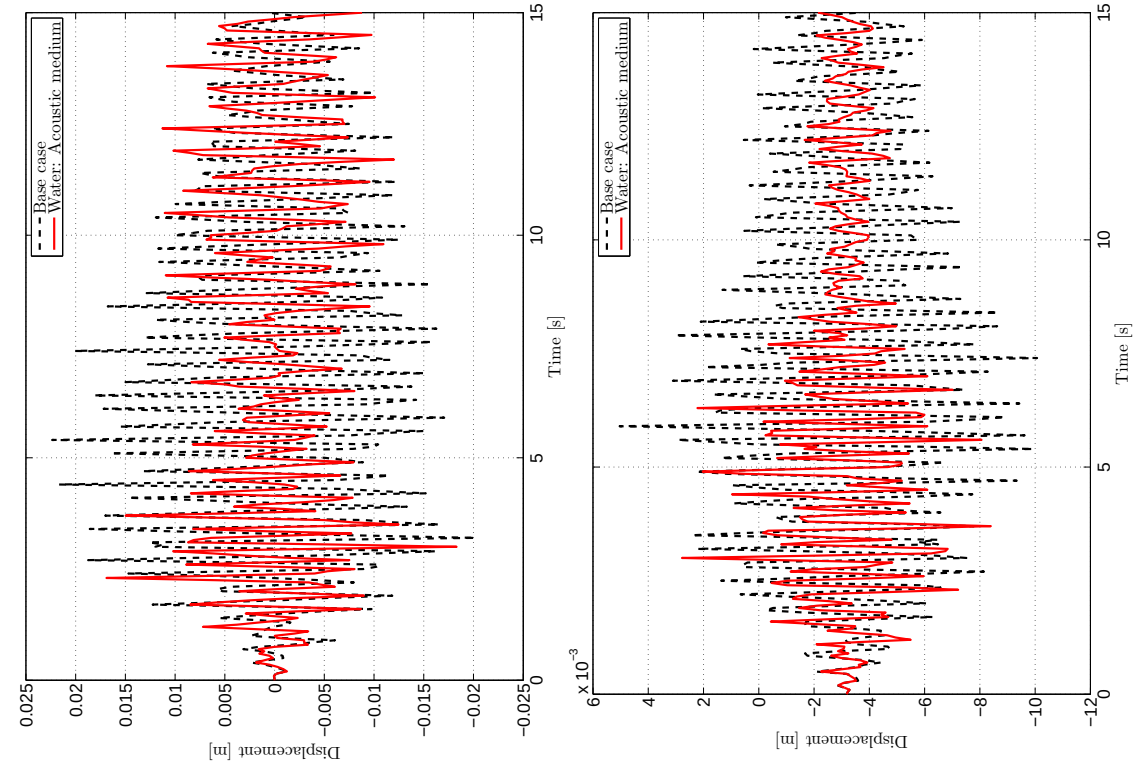

(c) Acoustic: Horizontal

(d) Acoustic: Vertical

Figure C.13: $T_R = 10\,000$ years

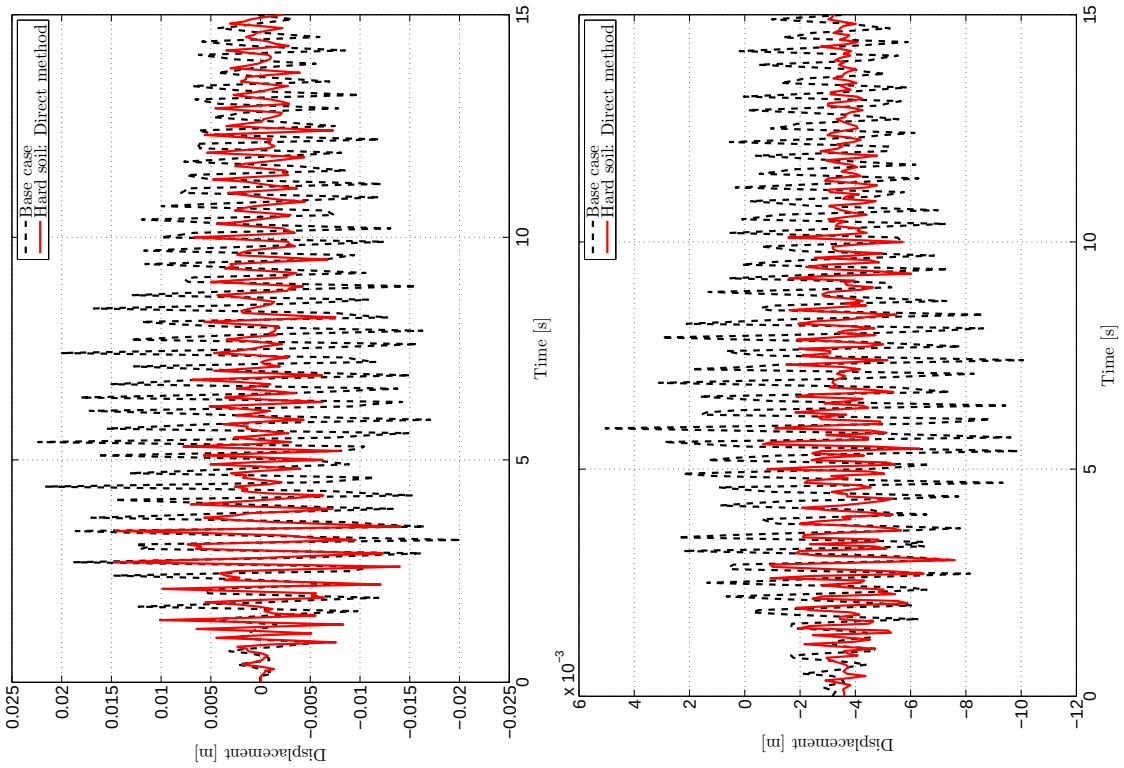

(a) Hard elastic layer: Horizontal

(b) Hard elastic layer: Vertical

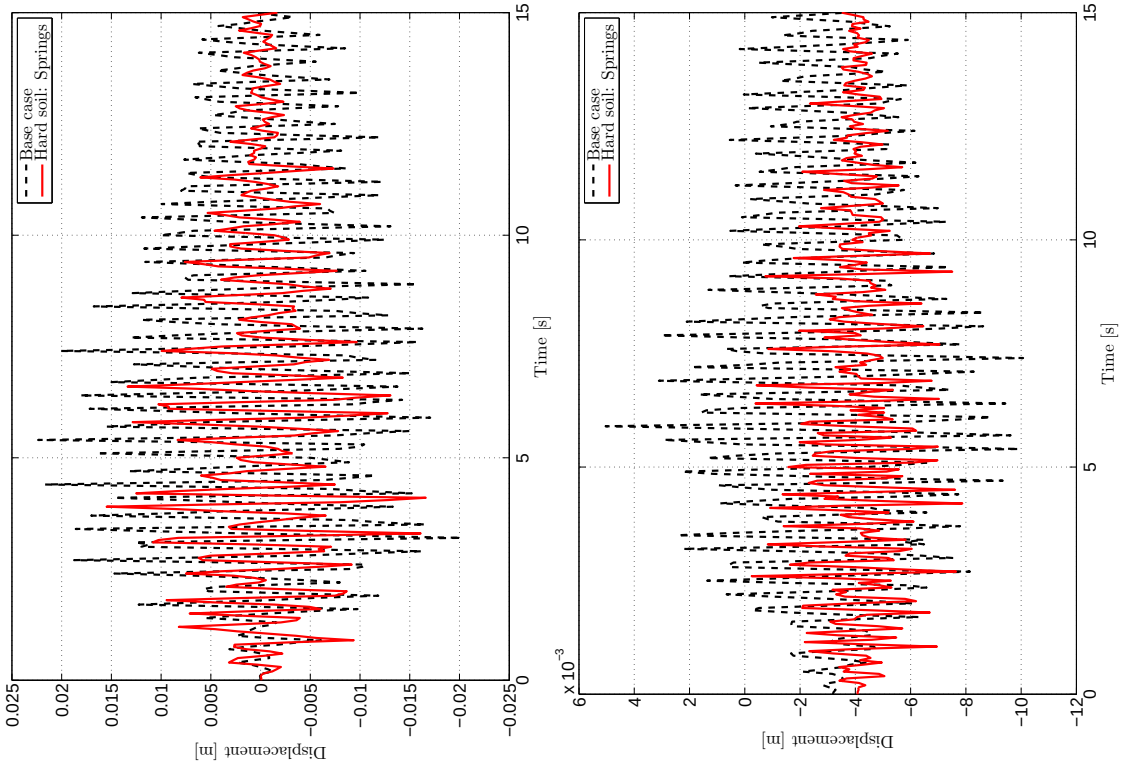

(c) Hard soil springs: Horizontal

(d) Hard soil springs: Vertical

Figure C.14: $T_R = 10\,000$ years

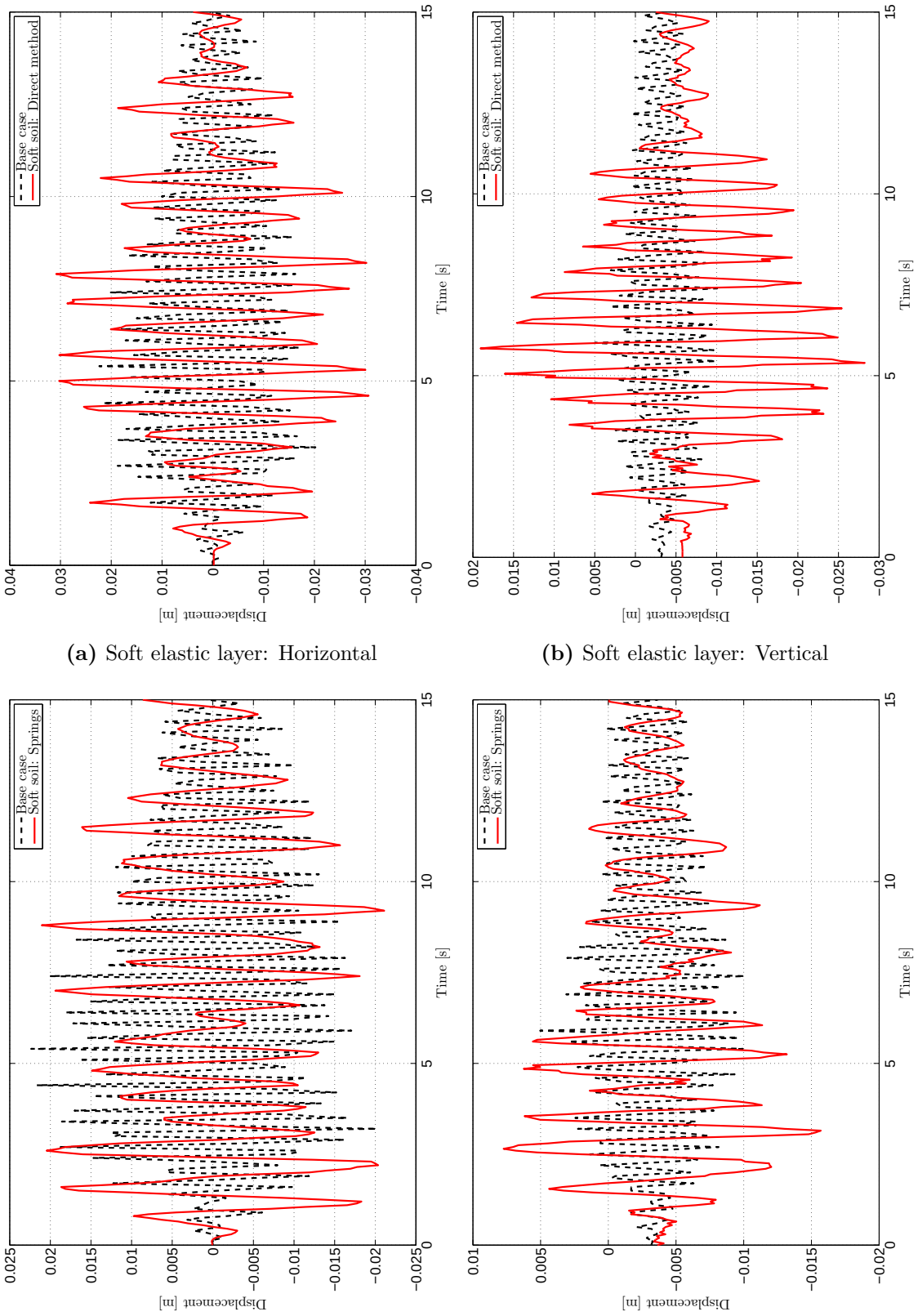

(a) Soft elastic layer: Horizontal

(b) Soft elastic layer: Vertical

(c) Soft soil springs: Horizontal

(d) Soft soil springs: Vertical

Figure C.15: $T_R = 10\,000$ years

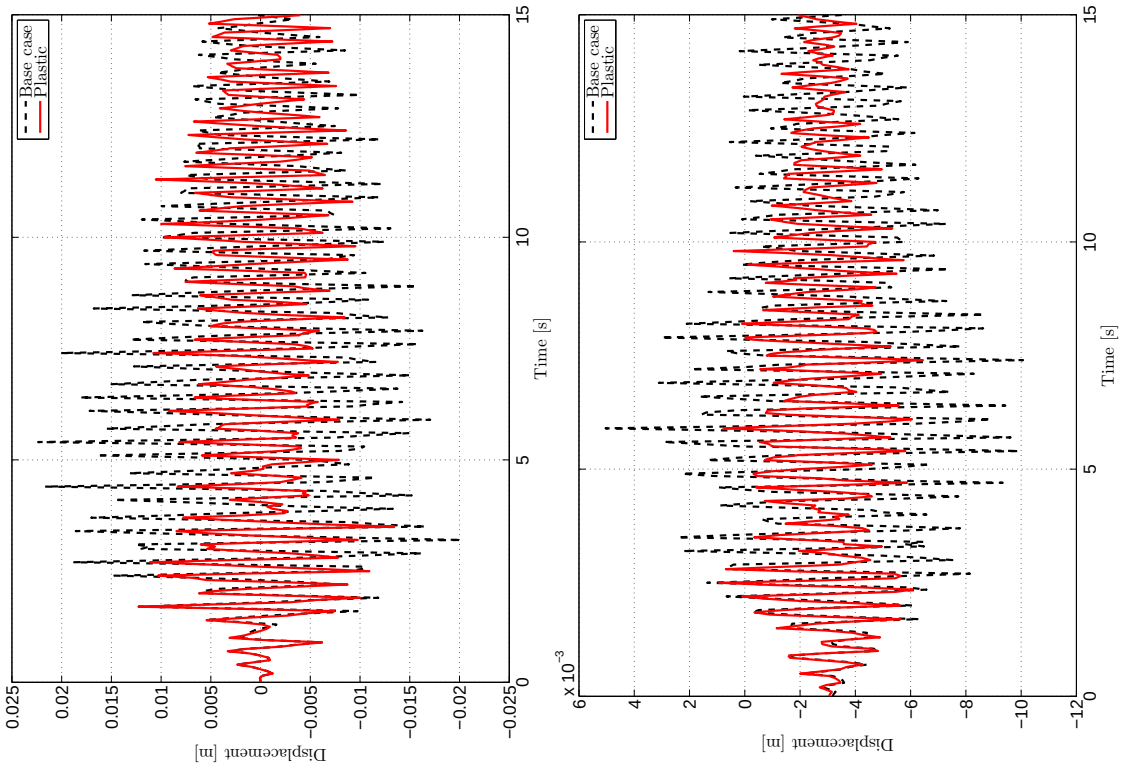

(a) Plasticity: Horizontal

(b) Plasticity: Vertical

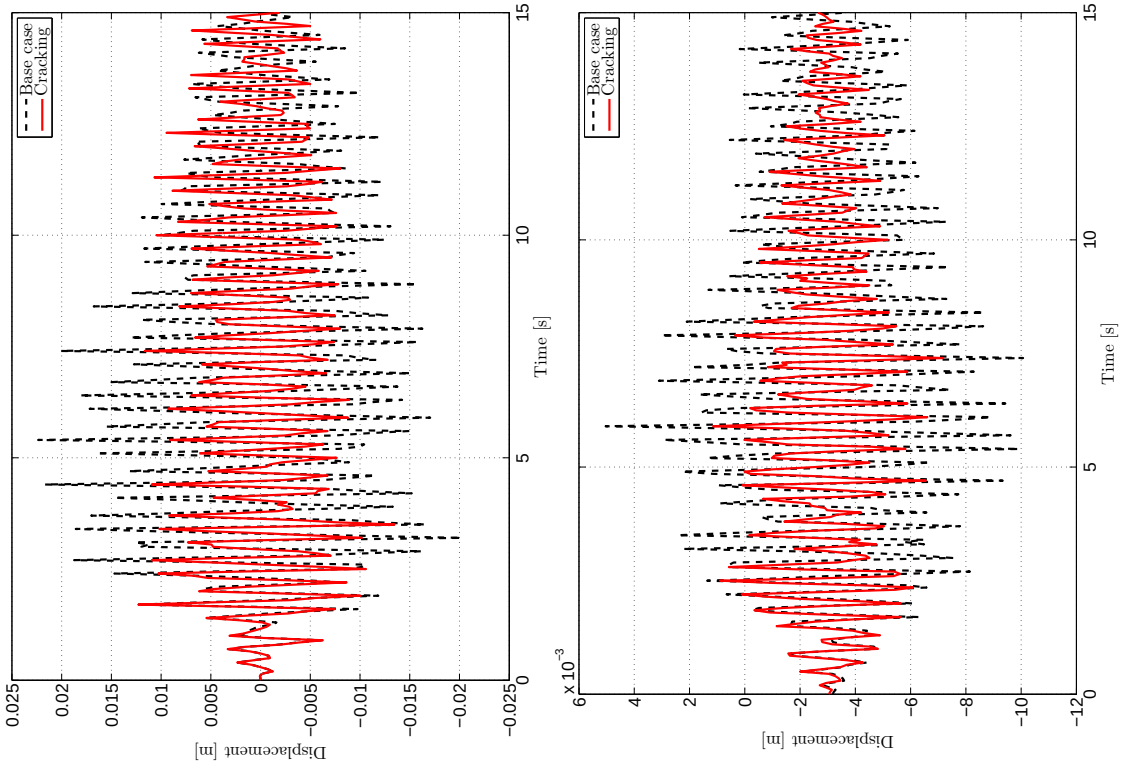

(c) Cracking: Horizontal

(d) Cracking: Vertical

Figure C.16: $T_R = 10\,000$ years

D Capacity checks

D.1 Utilization ratios

The following pages show utilization ratios for the omnipresent reinforcement mesh of $2\phi 20 s150$, as well as the concrete in compression and shear.

Horizontal Reinforcement of shaft, Outer Face

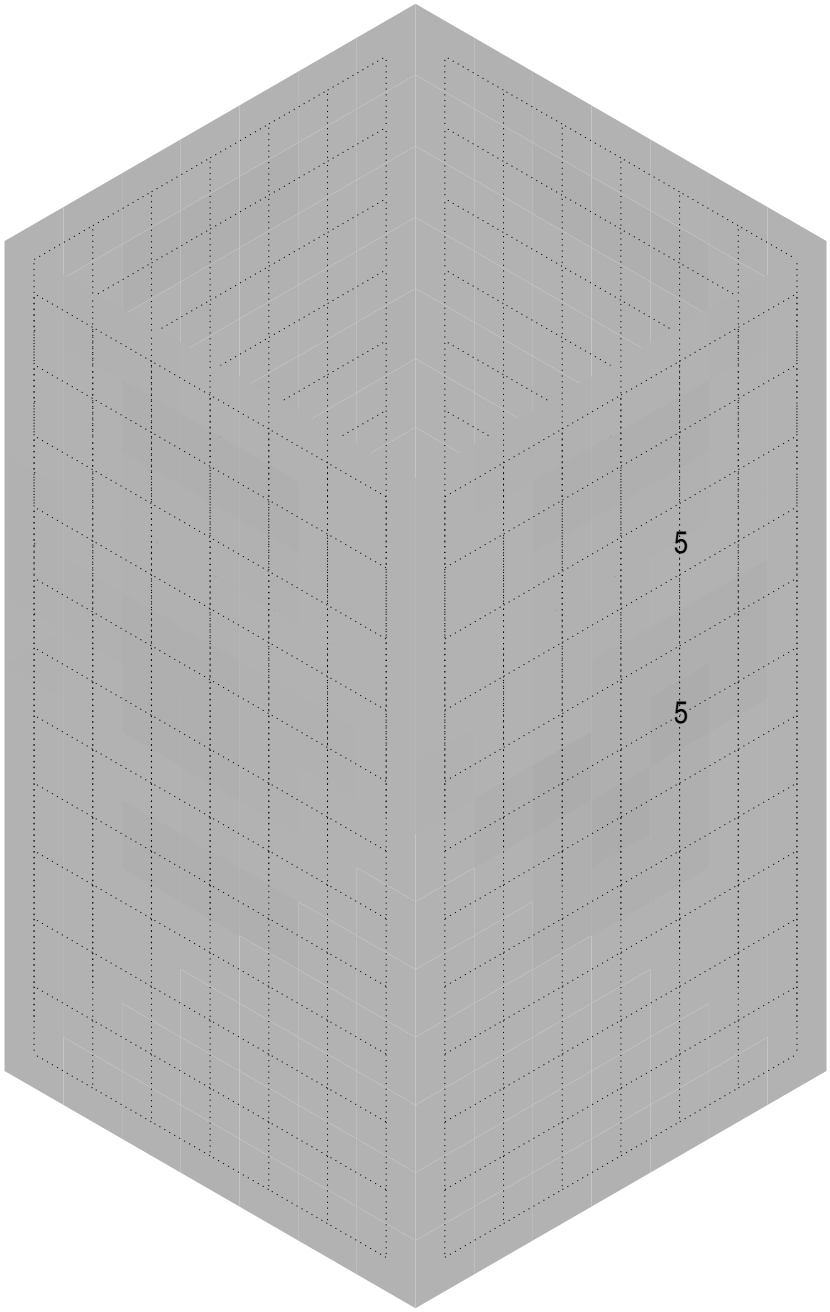

Figure D.1: Maximum = 5%

Horizontal Reinforcement of shaft, Inner Face

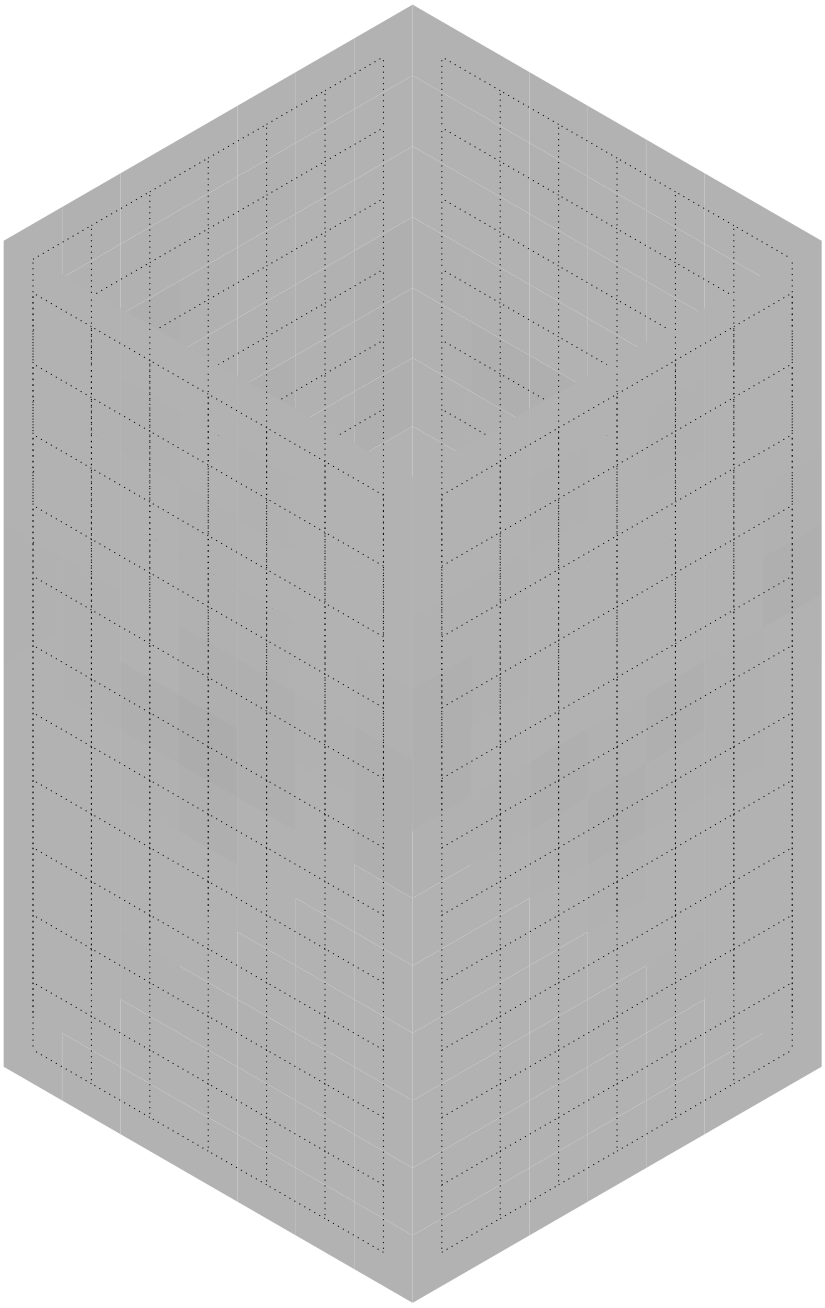

Figure D.2: Maximum = 4%

Vertical Reinforcement of shaft, Outer Face

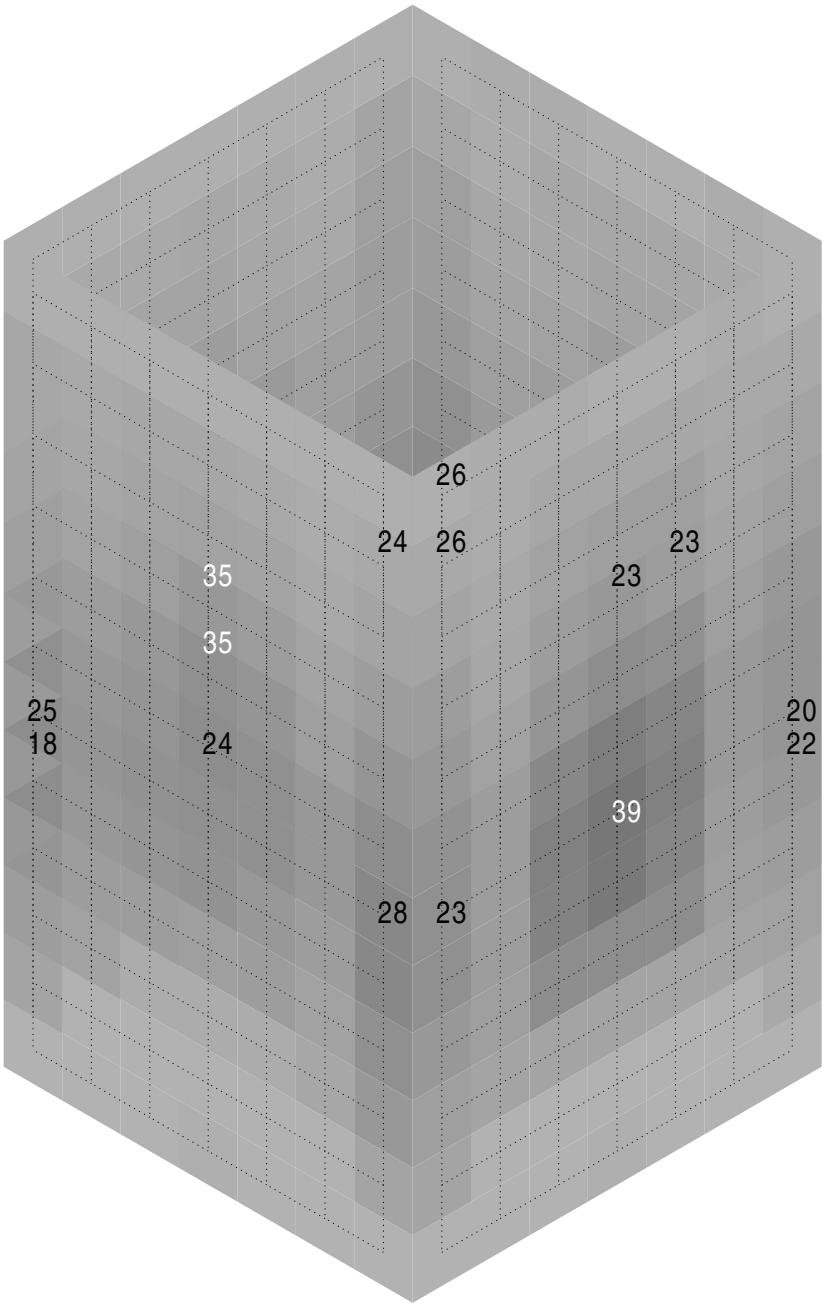

Figure D.3: Maximum = 14%

Vertical Reinforcement of shaft, Inner Face

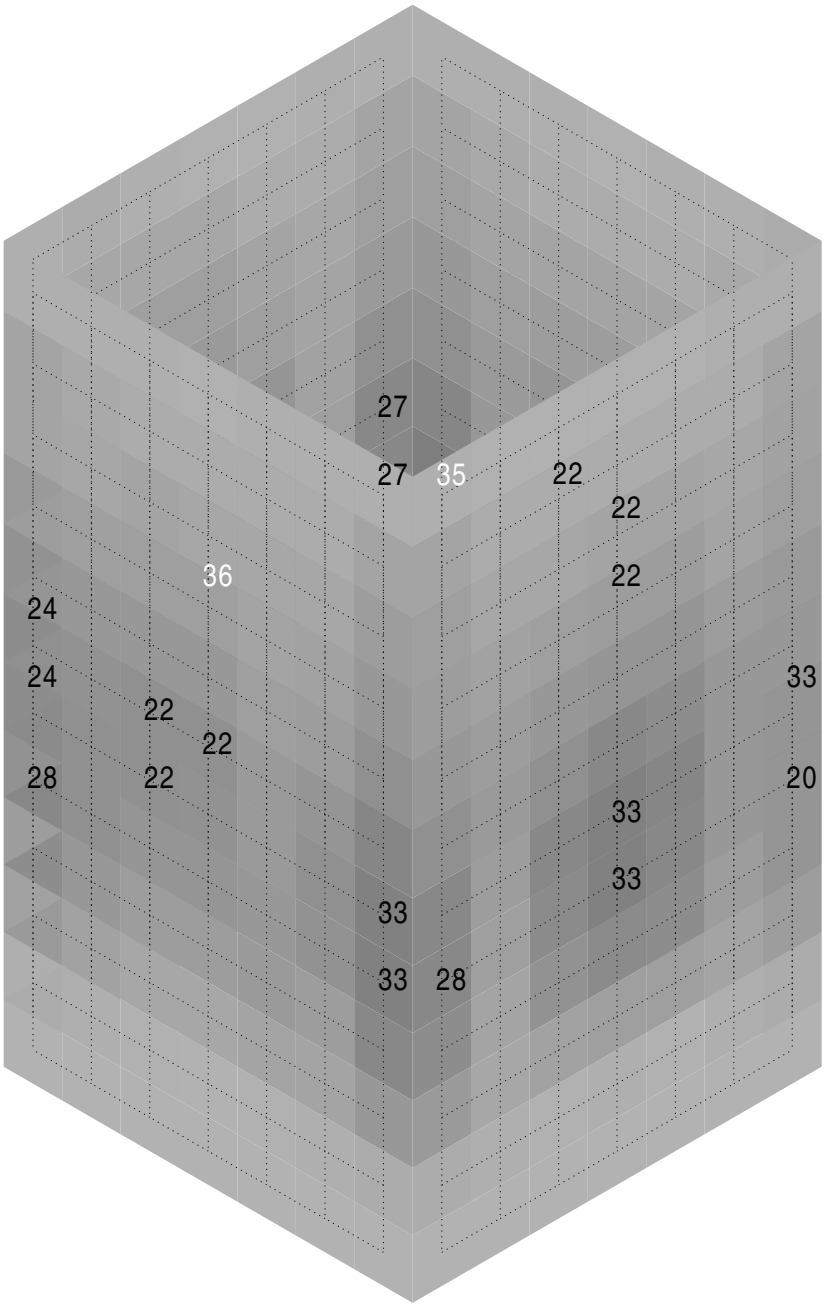

Figure D.4: Maximum = 14%

Concrete compression of shaft, Outer Face

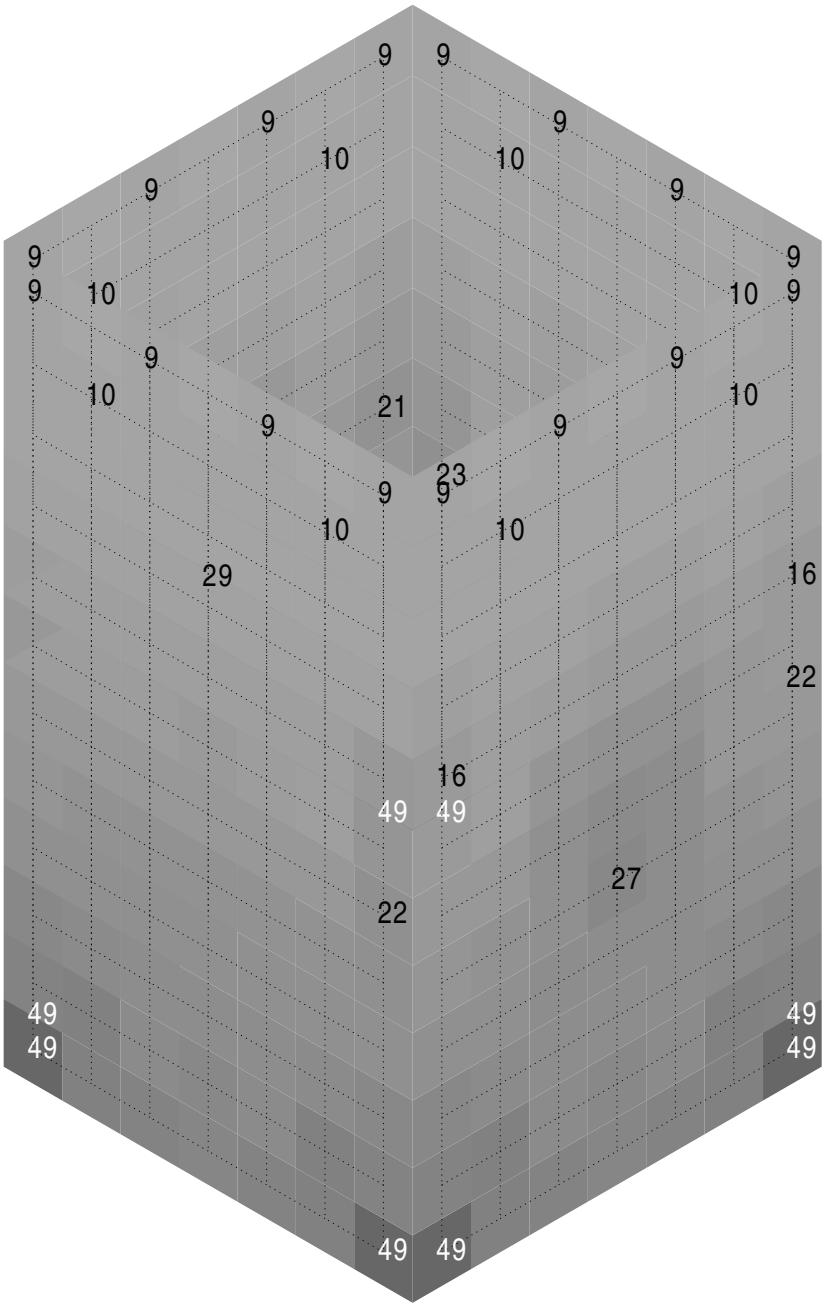

Figure D.5: Maximum = 14%

Concrete compression of shaft, Inner Face

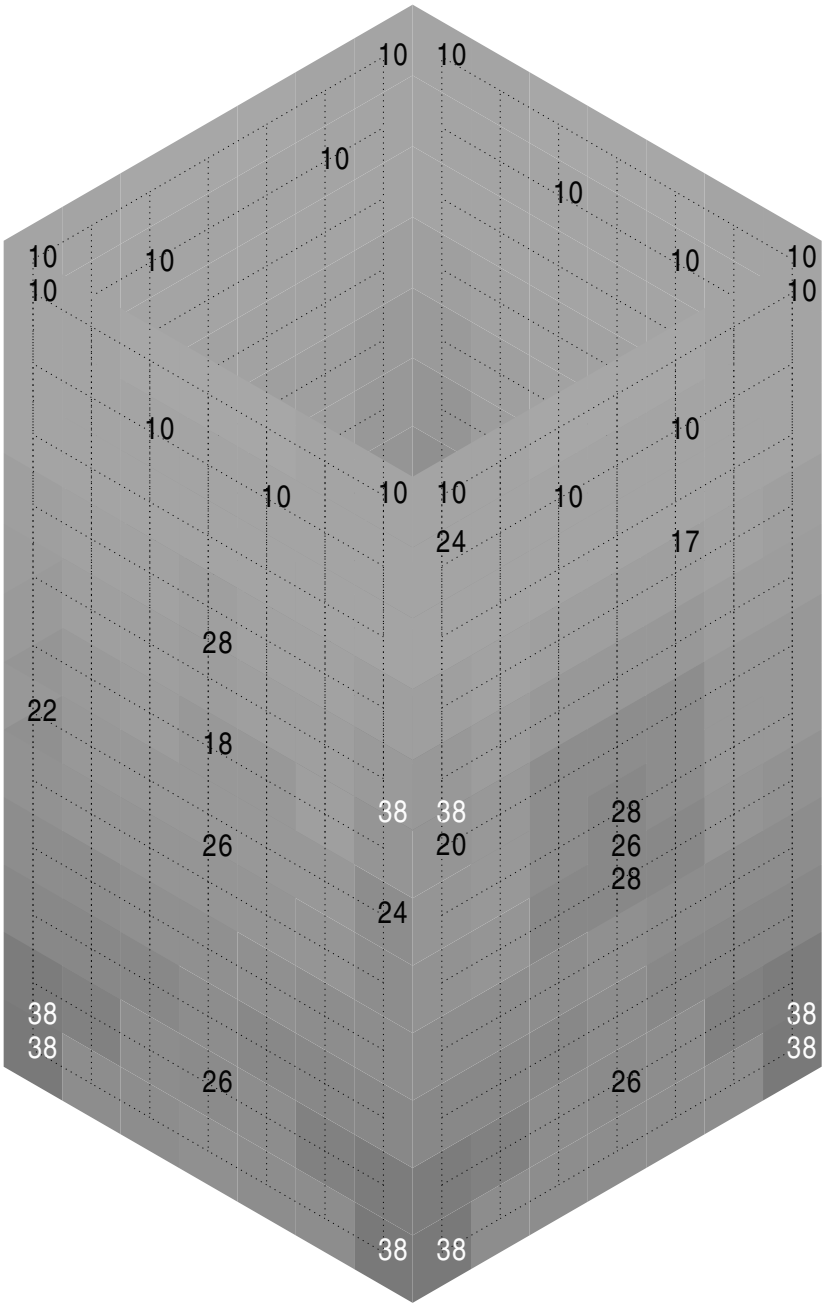

Figure D.6: Maximum = 14%

Concrete shear compression of shaft

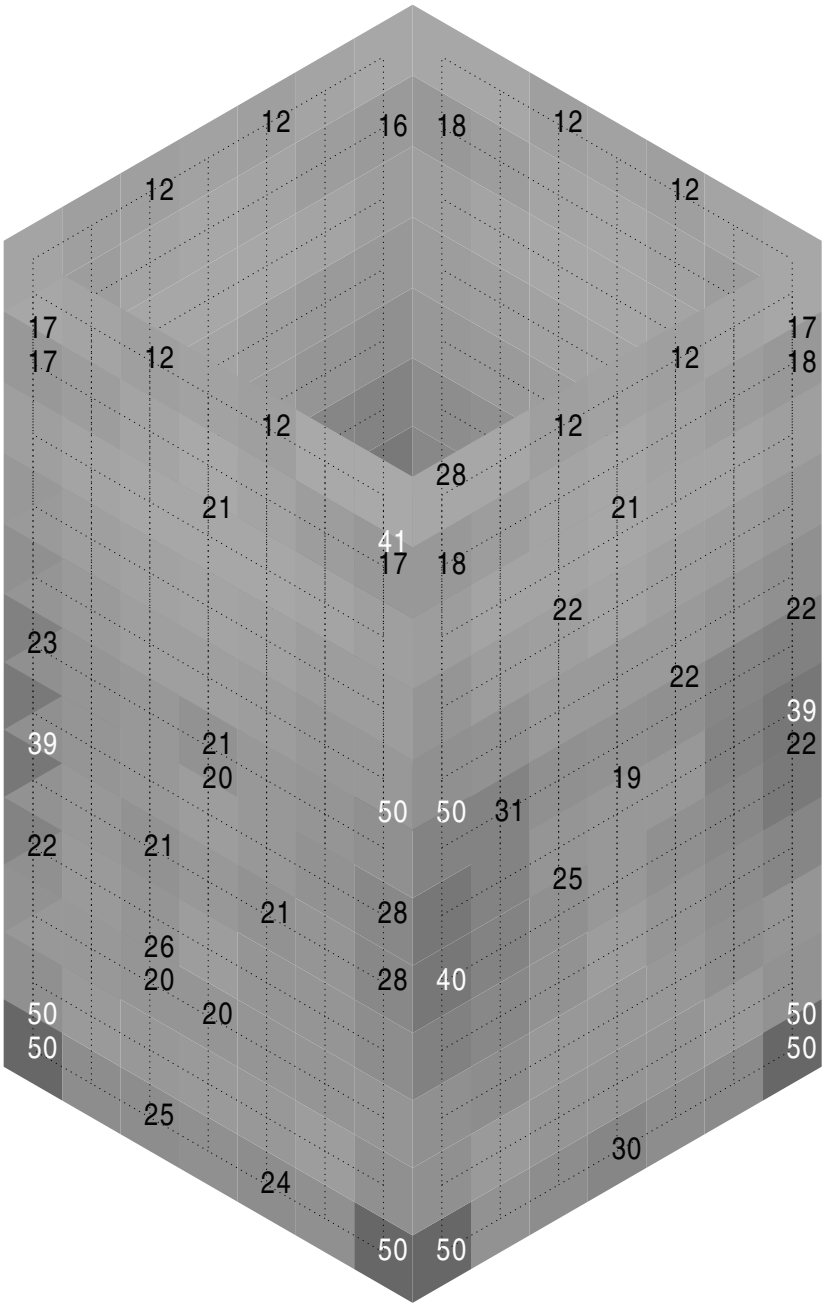

Figure D.7: Maximum = 14%

Horizontal Reinforcement of Lower Walls, Outer Face

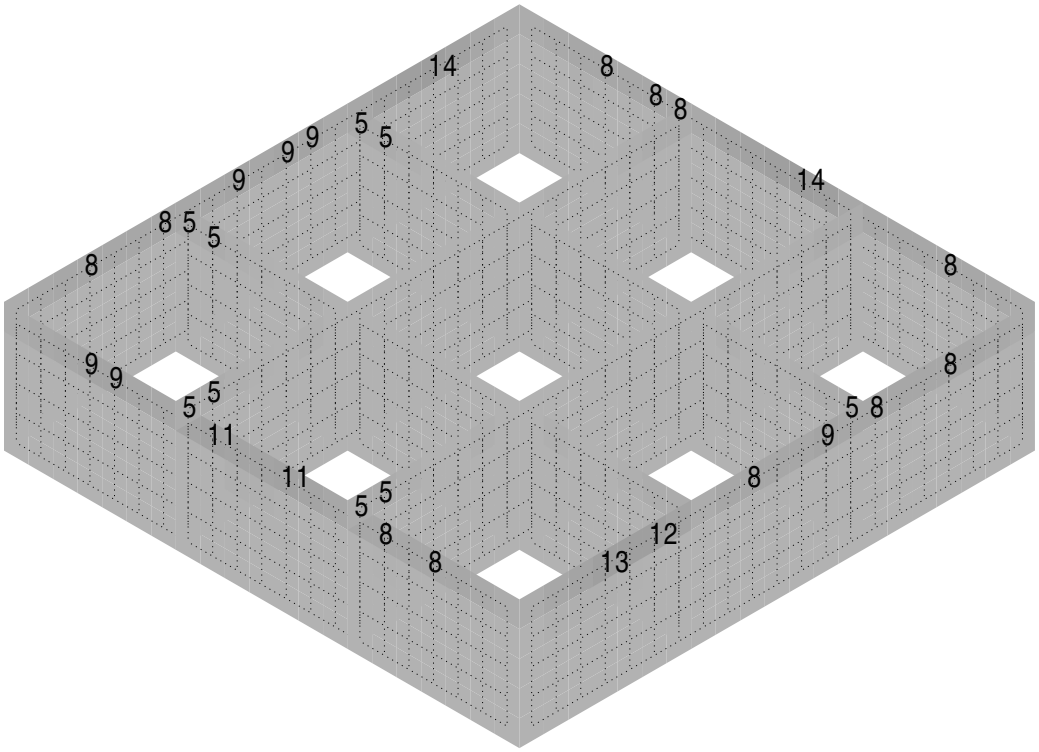

Figure D.8: Maximum = 14%

Horizontal Reinforcement of Lower Walls, Inner Face

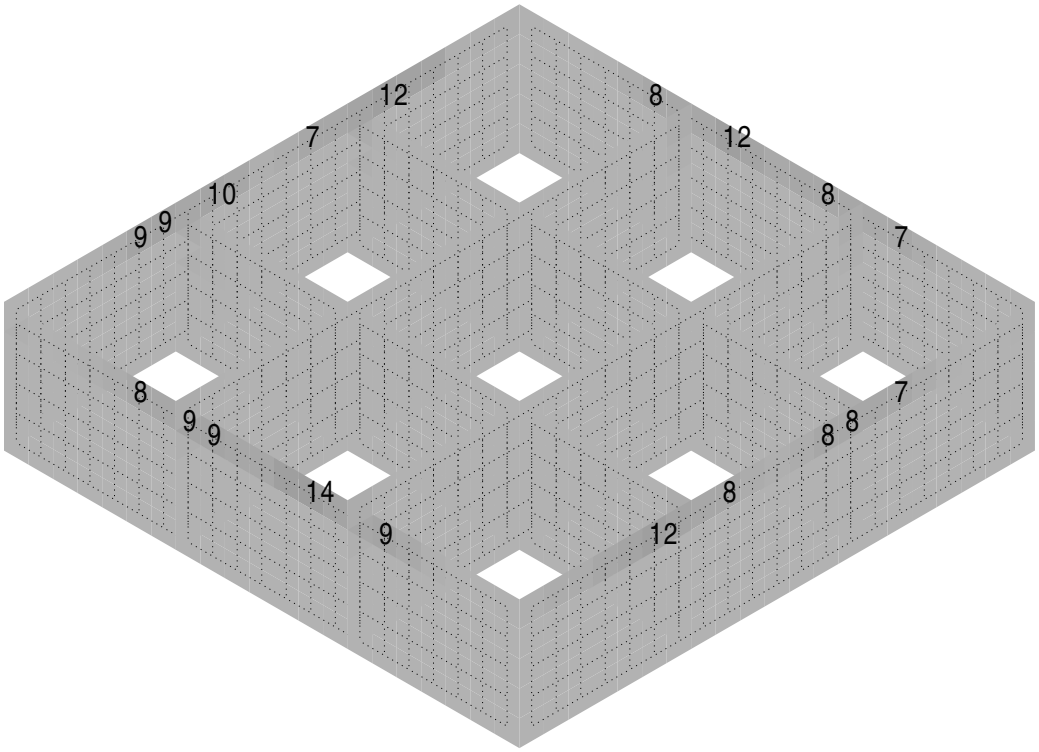

Figure D.9: Maximum = 14%

Vertical Reinforcement of Lower Walls, Outer Face

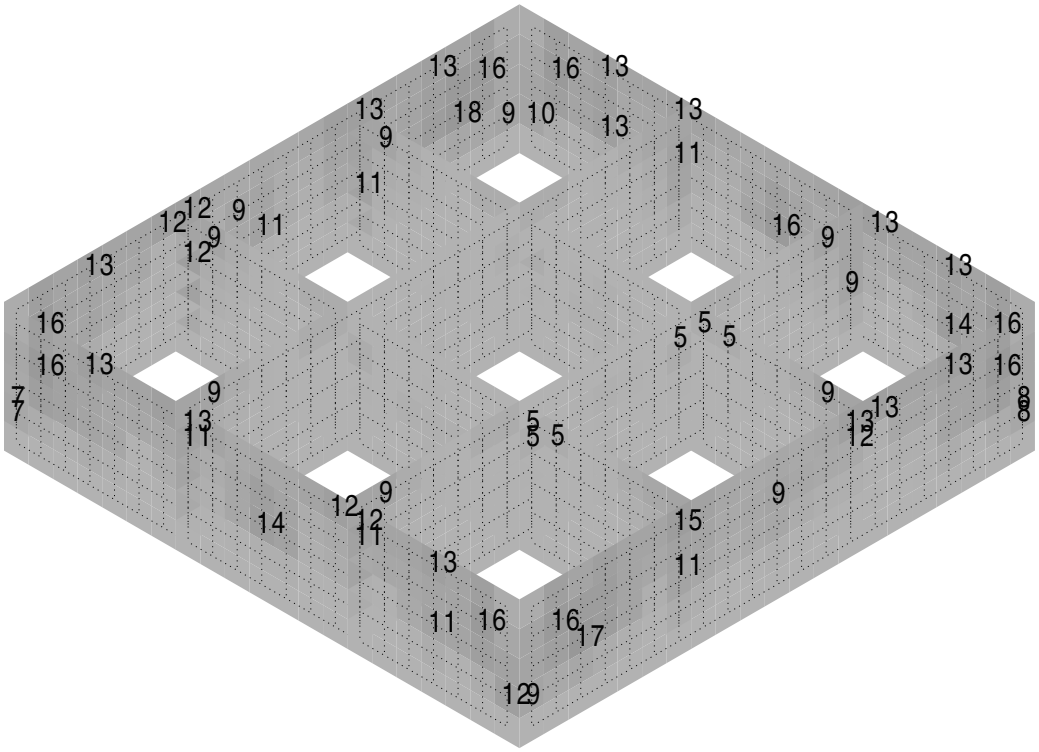

Figure D.10: Maximum = 18%

Vertical Reinforcement of Lower Walls, Inner Face

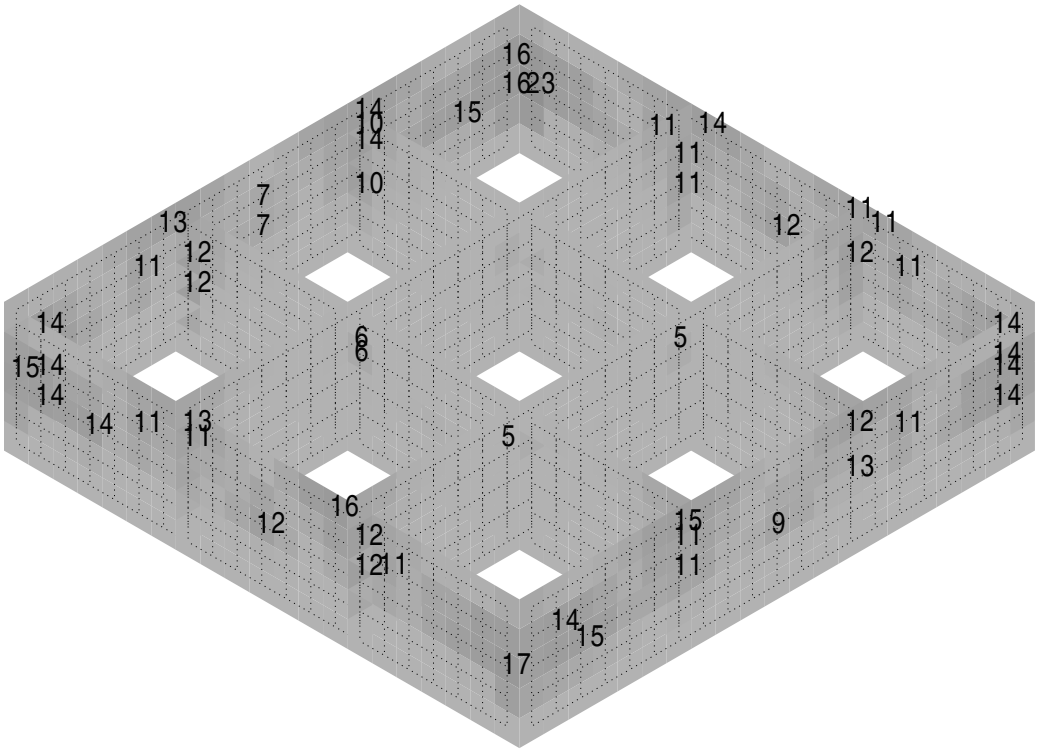

Figure D.11: Maximum = 23%

Concrete compression of Lower Walls, Outer Face

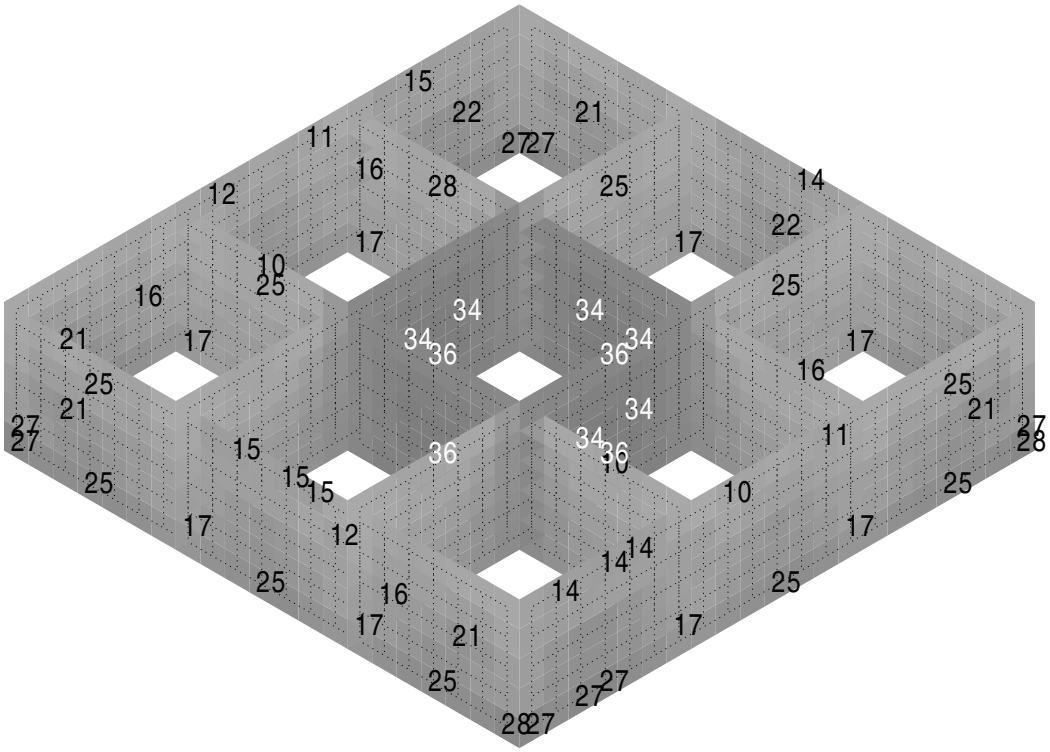

Figure D.12: Maximum = 36%

Concrete compression of Lower Walls, Inner Face

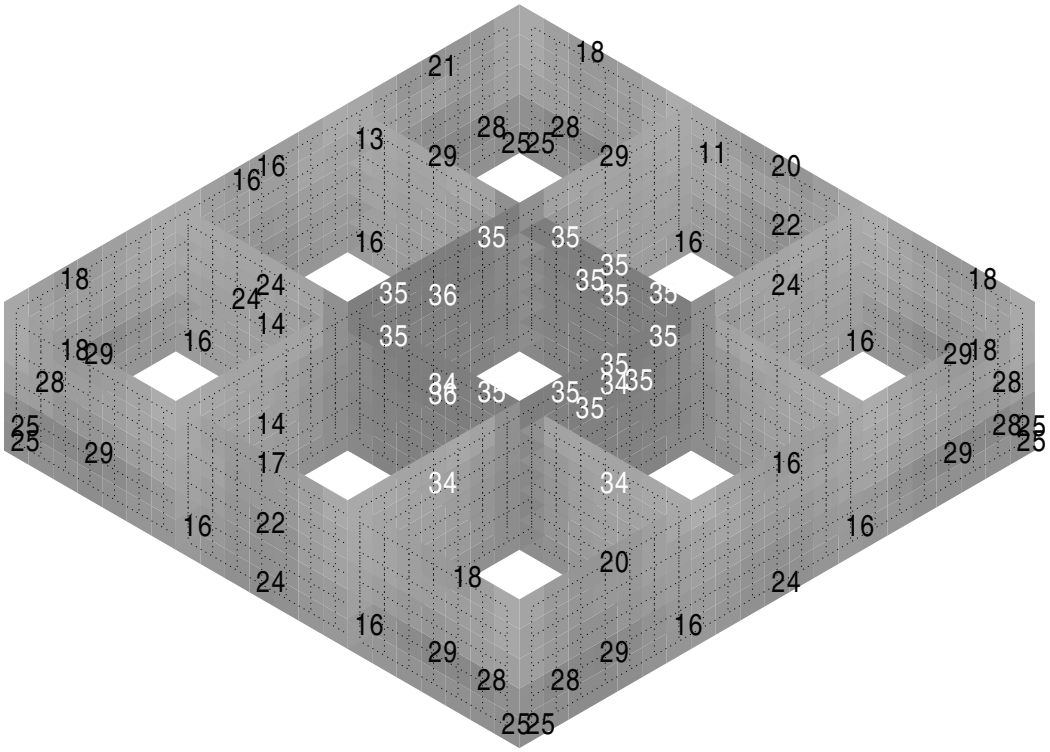

Figure D.13: Maximum = 36%

Concrete shear compression of Lower Walls

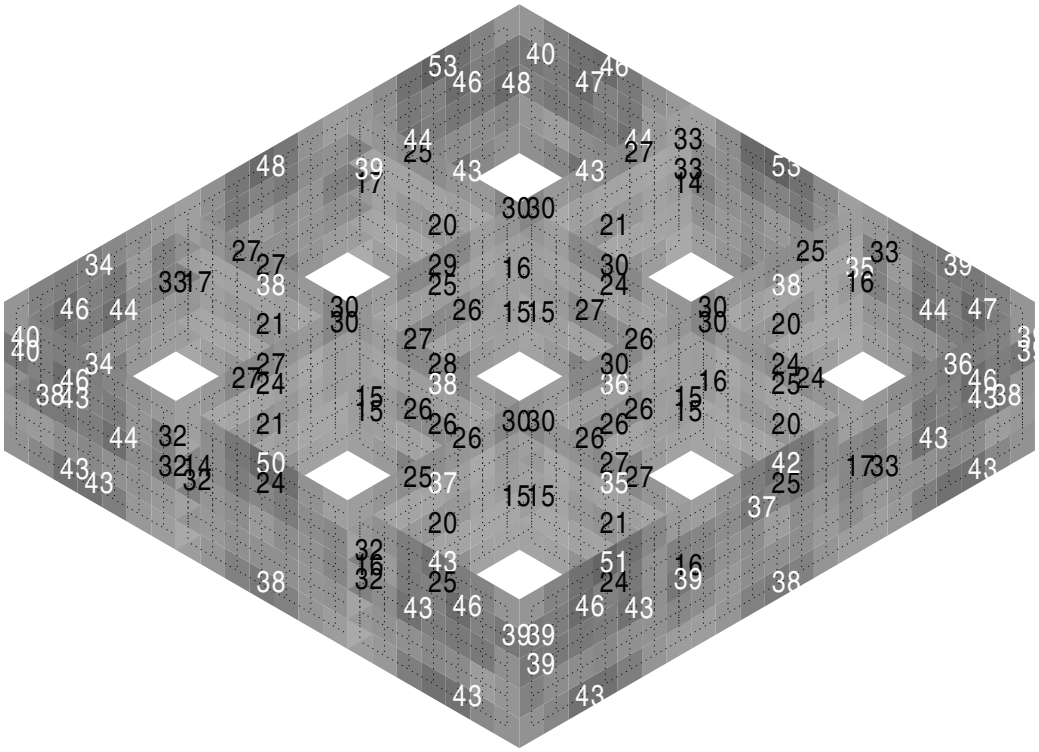

Figure D.14: Maximum = 53%

Horizontal Reinforcement of Caisson Floor, Bottom

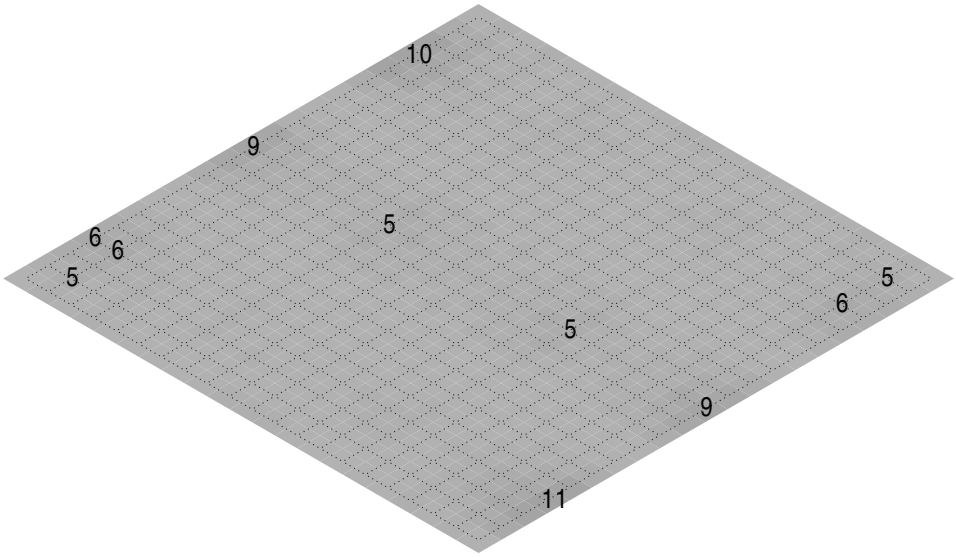

Figure D.15: Maximum = 11%

Horizontal Reinforcement of Caisson Floor, Top

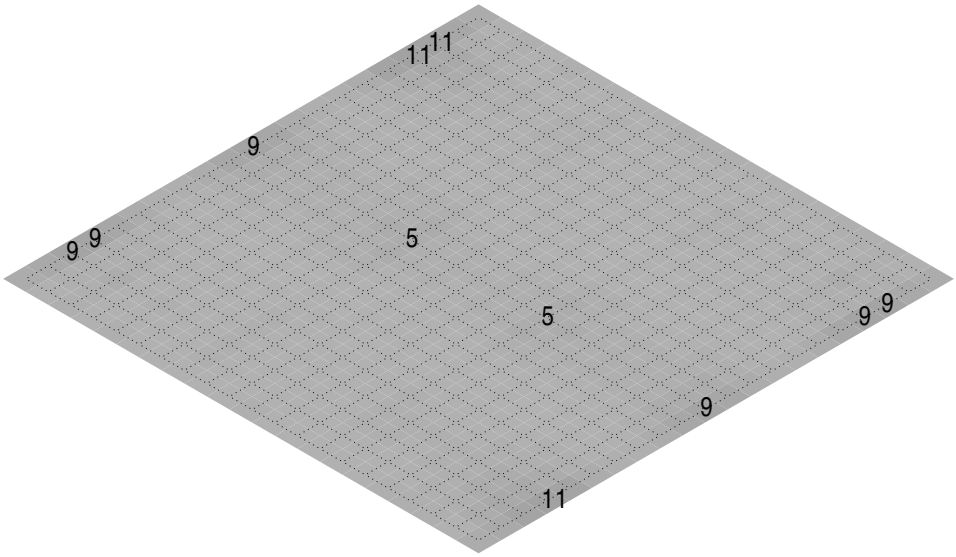

Figure D.16: Maximum = 11%

Vertical Reinforcement of Caisson Floor, Bottom

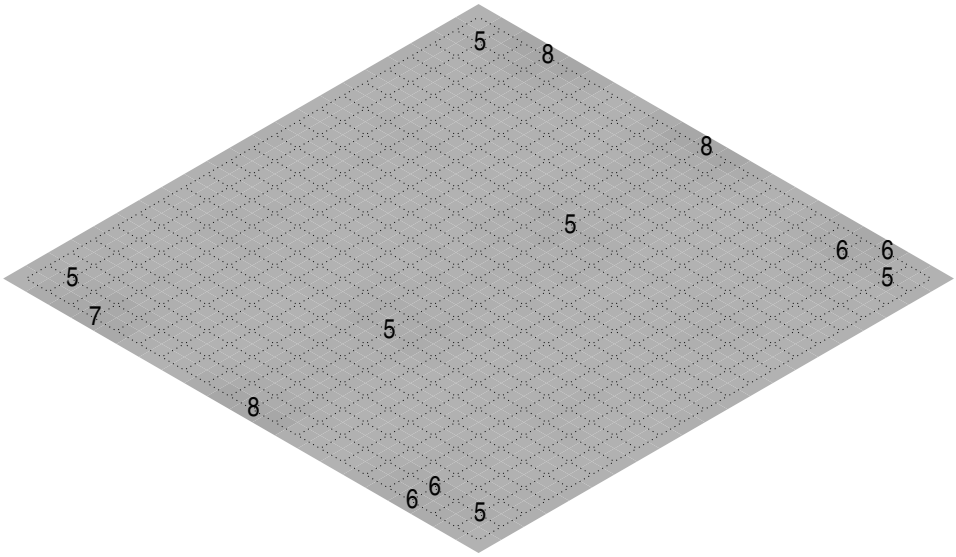

Figure D.17: Maximum = 8%

Vertical Reinforcement of Caisson Floor, Top

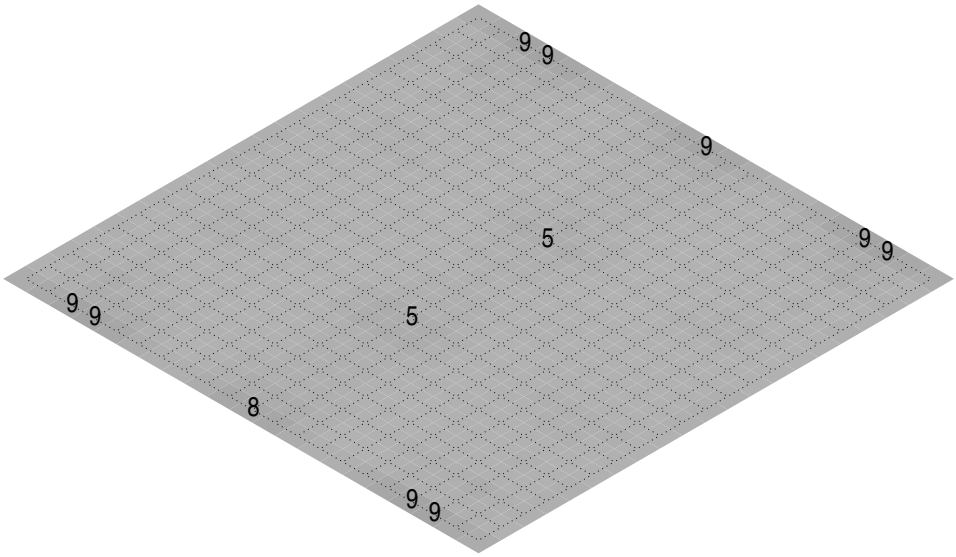

Figure D.18: Maximum = 9%

Concrete compression of Caisson Floor, Bottom

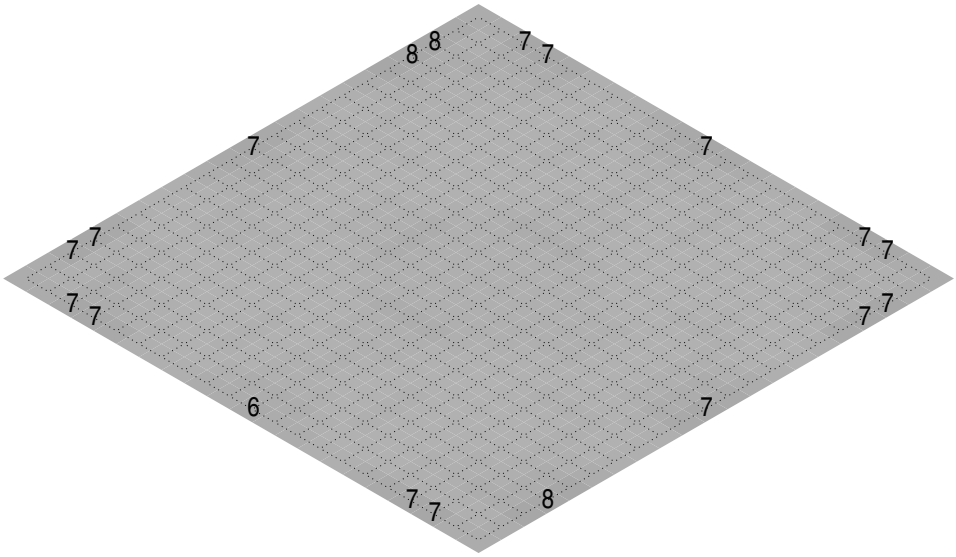

Figure D.19: Maximum = 8%

Concrete compression of Caisson Floor, Top

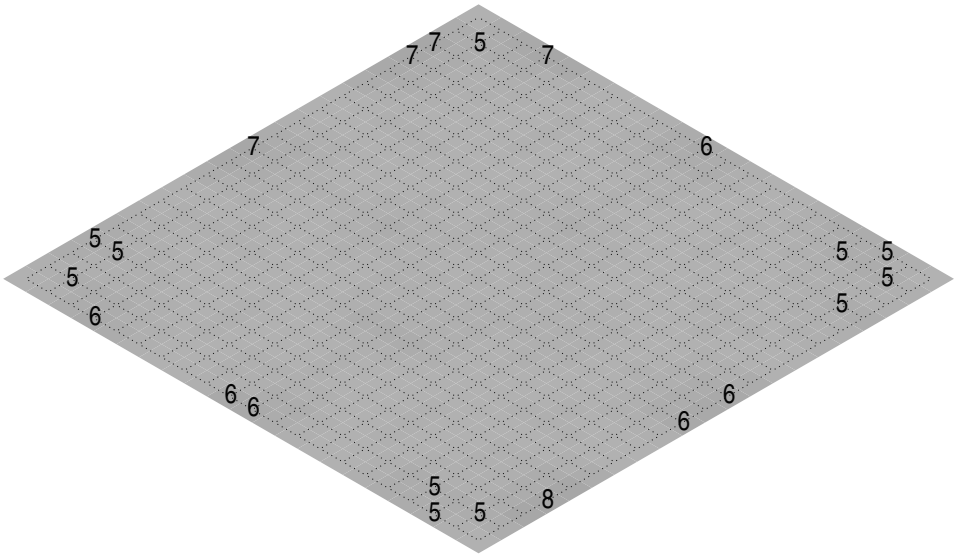

Figure D.20: Maximum = 8%

Concrete shear compression of Caisson Floor

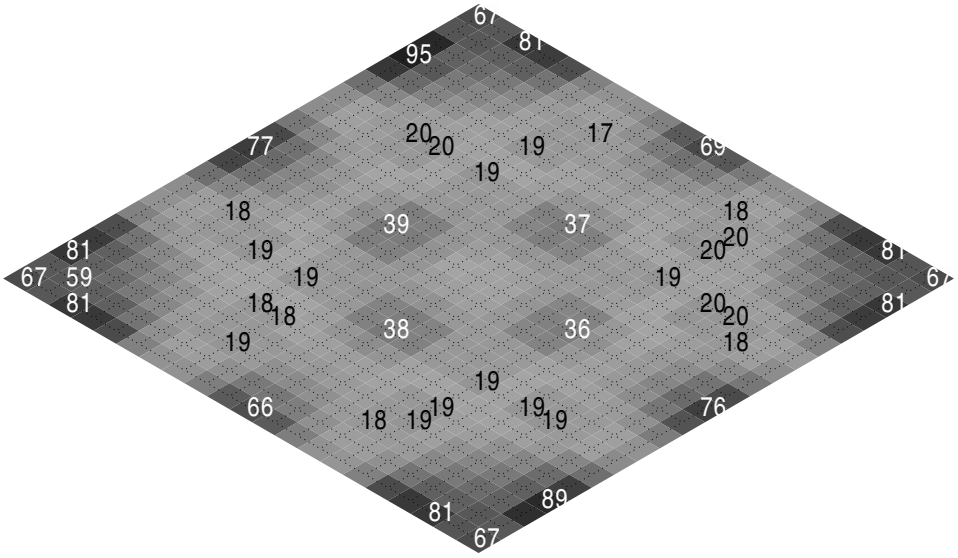

Figure D.21: Maximum = 95%

Horizontal Reinforcement of Caisson Roof, Top

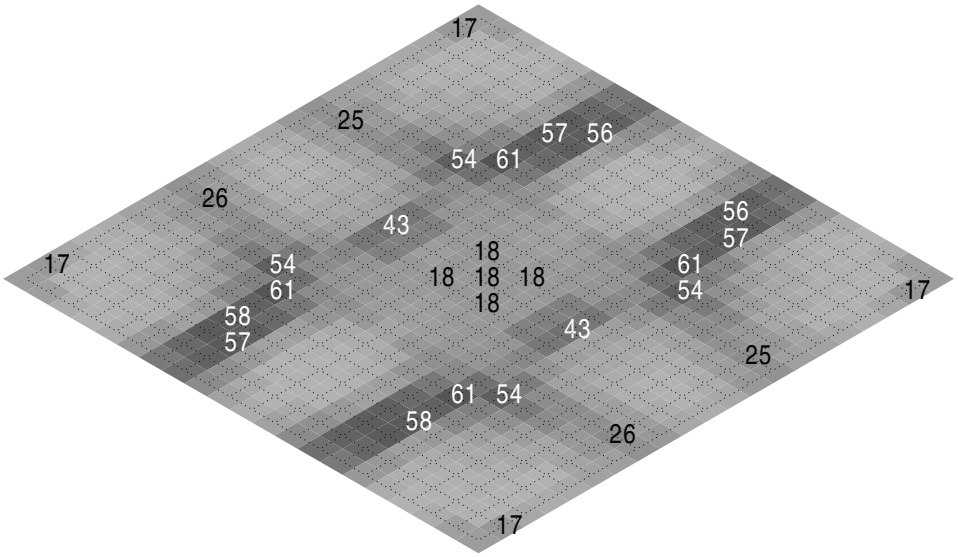

Figure D.22: Maximum = 61%

Horizontal Reinforcement of Caisson Roof, Bottom

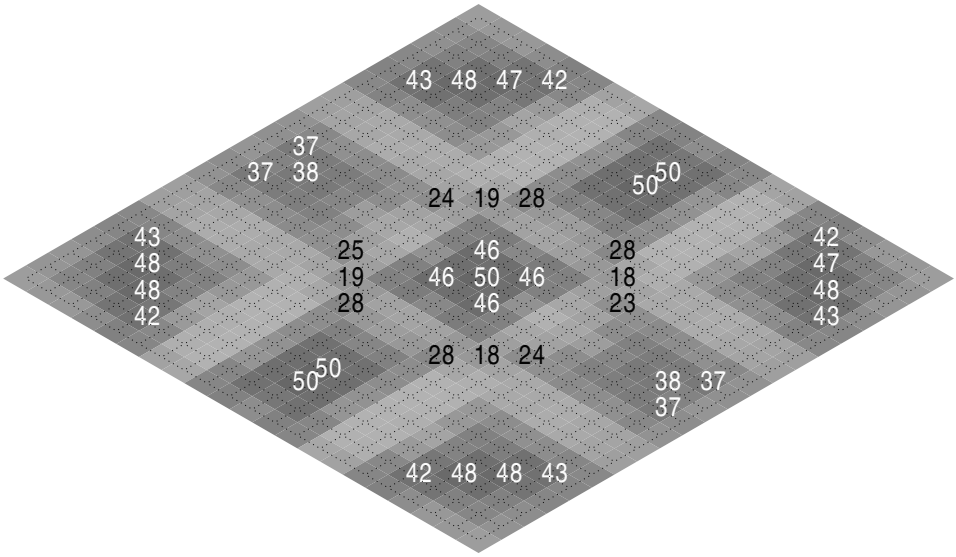

Figure D.23: Maximum = 50%

Vertical Reinforcement of Caisson Roof, Top

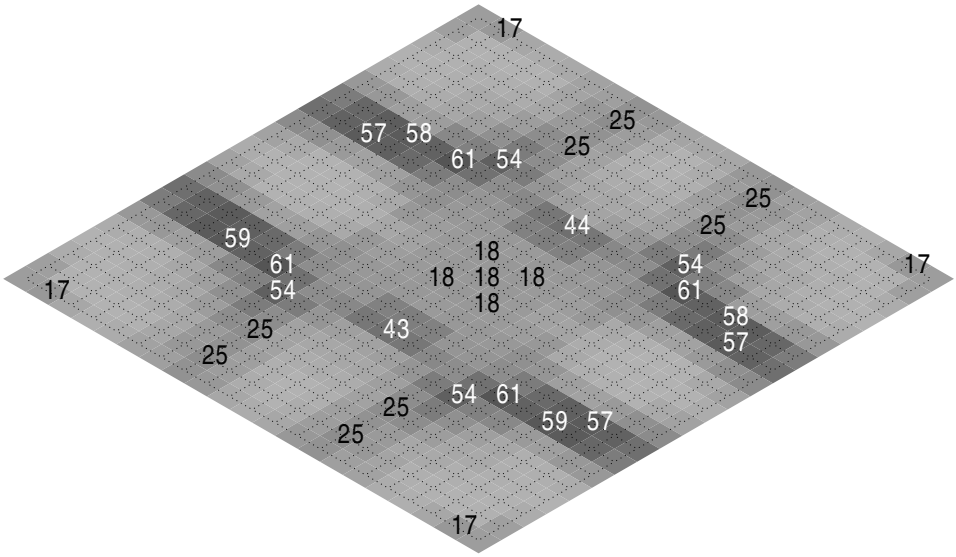

Figure D.24: Maximum = 61%

Vertical Reinforcement of Caisson Roof, Bottom

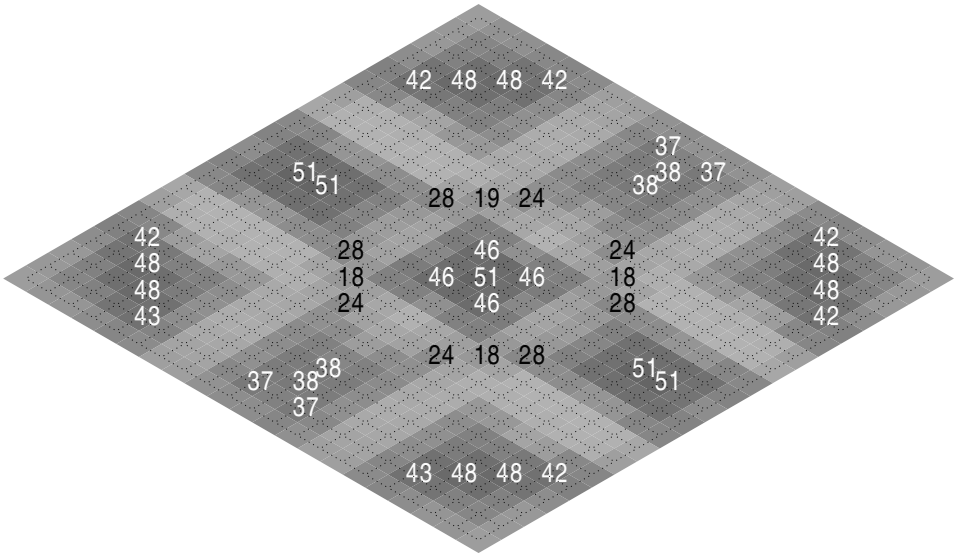

Figure D.25: Maximum = 51%

Concrete compression of Caisson Roof, Top

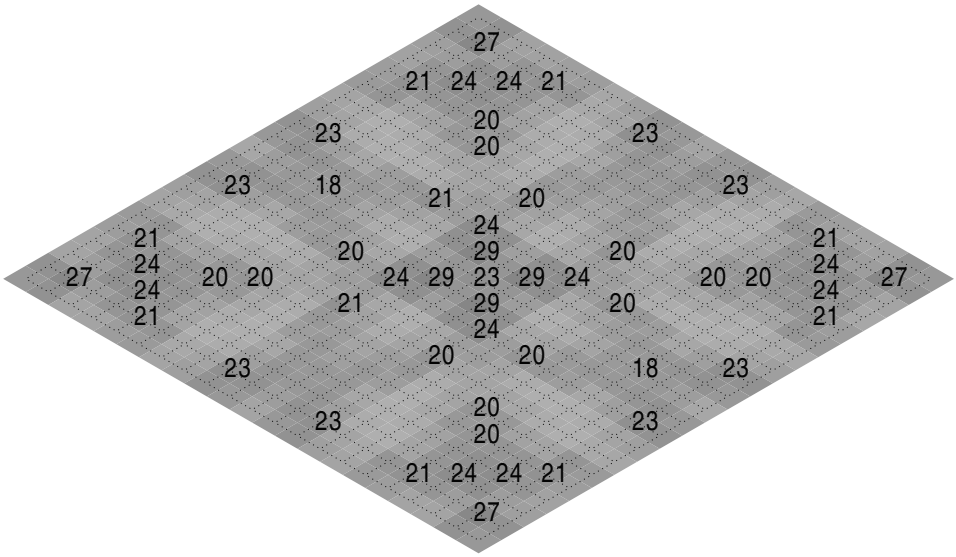

Figure D.26: Maximum = 29%

Concrete compression of Caisson Roof, Bottom

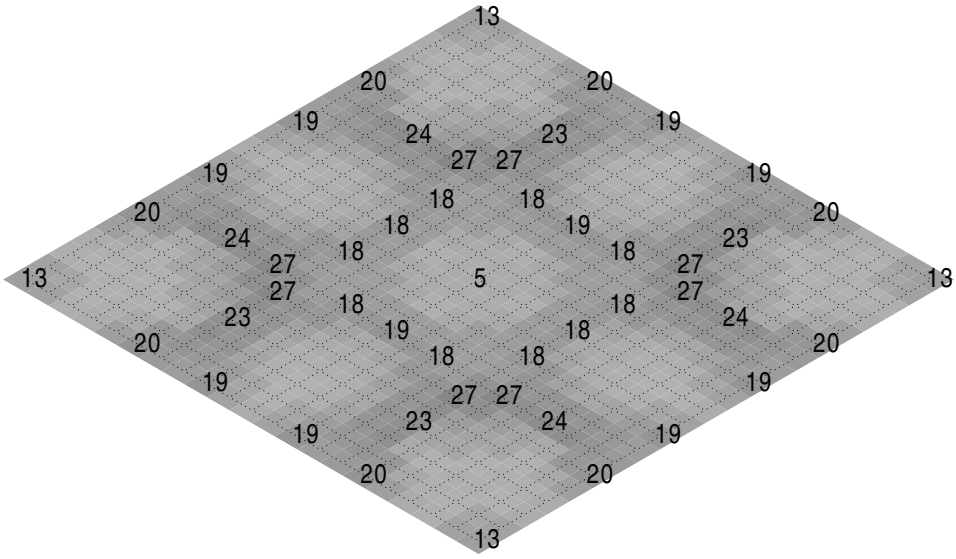

Figure D.27: Maximum = 27%

Concrete shear compression of Caisson Roof

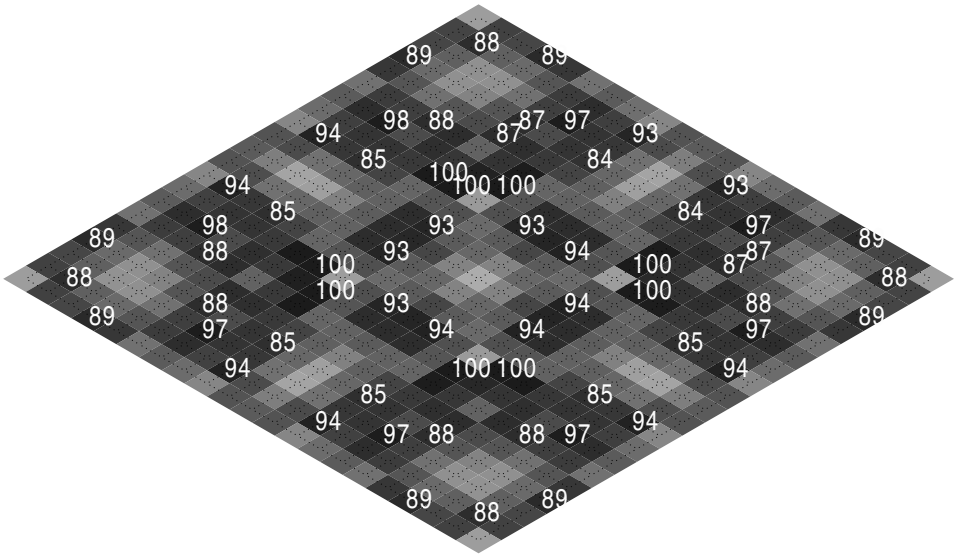

Figure D.28: Maximum = 100%

D.2 Shear reinforcement

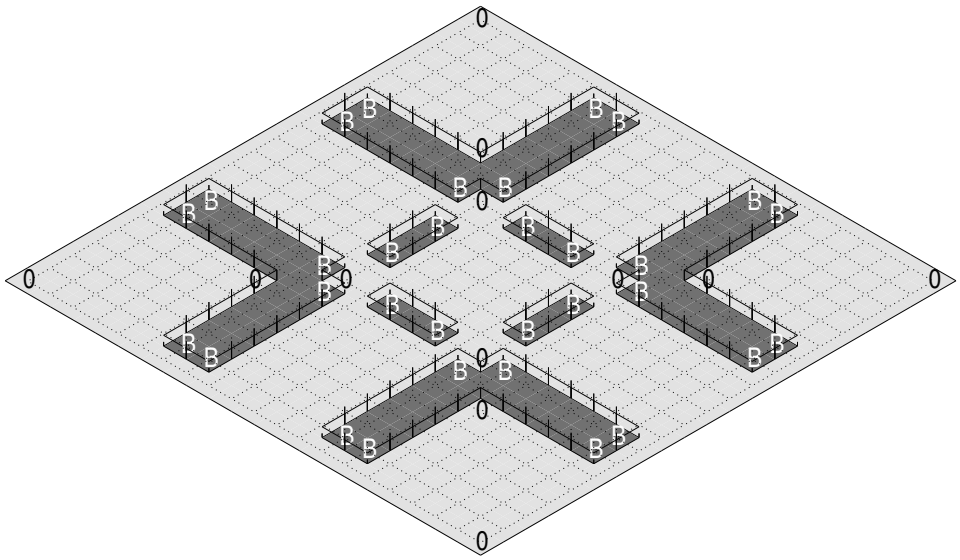

Figure D.29: Placement of ϕ14s250s250 in the caisson roof.

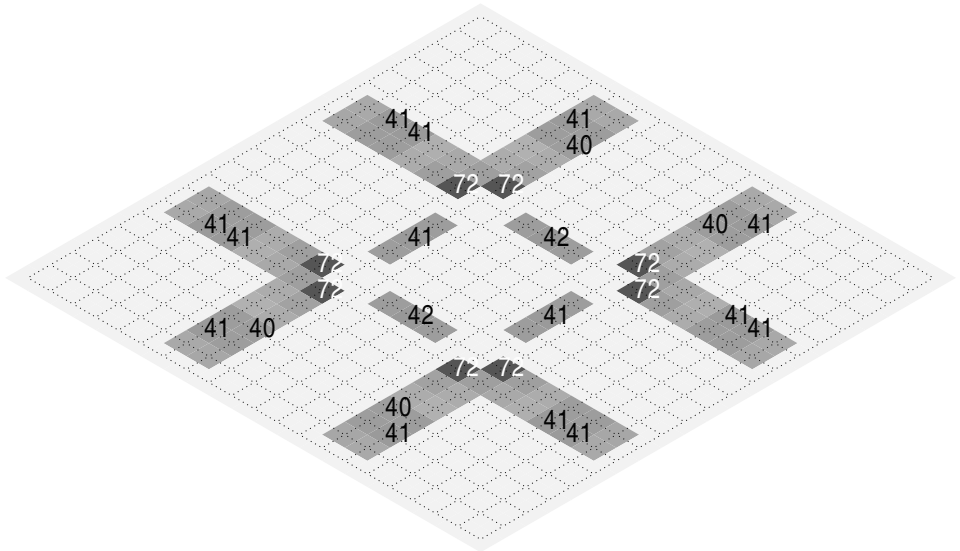

Figure D.30: Shear reinforcement utilization ratios.

E Response Spectrum Evaluation

This appendix concerns itself with the comparison of response spectrum and time history analysis and is supplementary to section 6.1.2. Used in comparison are the nodal moments and shear forces. Due to the symmetry of the structure, moments and forces are given only for one of the horizontal principle axes.

E.1 1000-year Earthquake

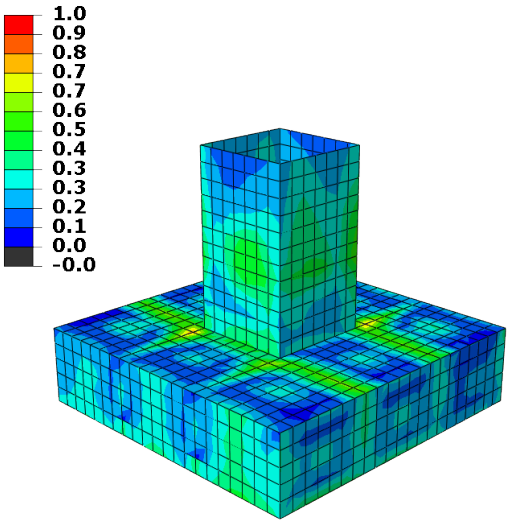

(a) Absolute sum of peak values

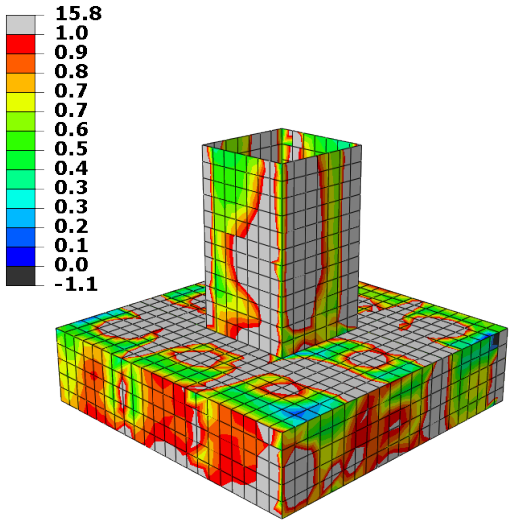

(b) CQC.

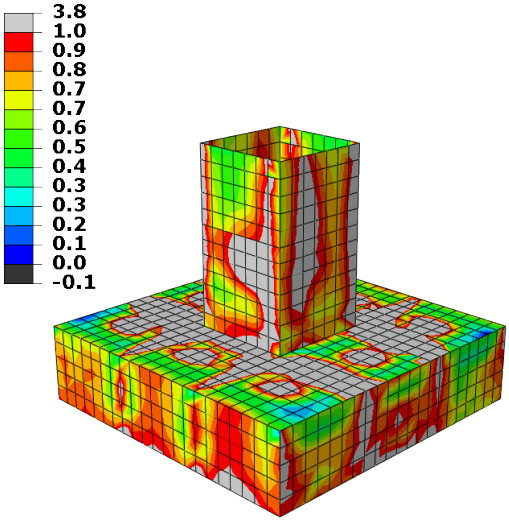

(c) SRSS.

Figure E.1: Ratio plots of moments.

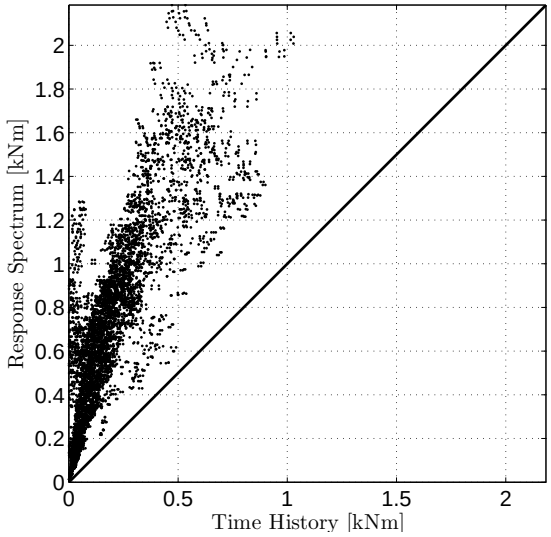

(a) Absolute sum of peak values.

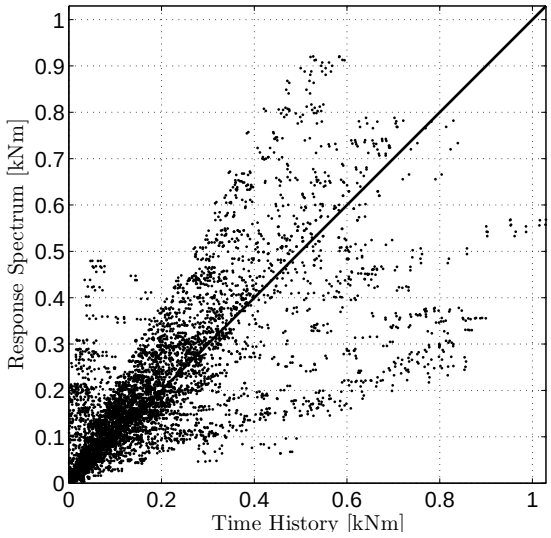

(b) CQC.

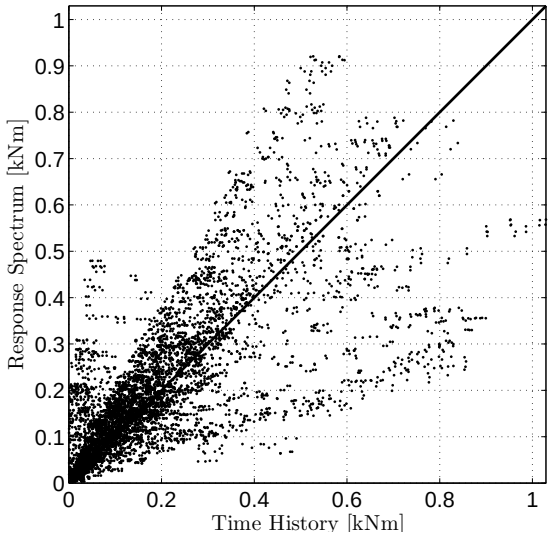

(c) SRSS.

Figure E.2: RS-TH plots of moments.

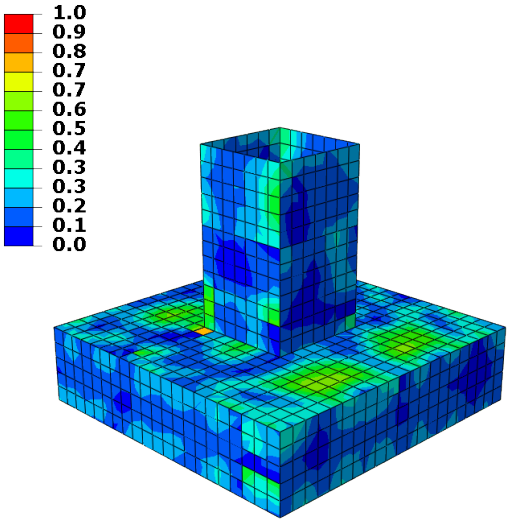

(a) Absolute sum of peak values

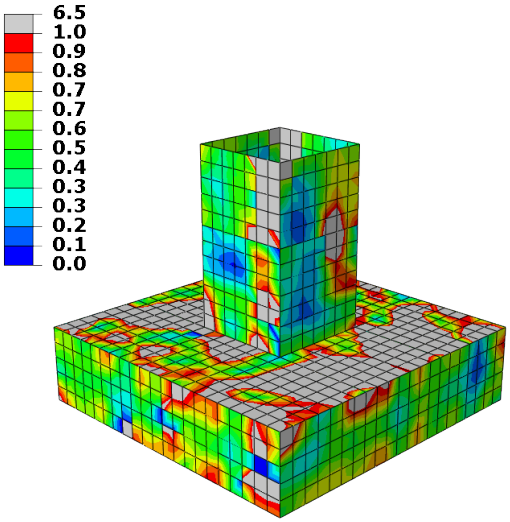

(b) CQC.

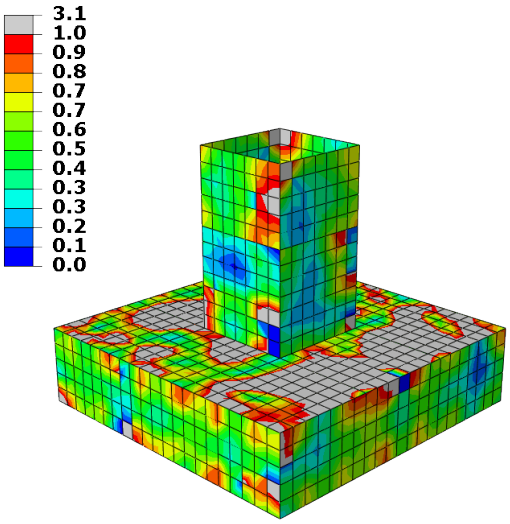

(c) SRSS.

Figure E.3: Ratio plots of shear forces.

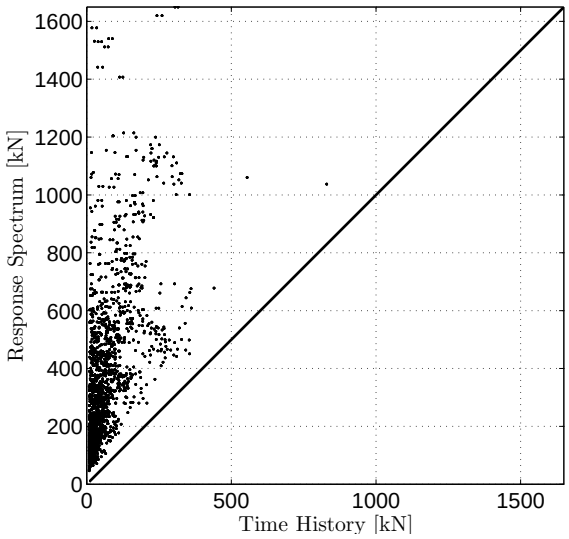

(a) Absolute sum of peak values.

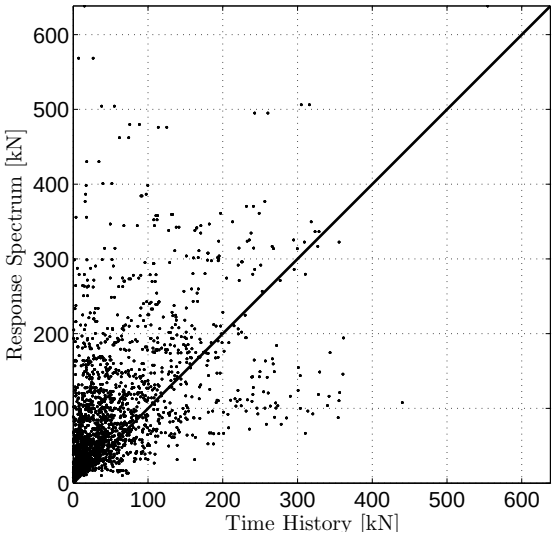

(b) CQC.

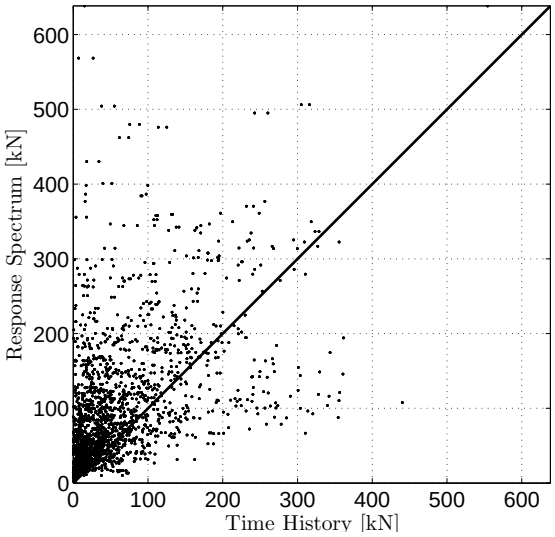

(c) SRSS.

Figure E.4: RS-TH plots of shear forces.

E.2 3000-year Earthquake

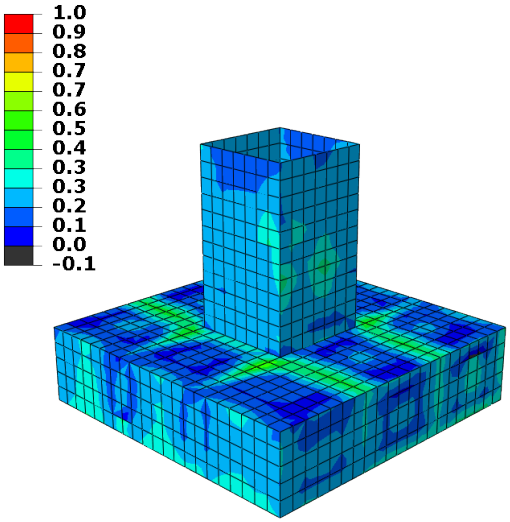

(a) Absolute sum of peak values

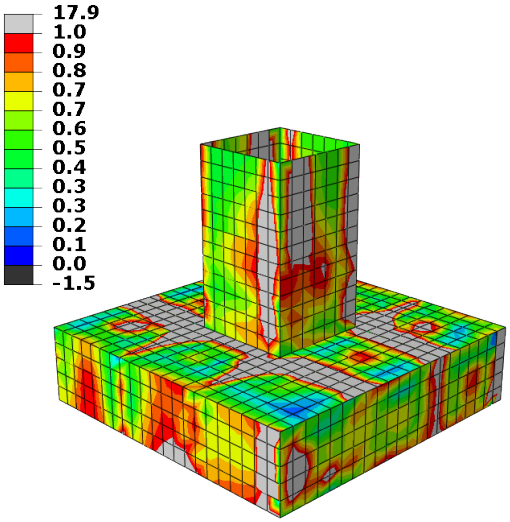

(b) CQC

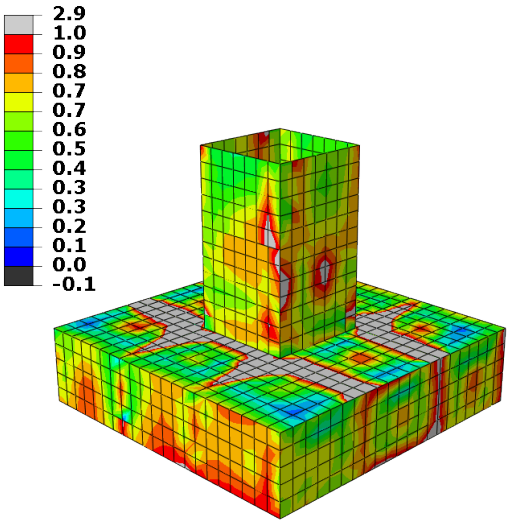

(c) SRSS

Figure E.5: Ratio plots of moments.

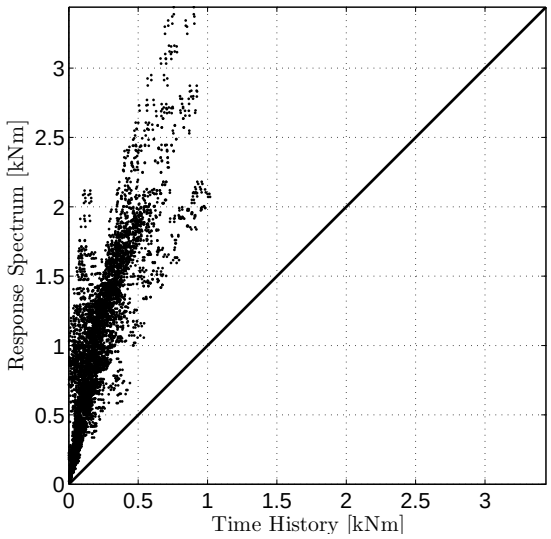

(a) Absolute sum of peak values.

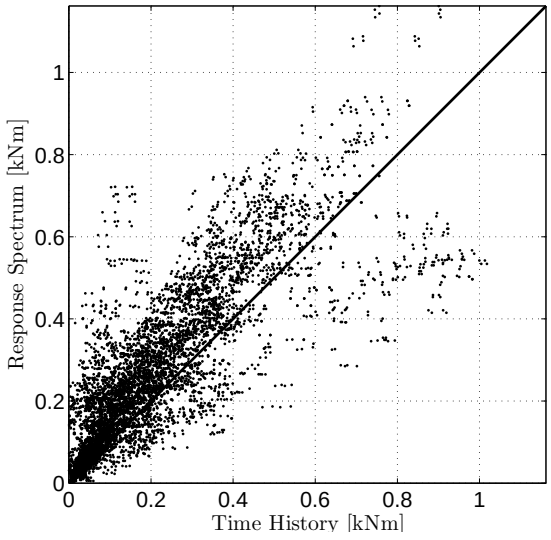

(b) CQC.

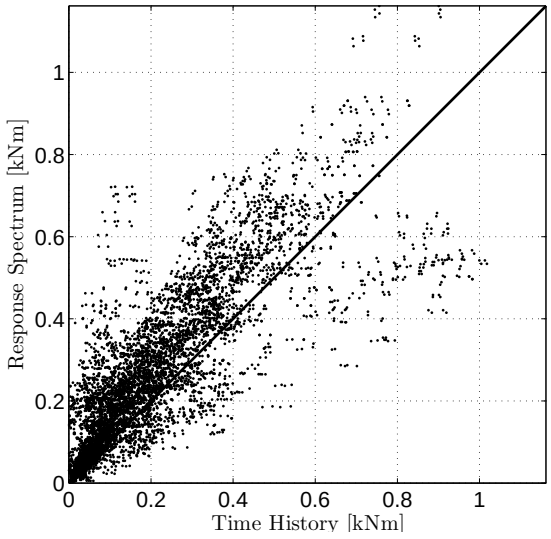

(c) SRSS.

Figure E.6: RS-TH plots of moments.

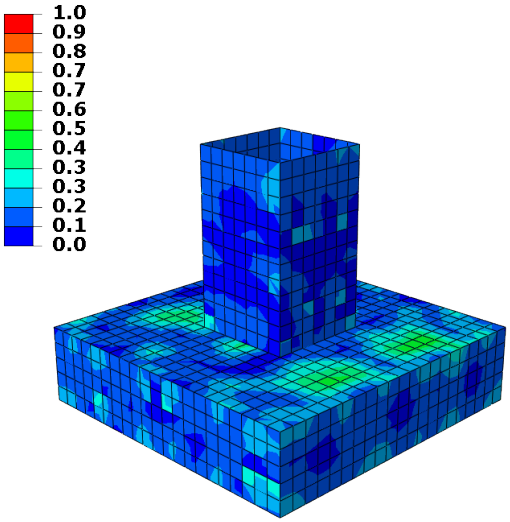

(a) Absolute sum of peak values

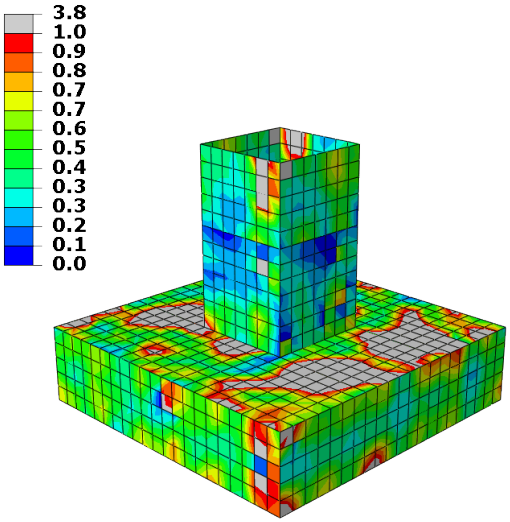

(b) CQC

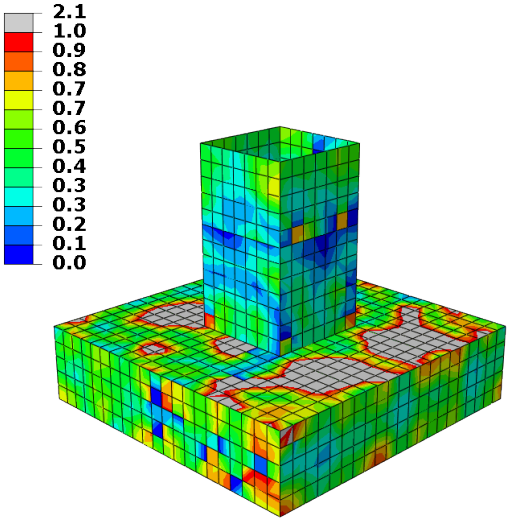

(c) SRSS

Figure E.7: Ratio plots of shear forces.

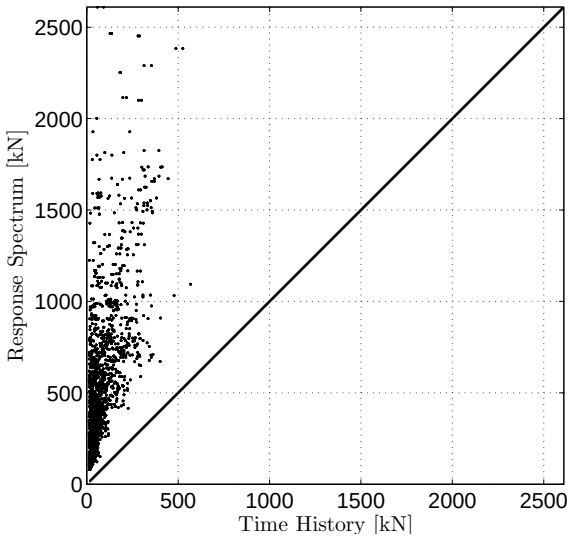

(a) Absolute sum of peak values.

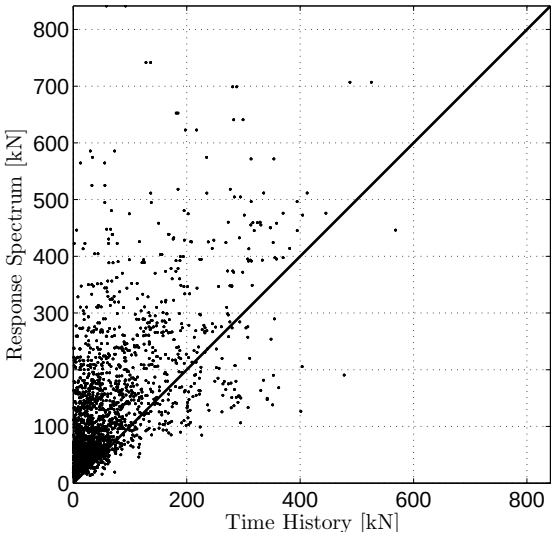

(b) CQC.

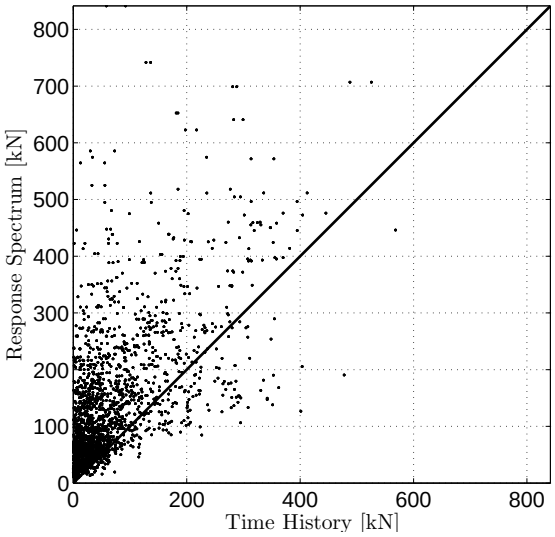

(c) SRSS.

Figure E.8: RS-TH plots of shear forces.

E.3 10 000-year Earthquake

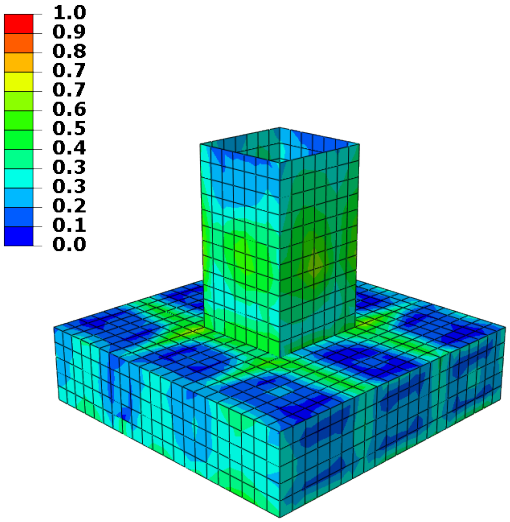

(a) Absolute sum of peak values

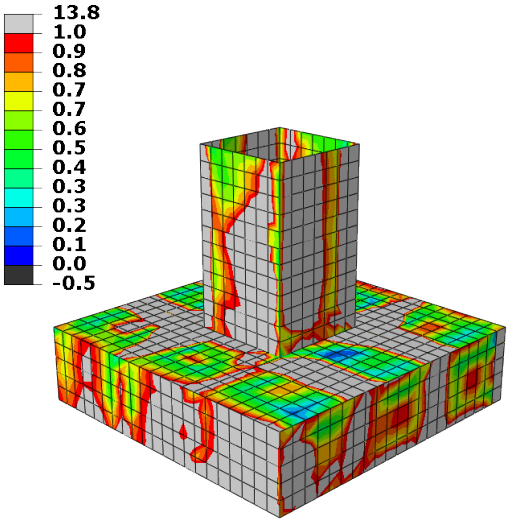

(b) CQC.

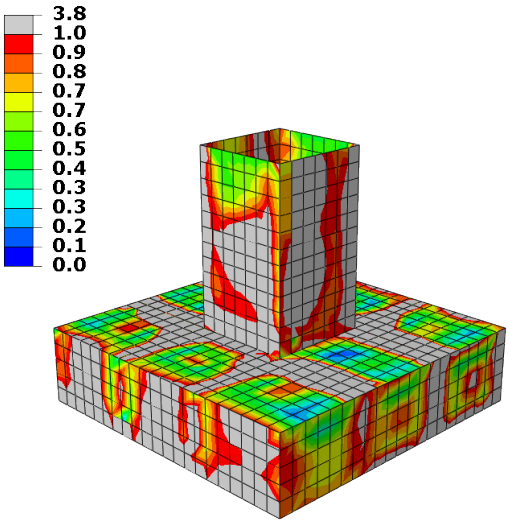

(c) SRSS.

Figure E.9: Ratio plots of moments.

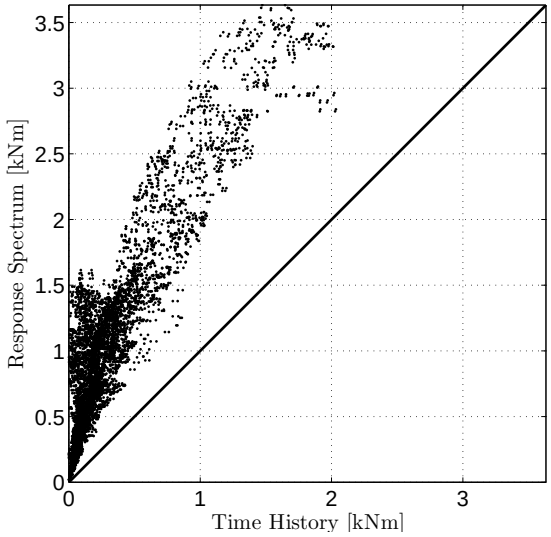

(a) Absolute sum of peak values.

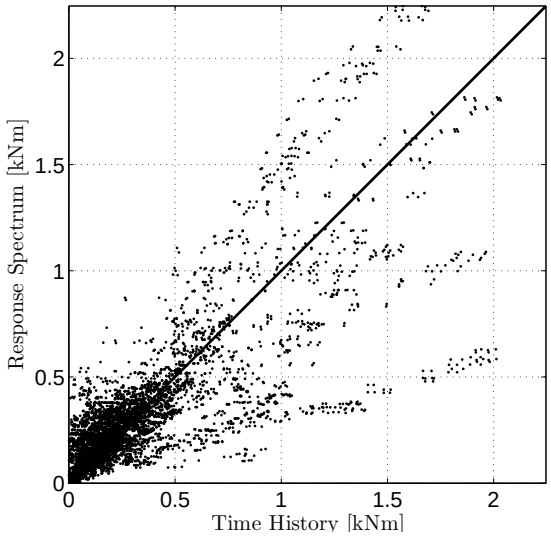

(b) CQC.

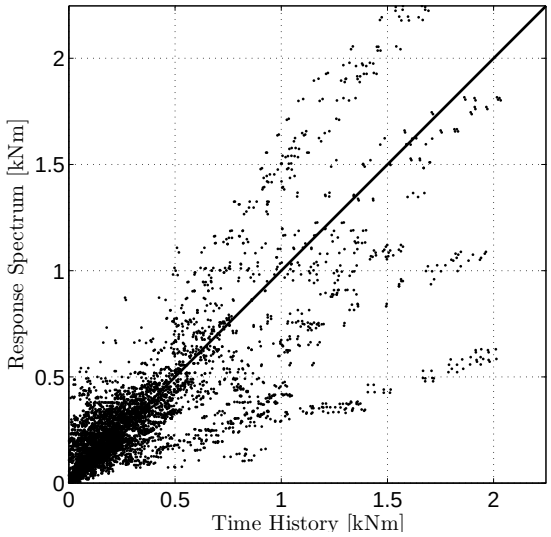

(c) SRSS.

Figure E.10: RS-TH plots of moments.

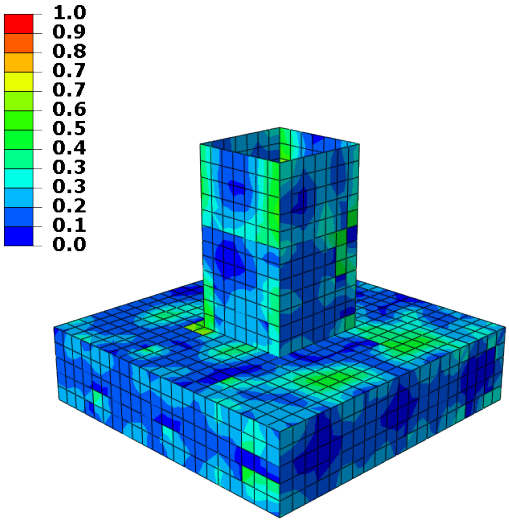

(a) Absolute sum of peak values

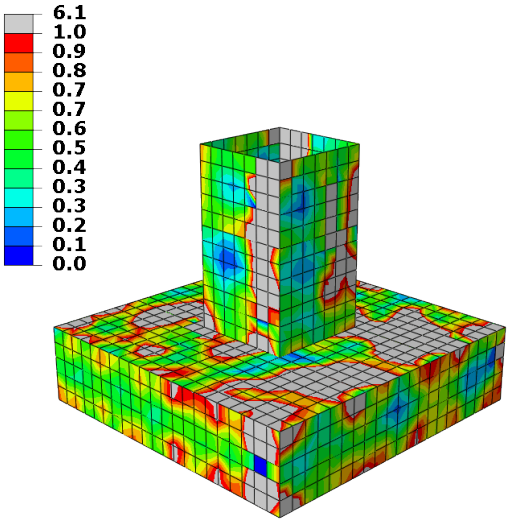

(b) CQC.

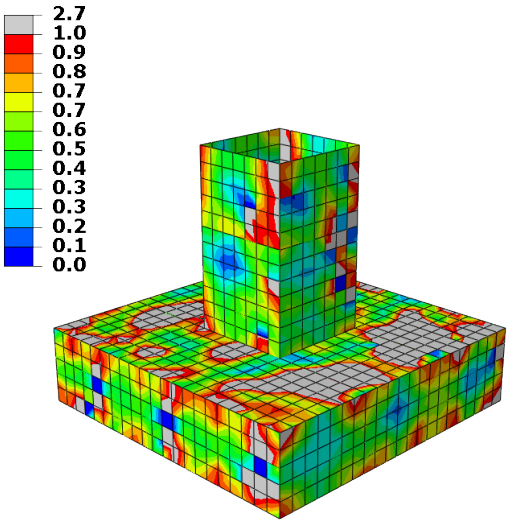

(c) SRSS.

Figure E.11: Ratio plots of shear forces.

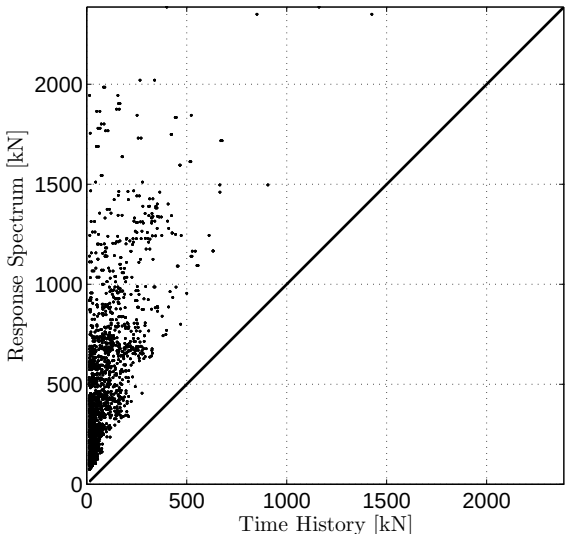

(a) Absolute sum of peak values.

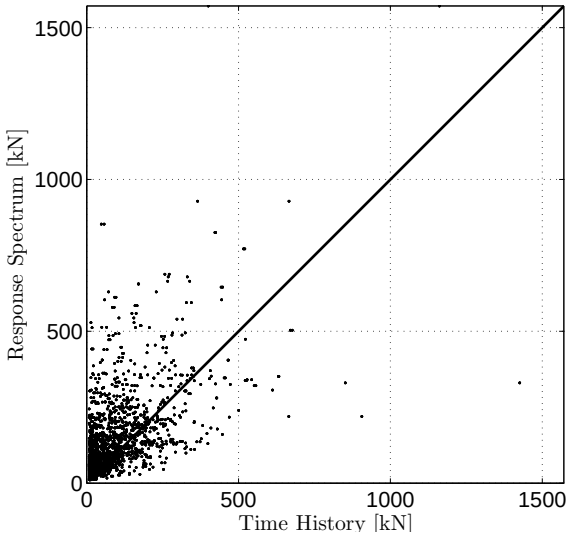

(b) CQC.

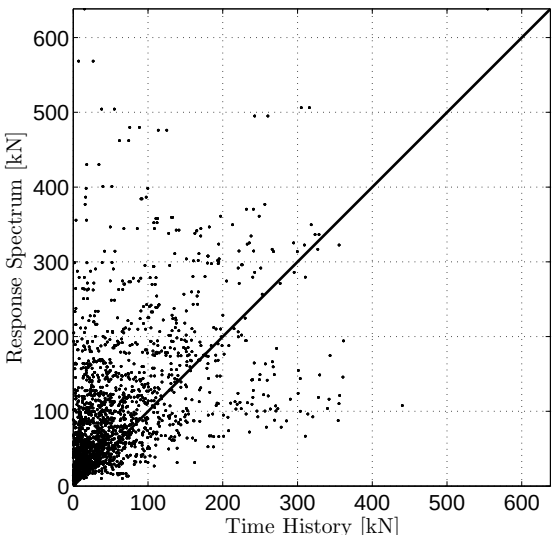

(c) SRSS.

Figure E.12: RS-TH plots of shear forces.

F Environmental effects

F.1 Presence of water

In the following, the effects of surrounding water are illustrated by a comparison of participation factors and response spectra for the different return periods. Note that the response spectra are scaled, such that only their shapes are relevant.

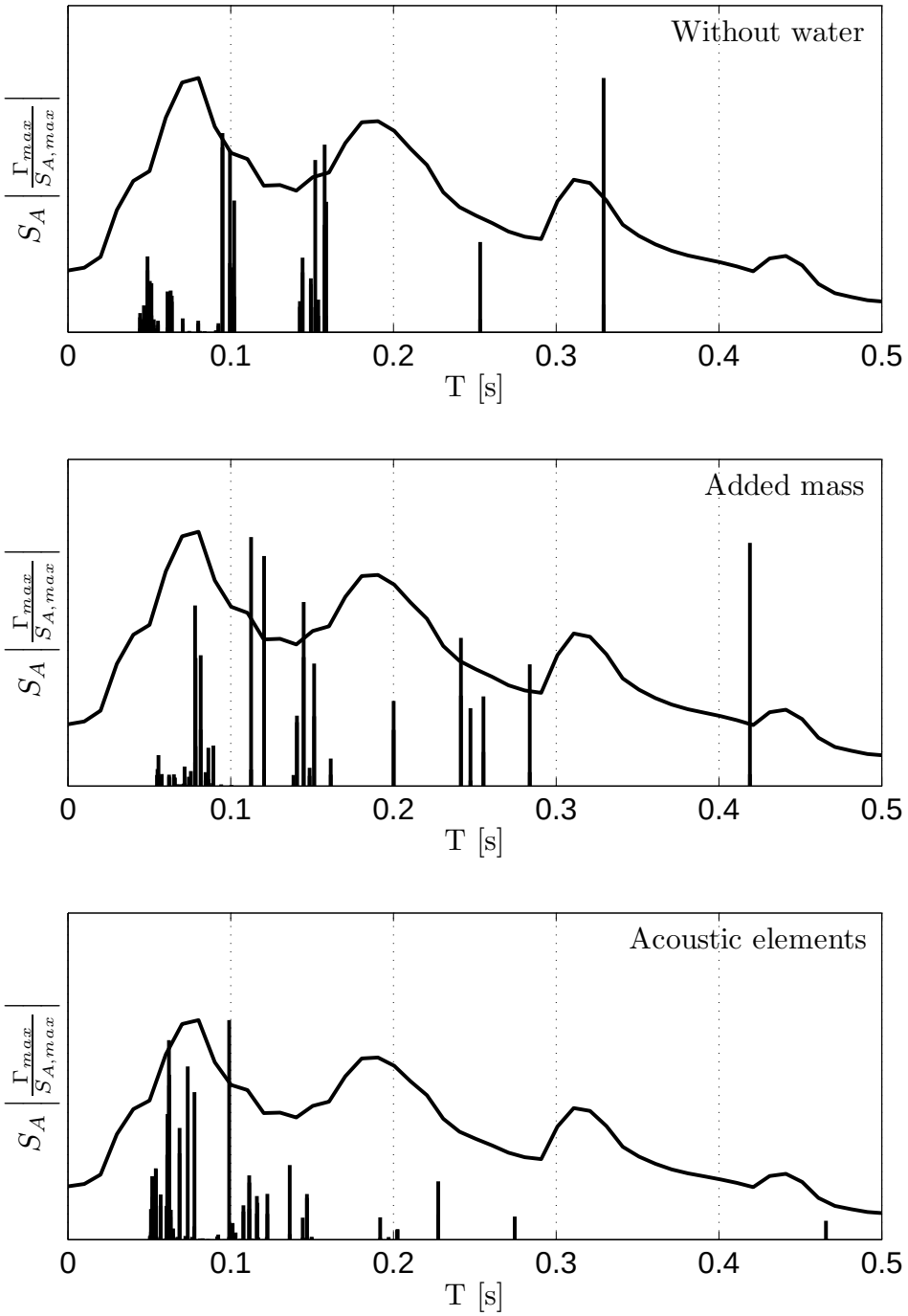

Figure F.1: $T_R = 475$ years

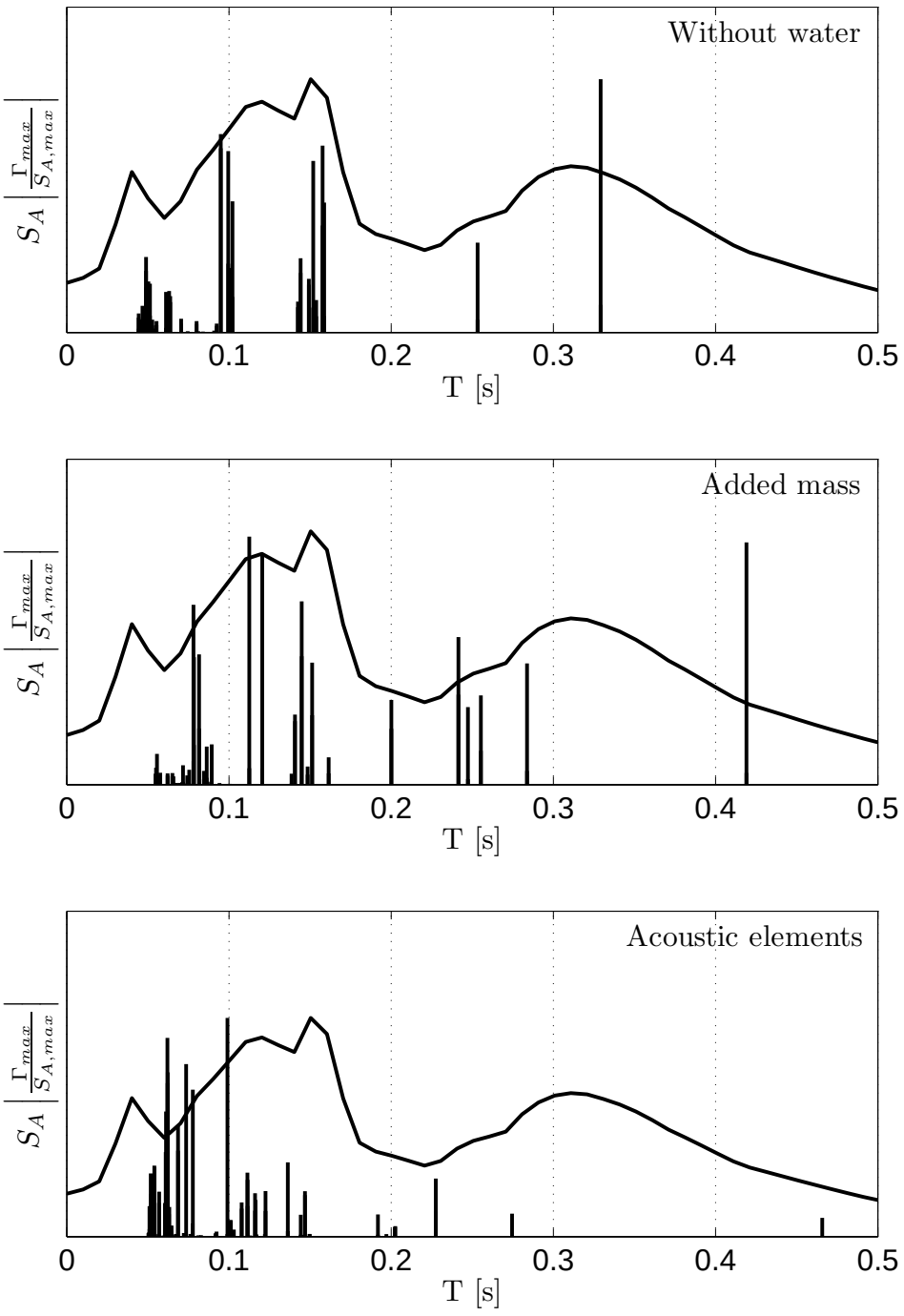

Figure F.2: $T_R = 1000$ years

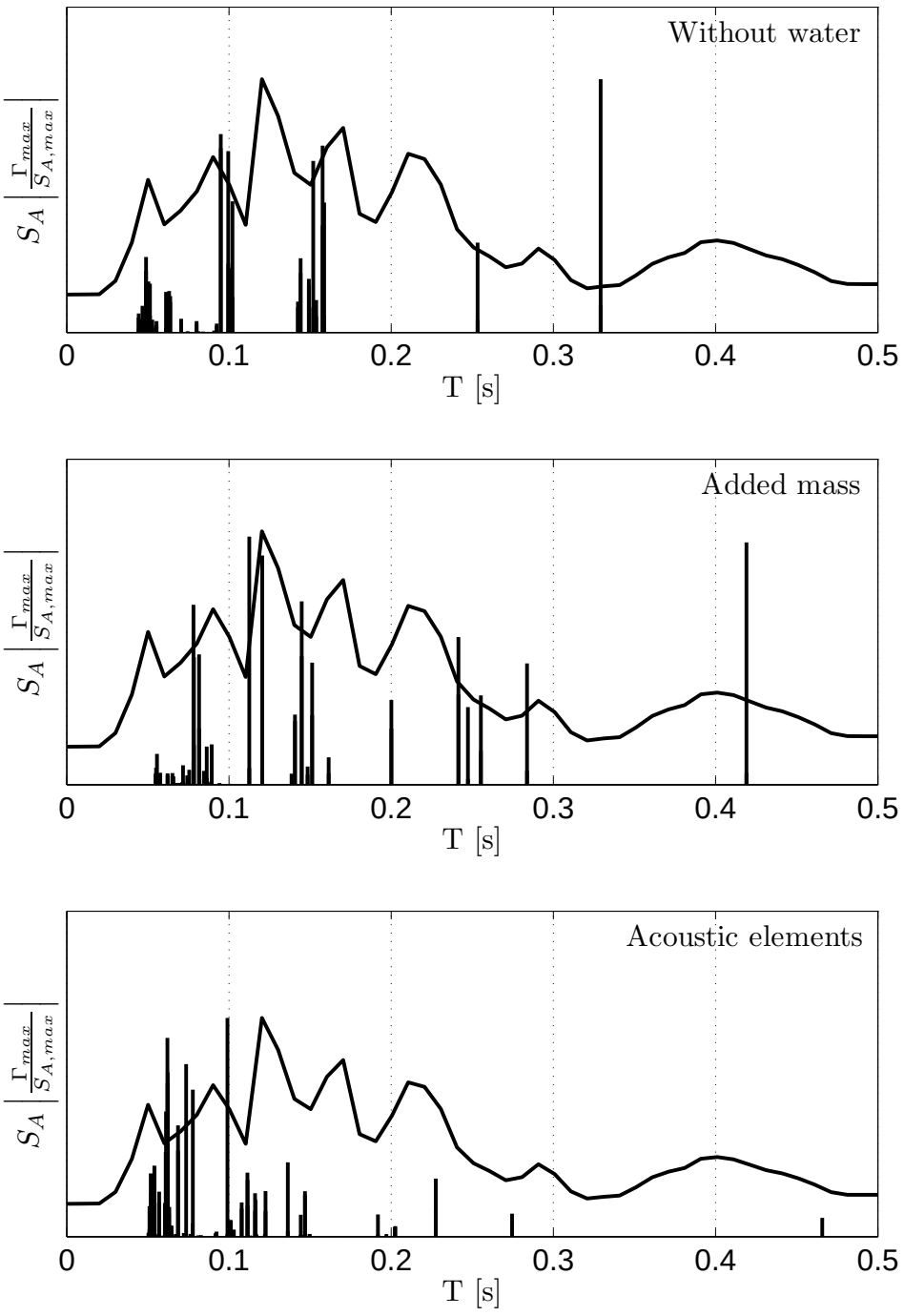

Figure F.3: $T_R = 3000$ years

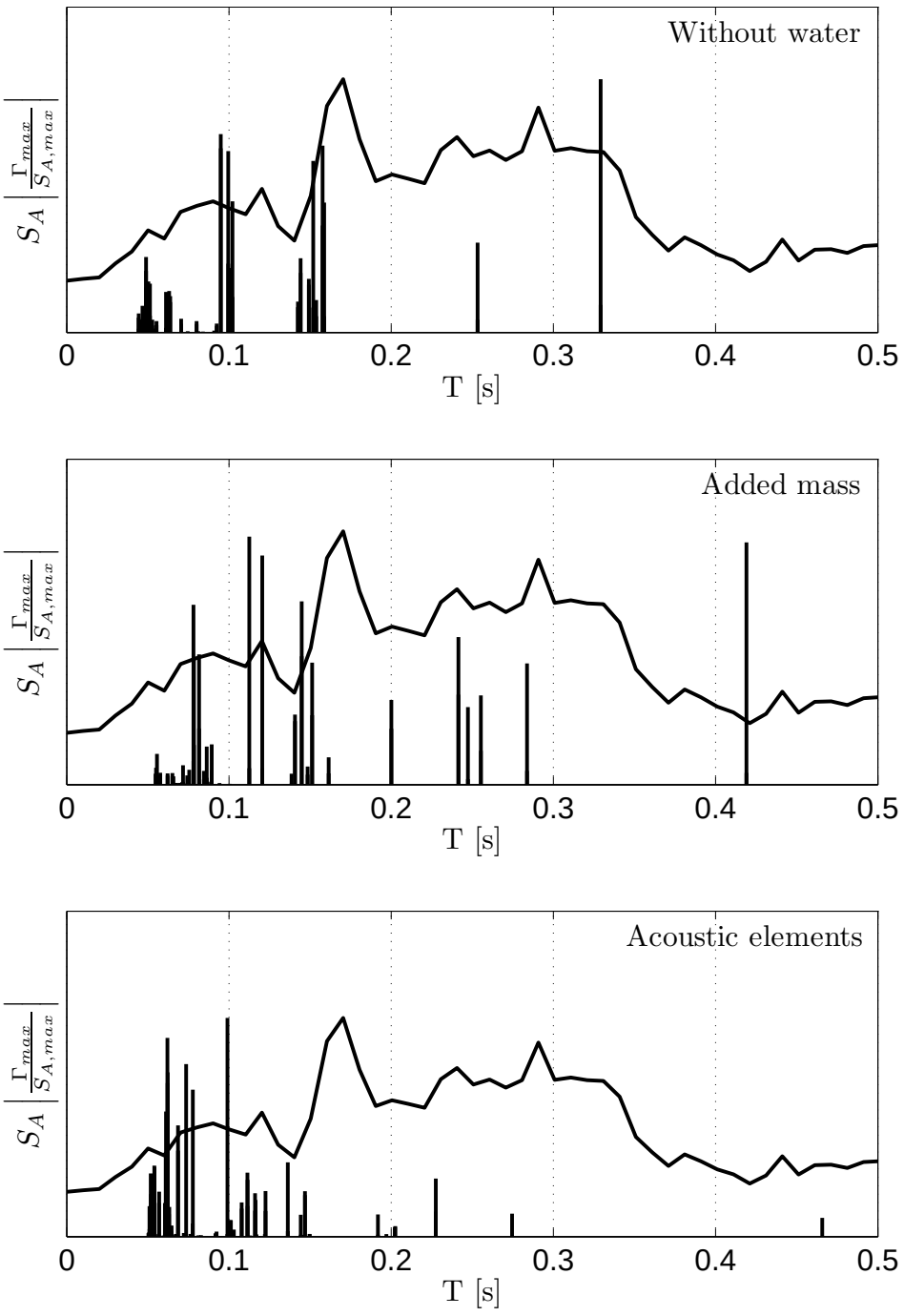

Figure F.4: $T_R = 10\,000$ years

F.2 Soil amplification

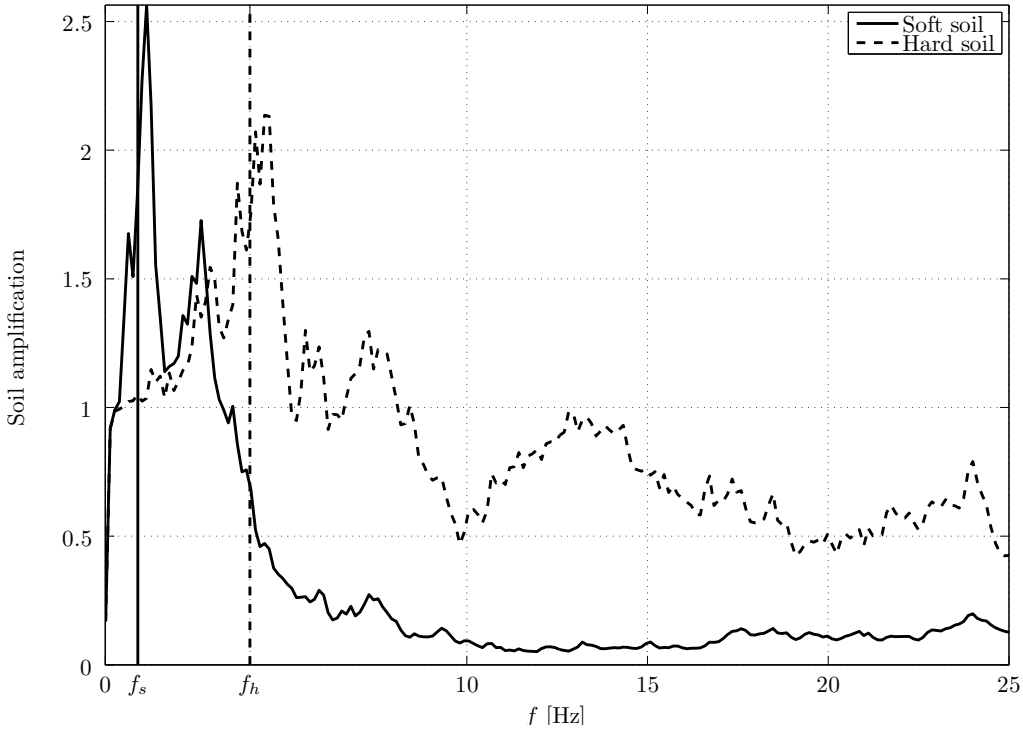

Figure F.5: $T_R = 475$ years, Horizontal

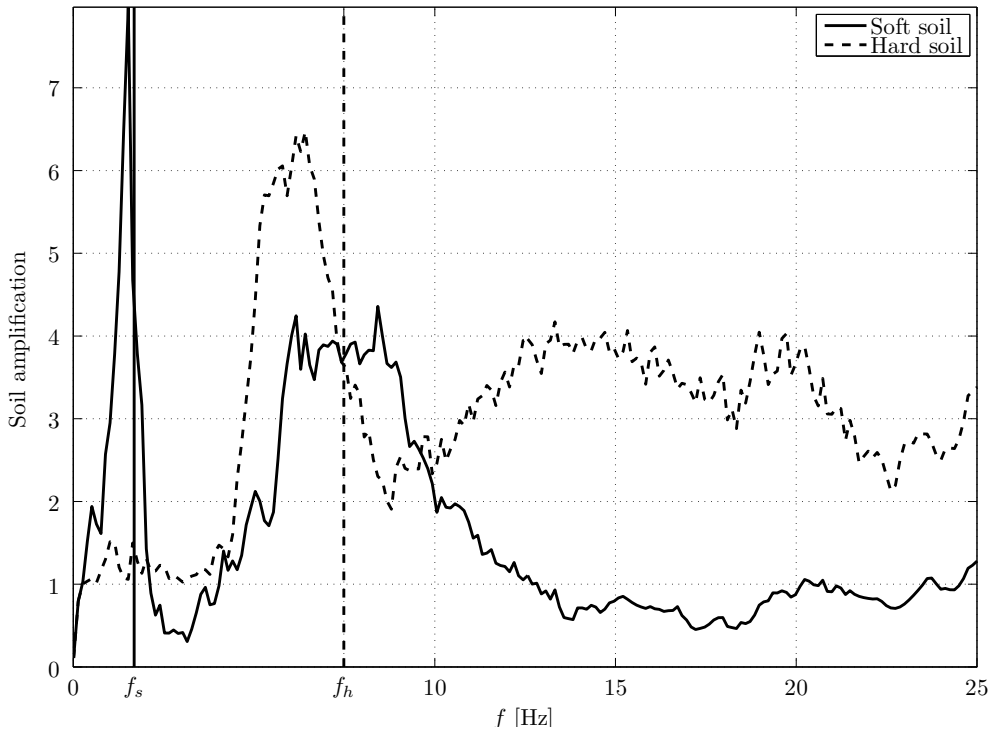

Figure F.6: $T_R = 475$ years, Vertical

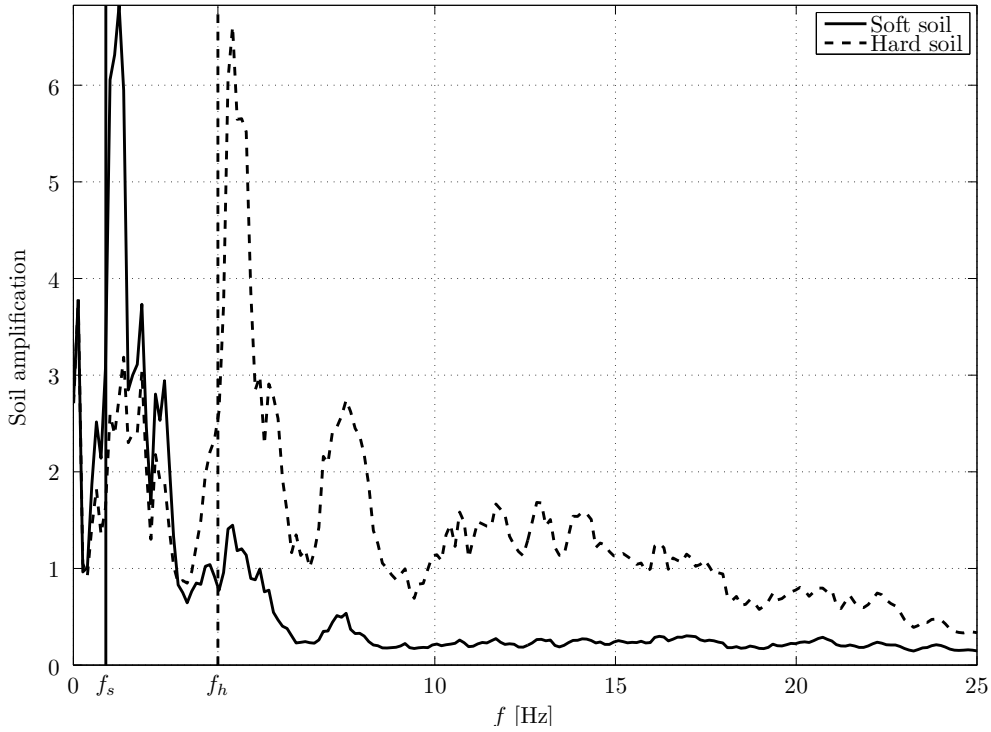

Figure F.7: $T_R = 1000\,\text{years}$, Horizontal

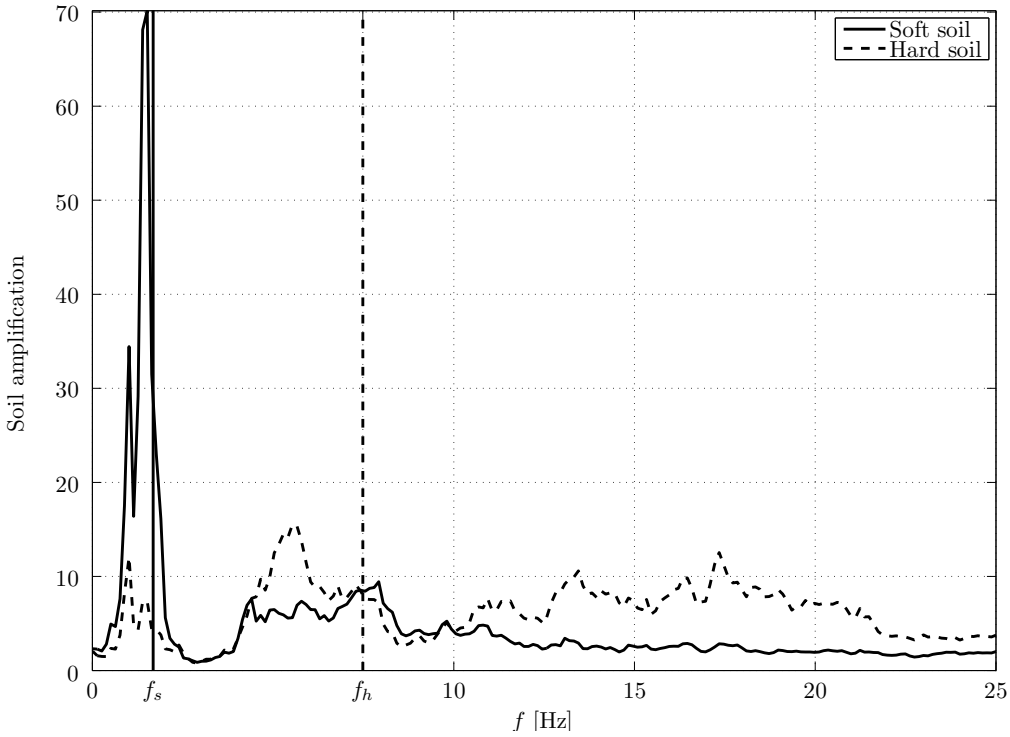

Figure F.8: $T_R = 1000\,\text{years}$, Vertical

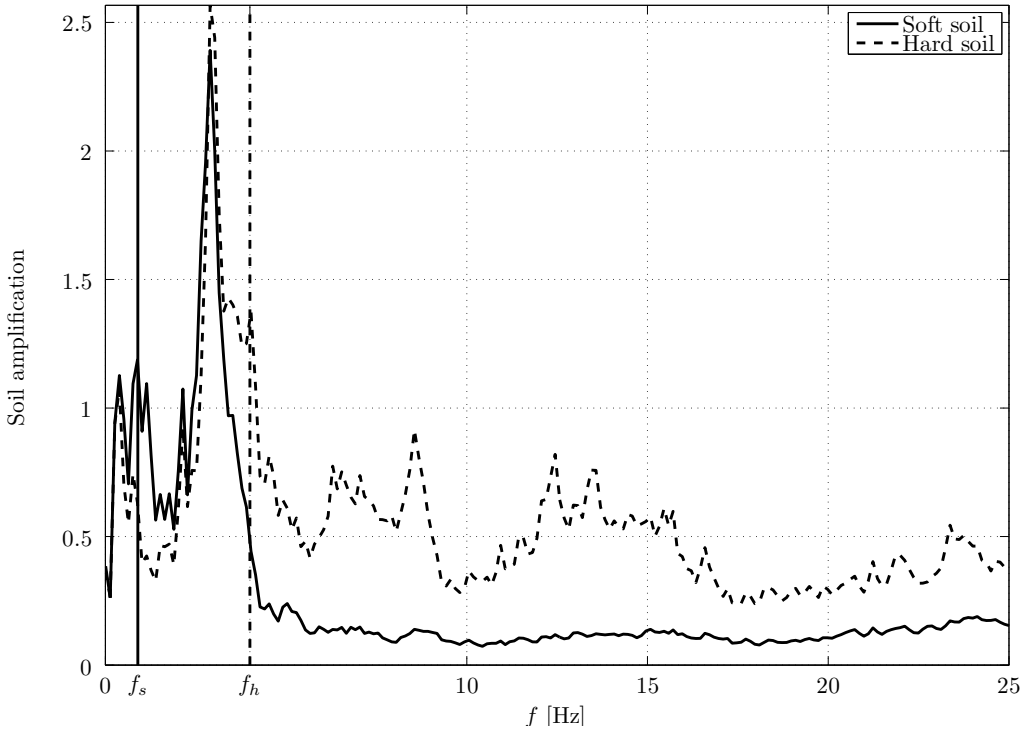

Figure F.9: $T_R = 3000\,\text{years}$, Horizontal

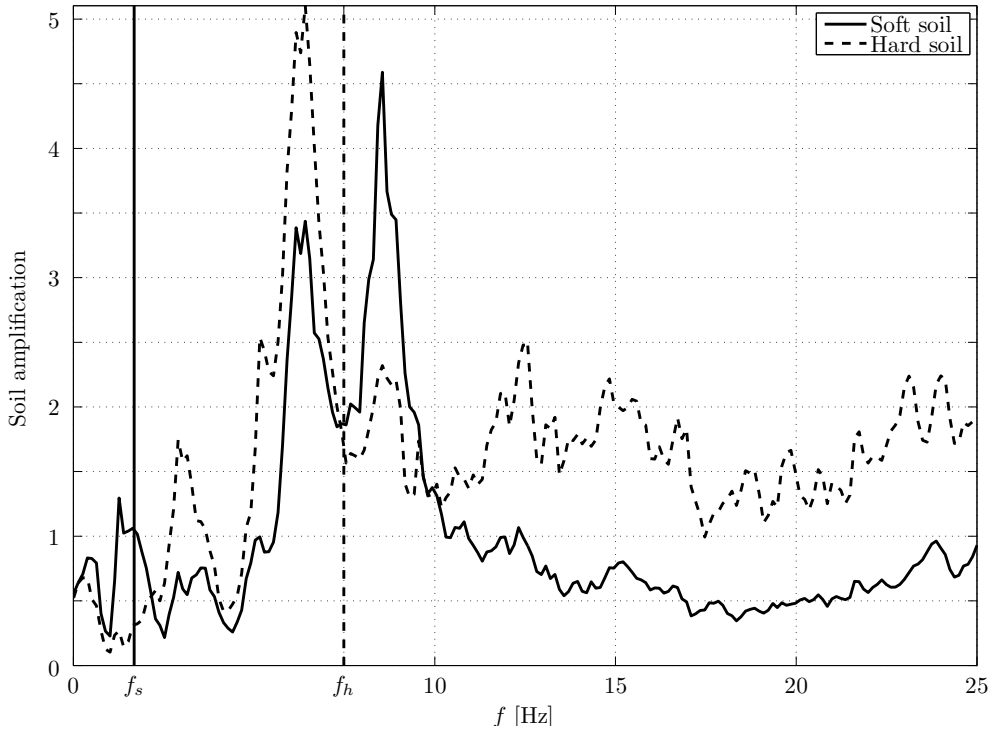

Figure F.10: $T_R = 3000\,\text{years}$, Vertical

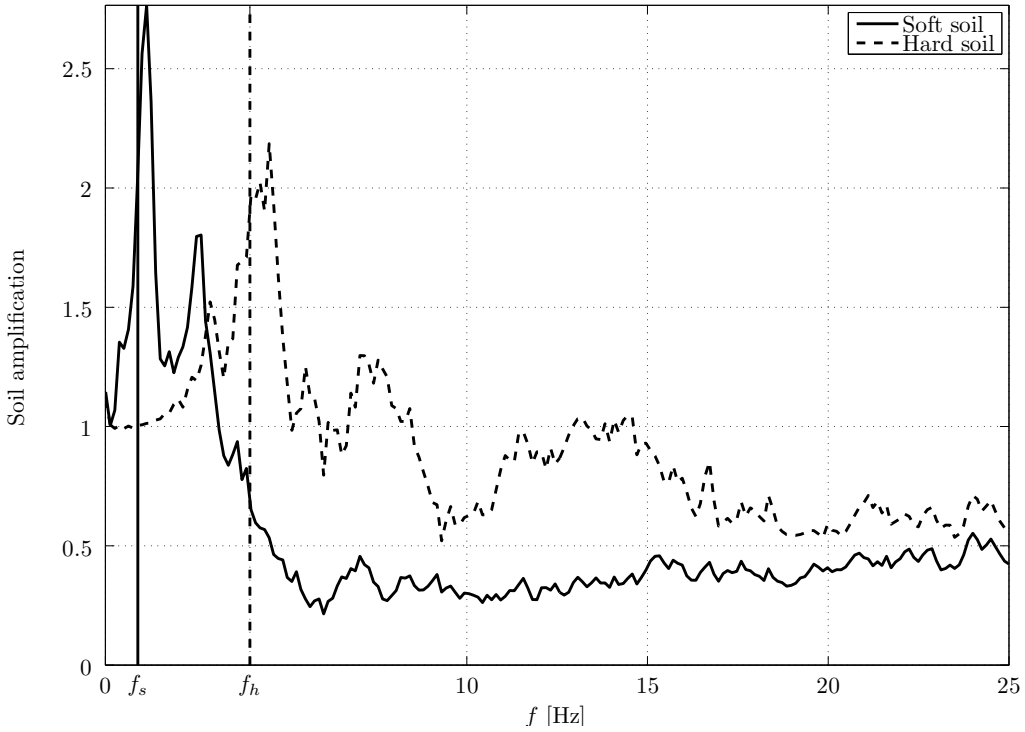

Figure F.11: $T_R = 10\,000$ years, Horizontal

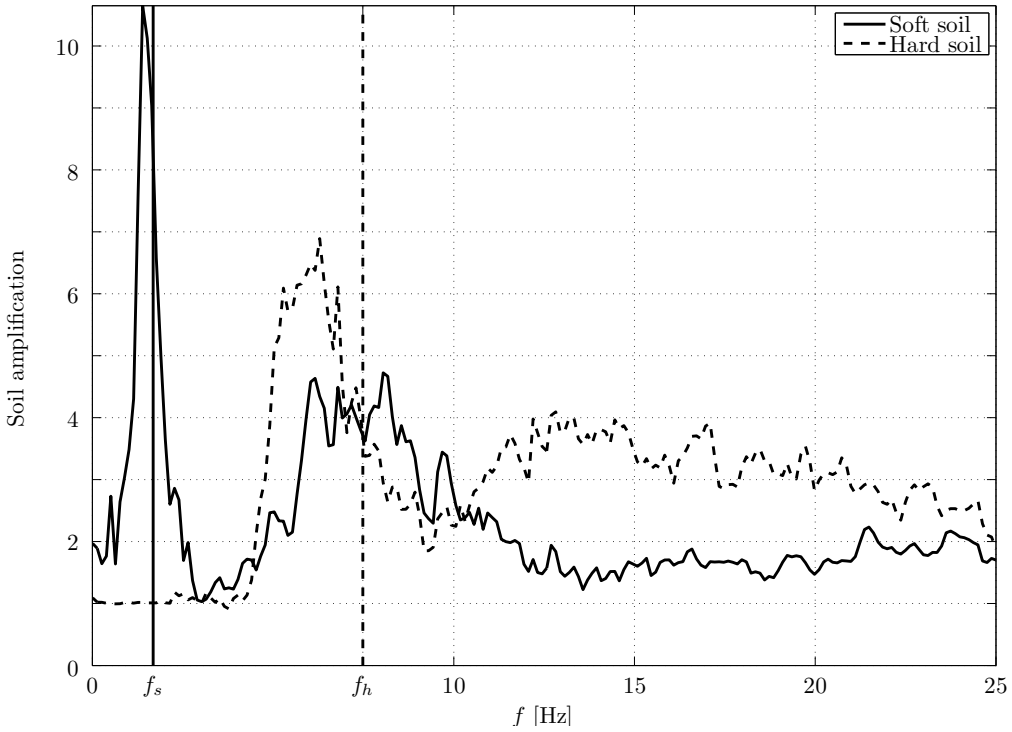

Figure F.12: $T_R = 10\,000$ years, Vertical